EXPERIMENTAL AND NUMERICAL INVESTIGATION OF TWO-DIMENSIONAL PHOTONIC CRYSTALS FOR APPLICATION IN INTEGRATED OPTICS

THÈSE N^O 2949 (2004)

PRÉSENTÉE À LA FACULTÉ SCIENCES DE BASE

Institut de photonique et d'électronique quantiques

SECTION DE PHYSIQUE

ÉCOLE POLYTECHNIQUE FÉDÉRALE DE LAUSANNE

POUR L'OBTENTION DU GRADE DE DOCTEUR ÈS SCIENCES

PAR

David LEUENBERGER

M.Sc. in Physics, Université de Berne
de nationalité suisse et originaire de Rohrbachgraben (BE)

acceptée sur proposition du jury:

Dr R. Houdré, directeur de thèse
Dr D. Erni, rapporteur
Prof. A. Forchel, rapporteur
Prof. M. Ilegems, rapporteur
Prof. O. Martin, rapporteur

Lausanne, EPFL
2004

Contents

To my family

Abstract

Two-dimensional (2D) photonic crystals (PhCs) at near-infrared wavelengths are promising candidates for novel integrated optics applications. The main focus being on 'all PhC' monolithically integrated optical circuits. Because of well established fabrication technologies particular emphasis is on 'quasi' 2D PhCs where a 2D lattice of air holes is etched through a planar step-index waveguide providing the optical confinement in the third dimension. This approach has been successfully demonstrated both in GaAs and InP-based systems.

We have studied vertical low-index-contrast structures both in GaAs and InP. These structures suffer inherently from radiation losses that are strongly affected by the air hole depth and shape. A semi-analytical 'ε''-model' enables out-of-plane scattering to be described by an effective imaginary dielectric constant in the air-holes which can be used in 2D finite difference time domain (FDTD) calculations. The model, once validated by 3D FDTD, allows us to deduce from optical simple slab transmission measurements the structural parameters (*e.g.* size, depth and form of the hole).

The experimental transmission spectra are obtained with the so-called 'internal light source technique' (ILS), which allows for quantitative normalised transmission measurements, thus eliminating the uncertainties due to the in-out coupling arising in alternative characterisation techniques, *i.e.* end-fire. The ILS technique proved to be a versatile method without stringent limits for assessing the fabrication parameters (air-filling factor and loss) but also proved to be suitable for testing building blocks.

In this thesis different building blocks were fabricated in the GaAs system and analysed using diverse modeling techniques (*e.g.* plane wave expansion, FDTD and coupled mode theory). The first building block was used to study contra-directional coupling of the fundamental mode with higher-order modes in channel waveguides. It is an extension of the work on waveguides with symmetric periodic corrugation to the case of multi periodicity. We showed that by breaking the translational symmetry in these structures referred to as hybrid waveguides, the number of mini-stopbands is increased and not, as one could have expected, decreased.

A second building block analysed to guide light around the corner, are cavity resonant bends (CRBs). As our analysis showd that CRBs work best with non-degenerate cavity modes, different low-symmetry order cavities were studied with differ coupling coefficients between cavity and waveguides. Unfortunately, the resulting peak transmission and overall performance was below our expectations.

An important building block in integrated optics are directional couplers. They have a potential for applications such as 3dB-intensity splitting or channel add-drop filtering. To reduce the coupling length, transmission measurements of a series of coupler structures of different lengths were taken. In the case of two W3 waveguides separated

by a single row, the coupling length proved to be very dependent on the hole diameter in the single row. For this case the experimentally determined coupling length, which has been validated by both PWE and FDTD simulations, was of the order of 350 periods which corresponds to an absolute length of about 80 μm, a value that is small for conventional optics, but rather large for the domain of PhC optics where due to the unusually high propagation losses the integrated circuit has to be kept small. This value could, however, be reduced by a factor of at least three when reducing the ratio between the barrier hole and the nominal hole radius to 0.5.

Finally we studied the waveguides needed to connect the different building blocks. The standard solution are channel waveguides, line-defects obtained by omitting a number of rows of holes. An alternative approach are coupled cavity waveguides (CCWs). They not only offer the potential for waveguiding but may also be used for non-linear optics by exploiting the special dispersion properties of CCWs (*e.g.* low group-velocity). A tight-binding model has been set-up that describes the interaction between the neighbouring cavities and that allows one to deduce the dispersion properties of the chain from the single cavity field distribution.

Résumé

Les cristaux photoniques (CPs) bidimensionnels (2D) pour le proche infrarouge sont des candidats prometteurs pour des applications innovantes pour l'optique intégré. L'objectif ultime est la réalisation de circuits optiques 'tout CPs'. En raison de la maturité des technologies associées, une attention particulière s'est tournée vers les CPs 'quasi 2D' constitués d'un réseau 2D de trous d'air gravés dans un guide d'onde planaire constitué d'une hétérostructure d'indice qui permet le confinement optique dans la troisième dimension. Cette approche a été démontrée avec succès aussi bien dans les systèmes à base de GaAs et que dans ceux à base d'InP.

Nous avons étudiés des structures verticales à faible contraste d'indice à la fois dans le GaAs et dans l'InP. Ces structures souffrent intrinsèquement de pertes radiatives dont l'intensité dépend de la profondeur et de la forme des trous. Le modèle semi analytique dit 'ε'''' permet de décrire la diffusion hors plan par une constante diélectrique imaginaire dans les trous et peut être implémenté dans les algorithmes de Différences Finies dans le Domaine Temps (FDTD, Finite Difference Time Domain). Après généralisation au cas tridimensionnel, ce modèle permet de déduire des paramètres structurels comme la taille, la profondeur ou la forme des trous à partir des mesures optiques de transmission à travers de simples pavés de CPs.

Les spectres de transmission expérimentaux sont obtenus par la technique dite de la 'source interne de lumière' (Internal Light Source, ILS). Cette technique autorise des mesures quantitatives de transmission et élimine certaines incertitudes inhérentes aux autres techniques, comme le couplage entrée-sortie dans la technique dite 'End-fire'. La technique ILS s'est avérée être une méthode efficace et sans véritable point faible pour évaluer les paramètres de fabrication (facteur de remplissage, pertes) et tester des composants élémentaires.

Dans le cadre de cette thèse, plusieurs composants élémentaires ont été fabriqués sur des échantillons GaAs et analysés au moyen de diverses techniques de modélisation comme la décomposition en ondes planes (Plane wave expansion, PWE), la FDTD ou la théorie des modes couplés. En premier lieu, nous avons étudié le couplage contra directionnel du mode fondamental d'un guide d'onde avec les modes d'ordre supérieur, généralisant ainsi les travaux sur les guides corrugués. En brisant la symétrie de translation de nos guides, nous avons obtenus des guides hybrides pour lesquels le nombre de mini-bande interdites, contrairement à notre intuition initiale, augmente.

En second lieu, nous avons étudié la possibilité de faire tourner la lumière au moyen de virages à cavités résonantes (Cavity resonant bends, CRBs). Comme notre analyse montrait que les CRBs fonctionnent mieux avec des modes de cavité non dégénérés, diverses cavités à faible ordre de symétrie ont été étudiées. Malheureusement, les pics de transmission correspondant et les performances globales n'ont pas atteint les niveaux

escomptés.

Les coupleurs directionnels constituent un composant important de l'optique intégré en raison de leurs applications potentielles comme le filtrage 'add-drop' ou le démultiplexage à faibles pertes. Afin de réduire la longueur de couplage, nous avons mesuré la transmission de coupleurs de longueurs différentes. Dans le cas de deux guides W3 séparés par une unique rangée de trous, la longueur de couplage s'est avérée fortement dépendante du diamètre des trous de la rangée de séparation. La longueur de couplage déterminée expérimentalement fut de l'ordre de 350 périodes, soit une longueur absolue d'environ 80μm. Cette distance, confirmée par les simulations FDTD et PWE, est certes faible pour l'optique traditionnelle, mais relativement grande pour l'optique dans les CPs où les pertes de propagation sont très élevées. Nous pouvons en revanche espérer réduire cette distance au minimum d'un facteur 3 en réduisant de 50 % le diamètre des trous de la rangée de séparation.

Enfin, nous avons étudiés les guides nécessaires à la connexion entre les différents composants élémentaires. Les solutions standard sont obtenues en omettant une ou plusieurs rangées de trous dans le CP. Les guides à cavité couplées constituent une autre alternative. Non seulement intéressants pour leurs propriétés de guidage, leurs propriétés de dispersion originales (faible vitesse de groupe) peuvent aussi être utilisées pour l'optique non linéaire. Un modèle a été développé pour décrire l'interaction entre les cavités voisines et obtenir les propriétés de dispersion de la chaîne à partir de la connaissance du champ dans la cavité élémentaire.

Zusammenfassung

Zweidimensionale (2D) Photonische Kristalle (PKs) für das nahe Infrarot sind viel versprechende Kandidaten für neuartige Anwendungen in der Integrierten Optik. Der Fokus liegt auf komplett PK basierten monolithisch integrierten optischen Chips. Spezieller Nachdruck wird auf 'quasi' 2D PKs gelegt wo ein 2D Gitter von Löchern durch einen flachen Schichtwellenleiter geätzt wird, der für die vertikale Führung der Mode verantwortlich ist. Das Potential dieses Ansatzes wurde schon mehrmals für GaAs und InP-basierte System unter Beweis gestellt.

Sowohl in GaAs als auch in InP haben wir vertikale Strukturen mit schwachem vertikalem Indexunterschied untersucht. Solche Strukturen leiden naturgemäss unter Strahlungsverlusten welche stark von der Tiefe und Form der Löcher beeinflusst werden. Ein halbanalytisches 'ε''-Modell' erlaubt die Streuverluste in eine effektive komplexe Dielektrizitätszahl in den Löchern zu übersetzten, welche dann in 2D Finite Difference Time Domain (FDTD) Simulationen integriert werden kann. Das Modell, einmal durch 3D FDTD bestätigt, erlaubt von Transmissionsmessungen von simplen PK Blöcken die strukturellen Parameter (Grösse, Tiefe und Form der Löcher) abzuleiten.

Die experimentellen Transmissionsspektren werden mit der so genannten 'Internal Light Source (ILS) Technik' aufgenommen, welche quantitative normalisierte Messungen erlaubt und befreit ist von Unsicherheiten im Zusammenhang mit dem ein- und auskoppeln von Licht, wie es z.B. der Fall ist bei der 'End-fire' Technik. Die ILS Technik hat sich als zuverlässige Technik bewährt, um die Fabrikationsparameter zu bestimmen, aber auch für die Messung von komplizierteren Bausteinen.

Verschiedene Konzepte und Bausteine wurden im GaAs System fabriziert. Sie alle wurden mit verschieden numerischen Methoden ('Plane Wave Expansion (PWE)', FDTD und der Theorie der gekoppelten Moden) analysiert. Der erste Bausteine war dazu bestimmt, die Co-direktionelle Kopplung in PK Kanal-Wellenleitern zu untersuchen. Es handelt sich dabei um eine Erweiterung der Arbeit auf Wellenleitern mit periodischen Rändern. Wir haben gezeigt dass das Durchbrechen der Translations Symmetrie nicht zu einer Abnahme sondern zu einer Zunahme von so genannten Mini-Stopbändern führt.

Ein anderer Baustein in der Integrierten Optik sind Direktionelle Koppler. Sie könnten potentiell als 3dB-Intensitätssplitter oder als 'Add-drop'-Filter eingesetzt werden. Die Ausmessung von Kopplern mit verschieden Längen erlaubt es einen die Kopplungslänge zu bestimmen. Im Fall von zwei W3 Wellenleitern von einer Lochreihe separiert zeigte sich die Kopplungslänge sehr abhängig vom Lochdurchmesser in der Barriere. Die experimentell bestimmte Kopplungslänge, welche sowohl durch PWE als auch durch FDTD Simulationen bestätigt wurde, war 350 Perioden was ungefähr einer Länge von 80 μm entspricht. Dieser Wert ist klein in Bezug auf konventionelle inte-

grierte Optik, jedoch eher gross im Vergleich zu PK Bausteinen, wo die Propagations Verluste grösser sind und die Bausteine deshalb klein gehalten werden sollten. Dieser Wert könnte jedoch um mindestens einen Faktor 3 reduziert werden, wenn die Löcher in der Barriere nur halb so gross gemacht würden wie die umliegenden.

Um verschiedene Bausteine auf dem gleichen Chip zu verbinden braucht man Wellenleiter. Die übliche Lösung sind Liniendefekte wo eine gewisse Anzahl von Lochreihen ausgelassen wird. Ein alternative Ansatz sind 'Coupled Cavity Waveguides (CCWs)'. Sie können potentiell nicht nur als Wellenleiter eingesetzt werden, sondern auch für exotischere Anwendungen aus der Nichtlinearen Optik welche oft auf den speziellen Dispersionseigenschaften von CCWs basieren (z.B. kleine Gruppengeschwindigkeiten). Wir haben ein 'Tight-binding' Modell entwickelt, welches die Interaktion zwischen den einzelnen Nachbarskavitäten beschreibt und welches erlaubt die Dispersionseigenschaften einer Kette aus Kavitäten aus der Feldverteilung der einzelnen Kavität abzuleiten.

Planare PKs haben jetzt ein Reifestadium erreicht wo sie als neue Materialien für die Integrierte Optik in Betracht gezogen werden können.

Preface

Photonic crystals (PhCs) consist of periodic arrangements of dielectric (or metallic) elements with a strong dielectric contrast [1]. In these structures, the achieved wavelength-scale periodicity affects the properties of photons in a way similar to that in which semiconductor crystals affect the properties of electrons. Light propagation along particular directions is forbidden within relatively large energy bands known as photonic bandgaps (PBGs) in analogy with the concept of electronic bandgap in semiconductors. The term 'photonic band gap' was introduced by E. Yablonovitch via his pioneering paper on 'Inhibited spontaneous emission in solid state physics and electronics' in 1987 [2].

Initially proposed as a generalization of 1D dielectric Bragg mirrors to two or three directions [2,3], PhCs have opened new ways to tailor the lightmatter interaction and in particular to control spontaneous emission [2,4]. Moreover, the introduction of line or point defects into simple PhCs results into allowed photonic states inside the stopgap, whose shapes and properties are dictated by the nature of the defect, e.g., guided modes propagating in a line defect or cavity modes confined in a point defect (see Fig 1).

(a)   (b)
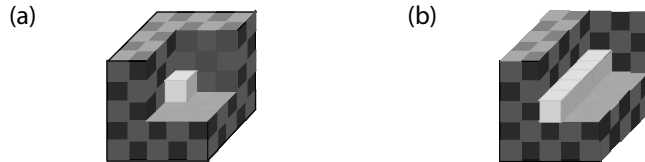
Figure 1: Periodic electromagnetic media can trap light in a) cavities (0D point defect), b) in waveguides (1D-defects, wires)
[Un medium périodique électromagnétique peut enfermer de la lumière dans a) une cavité (défaut ponctuel 0D), b) dans un guide d'onde (défaut unidimensionnel).]

A material with a three-dimensional (3D) complete photonic band gap may be named *photonic insulator* [5] by analogy to electronic structures. Photons with an energy inside the band gap will be rejected whatever direction in which they attempt to penetrate the material. This rejection of light leads to many interesting properties. One of these properties, the inhibition of spontaneous emission, initiated research into novel light emitters and zero-threshold lasers. It is based on a modification of the density of states in the energy region of the electronic band gap. The goal is not to inhibit spontaneous emission completely (because this would also inhibit stimulated emission), but to allow it to go only into the one lasing mode. Another key property is the suppression of light propagation inside the band gap of bulk PhC, and related to it, the strong confinement of light and the existence of high-reflecting omni-directional mirrors. This potentially opens the way to high-Q cavities with an extremely small

cavity volume in the order of λ^3 which may allow the spontaneous emission to be enhanced by means of the Purcell effect [6] (which scales with Q/V_{cav}). The quality factors are, however, limited by optical scattering induced by the sidewall roughness [7].

On the other hand, strong confinement of guided modes inspired several groups in the mid-nineties to use PhCs in the domain of integrated optics [8–10]. It has been shown that, although an omnidirectional PBG is only possible in 3D PhCs, a 2D PhC combined with a step-index waveguide in the vertical direction offers enough light control for integrated optics applications. Since then the ever-growing subject (especially 2D PhC) has drown the attention of optics industry. As opposed to conventional integrated optics devices that are measured in millimeters, this new generation of PhC devices should operate on the nanoscale. This reduction in size is crucial for high-density integration of different functionalities on a single chip, providing a counterpart to electronically integrated circuits. The advantages are a huge saving in chip-size on the one hand and the promise of novel functionalities on the other. Many promises have been made by the PhC research community in the years 2000-2002 about the potential applications of PhCs. These optimistic prognoses have been nourished by the visionary but a little bit theoretical proposals from the Massachusetts Institute of Technology (MIT). A large part of their simulations have been performed on the 'pillar in air system', a pure two-dimensional model system which provides single-mode operation for channel waveguides with one missing row of pillars (W1), but which provides no vertical confinement. Also, the crucial role of loss, as it occurs in real-world applications, was often underestimated. Fabrication tolerances were often not considered.

Alongside the telecom boom, many research groups focused on the development of devices for all-optical networks. In optical networks two different philosophies are established: 1) packet-switching, 2) wave-length division multiplexing (WDM) and its derivatives. The potential of PhCs lies rather in the second one where a multitude of different channels have to be separated, combined and redirected. The separation of the closely spaced channels may take advantage of the high dispersiveness and the availability of high-Q cavities in PhCs. The functionalities to be covered include filters, add-drop filters, dispersive elements (*e.g.* superprism), Y-splitters, combiners. A lot of 'engineering' had to and still has to be done to develop these concepts. The high index-contrast present in PhCs required novel modelling techniques with respect to conventional integrated optics (*e.g.* the beam-propagation method was not applicable). The methods can be divided into frequency domain methods (*e.g.* the plane wave expansion method (see chapter 4), multipole expansion method, modal expansion) and time-domain methods (*e.g.* finite difference time-domain (FDTD)). Although most simulations are performed in two dimensions, full three-dimensional simulations (*e.g.* 3D FDTD) are getting increasingly popular, due to the availability of better algorithms and faster super-computers. The modelling tools have reached a very high quality level and fabrication lags somewhat behind. Nevertheless huge progress has been made in fabrication of both 2D and 3D structures.

The main issues in the PhC world during the last four years have been:

. Dimensionality: Do we need structures with a full 3D band gap or can we get around with a 2D band gap combined with a vertical index guiding structure? If so, should we opt for a low-index contrast or a high-index contrast structure?

. Losses: Which are the main sources and how can they be understood, modelled and finally reduced? What are the fabrication tolerances?

. Outside-world connection: PhCs integrated circuits are meant to be small. How can one couple most efficiently from a fibre into a PhC?

The year 2003 and especially the Ascona workshop[1] revealed some disillusionment about the sectors in which the PhCs may outstrip the performance of conventional integrated optics and the directions in which the real potential of PhCs lay. With the crash in the telecom sector, a trend to address some more fundamental questions in PhC physics (*e.g.* quantum optics in PhCs, nonlinear phenomena) could be observed.

Another hot topic in Ascona were losses, which seem excessively high compared to conventional integrated optics when indicated in dB/cm. It is, however, still not clear in which units the losses should be measured (*e.g.* dB/mm, dB/μm , dB/device, dB/building block).

The present work deals with two-dimensional low vertical index contrast PhC slabs. It investigates both experimentally and theoretically some of the more basic building blocks of PhC-based integrated optics. This includes the investigation of the scattering and mode-coupling mechanism in non-symmetric straight waveguides.

The manuscript is divided into eight chapters. The first three chapters have an introductory character. Chapter 1 introduces the basic PhC concepts that are needed throughout the manuscript. A presentation of the different fabrication techniques available for two-dimensional PhCs, how they work and the present state-of-the-art is given in chapter 2. Chapter 3 explains in detail the optical properties of the samples, the internal-light-source (ILS) method, the performance of the set-up, the basic optical characterisation and the influence of the third dimension in two-dimensional PhC slabs (loss model). In chapter 4 the the plane-wave expansion (PWE) method and its potentials and limitations are investigated in detail. Chapter 5-7 follow a classical line of a short presentation of the underlying idea, then the optical measurements, followed by a thorough discussion supported by modelling, and finally a short conclusion.

For the interpretation of the experimental data, the FDTD method provided an extremely valuable and complementary tool. The 2D FDTD code, which stems from a collaboration with Dr. Mario Agio from the university of Pavia, Italy and FORTH, Greece, became accessible only after the samples were already fabricated. Therefore it could not be applied on the design optimisation process before the mask writing.

The last chapter is a theoretical work on coupled cavity waveguides (CCWs) and their dispersion properties. A tight-binding model is presented and successfully compared with the plane wave method. The work is rounded off by an overall conclusion and perspective section.

This thesis has been performed in the framework of the European project 'Photonic crystals for integrated optics' (PCIC) which is part of the European Union Information Societies Technology (IST) program. The project partners were: University of Würzburg (Germany), Ecole Polytechnique Palaiseau (EPP) (France), Foundation for

---

[1]Workshop and EOS Topical meeting on "Two Dimensional Photonic Crystals" August 25-30, 2002 Monte Verità, Ascona, Switzerland.

Research and Technology - Hellas (FORTH) (Greece), Royal Institute of Technology (KTH) (Sweden) and Opto+ (France).

The last part of the thesis was carried out in the framework of the National Centre of Competence in Research (NCCR) in Quantum Photonics.

Lausanne, January 2004

Chapter 1

Basic properties of photonic crystals

1.1 The photonic crystal zoo

There exists a large variety of different types of PhCs. They may be coarsely distinguished according to whether their dielectric function is periodic in one, two or three dimensions (as schematically shown in Fig. 1.1). Although a full band gap (no propagating solutions for any direction and any polarisation) exists only in three dimensions, for many applications a 2D or even a 1D (pseudo)-band gap is sufficient.
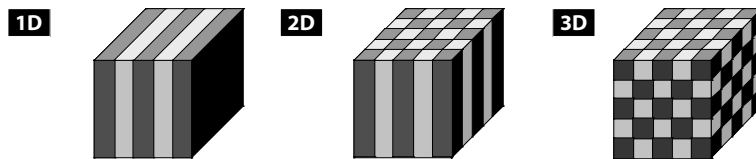
Figure 1.1: Schematic illustration of one-dimensional (1D), two-dimensional (2D), and three-dimensional (3D) photonic crystals (from Joannopoulos *et al.* [1]).
[Représentation schématique des cristaux photoniques à une dimension (1D), à deux dimensions (2D) et à trois dimensions (d'après Joannopoulos et al. [1]).]

1.2 One-dimensional photonic crystals

A type of one-dimensional PhC, known as multi-layer stack or **Bragg mirror**, had already been studied at the beginning of the twentieth century. It is a multilayer structure consisting of alternating layers of material with different refractive indices where the optical thickness of each layer corresponds to a quarter vacuum wavelength. Such a structure can be fabricated relatively easily by deposing alternatingly layers of two different materials on a substrate. The Bragg reflector has found many applications ranging from dielectric mirrors for high-power lasers to vertical cavity surface emitting semiconductor lasers (VCSELs).

Let us consider first the case of a plane wave with wavevector k impinging at **normal incidence** on a Bragg mirror with period a (see Fig. 1.2). Because of the periodicity in y-direction, the electromagnetic modes of the stack can be characterised by the wavevector k_y, with k_y restricted to $-\pi/a < k_y \leq \pi/a$ (Bloch theorem, see section 1.5.2). At each interface between different dielectrics a part of the light is reflected, but at every second interface an additional phase-shift of π does occur upon reflection.
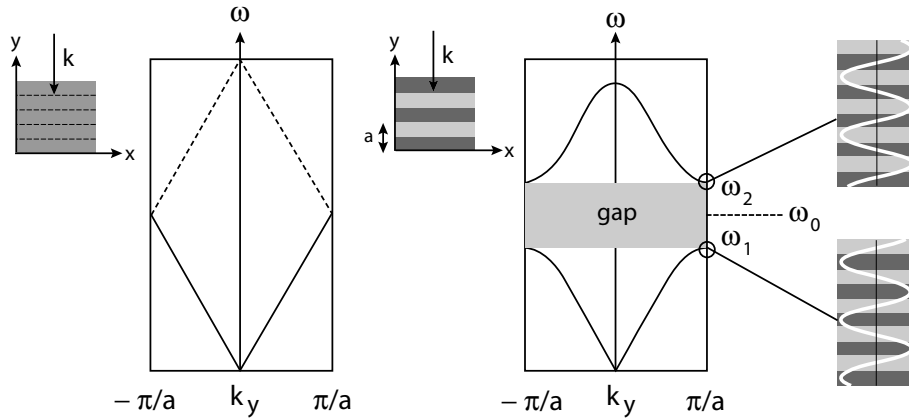
Figure 1.2: Left: Dispersion relation $\omega(k)$ of a uniform medium at normal incidence: The dashed lines show the 'folding' effect of applying Bloch theorem with an artificial periodicity a. Right: Dispersion relation of a one-dimensional periodic dielectric medium at normal incidence, where the anticrossing between the two counterpropagating modes has opened a gap at the $k = \pm\pi/a$ Brillouin-zone boundaries.
[A gauche: Relation de dispersion $\omega(k)$ d'un milieu uniforme sous incidence normale: La ligne pointillée montre l'effet de repliage des bandes en appliquant le théorème de Bloch avec une périodicité artificielle a. A droite: Relation de dispersion d'un milieu périodique unidimensionnel sous incidence normal où l'anticroisement entre les deux modes contra-propagatifs a ouvert une bande interdite au bord de la zone de Brillouin à $k = \pm\pi/a$.]

The phase difference between two successively reflected waves is $\phi = ka + \pi$. The total amount of reflected light is only important when $\phi \approx 2\pi$, *i.e.* the reflected waves interfere constructively. This is the case at the border of the Brillouin-zone. The superposition of the incident wave ($k_y = \pi/a$) and the reflected wave ($k_y = -\pi/a$) results in a standing wave pattern. The coupling of the two counter-propagating waves (with the same energy ω_0) by the reciprocal vector $G = 2\pi/a$ of the grating results in a band-splitting that removes the degeneracy and generates two standing wave modes with energies ω_1 and ω_2. The lower mode with $\mathbf{E} \propto \cos ky$ has its electrical field power concentrated in the high-ε region. The upper mode with $\mathbf{E} \propto \sin ky$, on the contrary, has its electrical field power concentrated in the low-ε region.

In one dimension and at normal incidence the bandwidth $\Delta\omega$ of the stop band in the frequency domain depends on the index contrast as [11].

$$\Delta\omega = \frac{4}{\pi}\omega_0 \sin^{-1}\left(\frac{n_{\mathrm{high}} - n_{\mathrm{low}}}{n_{\mathrm{high}} + n_{\mathrm{low}}}\right) \tag{1.1}$$

, where n_{low} and n_{high} depict the refractive indices of the two dielectric materials. The gap closes continuously with decreasing index contrast.

In the case of **oblique incidence** the situation becomes slightly more complex. The incident light can either be TE polarised (electrical field is perpendicular to the plane of incidence) or TM polarised. Without loss of generality, it can be assumed that $k_z = 0$. In this case the dispersion is a function of k_x *and* k_y. The structure being homogenous in x-direction, the k_x component of the incident wave is conserved whereas k_y is only
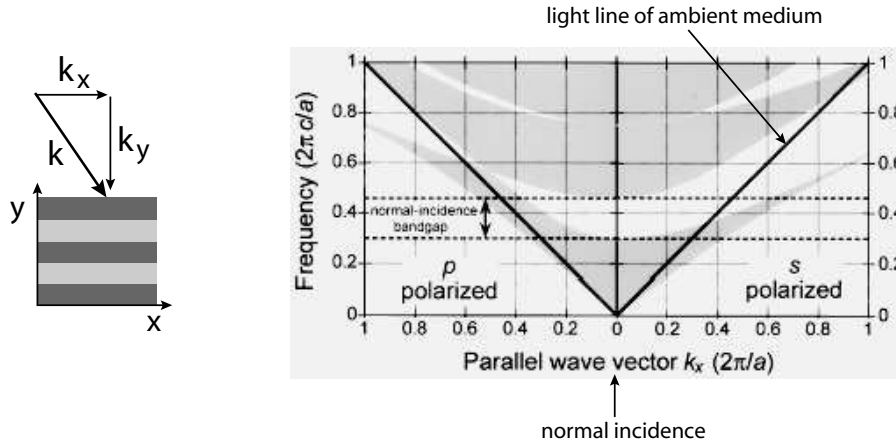
Figure 1.3: Projected band structure of a quarter-wave stack with $n_1 = 1$ and $n_2 = 2$. Modes exist only in the shaded regions. The s-polarised (TE) modes are plotted to the right of the origin, the p-polarised (TM) modes to the left (from J.N. Winn *et al.* [12]).
[*Structure de bande projetée d'une multicouche quart d'onde avec $n_1 = 1$ et $n_2 = 2$. Les modes existent seulement dans les régions ombrées. Les modes polarisés s (TE) et polarisés p (TM) sont indiqués respectivement à droite et à gauche de l'origine (d'après J.N. Winn et al. [12]).*]

defined modulo some reciprocal lattice vector and can be described by a wavevector K inside the first Brillouin zone. In this case it is convenient to project the $\omega(k_x, K)$ function onto the $\omega - k_x$ plane. The projected band structure is displayed in Fig. 1.3. In the gray regions there are electromagnetic modes for some values of K, whereas in the white regions there are no electromagnetic modes regardless of K. The solid line depicts the light line $\omega = ck_x$ of the ambient medium, *i.e.* vacuum.

At $k_x = 0$ the gap-width corresponds to the case of normal incidence (see Fig. 1.2). As $k_x \to \infty$ the projected bands converge to discrete values. This is due to the fact that for large k_x the modes become largely confined to the slabs with a high index of refraction and couple only weakly between different layers. Therefore they become independent of k_y [13]. It should, however, be noted that for a *semi*-infinite stack in a surrounding medium the system is no longer periodic in y-direction and can no longer be classified by a single value of k_y. These modes must be written as a weighted sum of plane waves with all possible k_y [12].

1.3 Two-dimensional photonic crystals

Although even in a 1D PhC omnidirectional reflection can be achieved under certain conditions [12,13], they are lacking design freedoms for the conception of photonic integrated circuits.

A purely 2D PhC would be periodic in the $x - y$-plane and infinitely extended along the z-direction, *i.e.* k_z is conserved. Such a system does not exist in reality, but a good approximation is attained by PhCs based on macroporous silicon (see Fig. 1.4). They are fabricated by electrochemical etching of pre-patterned silicon wafers. Very high aspect ratios of around 67:1 can be achieved leading to hole depths of $100\,\mu$m for
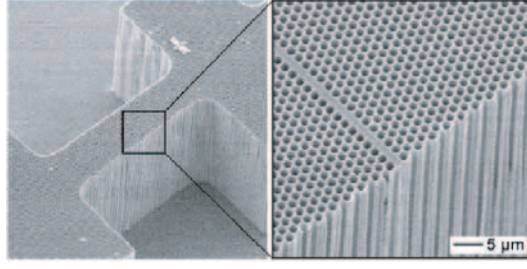
Figure 1.4: a) Laterally structured porous silicon sample with a line defect. The pores are
separated by 1.5 μm and 100 μm deep (from Birner *et al.* [14]).
*[Echantillon de silicium macroporeux avec un défaut unidimensionnel. Les pores
sont séparés de 1.5 μm et sont profond de 100 μm (d'après Birner et al. [14]).]*

a crystal period of 1.5 μm [14]. When working with a plane wave, this crystal behaves
like an ideal 2D structure.

In this thesis a different approach based on slab-structures, in which a vertical con-
finement is provided by index guiding, provided that $n_{\text{core}} > n_{\text{cladd}}$, has been followed.
Although these PhC slabs can confine light in three dimensions, the index confinement
in the vertical direction is not complete, but still sufficient for many integrated optics
applications.

1.3.1   Slab polarisation

The translational symmetry breaking by the vertical structure has consequences for the
light polarisation: In purely 2D PhCs the fields are homogenous in z-direction and the
distinction between TE and TM polarisation is exact. In slab structures the fields vary
as a function of the z-coordinate (see Fig 1.5).
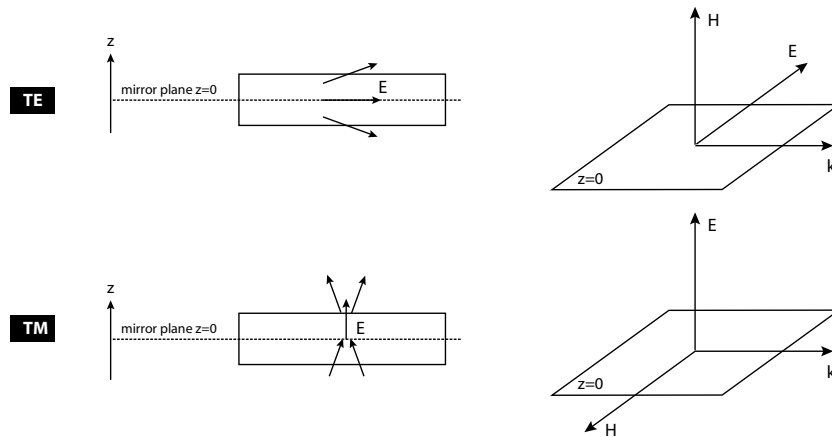
Figure 1.5: The polarisation inside the slab is defined with respect to the mirror plane at
$z = 0$. The electrical field distribution may either be even (TE-like) or odd
(TM-like).
*[La polarisation à l'intérieur du guide d'onde planaire à $z = 0$. La distribution
du champ électrique peut être soit paire (type TE) ou impaire (type TM).]*

For example, the field components of a TE PhC slab mode are (H_x, H_y, H_z) for
the magnetic field and (E_x, E_y, 0) for the electric field. However, when considering the

mirror plane $z = 0$ in the core layer of the symmetric structure, it still makes sense to distinguish between even (TE-like) and odd (TM-like) modes (which are purely TE/TM in the mirror plane itself) and the eigenvalue problem for the electromagnetic field is reduced to a single vertical component, *e.g.* H_z for TE-polarisation. For asymmetric PhC slab structures this separation breaks down [1] and the calculation of modes has to include all three field components. With the exception of the air-bridge membrane structures, a thin dielectric slab suspended in air, the vertical waveguide structure usually lacks an exact mirror symmetry with respect to the middle of the core layer. This might lead to polarisation mixing, especially at defects. In practice the symmetry braking can be weak if the index contrast is sufficiently high (so that the modes are strongly confined in the slab).

1.3.2 Lattice parameters

In two dimensions the most studied geometries are the square and the triangular lattice (see Fig. 1.6). Each of them is spanned by two direct lattice vectors. To each direct lattice a reciprocal lattice is assigned. When given a set $\mathbf{a}_1, \mathbf{a}_2, \mathbf{a}_3$ of direct lattice vectors (in the 2D case $\mathbf{a}_3$ can be chosen arbitrarily, *e.g.* $\mathbf{a}_3 = (0, 0, 1)$), the corresponding set $\mathbf{b}_1, \mathbf{b}_2, \mathbf{b}_3$ of reciprocal vectors is defined by $\mathbf{a}_i \cdot \mathbf{b}_j = 2\pi \delta_{ij}$. The solution to these equations is given by:

$$\mathbf{b}_1 = 2\pi \frac{\mathbf{a}_2 \times \mathbf{a}_3}{V_c}, \quad \mathbf{b}_2 = 2\pi \frac{\mathbf{a}_3 \times \mathbf{a}_1}{V_c} \quad \mathbf{b}_3 = 2\pi \frac{\mathbf{a}_1 \times \mathbf{a}_2}{V_c} \tag{1.2}$$

with $V_c = \mathbf{a}_1(\mathbf{a}_2 \times \mathbf{a}_3)$ being the volume of the primitive unit cell.
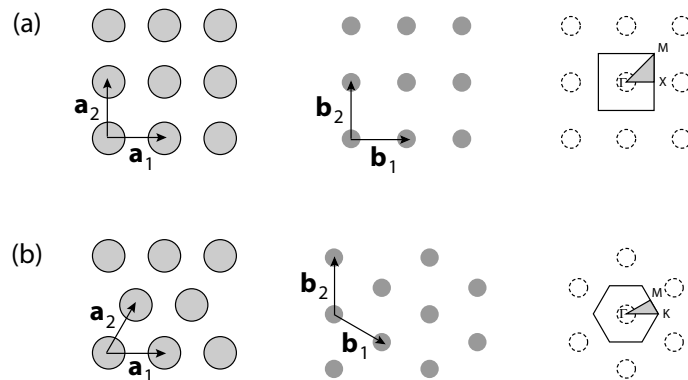
Figure 1.6: Direct lattice, reciprocal lattice and Brillouin zone including symmetry points of the two most common lattices in two dimensions: a) square lattice, b) triangular lattice.
[Réseau direct, réseau réciproque et zone de Brillouin avec les points de symétrie des deux réseaux les plus répandus: a) réseau carré, b) réseau triangulaire.]

Another important parameter is the (air)-filling factor which indicates the fraction of the hole or cylinder surface with respect to the total surface of the unit cell. The lattice parameters of the square and the triangular lattice are specified in Table 1.1.

---

[1]However, for an un-patterned asymmetric slab it is still possible to decouple the TE and TM equation set [15]

	geometry	
	square lattice	triangular lattice
direct vectors	$\mathbf{a}_1 = (1, 0)$; $\mathbf{a}_2 = (0, 1)$	$\mathbf{a}_1 = (1, 0)$; $\mathbf{a}_2 = (\frac{1}{2}, \frac{\sqrt{3}}{2})$
reciprocal vectors	$\mathbf{b}_1 = \frac{2\pi}{a}(1, 0)$; $\mathbf{b}_2 = \frac{2\pi}{a}(0, 1)$	$\mathbf{b}_1 = \frac{2\pi}{a}(1, -\frac{1}{3}\sqrt{3})$; $\mathbf{b}_2 = \frac{2\pi}{a}(0, \frac{2}{3}\sqrt{3})$
f	$\frac{R^2\pi}{a^2}$	$\frac{2\pi}{\sqrt{3}}\frac{R^2}{a^2}$
unit cell surface	a^2	$\frac{\sqrt{3}}{2}a^2$

Table 1.1: Direct and reciprocal vectors of the square and triangular lattice.
[Vecteurs directs et réciproques des réseaux carrés et triangulaires.]

1.3.3   Dispersion relation of the bulk crystal

The bulk crystal is characterised by its dispersion relation. It provides useful information on pseudo-gaps in directions of symmetry and the occurence of a complete gap. Fig. 1.7 shows the band diagram of an ideal 2D PhC calculated by the plane wave expansion method (PWE) with the vertical direction included by means of an effective index in the dielectric (see chapter 4).
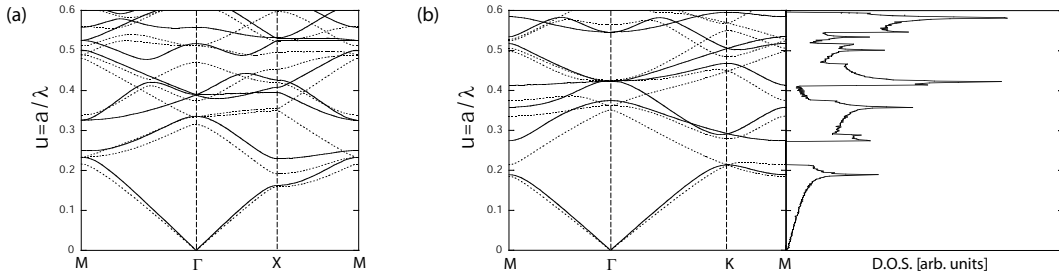
Figure 1.7: Band diagrams of a 2D PhC consisting of air holes inside dielectric matrix calculated by PWE for TE (solid line) and TM polarisation (dotted line) ($f = 0.3$, $\varepsilon_{\mathrm{sub}} = 11.4$, $\varepsilon_{\mathrm{cyl}} = 1$): a) square lattice, b) triangular lattice. For TE polarisation the density of states (D.O.S.) is indicated.
[Diagramme de bande d'un cristal photonique 2D constitué de trous d'air dans une matrice diélectrique, calculé par la méthode des ondes planes pour la polarisation TE (ligne solide) et TM (ligne pointillée) ($f = 0.3$, $\varepsilon_{sub} = 11.4$, $\varepsilon_{cyl} = 1$): a) réseau carré, b) réseau triangulaire. Pour la polarisation TE la densité d'état (D.O.S.) est indiquée.]

It depicts the dispersion of TE modes (solid lines) and TM modes (dotted lines) along the main symmetry directions of the square and the triangular lattice for the case of air holes in GaAs ($\varepsilon_{\mathrm{sub}} = 11.4$) and for a fill factor of 30 %. For the triangular lattice a band gap opens for TE polarisation for $u = a/\lambda = 0.21 - 0.27$. In two and three dimensions the band gap formation is actually due to scattering processes. Neither the square nor the the triangular lattice possesses a TM gap for this set of parameters. Generally speaking TE gaps are favoured by connected high index areas whereas TM gaps are favoured by connected sites of low index material, *e.g.* dielectric pillars in air. The triangular lattice usually has a larger band gap than the square lattice. This can be attributed to the fact that the Brillouin zone of the triangular lattice has a higher rotational symmetry than the square one. For the case of TE polarised modes in a triangular lattice, the density of states (D.O.S) is shown in Fig. 1.7(b). It is formally

defined as:

$$\text{D.O.S} = \sum_n \sum_{\mathbf{k} \in \text{B.Z.}} \delta(\omega - \omega_n(\mathbf{k})) \tag{1.3}$$

where n is the band number and $\mathbf{k}$ is the wavevector lying inside the Brillouin zone (B.Z.). The calculation of the D.O.S. provides a cross-check for the existence of the band gap because every point in the Brillouin zone is sampled whereas in the case of the band diagram only the main symmetry directions are traced.

In Fig. 1.8 the modulus of the TE-polarised electric field maps is plotted at different symmetry points of the Brillouin zone of the triangular lattice. By analogy to the one-dimensional case, the electric field in the lower band is concentrated in the high-ε region between the holes whereas in the second band the electric field energy is concentrated inside the low-ε holes. Because the high-ε material is usually a dielectric and the low-ε material is mostly air, the lower and upper band are called dielectric- and air-band, respectively.
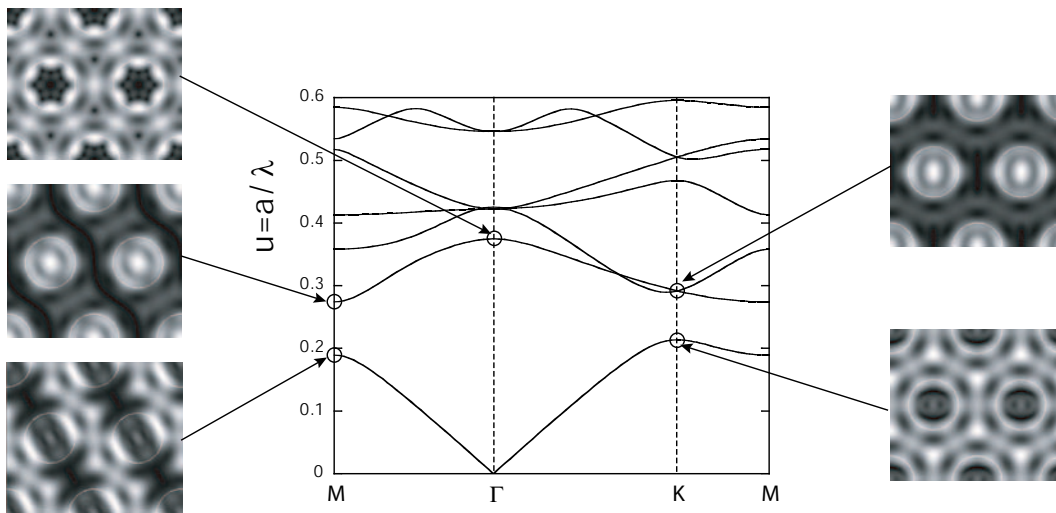
Figure 1.8: Band-diagram of a triangular lattice of air holes for TE polarisation: The modulus of the electric field has been evaluated for the dielectric- and air-band at the symmetry points of the Brillouin zone of the bulk PhC (Parameters: $f = 0.3$, $\varepsilon_{\text{sub}} = 11$, $\varepsilon_{\text{cyl}} = 1$).
[*Diagramme de bande d'un réseau triangulaire pour la polarisation TE: Le module du champ électrique a été évalué pour la bande diélectrique et la bande air pour les points de symétrie de la zone de Brillouin du cristal massif (Paramètres: $f = 0.3$, $\varepsilon_{sub} = 11$, $\varepsilon_{cyl} = 1$).*]

1.3.4 Gap maps

Gap maps are an important tool for choosing the appropriate filling factor f (see Fig. 1.9). It is a visualisation of the lower and upper band edges for gaps of different orders and polarisations. It immediately displays for which value of f a complete 2D band gap exists. The gap maps are calculated for the GaAs case between $f_1 = 0.1$ and $f_2 = 1$, where for the triangular lattice the close-packed condition is reached at $f = 0.9$. In the square lattice the first and the second TE gap open at $f = 0.35$ and the first TM gap opens at $f = 0.5$. In the triangular case the TE gap opens at $f = 0.11$ and grows

with increasing radius until it reaches a maximum at $f = 0.73$. The opening of the TM gap does not start until $f = 0.63$. The region of the complete (2D) band gap is given by the intersection of the TE and TM gap which happens in the frequency window $u = 0.37 - 0.56$. In general the band edges shift to higher frequencies with increasing air-filling factor, which agrees with a reduction in the average dielectric constant ($\varepsilon_{\mathrm{aver}} \doteq f \cdot \varepsilon_{air} + (1 - f) \cdot \varepsilon_{sub}$). The triangular lattice is preferable to the square lattice since it possesses a larger TE gap, which additionally opens at lower fill factor.
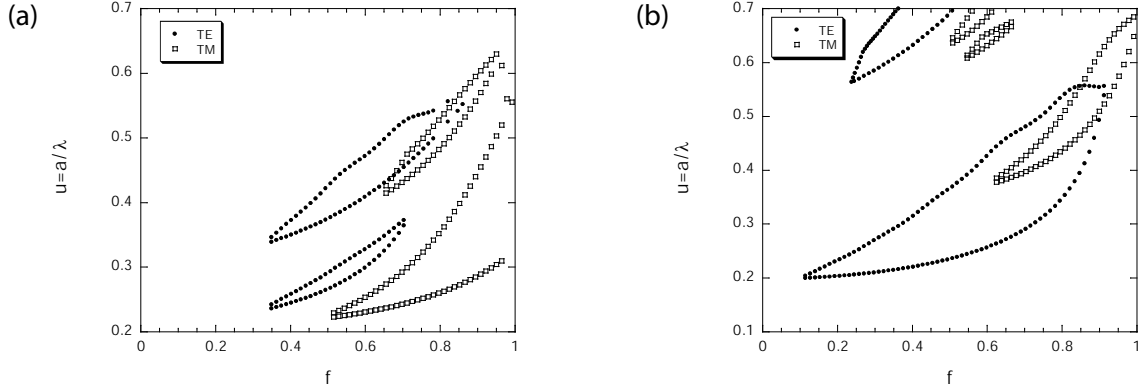
Figure 1.9: Gap maps of 2D lattices of air-holes in a dielectric matrix ($\varepsilon = 11.4$): a) square lattice, b) triangular lattice.
[Cartes des bandes interdites d'un réseau de cylindres d'air dans une matrice diélectrique ($\varepsilon = 11.4$): a) réseau carré, b) réseau triangulaire.]

When considering the first-order TE gap of a triangular lattice of air holes in a dielectric, one notes that the gapwidth and gap position is related to the dielectric contrast between the substrate and the air holes ($\varepsilon = 1$). For decreasing index contrast the gapwidth decreases and the gap position shifts to higher energies since the average index declines (see Fig. 1.10). In opposition to the 1D case, the gap closes abruptly when the index contrast falls below a certain threshold.
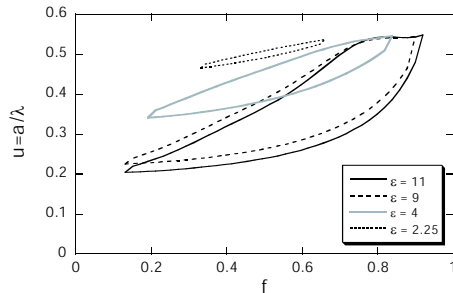
Figure 1.10: First order TE gap of a triangular lattice of air-holes as a function of f for different dielectric constants of the substrate.
[Bande interdite de premier ordre en polarisation TE d'un réseau triangulaire de trous d'air en fonction de f pour différentes constantes diélectriques du substrat.]

1.3.5   High versus low vertical index contrast

The 2D slab structures can be divided into high-index and low-index contrast. Either of them has its advantages and drawbacks. The main issue with 2D slab structures is out-of-plane loss.

1.3.5.1 High vertical index contrast

Examples of high-index contrast structures are membranes suspended in air, silicon on insulator or $GaAs$ on Al_xO_y (see Fig. 1.11). In the latter case the high vertical index-contrast is achieved by wet oxidation of the underlying $Al_{0.9}Ga_{0.1}As$ layer to give a layer of Al_xO_y [16]. The index contrast between the GaAs core is $\Delta n = 2.5$ and $\Delta n \approx 2$ with respect to the air and Al_xO_y cladding, respectively. In the case of silicon on insulator the Δn between the Si core and the SiO_2 substrate is 2.
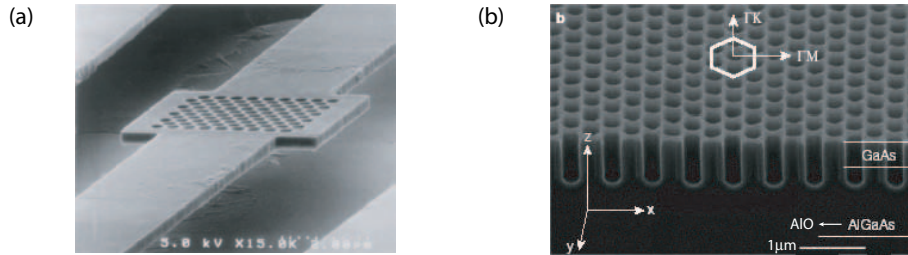
Figure 1.11: Two possible implementations of 2D PhC with a high vertical index contrast: a) 270 nm thick air-bridge $Al_{0.1}Ga_{0.9}As$ membrane (from Kawai *et al.* [17]), b) PhC slab with $\sim 0.5\,\mu$m deep holes etched through the GaAs top waveguide and partially into the Al_xO_y layer which acts as low refractive index ($n \approx 1.5$) cladding (from Chow *et al.* [16]).
[*Deux exemples typiques d'un cristal photonique bidimensionnel à haut contraste d'indice vertical: a) Membrane d'$Al_{0.1}Ga_{0.9}As$ suspendue dans l'air d'épaisseur 270 nm (d'après Kawai et al [17]), b) Cristal photonique planaire avec des trous profonds de $\sim 0.5\mu$m, gravés partiellement dans la couche Al_xO_y qui fonctionne comme gaine de bas indice ($n \approx 1.5$) (d'après Chow et al. [16]).*]

1.3.5.2 Low vertical index contrast

The samples studied in this thesis are based on low-index contrast structures. The periodic structure is a triangular lattice of holes etched into the vertical slab structure. The PhC works as a 2D first-order diffraction grating, *i.e.* the period is about half of the wavelength of the mid-gap. A welcomed side effect of low-index contrast structures is that their dispersion properties are very similar to the ideal 2D case in contrast to the high-index contrast structures where the mode energies are considerably blue-shifted [18]. The effective index method, where the vertical slab structure is taken into account simply by means of the effective index of the first guided slab mode, is always valid for low-index-contrast as long as the slab waveguide is single mode for the region of interest [19].

1.3.5.3 The light line problem

The light line is a very important concept when considering the influence of the third dimension in the case of 2D photonic crystals, with a vertical slab geometry. It is a reformulation of the condition for total internal reflection in terms of wavevector conservation: 'Snell-Descartes' law states that the parallel wavevector component is

conserved at the interface:

$$\beta_1 = \beta_2 \quad \longrightarrow \quad k_0 n_1 \sin \theta_1 = k_0 n_2 \sin \theta_2 \quad \longrightarrow \quad \frac{\sin \theta_1}{\sin \theta_2} = \frac{n_2}{n_1} \tag{1.4}$$

The critical angle is given by the condition $\theta_2 = \pi/2$.

$$\beta_1 = k_0 n_2 \sin \frac{\pi}{2} = \frac{\omega}{c} n_2 \quad \longrightarrow \quad \omega(\beta_1) = \frac{c\beta_1}{n_2} \tag{1.5}$$

where β_1 is the wavevector inside the core, parallel to the interface, n_2 denotes the refractive index of the cladding and $\omega(\beta_1)$ identifies the *light line*.

For simplicity let us consider the dispersion relation of a simple slab waveguide with refractive index n_1 surrounded by a medium with index $n_2 < n_1$. The dispersion diagram is actually divided into three distinct regions (see Fig. 1.12): (I) In the region below the light line of the core no modes can exist. (II) Between the core and the cladding light line the truly guided modes are situated. They exhibit very low propagation losses and their field profile decays exponentially into the cladding. (III) The region above the cladding light line, the *light cone*, comprises the continuum of radiative modes.

In the case of PhC slab waveguides, the guided modes are guided Bloch modes and the radiative spectrum contains resonances (leaky modes) that are characterised by a Lorentzian curve with a mean value which defines the energy of the band and a width which is proportional to the out-of-plane loss [18]. These quasi-guided modes have an oscillatory profile inside the cladding.
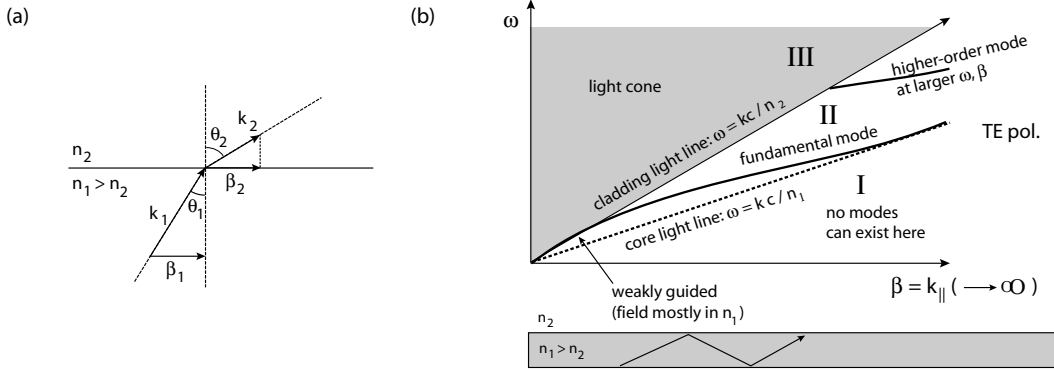
Figure 1.12: a) Schematic representation of Snell-Descartes' law, b) Guided mode dispersion of TE modes in a dielectric slab. The concept of the light line is equivalent to the condition for total internal reflection expressed in terms of $k_{\parallel}$ conservation. *[a) Représentation schématique de la loi de Snell-Descartes, b) Dispersion des modes guidés en TE dans un guide plan. Le concept de la ligne de lumière est équivalent à la condition de réflexion totale interne exprimé en termes de conservation de $k_{\parallel}$.]*

In symmetric vertical waveguides the truly guided modes are situated below the cladding light line. In the case of asymmetric waveguides there are two light lines: one for the upper cladding (*e.g.* air) and one for the lower cladding (*e.g.* substrate). Thus there exist truly guided modes, modes that leak into the substrate and modes that leak both into the substrate and into air.

So far we have only considered modes in an un-patterned slab structure, but the same principles apply to the vertical confinement of modes in 2D PhC slab structures. In the case of 2D PhCs the lightline is defined by $\omega(\mathbf{k}) = |k|c/n$ where $\mathbf{k} = (k_x, k_y)$ is traced along the main symmetry directions (see Fig. 1.13).
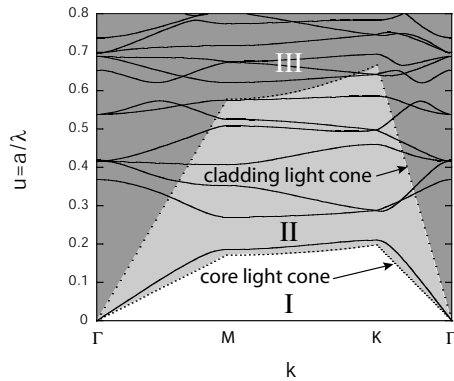
Figure 1.13: Dispersion relation of a triangular lattice (TE polarisation). In region I no modes can exist, region II contains truly guided bulk modes and III depicts the radiative region of leaky modes.

[Relation de dispersion d'un réseau triangulaire de cylindres d'air en polarisation TE. Dans la région I il n'existe pas de modes, la région II contient des modes du cristal massif réellement guidés et III décrit la région radiative des modes de fuite.]

In consideration of the light line problem one would rather favour high-index contrast structures. In these structures linear *WN* waveguides, consisting of N missing rows of holes along ΓK , can be implemented that support absolutely lossless Bloch modes propagating well below the light line [20]. This can be understood in the sense that the scattered waves of different holes interfere destructively. However, the Bloch mode is only lossless as long as there is translational symmetry. A reason for a symmetry breaking could be a cavity or a bend, thus elements that will naturally be present in a photonic integrated circuit. In this case also the strong confinement waveguides will exhibit losses. Additionally, the high-contrast structure is more sensitive to fabrication imperfections (*e.g.* roughness).

Is it more advantageous to have a structure that scatters both on the straight sections and at the defects with a low strength or to have a system that scatters mainly at defects but with a higher strength ? A question that has yet been definitely answered by the PhC community and whose answer will probably depend on the type of application that is pursued.

1.4 Three-dimensional photonic crystals

While in the domain of 2D PhCs the research has mainly focused on triangular and square lattices, the additional dimension in 3D PhCs adds a lot of degrees of freedom for the design and conception of new PhCs. The choice of fabrication technologies is almost as large as the number of different designs. A complete overview of the state-of-the-art of 3D PhC fabrication technology would lie beyond the scope of this introductory section. Therefore a few typical examples from earlier designs and different approaches are given as an illustration. It should be noted that the search for the optimal structure (largest full band gap for every direction and polarisation) is still an on-going task. The prototype of 3D band gap materials is the diamond lattice. It is based on a face-centred-cubic (fcc) lattice with two 'atoms' per (primitive) unit cell. It provides an almost

spherical Brillouin-zone which is important for the omnidirectionality of the gap. The 'diamond bonds' allow the field of the lowest bands to concentrate in the connected dielectric structure.

The first 3D band gap structure has been proposed by K.M. Ho *et al.* consists of overlapping Si spheres arranged in a diamond structure [21]. The gap exists for refractive-index contrasts as low as 2 (see Fig. 1.14). Solid spheres inside an fcc lattice, on the other hand, do not have a gap.
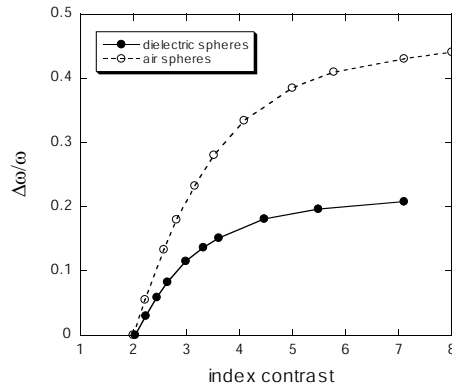
Figure 1.14: Gap to midgap frequency ratio ($\Delta\omega/\omega_g$) of the diamond structure as a function of the refractive index contrast. The dotted line is for the case of air spheres in dielectric with $f = 0.81$, and the solid line is for dielectric spheres in air with a filling ratio of $f = 0.34$ (from Ho *et al.* [21]).
[Largeur relative de la bande interdite ($\Delta\omega/\omega_g$) en fonction du contraste d'indice. La ligne pointillée est pour le cas des sphères d'air avec $f = 0.81$ dans le diélectrique, tandis que la ligne solide est pour le cas des sphères diélectriques dans l'air avec $f = 0.34$ (d'après Ho et al. [21]).]

One notes that unlike the one-dimensional case there exists a threshold in the index-contrast for the opening of a complete gap in the diamond structure.

The Yablonovite, a 3D structure with diamond-like symmetry proposed by E. Yablonovitch [22], has been first fabricated in the microwave region where fabrication consists of drilling holes into a triangular array of holes from three different azimuthal angles (separated by 120°) at an inclination of 35° from the vertical (see Fig. 1.15(a)). At Bell Communications Research in New Jersey, E. Yablonovitch fabricated a number of these crystals by drilling holes in a number of different dielectric materials in different ranges of dielectric constants. Ten years later a Yablonovite-like structure could be produced in macroporous silicon for the visible range by the combination of photoelectrochemistry (for the vertical pores) and focused-ion-beam etching (see Fig. 1.15(b)) [23].

Also an earlier design is the 'woodpile structure'. It has an fcc symmetry with a basis of two rods. For the infrared range fabrication is based on relatively standard microelectronics technology. It relies on a five-level stacking process based on the repetitive deposition and etching of multiple dielectric films (see Fig. 1.16(a)) [24]. The 'woodpile structure' is a good example to show how the same structure can be obtained with different fabrication techniques. S. Noda proposed wafer fusion of crossed striped GaAs or InP wafers (see Fig. 1.16(b)). The substrate of the top wafer is removed by a combination of chemical- and dry-etching processes [25]. Yet another approach is based on

two-photon absorption. It is based on the fact that the two-photon absorption probability depends quadratically on the intensity, so under tight-focusing conditions absorption is localised at the focus to a volume of the order of λ^3 [26]. In order to limit the laser power, this application requires compounds that exhibit a large two-photon absorption cross-section. Fig. 1.16(c) shows an SEM micrograph of the 'woodpile structure'.

An interesting 3D structure with large band gap proposed by Johnson *et al.* consists of a sequence of identical planar layers with a certain horizontal offset, repeating every third layer, to form an fcc lattice (see Fig. 1.17). The advantage of this structure is that it forms a bridge between the 3D and the 2D world. The layers can be thought
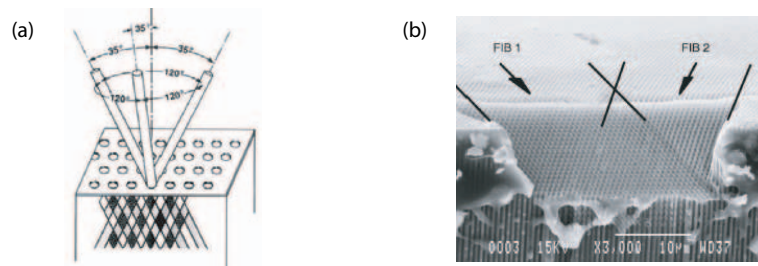
Figure 1.15: Yablonovite - an early PhC structure with a full 3D band gap: a) Drilling each hole of the mask from three different angles yields a fully 3D periodic fcc structure (from Yablonovitch *et al.* [22]). b) practical realisation of a Yablonovite-like structure in the optical regime: The structure is obtained by drilling holes by means of focused ion beam into macroporous silicon (from Chelnokov *et al.* [23]).
[Yablonovite - une des premières structures proposées ayant une bande interdite photonique 3D: a) En perçant chaque trou à partir du même masque sous trois angles différents, il résulte une structure 3D de périodicité fcc (d'après Yablonovitch et al. [22]). b) Réalisation pratique obtenue par la gravure de silicium macroporeux à l'aide d'un faisceau d'ions focalisés (d'après Chelnokov et al. [23]).]
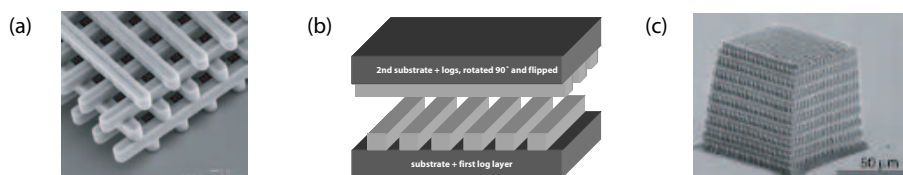
Figure 1.16: The 'woodpile' structure - an earlier design with a full band gap operating at infrared wavelengths: a) SEM micrograph of a structure fabricated by UV-lithography in silicon (from Lin *et al.* [24]). b) The same structure can also be fabricated by a wafer-fusion and substrate removing process (from Noda *et al.* [25]). c) SEM micrograph of a woodpile fabricated by a two-photon polymerisation process (from Cumpston *et al.* [26]).
[La structure 'tas de bois' - une des conceptions antérieures avec une bande interdite complète dans l'infrarouge: a) Image MEB d'une structure fabriquée par lithographie UV dans du silicium (d'après Lin et al. [24]). b) La même structure peut aussi être fabriquée par un procédé de fusion et élimination du substrat (d'après Noda et al. [25]). c) Image MEB d'un 'tas de bois' fabriqué par la polymérisation à deux photons (d'après Cumpston et al. [26]).]

of as an alternating stack of the two typical 2D PhC slab geometries: dielectric rods in air and air holes in a dielectric matrix.
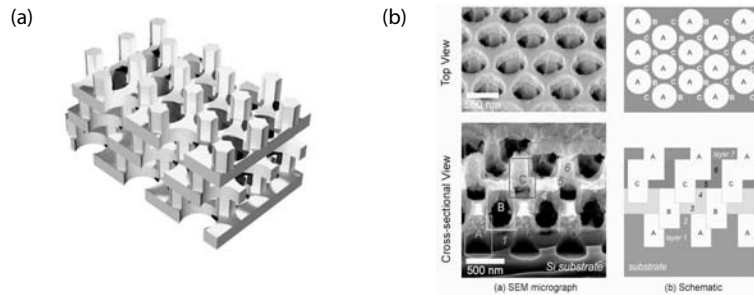
Figure 1.17: a) Diamond-like three-dimensional structure (rods ∼ 'bonds') proposed by S. G. Johnson et al. (MIT) [27]. b) and its practical realisation by M. Qi and H. Smith (MIT)
[Structure 3D ressemblant à une structure diamant (pilier ∼ 'liaisons') et sa réalisation pratique par M. Qi et H. Smith (MIT).]

A completely different class of 3D PhCs is the opals and the inverse opals (see Fig. 1.18). They can be fabricated rather easily by self-assembly techniques, suitable for mass production. This technique is much cheaper than lithographic-based methods and has been optimised to perfection to provide large areas of regular PhC.
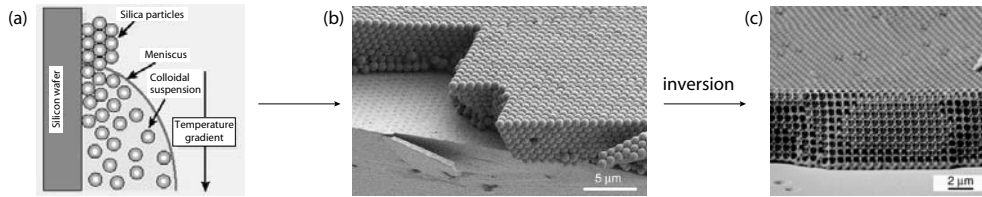
Figure 1.18: On chip growth of inverted opals by means of self-assembly: a) Silica particles are forced into an ordered arrangement on the surface of a vertical silicon wafer as the meniscus is swept downwards by evaporation of the solvent. An applied temperature gradient allows convective flow of the particles in order to minimize unwanted sedimentation (from Joannopoulos *et al.* [28]). b) Thin planar opal templates assembled directly on a Si wafer from 855 nm sized spheres (from Vlasov *et al.* [29]). c) First the opal structure is infiltrated with silicon and then the silica spheres are removed by wet etching yielding an inverted opal attached to the silicon chip (from Vlasov *et al.* [29]).
[Fabrication des opales inversées sur substrat par auto organisation: a) Les sphères de SiO_2 sont forcées de s'ordonner à la surface d'un substrat de silicium lorsque le ménisque se déplace vers le bas lors de l'évaporation du solvant. Un gradient de température appliqué empêche une sédimentation non désirée de particules (d'après Joannopoulos et al. [28]). b) Structure opale plane assemblée à partir de sphères de diamètre 855 nm directement sur un wafer Si (d'après Vlasov et al. [29]). c) Premièrement la structure opale est infiltrée avec du silicium et après les sphères de SiO_2 sont enlevées par gravure mouillée (d'après Vlasov et al. [29]).]

The first self-assembled opals have been obtained by sedimentation of silica (SiO_2) microspheres in solution into a close-packed fcc lattice solely by gravity. This results

in structures with a considerable number of stacking faults. This limitation has been overcome by Y.A. Vlasov *et al.* [29]. The crystal is self-assembled at the meniscus between a vertical substrate and a colloidal suspension. The applied temperature gradient provides particle flow and prevents sedimentation before the solvent has evaporated.

A structure with solid spheres in an fcc lattice does not have a gap, but the inverted structure has one. The inversion is done by infiltration of silicon into the voids between the spheres. The silicon spheres are then removed by wet-etching, yielding the inverted opal structure.

Other fabrication approaches not presented in this section are:

- X-ray interference lithography

- Stacking by micromanipulation

- Holographic lithography

- Two-photon holographic lithography

- Block copolymers

- Glancing angle deposition

- Auto-cloning

the list is not exhaustive.

1.5   Fundamental concepts

1.5.1   PhC scalability

An interesting feature of PhCs is their scalability, *i.e.* one may scale all the geometrical dimensions according to the wavelength of the light with which the crystal is sampled, keeping unchanged all the PhC properties (*e.g.* band gap). It allows one to test the concept of a device in GaAs at $\lambda = 1\,\mu$m, where the fabrication technology is mature, and transfer the results to InP ($\lambda = 1.5\,\mu$m) once the losses have been reduced to the same level.

The basic physics of the band gap is described by the so-called 'Master equation' for the magnetic field (see chapter 4 for details):

$$\nabla \times \frac{1}{\varepsilon(\mathbf{r})} \nabla \times \mathbf{H}_\omega(\mathbf{r}) = \left(\frac{\omega}{c}\right)^2 \mathbf{H}_\omega(\mathbf{r}) \tag{1.6}$$

Assuming that a PhC with a dielectric map $\varepsilon(\mathbf{r})$ is shrunken or expanded by a scaling factor s, *i.e.* the new map becomes $\varepsilon'(\mathbf{r}) = \varepsilon(\mathbf{r}/s) = \varepsilon(\mathbf{r}')$. We now make a change of variables in Eq. (1.6) by replacing $\mathbf{r}$ by $\mathbf{r}' = \mathbf{r}/s$. Thus $\mathbf{H}$ becomes $\mathbf{H}(\mathbf{r})' = \mathbf{H}(\mathbf{r}/s)$ and the Nabla operator ∇ turns into $\nabla' = s \cdot \nabla$, modifying Eq. (1.6) into:

$$\nabla \times \frac{1}{\varepsilon(\frac{\mathbf{r}}{s})} \nabla \times \mathbf{H}_\omega\left(\frac{\mathbf{r}}{s}\right) = \left(\frac{\omega}{c \cdot s}\right)^2 \mathbf{H}_\omega\left(\frac{\mathbf{r}}{s}\right) \tag{1.7}$$

For PhCs there is no fundamental length scale and there is a simple relationship between electromagnetic problems that differ only by a contraction or expansion of all distances. This scaling property will be extensively used for the lithographic tuning described in section 3.1.3.

Another scaling property is with respect to the dielectric contrast. By multiplying the dielectric map by a factor s^2, thus inserting $\varepsilon(\mathbf{r}) = \frac{\varepsilon'(\mathbf{r})}{s^2}$ in Eq. (1.6) one obtains:

$$\nabla \times \frac{1}{\varepsilon'(\mathbf{r})} \nabla \times \mathbf{H}_\omega(\mathbf{r}) = \left(\frac{\omega}{c \cdot s}\right)^2 \mathbf{H}_\omega(\mathbf{r}) \tag{1.8}$$

The eigenvectors (field profiles) do not change but the eigenvalues (mode energies) scale according to s: $\omega' = \omega/s$. Thus the physics, apart from a scaling factor, depends only on the ratio between the low index (ε_1) and high index (ε_2) dielectric material and not on their absolute values.

1.5.2   The Bloch-Floquet Theorem

Since the beginning of PhC research, one has searched for analogies between solids (periodic arrangement of atoms) and PhCs (periodic arrangement of dielectric material). Many useful concepts from solid state physics could be directly adopted to PhCs, one of them being the Bloch-Floquet theorem.

In solid state physics the Bloch-Floquet theorem is deduced by expanding the periodic crystal potential $V(x) = V(x + a)$ into a Fourier series summed over all reciprocal lattice vectors, *i.e.* $V(x) = \sum_G c_G e^{jGx}$ and inserting it into the stationary Schrödinger equation $\mathcal{H}\Psi = \epsilon\Psi$. The resulting set of algebraic equations is solved by a function of the form [30]:

$$\Psi_k(x) = e^{jkx} u_k(x) \quad \text{with} \quad u_k(x) \equiv \sum_G c_{k-G} e^{-jGx} \tag{1.9}$$

, where k is the Bloch wavevector lying in the first Brillouin zone. The Bloch theorem states that eigenfunctions of the Hamiltonian operator for a periodic potential are always of the form of Eq. (1.9). Since $u_k(x)$ is a Fourier series over the reciprocal lattice vectors, it is *per se* periodic with respect to a translation by a direct lattice vector, *i.e.* $u_k(r + R) = u_k$. In summary the electron wave functions inside a periodic crystal potential are plane waves modulated by a periodic function.

In the case of PhCs the periodic potential has to be replaced by the periodic dielectric map $\varepsilon(r)$ and the Schrödinger equation by the Master equation of the magnetic field:

$$\hat{\theta}\mathbf{H}(\mathbf{r}) = \lambda\mathbf{H}(\mathbf{r}) \quad \text{with} \quad \hat{\theta} = \nabla \times \left(\frac{1}{\varepsilon(\mathbf{r})}\nabla \times \quad \text{and} \quad \lambda = \frac{\omega^2}{c^2} \tag{1.10}$$

It is convenient to introduce the translation operator $\hat{T}_\mathbf{d}$ which shifts the argument of an arbitrary test function by the vector $\mathbf{d}$, *i.e.* $\hat{T}_\mathbf{d}f(\mathbf{r}) = f(\mathbf{r}+\mathbf{d})$. The eigenfunctions of the translational operator are plane waves and the eigenvalues complex numbers with modulus one:

$$\hat{T}_\mathbf{d}e^{j\mathbf{k}\mathbf{r}} = e^{j\mathbf{k}(\mathbf{r}+\mathbf{d})} = \underbrace{e^{j\mathbf{k}\mathbf{d}}}_{\lambda} e^{j\mathbf{k}\mathbf{r}} \tag{1.11}$$

In the case of a translation by a direct lattice vector Eq. (1.11) writes:

$$\hat{T}_{\mathbf{R}} e^{j\mathbf{k}\mathbf{r}} = e^{j\mathbf{k}\mathbf{R}} e^{j\mathbf{k}\mathbf{r}} \tag{1.12}$$

The eigenfunctions are specified by the wavevector $\mathbf{k}$; however, there are degenerate eigenfunctions that yield the same eigenvalue. In fact all modes with wavevectors of the form $\mathbf{k}' = \mathbf{k} + \mathbf{G}$, where $\mathbf{G}$ is an arbitrary reciprocal lattice vector, are degenerate. Applying the theorem that a linear combination of degenerate eigenfunctions is itself an eigenfunction to the same eigenvalue, the general solution of Eq. (1.12) is

$$\mathbf{H}_{\mathbf{k}}(\mathbf{r}) = \sum_n c_{\mathbf{k},n} e^{j(\mathbf{k}+\mathbf{G}_n)\cdot\mathbf{r}} = e^{j\mathbf{k}\mathbf{r}} \underbrace{\sum_n c_{\mathbf{k},n} e^{j\mathbf{G}_n\cdot\mathbf{r}}}_{\equiv u(\mathbf{r})} \tag{1.13}$$

where $u(\mathbf{r})$ is by construction a periodic function with $u(\mathbf{r} + \mathbf{R}) = u(\mathbf{r})$ and $\mathbf{H}_{\mathbf{k}}(\mathbf{r})$ thus has the form of a Bloch mode. Due to the discrete translation symmetry of the dielectric map, $\hat{\theta}$ commutes with $\hat{T}_{\mathbf{R}}$. Accordingly, the two operators possess a common set of eigenvectors and we have proven that the solutions to Eq. (1.10) are of the Bloch form.

Chapter 2

Sample fabrication

2.1 Fabrication steps

During this thesis several collaborations have been established within the European project 'Photonic Crystal Integrated Circuits' (PCIC). On the fabrication side notably the University of Würzburg (Germany), the Royal Institute of Technology-KTH (Sweden) and Opto+ Alcatel (France) have been involved (see Table 2.1).

Material	Growth	e-Beam lithography	Etching	discussed in chapter
InP	KTH	Uni Würzburg	Uni Würzburg	2, 3
InP	KTH	Uni Würzburg	KTH	2, 3
InP	Opto+ Alcatel	Opto+ Alcatel	Opto+ Alcatel	2, 3
GaAs	EPFL	Uni Würzburg	Uni Würzburg	2, 3, 5-7

Table 2.1: Fabrication places of the different GaAs and InP samples.
[Lieu de fabrication des différents échantillons GaAs et InP.]

The InP samples are mainly considered to illustrate the basic optical characterisation procedure (see chapter 3) and the out-of-plane loss model (see section 3.4), whereas the PhC-based devices studied in this thesis, *e.g.* cavity-bends, hybrid guides and linear couplers, were fabricated on GaAs.

2.1.1 Growth of the vertical heterostructure

The InP samples were grown by metal organic vapour-phase epitaxy (MOVPE), where as the GaAs samples were grown by means of molecular beam epitaxy (MBE).

In order to provide light confinement in the vertical direction, a waveguide structure consisting of a core and two cladding layers was grown. Additionally, an active layer consisting of either quantum wells (QWs) or quantum dots (QDs) was embedded in the core layer for the optical characterisation of the PhC structure (see chapter 3).
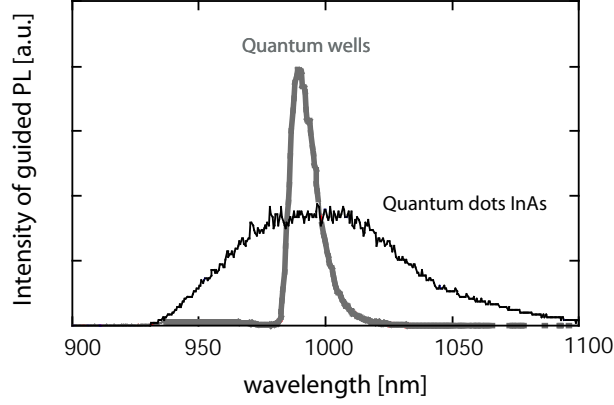
Figure 2.1: Guided lateral TE photoluminescence spectra excited at a large distance (100 μm) from the facet. The thin black line corresponds to quantum dots and is compared to quantum wells (gray line) (from D. Labilloy [31]).
[Spectres de photoluminescence collectés sur le signal guidé en polarisation TE à grande distance du bord (100 μm), lorsque les émetteurs sont des boîtes quantiques (trait noire fin) ou un puit quantique (trait gris) (d'après D. Labilloy [31]).]

In the GaAs samples emitters are self-assembled InAs QDs grown by MBE. These "atom-like" emitters typically feature very small linewidths, provided that the spectrum is not inhomogeneously broadened by variations in dot size and the observation is carried out at cryogenic temperatures. However, for the specific case of the ILS application the growth is optimised to obtain a very inhomogeneous QD distribution in order to provide a broad flat luminescence spectrum (see chapter 3).

A vertical structure with a 241 nm thick core with three embedded QD layers (see Table 2.2) has been chosen. In the InP system the growth of QDs is more difficult than

Thickness [Å]	Material	Refr. index	Function
–	air	1	
100	$GaAs$	3.48	Cap layer (oxidation protection)
3000	$Al_{0.2}Ga_{0.8}As$	3.39	Upper cladding (optical confinement)
200	$Al_{0.8}Ga_{0.2}As$	3.06	Electronic confinement layer
1000	$GaAs$	3.48	Core
410	$GaAs$+InAs-QDs	-	Core+Source
1000	$GaAs$	3.48	Core
4000	$Al_{0.8}Ga_{0.2}As$	3.06	Lower cladding (optical confinement)
–	$GaAs$	3.48	Buffer

Table 2.2: Vertical structure of GaAs sample containing three InAs quantum dot layers.
[Structure verticale contenant trois couches de boîtes quantiques InAs.]

in GaAs and therefore a set of two slightly detuned QWs is chosen as ILS (see Table 2.3). The composition of the $Ga_xIn_{1-x}As_yP_{1-y}$ waveguide layer, lattice matched to InP , was adjusted for a band gap corresponding to an emission wavelength of 1.22 μm . Separately, the compositions of the $Ga_xIn_{1-x}As_yP_{1-y}$ strain compensated quantum well packages (QW1 and QW2) were optimized with respect to the emission wavelength

1.55μm and 1.47μm, respectively. The corresponding PL spectra can be found in section 3.1.3.

Thickness [Å]	Material	Refr. index	Function
–	air	1	
200	InP	3.17	Upper cladding/cap
181	$Ga_{0.24}In_{0.76}As_{0.52}P_{0.48}$	3.35	Core / barrier
21	$Ga_xIn_{1-x}As_yP_{1-y}$	≈ 3.35	QW1 ($\lambda_1 \approx 1.55\mu m$)
30	$Ga_{0.24}In_{0.76}As_{0.52}P_{0.48}$	3.35	Core / spacer
21	$Ga_xIn_{1-x}As_yP_{1-y}$	≈ 3.35	QW2 ($\lambda_2 \approx 1.47\mu m$)
181	$Ga_{0.24}In_{0.76}As_{0.52}P_{0.48}$	3.35	Core / barrier
600	InP	3.17	Lower cladding/buffer
–	$n-InP$	3.15	Substrate

Table 2.3: Vertical structure of InP sample containing two quantum wells.
[*Structure vertical contenant deux puits quantiques.*]

The two QWs are placed symmetrically with respect to the centre of the core.

2.1.2   Etch-mask

Polymethyl Methacrylate (PMMA) resist is commonly used for its ability to provide high resolution in the electron beam lithography process (see section 2.1.3), but exhibits a poor selectivity in plasma etching. The thickness of the PMMA is limited to roughly $500 - 1000$ nm which would prevent hole depths greater than 1 μm. Therefore a two step process is adopted, which compromises the writing and etching of an intermediate dielectric hard etch mask in a first step and a pattern transfer into the heterostructure by dry etching in a second step. This allows one to etch holes with aspect ratios greater than 10 with a well-defined air-filling factor.

Depending on the dry etching technique either SiO_2 or Si_xN_y are used as hard mask, both for InP and GaAs. In terms of selectivity and etching anisotropy, both dielectric materials can be patterned equally well. For optimised etching conditions a maximum selectivity between the dielectric and the PMMA of 1.1:1 for wide area and 1:2 for PhC patterns with a diameter of 200 nm can be found [32].

In the case of SiO_2 a typically 200 nm [33] up to 350 nm [34] thick film is deposited by Plasma Enhanced Chemical Vapor Deposition (PECVD) on the cleaned surface. The polycristalline film is grown at a low temperature (250°C) utilizing silane (SiH_4) as processing gas.

Which hard mask has the better selectivity with respect to InP or GaAs depends a lot on the applied dry etching technique (see section 2.1.4). The selectivities for the different material and dry etching combinations are listed in Table 2.4 (the acronyms of the different dry etching techniques are explained in detail in section 2.1.4).

2.1.3   Electron beam lithography (EBL)

In standard optical lithography the resolution is limited by the wavelength of light used for the exposure. In PhC the typical length scale (hole diameter) for the smallest

	InP					
	ECR		ICP		CAIBE	
	SiO_2	Si_xN_y	SiO_2	Si_xN_y	SiO_2	Si_xN_y
selectivity to mask	18:1 [35]			11:1 [32]	25:1 [36]	20:1 [37]
etch chemistry	Cl_2/Ar			Si/Cl_4	Cl_2/Ar	Cl_2/Ar
	GaAs					
	ECR		ICP		CAIBE	
	SiO_2	Si_xN_y	SiO_2	Si_xN_y	SiO_2	Si_xN_y
selectivity to mask					3:1 [34]	
etch chemistry					Cl_2/Ar	

Table 2.4: Selectivity of InP and GaAs versus SiO_2 or Si_xN_y dielectric mask for the different dry etching techniques
[*Sélectivité de InP et GaAs vis-à-vis des masques diélectriques SiO_2 ou Si_xN_y pour différentes techniques de gravure sèche.*]

periods is of the order of 100 nm. More precisely it can be shown that the decay length of the diffracted wave with wavelength λ at the edge of the mask is given by $\Delta x = \frac{3}{2}\sqrt{\lambda(z + \frac{d}{2})}$, where d is the thickness of the resist and z the spacer width between mask and resist (see Fig. 2.2). Even if assuming an infinitely thin mask (z=0), standard lithography ($\lambda = 300\,\text{nm}$) yields a decay length of $\Delta x = 400\,\text{nm}$, which is clearly larger than the hole period.
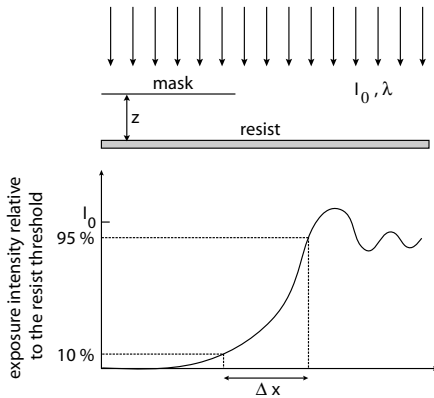

Figure 2.2: Diffraction image of the field near the border of a semi-infinite plane.
[*Image de diffraction d'un champ proche du bord d'un plan semi-infini.*]

Due to the diffraction limit this can no longer be patterned by standard lithography but is typically performed by electron beam lithography (EBL).

EBL [38] is a technique for creating extremely fine patterns ($\leq 0.1\,\mu\text{m}$) for integrated circuits due to the very small spotsize. EBL is usually done with direct writing systems where a small electron beam spot is moved with respect to the wafer to draw the mask pattern. Electron beam resists, the recording and transfer media for EBL, are modified by electron exposure. PMMA, the standard positive high-resolution electron beam resist, possesses a high sensitivity and a nominal resolution of 10 nm.

There are a few constrictions with respect to the theoretical accuracy of EBL due to electron-solid interactions. This includes forward scattering, back scattering and the production of secondary electrons. The forward scattering leading to an increased effective beam diameter can be minimized by choosing a thin resist and the highest

available accelerating voltage (*e.g.* 100 kV). A second advantage of the high electron energy is the reduced beam deflection due to the charging of the dielectric mask [35]. The secondary electrons with energies from 2 to 50 eV, accounting for the actual resist exposure, yield an effective beam widening of roughly 10 nm. Back-scattered electrons are electrons that have penetrated through the resist into the substrate where they have been scattered by wide angles towards the resist, leading to an additional resist exposure. These electrons, together with the fast secondaries (energy roughly 1 keV), account for the *proximity effects* (see Fig. 2.3).
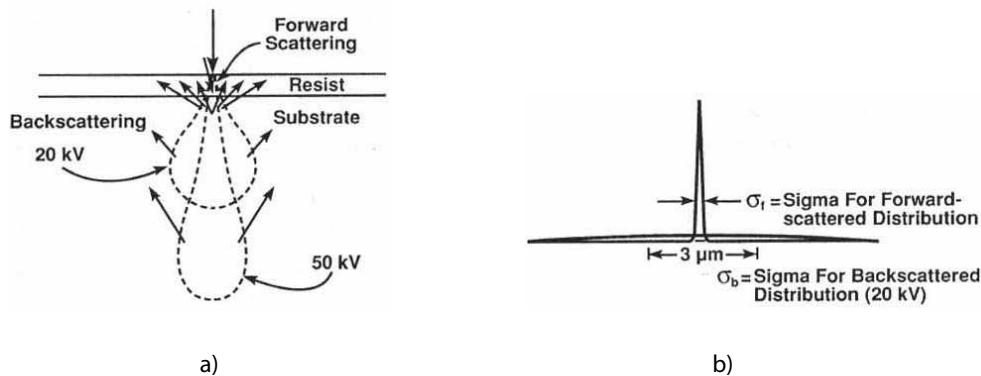

Figure 2.3: Electron scattering in electron resist exposure. a) back scattering distribution at different ion energies. b) exposure distribution due to the forward-scattered and back-scattered electrons (from Thompson *et al.* [39]).
[*Diffusion électronique: a) Distribution de rétro-diffusion à des énergies différentes. b) Distribution d'exposition des électrons avant- et rétro-diffusés (d'après Thompson et al. [39]).*]

This means that small features close to big structures are over-exposed whereas small isolated structures are under-exposed. In the case of PhCs the proximity effects lead to local variations in the air-filling factor between the middle and the border of the pattern. In the extreme case two separate features of a structure cannot be distinguished any more (see Fig. 2.4).
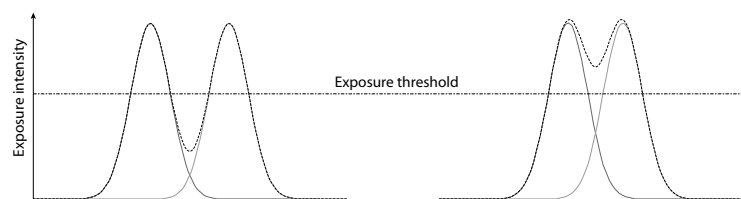
Figure 2.4: Two isolated features of a mask may be reproduced as a single one if the sum of the tails of the two exposure distributions exceed the threshold value of the resist.
[*Deux détails isolés d'une structure ne peuvent pas être résolus si la somme des queues des distributions dépasse le seuil de développement de la résine.*]

Therefore a *proximity effect correction* is indispensable in order to obtain a mask where the written diameter corresponds to the coded one. There are basically three possibilities:

Dose modulation: A different dose is assigned to each individual sub-pattern. The calculation of the interaction between the different sub-patterns is a very intensive computational task. Although the actual effect of electron scattering is to increase the dose received by large areas, for practical reasons proximity correction is normally thought of in terms of the large areas receiving a base dose of unity, with the smaller and/or isolated features receiving a larger dose to compensate [38].

Pattern biasing: The extra dose that dense patterns receive is compensated by slightly reducing their size. That has the advantage that it can be adopted in EBL systems that are not capable of dose modulation. The pattern biasing has less dynamic range than the dose modulation since it cannot be applied to features with dimensions close to the scale of the pixel spacing. Its computation is as costly as for dose modulation.

Background dose correction 'GHOST': First the negative pattern is written with a defocused beam in order to mimic the back scattering. In a second step the pattern is normally written, resulting in an exposure free of proximity effects (see Fig. 2.5). The method is fast since it does not require computation, but it does not properly correct for forward scattering.
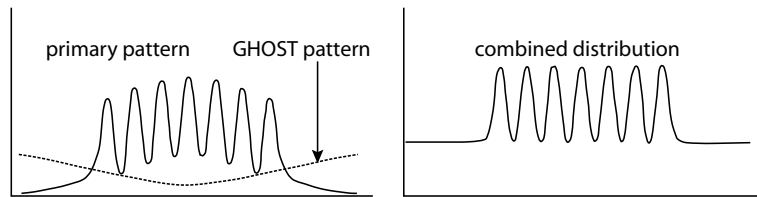

Figure 2.5: In the GHOST technique the primary pattern is overlaid by the negative background profile in order to correct for the back scattering.
[Dans la technique GHOST l'enveloppe négative du profil est superposé à la structure primaire pour corriger l'effet de la diffraction en arrière.]

Recently an efficient, PhC-specific correction scheme has been presented which relies on the inherent periodicity of the underlying PhC structure [40]. The approach, in which the structures are represented as binary matrices, leads to a set of linear equations.

Dose modulation and pattern biasing have been chosen for the GaAs samples in this thesis. On the other hand, it should be noted that high acceleration voltages (100 kV) lead to large penetration depths of the electrons and therefore a broad spatial in-plane distribution of back-scattered electrons in the order of $\geq 10\,\mu$m on InP and GaAs substrates. This is larger than the typical extension of a PhC structure and the contribution of backscattered electrons can be taken into account by a constant background dose.

Some EBL systems write the structure with respect to a cartesian grid of pixels. The finite positional resolution of 5 nm in combination with the inherent difference between the cartesian grid and the hexagonal structure may lead to small distortions [33].

In the case of the GaAs samples described in this thesis an e-beam with an acceleration voltage of 100 kV and a beam current of 1 nA was used to define the PhC pattern in a 500 nm-thick PMMA resist [34].
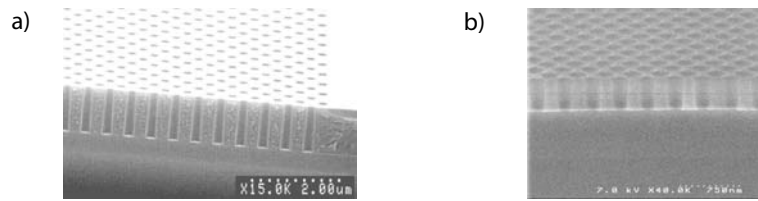
Figure 2.6: a) Holes with 200 nm diameter in 1 μm resist exposed with 100 keV e-beam lithography. b) Dielectric mask after etching.
[*a) Trous d'un diamètre de* 200 nm *dans une résine épaisse de* 1 μm *produits par une machine à faisceau d'électrons de* 100 keV. *b) Masque diélectrique après gravure.*]

After development in 1:3 methylisobutylketone/propanol the obtained PMMA mask (Fig. 2.6(a)) is usually transferred into the SiO_2 layer by CHF_3/Ar-based reactive ion etching (RIE) [41] (Fig. 2.6(b)). After removal of the PMMA the SiO_2 hard mask is utilized as a dry etch mask for the GaAs heterostructure.

2.1.4 Dry Etching techniques

Dry etching is basically a combination between chemical etching and sputtering induced by ions, which could be described as "atomic scale sandblasting" [42].

A generic dry etching system consists of a plasma production unit, a unit to acceler-ate the positive ions towards the sample and a process gas mixture of chemically active species (*e.g.* Cl_2) and a chemically inactive gas (*e.g.* Ar). The plasma is produced by applying an alternating electrical field which completely ionises the processing gas. Inside the plasma the Cl_2/Ar gas is split into $Cl\cdot$ radicals on one side and negative and positive (*e.g.* Ar^+) ions. The radicals are transported by the gas flow and the positive ions are accelerated towards the negatively biased sample and contribute in various ways to the etching process [42] (see Fig. 2.7). The positive ion bombardment gener-ates 'active' sites where radicals can adsorb by destroying the surface protection layer. Due to the directionality of the ion beam this occurs preferentially at the hole bottom than at the sidewalls. The reaction between adsorbed radicals and the semiconductor is enhanced by the positive ions an forms new reaction products. The products desorb and are sputtered away by the ions. The chemical reaction rate and the desorption rate are also influenced by temperature.

The advantage of dry etching is that the contribution of the physical and the chemi-cal component can be tuned individually. At one extreme, by placing the wafer very far away from the plasma only chemically reactive species reach it. Chemical etching can be both isotropic or anisotropic. Isotropic processes will cause undercutting of the mask layer by the same distance as the etch depth. Anisotropic processes allow the etching to stop on certain crystal planes in the substrate, but these planes cannot be vertical to the surface when etching holes. At the other extreme, by accelerating ions out of the plasma and directing them at the wafer, only the physical component of the etch is received. This results in a highly directional anisotropic etch, but it can also create excessive damage. However, the total etch rate is more than the sum of the physical and chemical etch rates of these components [43] and the surface reactions enhanced by the ion bombardment indeed very complicated.

The requirements for low-index contrast 2D PhC etching are:

. **Highly anisotropic deep etching** of small diameter (D) holes (aspect ratio better than 20 for diameters around 200 nm) with good spatial uniformity.

. Simultaneous etching of small ($D = 100$ nm) and larger ($D \geq 200$ nm) holes at constant etch depth.

. **High selectivity** between the mask and the material is a prerequisite for deep etching and allows accurate pattern transfer from the mask into the material, especially if there are different hole sizes.

. **Vertical walls** with small surface roughness in order to minimize out-of-plane scattering losses.

In the case of InP etching the most critical point is the control of the chemical contribution due to the very different atomic mass of In and P elements. Bombarding argon ions preferentially sputter phosphorus atoms whereas chlorine enhances the removal of indium atoms by reacting with them to form volatile etch products ($InCl_x$). However, since the vapour pressure of $InCl_x$ is too low at room temperature, the sample must be heated to remove the reaction product efficiently [41].

Chlorine/argon based chemistry is frequently used for the etching of GaAs . As the reaction product (*e.g.* $GaCl_3$ and Ga_2Cl_6) have a high vapour pressure at room temperature, they easily desorb from the surface and therefore the process temperature is not a crucial parameter [34].

The efficiency of the ion bombardment depends greatly on the plasma density and pressure [43]. A high plasma density at low pressure increases the ion bombardment efficiency due to the increased mean free path length, but renders it more difficult to maintain the plasma. In this case high electrical power usually at radio frequency has
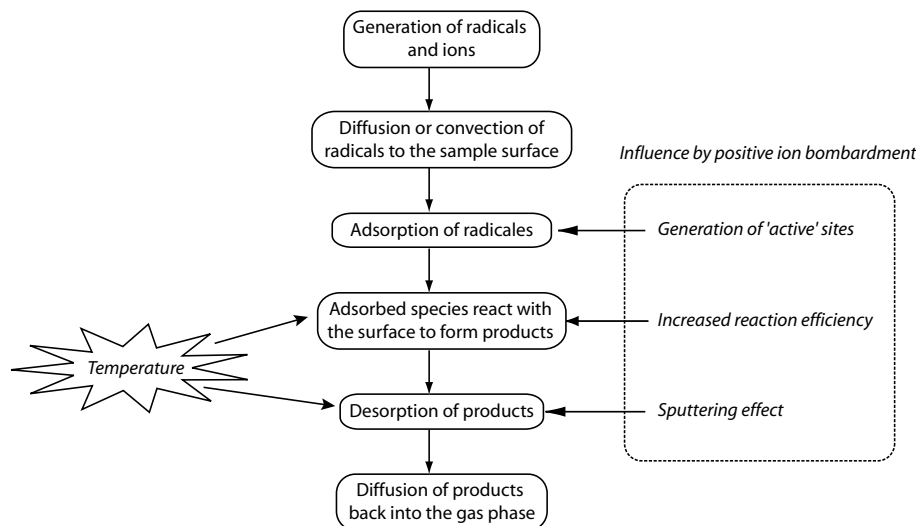

Figure 2.7: Stepwise description of the dry etching mechanism. Note the manifold influence by the positive ion bombardment.
[*Description du mécanisme de la gravure sèche. Notez l'influence variée du bombardement d'ions positifs.*]

to be coupled to the plasma. A positive effect contributing to high aspect ratios is the wall passivation through the formation of a thin polymeric protective layer on the wall surface, since it forms only if there is no ion bombardment. Often the PMMA (polymer) contributes to its formation [42].

In almost all the dry etching techniques the etch rate of smaller holes lags behind that of bigger holes. This lag effect may be caused by 1) ion shadowing, *i.e.* the screening of the ion beam by the mask edge, 2) deflection of the ions due to mask charging, and 3) redepositing of the etch products on the hole walls. At the present time it is difficult to identify the dominant mechanism [41].

When categorising the different etching techniques one distinguishes between reactive ion etching (RIE) based techniques where the sample is inside the plasma chamber with no independent control of the physical and the chemical contribution in the etching mechanism and reactive ion beam etching (RIBE) techniques (*e.g.* CAIBE), where the two contributions can be tuned separately. Within the RIE class the plasma density serves as a criterion to differentiate between low-density plasma techniques, *e.g.* capacity coupled plasma (CCP-RIE) and dense plasma techniques, *e.g.* electron cyclotron resonance (ECR-RIE) and inductively coupled plasma (ICP-RIE) (see Table 2.5).

CCP-RIE: In this technique the plasma is produced between the rf-driven sample holder and the grounded top-plate (see Fig. 2.8). High etch rates are linked to high input power and high bias of the powered electrode leading to undesired high ion energies. On the other hand, it proves difficult in this configuration to sustain the plasma at low pressure, in order to render the ion bombardment more efficient. The hole depth decreases with decreasing hole size and the etch rate of nanometer-sized features ($\varnothing = 490$ nm) lags behind the etch rate for micrometer-sized InP test patterns by a factor larger than two (RIE lag) [37]. The etch depth depends greatly on the feature size and is inherently limited to 1 μm corresponding to aspect ratios of the order of 2.3 .
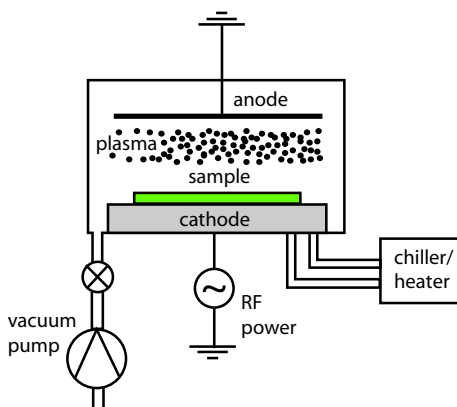
Figure 2.8: Schematic representation of a CCP etch tool.
[Schéma d'une machine de gravure à plasma de type CCP.]

In the case of the GaAs samples described in this thesis, the CCP-RIE technique was used to transfer the pattern into the SiO_2 mask. A gas mixture of $CHF_3/Ar = 2:1$ was used. Low power (50 W) in combination with a pressure of $3 \cdot 10^{-2}$ mbar prevents the PMMA from melting and SiO_2 layers up to 350 nm thick can be perforated [34].

ECR-RIE: This configuration offers a higher plasma density than CCP-RIE which is obtained by transferring microwave power to the electrons at the cyclotron resonance (see Fig. 2.9). The ion energy can be controlled independently of the plasma density by tuning the rf-power applied to the sample holder. However, it proves difficult and expensive to scale the technique to large wafer sizes and in some cases plasma mode-hopping occurs.

In the case of the GaAs samples described in this thesis, the hole pattern was transferred into the semiconductor by a Cl_2/Ar-based ECR process leading to hole depths of 0.9 [44] - 1.1 μm with vertical sidewalls.

In the case of InP hole depths of 3-4 μm [34] with vertical sidewalls can be reached with an Cl_2/Ar gas mixture and a ECR power of 1000 W. The high ECR power facilitates the desorption of $InCl_3$ as it indirectly heats the sample.
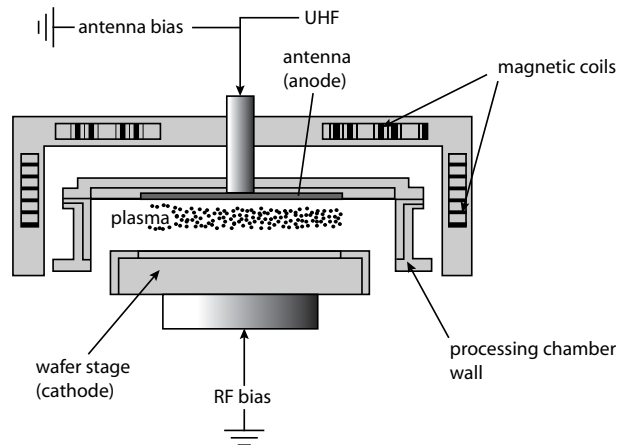

Figure 2.9: Schematic representation of an insulating layer ultra high frequency (UHF) ECR etching chamber. Stable uniform plasma is produced in the $3 - 10$ cm wide gap by UHF waves from a flat antenna coupled with a magnetic field.
[Schéma d'une ECR à fréquence ultra-haute (UHF). Un plasma uniforme et stable est produit par les ondes UHF émergeant d'une antenne plate couplée à un champ magnétique.]

ICP-RIE: The electrical power is transferred to the plasma by means of an inductive coil generating a vertical magnetic field which then induces an electrical field which confines the accelerated electrons in a circular motion (see Fig. 2.10). This allows for adjusting the plasma density without touching the sample bias voltage between the electrodes, *i.e.* the ion energy. Etch depths as large as $4.5\,\mu$m corresponding to aspect ratios as high as 14 [45] have been achieved in InP using $SiCl_4$-based chemistry.
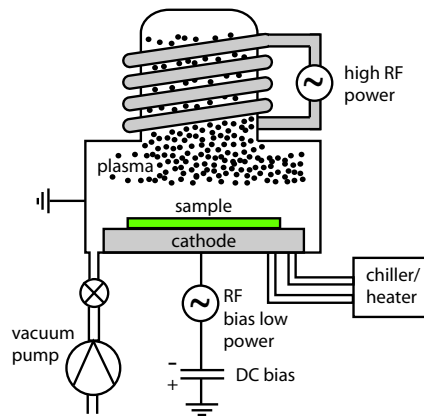
Figure 2.10: Schematic representation of an ICP high
density plasma etch machine.
*[Schéma d'une machine de gravure à
plasma de haute densité de type ICP.]*

CAIBE: In contrast to the previously described methods, typical for the RIBE technique, the argon plasma is produced in a chamber separated from the sample (see Fig. 2.11). A reactive gas (chlorine) is introduced very close to the sample in order to enhance the etching rate by the chemical component. In the case of InP etching this configuration allows separate adjustment of the chemical ($Cl\cdot$ radicals) and the physical component (Ar^+ ions) and is supposed to be very flexible and efficient. In the case of Ar/Cl_2-based CAIBE, both shape and depth of the holes depend on sample temperature, Cl_2-flow and etching duration [37]. The sample temperature, a crucial parameter, can be varied by means of a halogen lamp (see Fig. 2.11) and measured on the sample holder using a thermocouple [46]. In the case of InP the hole morphology was found to be optimal at a temperature of about 220 °C and an etch interval of 20 min [41]. The etch depth depends on the feature size (lag effect) and ranges from 2.5 to 4.5 μm. For hole diameters as small as 220 nm holes deeper than 2 μm can be achieved [46].
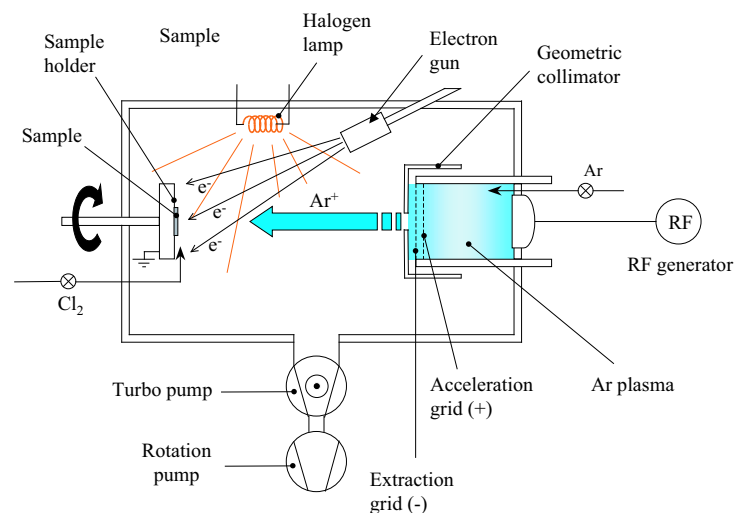

Figure 2.11: Schematic representation of an Ar/Cl_2-based CAIBE etching tool (figure from
M. Mulot *et al.* [37]).
*[Schéma d'un outil de gravure du type CAIBE à base de Ar/Cl_2 (figure de M.
Mulot et al. [37]).]*

A classification of the different etching techniques is presented in Table 2.5.   The

general processing steps for the patterning of GaAs and InP samples are summarised
in Fig. 2.12.
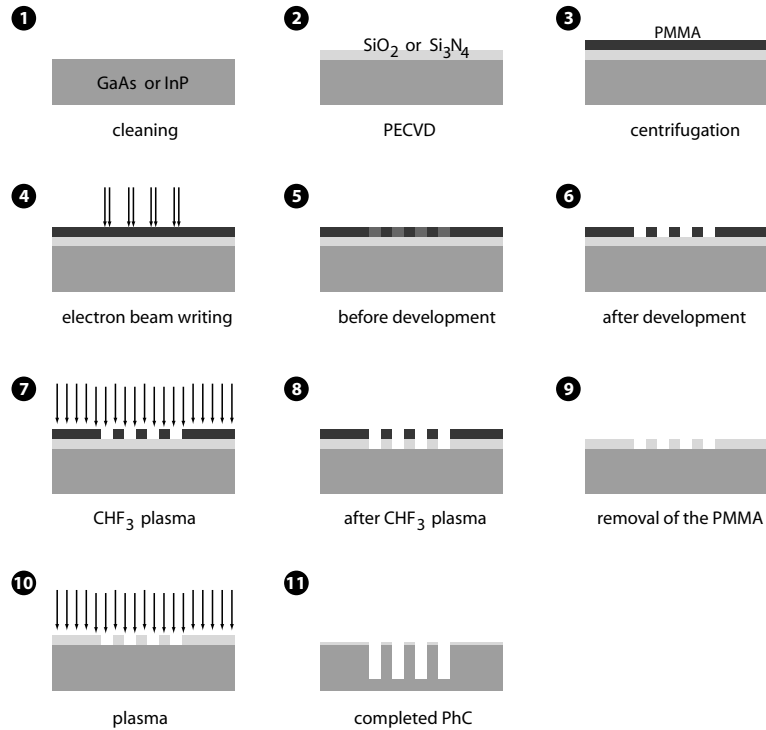
Figure 2.12: Patterning of PhCs, 1-3: sample preparation, 4-6: the PMMA mask is written
and developed, 7-9: the PMMA mask is transferred on the dielectric mask,
10-11: the structure is transferred into the semiconductor.
[1-3: Préparation de l'échantillon , 4-6: définition du masque, 7-9: transfert
du masque PMMA sur silicium, 10-11: transfert du masque silicium sur le
semi-conducteur.]

	RIE			RIBE
	low density plasma	high density plasma		
	CCP	ECR	ICP	CAIBE
Independent control of physical and chemical etching	no	no	no	yes
Independent control of plasma density and ion energy	no	yes	yes	yes
RIE-Lag	++	+	+	+
Scalability to large wafersizes	yes	no	yes	yes
Etch gas for InP	$Ar/CH_4/H_2$	Cl_2/Ar	$SiCl_4$	Cl_2/Ar
Etch gas for GaAs	$SiCl_4/Ar/O_2$	Cl_2/Ar		Cl_2/Ar

Table 2.5: Classification of the main dry etching techniques.
[Classification des méthodes principales de la gravure sèche.]

2.2 State-of-the-art of the fabrication technology

Table 2.6 represents the state-of-the art of the different PhC etching techniques.

In **CCP** the holes have a "jar-shape" which is due to a redeposition of etch products from the ion sputtering coupled with a lower chemical etch rate at the bottom of the hole [37]. The hole depth is limited by inefficient removal of the etch products, which may be due to the low plasma density and which is influenced by the temperature, too.

The holes etched by **ECR** suffer from the tapered form and the depth fluctuations but reach a sufficient depth of up to 3.2 μm with an aspect ratio of 16 [35] in case of InP. On GaAs the technique provides 1.1 μm deep holes with cylindrical shape.

The **ICP** provides very vertical and parallel walls and a good uniformity of hole shape, depth and size over the whole PhC pattern. In comparison to other methods, the ICP yields an increased wall roughness. The etch rate decreases with decreasing hole diameter, whereas the aspect ratio remains nearly constant for hole diameters between 200 nm and 330 nm. The hole depth is partly limited by the poor selectivity ($\approx 11:1$) between InP and the mask. In case of InP hole depths up to 4.5 μm with a fill factor of only 25 % have been reached [32].

In **CAIBE** there remains the problem of the tapered hole bottoms. However, if the etched holes are sufficiently deep ($> 3\ \mu$m) it may not be of serious concern. Also with this technique, the etch rate decreases with decreasing hole size (lag effect). The lag effect is less pronounced in CAIBE due to lower operating pressures and the collimated Ar-ion beam. The main limitation that prevents deeper etching is the thickness of the SiO_2 mask (250 nm), which is close to the maximum thickness that can be patterned by EBL using PMMA [47]. Note that mask widening induced by lateral mask edge erosion limits the minimal mask thickness that should not be under-run, to at least 50 nm. This faceting causes an increase of the air-filling factor. The mask edge erosion could be significantly reduced by using metal masks instead of dielectric masks [37].

2.3 Conclusion on sample fabrication

In conclusion, with all the dry etching technologies (ECR, ICP and CAIBE), very deep holes, up to 4 μm in InP, can be obtained. This is sufficient for passive and active PhC integration. Well cylindrically-shaped holes down to the beginning of the lower cladding can be achieved with all techniques, while a tapering close to the bottom of the structures occurs in the case of ECR and CAIBE . This non-ideal shape of the bottom parts theoretically leads to additional losses (see section 3.4) which is, however, tolerable due to the great hole depth. With CAIBE, aspect ratios of up to 20 are feasible.

SEM images deliver local information about the hole shape. It should, however, be noted that it is a delicate task to determine for example the fill factor from SEM images: The top view of the holes is not significative for the average diameter inside the hole and in the case of lateral images, the cleavage may not exactly pass through the centres of the holes, which may alter the image and deform the holes. Additionally, global PhC properties (averaged over many wavelengths), *e.g.* mean air-filling factor, out-of-plane losses, band gap, transmission are only accessible by optical characterisation (see chapter 3).
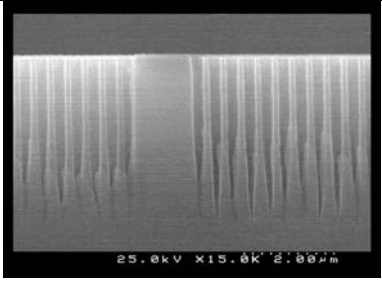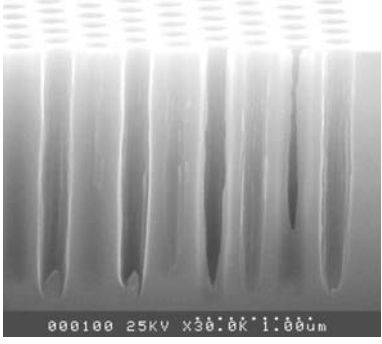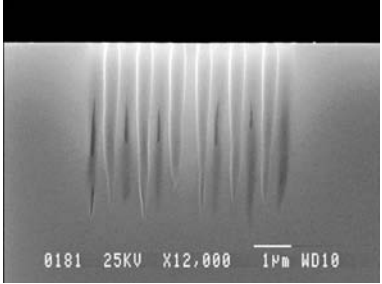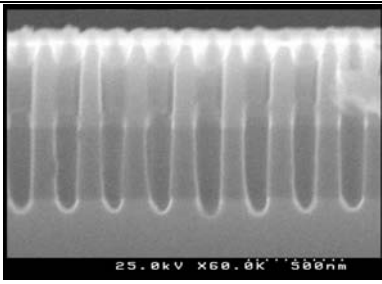
		Hole shape	Etch depth (μm)	Aspect ratio	Limiting factors
ECR (InP)		tapered	3-4	16	mask selectivity
ICP (InP)		cylindro-conical	4.5	14	mask selectivity
CAIBE (InP)		tapered	2.5-4.5	10-20	mask thickness/ removal of etch products
ECR (GaAs)		cylindrical	1.1	6	mask thickness

Table 2.6: SEM images and state-of-the-art performance of PhC etching technologies available at PCIC project partners. Photos are courtesy of University of Würzburg (UWUERZ), Opto+, KTH and again UWUERZ (from top to bottom).
[Images de microscope électronique à balayage (MEB) et performances de pointes de la gravure des cristaux photoniques disponibles auprès des partenaires du projet PCIC. Photos avec l'aimable autorisation de l'université de Würzburg (UWUERZ), Opto+, KTH et de nouveau UWUERZ (de haut en bas).]

Chapter 3

Optical characterisation

3.1   The internal light source (ILS) technique

3.1.1   Experimental Principle

Introduced at Ecole Polytechnique Palaiseau (EPP) in 1996, the internal light source (ILS) technique has been successfully applied to the study of quasi-2D PhC structures deeply etched in GaAs-based vertical step-index waveguides [48]. The ILS technique has been demonstrated to be a powerful tool both to assess some fundamental PhC properties and to measure reflection (R), transmission (T), and diffraction (D) [49–52]. It also proved to be a powerful tool for the characterisation of more complicated structures such as Fabry-Pérot cavities [53], two-dimensional hexagonal cavities [48] or straight waveguides [54]. The application range of the ILS technique has the been expanded by EPP from the GaAs to the InP material system [55,45,56]. The basic principles remain the same but the detection at $\lambda = 1.55\,\mu$m becomes more demanding in terms of equipment. A setup based on the same principle and capable to measure simultaneously in both material systems has been set up here at EPFL [41,57,45,58,59].

In a few words the ILS technique is based on an internal light source (photoluminescence excited by a pump laser) that is positioned in such a way that the light propagates through the PhC structure and afterwards is collected at the facet. The source is then displaced into an unpatterned region at equal distance from the facet and the collected signal serves as a reference to normalise the primary signal (see Fig. 3.1).
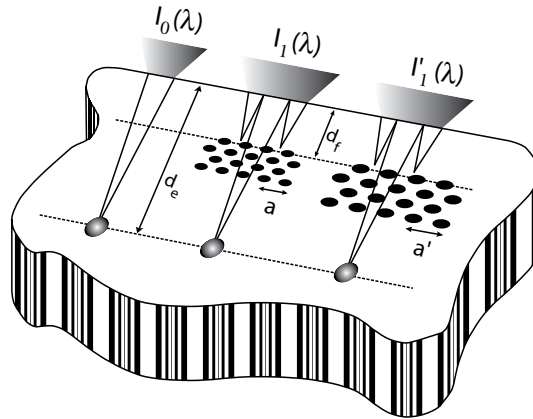
Figure 3.1: Experimental configuration for simple PhC transmission measurements. The distance between the pattern and the facet (d_f) and the excitation distance (d_e) is kept constant. The reference $I_0(\lambda)$ is taken in an unetched area and $I_1(\lambda)$ spectra are collected from PhC slabs with different periods.
[Configuration expérimentale pour des mesures de transmission des cristaux simples. La distance entre la structure et la facette (d_f) et la distance d'excitation (d_e) sont gardées constantes. La référence $I_0(\lambda)$ est prise dans une région sans structure et les spectres $I_1(\lambda)$ sont mesurés à partir des cristaux photoniques de différentes périodes.]

3.1.2 Normalisation of transmission measurements

The reference signal and the PhC-related signal are measured keeping constant the distance between the excitation points and the cleaved facet. Provided that the photoluminescence (PL) emission remains homogeneous, the normalisation of transmission measurements through standard test-structures (*e.g.* simple slabs and Fabry-Pérot cavities) is given by the ratio $I_1(\lambda)/I_0(\lambda)$ which yields the absolute transmission spectrum.

3.1.3 Lithographic tuning

Due to the limited width of the probed spectral range ($\Delta\lambda \approx 100$ nm for InP and $\Delta\lambda \approx 150$ nm for GaAs , respectively) the so called 'lithographic tuning' [48] approach is applied (see Fig. 3.1). Instead of fabricating several samples with appropriately tuned active layers, the emission wavelength is kept constant and the scaling property of PhCs [1] is exploited (see section 1.5.1). PhC slabs with different period a values and constant air filling factor f are measured and the whole PhC is explored as a function of the reduced frequency $u = a/\lambda$, *i.e.* the spectra corresponding to different periods are stitched together. For example in the case of GaAs 9 different periods are required to accurately scan the band gap and the two band edges.

3.1.4 Signal collection

3.1.4.1 The three signals

In Fig. 3.2(a), the general configuration for ILS experiments is illustrated.

A pump laser is focused vertically on the heterostructure and excites inside the active layer Photoluminescence (PL) emission, constituting a built-in light source. The active layer of the samples consist in two embedded quantum wells (QWs) in the case of InP and in three quantum dot (QD) layers in the case of GaAs. A detailed description of the different active sources and their properties is presented in section 3.1.5. The ILS technique provides spatial resolution (limited by the spot size of $\varnothing = 2.5\,\mu$m) for the positioning of the source on the sample. Part of the PL light propagates parallel to the surface as a guided mode and interacts with the PhC structure. Then, the image of the guided beam escaping from the sample through the cleaved facet is coupled into a multimode optical fibre ($\varnothing = 100\,\mu$m) for spectral analysis. Due to refraction at the layer boundaries, three different beams come out from the cleaved facet after propagation through air, substrate, and inside the guide, respectively (see Fig. 3.2(a)). When focusing on the facet the air signal appears as half circle above the facet with a radius $d \cdot N.A.$, the substrate signal appears on the opposite side as half circle with radius $\frac{d}{n} \cdot N.A.$ and the guided mode signal as bright in-plane bar.

The guided signal is collected by focusing a collection objective on the facet. The collected light is then separated by a beam splitter and partly directed on a camera and partly coupled into a fibre. This allows to perform a spatial analysis on the different lateral signals. The exact position of the fibre with respect to the facet and the different signals can be found out by injecting light into the fibre in the opposite way and imaging
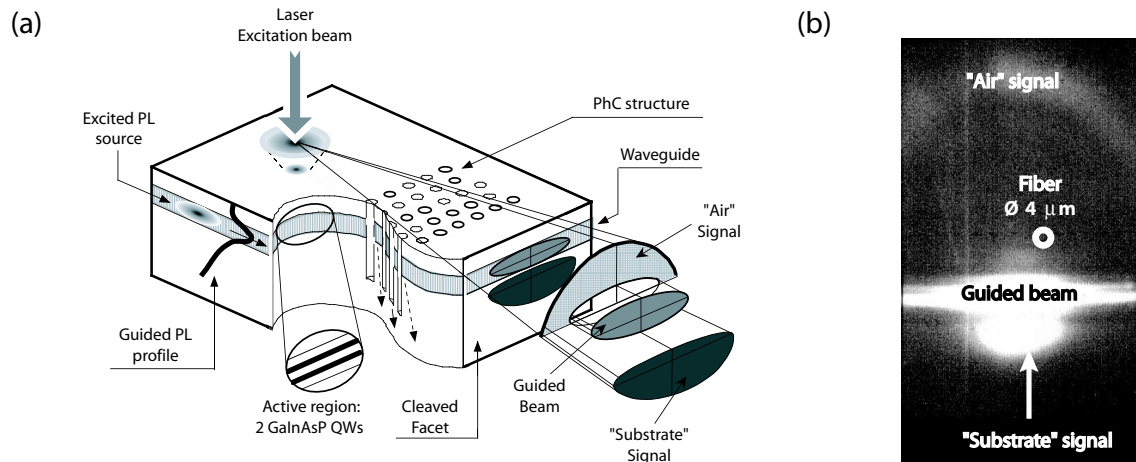
Figure 3.2: a) General experimental configuration for ILS measurements: Photoluminescence emission is excited inside the active region embedded in a slab waveguide structure and then guided towards the PhC structure. The three beams escaping from the cleaved facet after propagation through air, substrate and core are sketched. b) Typical image of the signals when the collection optics is focused on the cleaved facet. The white circle ($\varnothing = 4\,\mu$m) represents the conjugate image of the collection fibre.

[a) Dispositif expérimental d'une mesure à source interne: La photoluminescence est excité dans la région active incorporée dans un guide d'onde plane. Les trois faisceaux sortant de la facette clivée après s'être propagé dans l'air, le substrat et le guide sont indiqués. b) Image typique des signaux lorsque l'optique de collection est focalisée sur la face clivée. Le cercle blanc ($\varnothing = 4\,\mu$m) représente l'image conjuguée de la fibre de collection.]

the conjugated fibre image. Fig. 3.2(b) shows a typical image that is obtained when the collection optics is focused on the facet. The guided beam appears as a focused bright line along the edge while the white circle ($\varnothing = 4\mu$m) represents the conjugate image of the collection fibre. The guided contribution can be selected and spatially resolved, aligning the circle with the bright line.

3.1.4.2 Virtual source position

The refraction at the facet creates a virtual source inside the semiconductor from where the escaping beams leave. The virtual source position can be calculated by Snell-Descartes' law which is approximated in the limit of small angles by $\tan\theta \approx n\tan\theta_i$. On the other hand $\tan\theta_i = s/d_0$ and $\tan\theta = s/d_v$ (see Fig. 3.3). Putting all together, one obtains $d_v = d_0/n$.
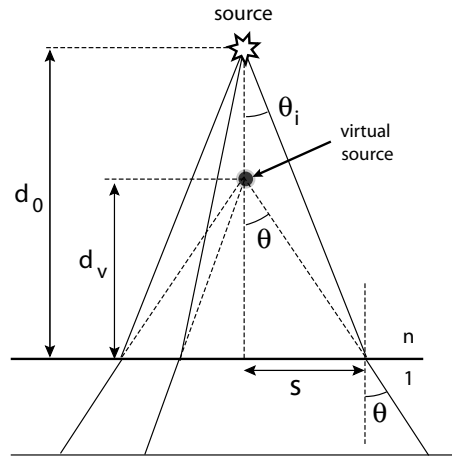

Figure 3.3: Geometrical construction in order to obtain the position of the virtual source. *[Construction géométrique pour obtenir la position de la source virtuelle.]*

3.1.4.3 Excitation distance

In the case where the source is placed in an un-patterned part of the sample, the guided mode propagates radially in every direction. Due to the high refractive index of the semiconductor, only the light impinging in an angle below the critical angle ($\theta_c = 18\,^\circ$ for InP and $17.3\,^\circ$ for GaAs) can escape at the facet. A big part of this light will leave the facet with very large angles and is not able to enter the collection cone ($\theta = 30\,^\circ$ of the objective. The *limiting* angle θ_l describes the cone inside the semiconductor that leaves the facet with the angle θ and is given by the effective index of the guided mode and the numerical aperture ($N.A. = 0.5$) of the collection objective (see Fig. 3.4). The value of θ_l is $8.9\,^\circ$ for InP and $8.6\,^\circ$ for GaAs.

There exist now two regimes named (a) and (b) wether the source is placed far from the facet (Fig. 3.4(a)) or close to it (Fig. 3.4(b)). In the regime (b) the total amount of the light within the angle θ_l is collected by the objective. In the regime (a) the collection angle is limited by the spotsize ($D = 4\,\mu$m) of the conjugate image of the collection fibre, which improves the angular selectivity of the measurement. It is thus preferable to work in regime (a) where the angular resolution is spotsize limited and

the effective internal *selection* angle is given by $\theta_s = \arctan\left(\frac{D}{2d_0}\right)$ which is smaller than θ_l (see Fig. 3.4).

The distance d_{limit} that marks the transition between the two regimes is given by the condition

$$\theta_s = \theta_l \quad \rightarrow \quad \frac{D}{2d_{\mathrm{limit}}} = \tan\theta_l \quad \rightarrow \quad d_{\mathrm{limit}} = \frac{D}{2\tan\theta_l} \tag{3.1}$$

When assuming a point-like source, d_{limit} is $13\,\mu\mathrm{m}$ for both InP and GaAs. For the point-like source the angular selectivity is given by the selection angle θ_s under which the conjugate fibre image is seen from the source, *i.e.* $\theta_s = \frac{D}{2d}$.

However for positions close to the facet, the extension of the source ($\varnothing = 4\,\mu\mathrm{m}$) has to be taken into account. For a source with diameter $S = 2\,\mu\mathrm{m}$ the angular resolution is $\theta_s = \frac{D+S}{2\theta_l}$ [31] and one obtains $d_{\mathrm{limit}} = 22\,\mu\mathrm{m}$.

The angular selectivity is important for the measurement of PhC samples where the optical properties depend a lot from the incidence angle with respect to the symmetry axis of the crystal.

In summary one can state that if the excitation distance d_0 is larger than d_{limit}, the cross-talk between the three signals is negligible and the selective analysis of the guided
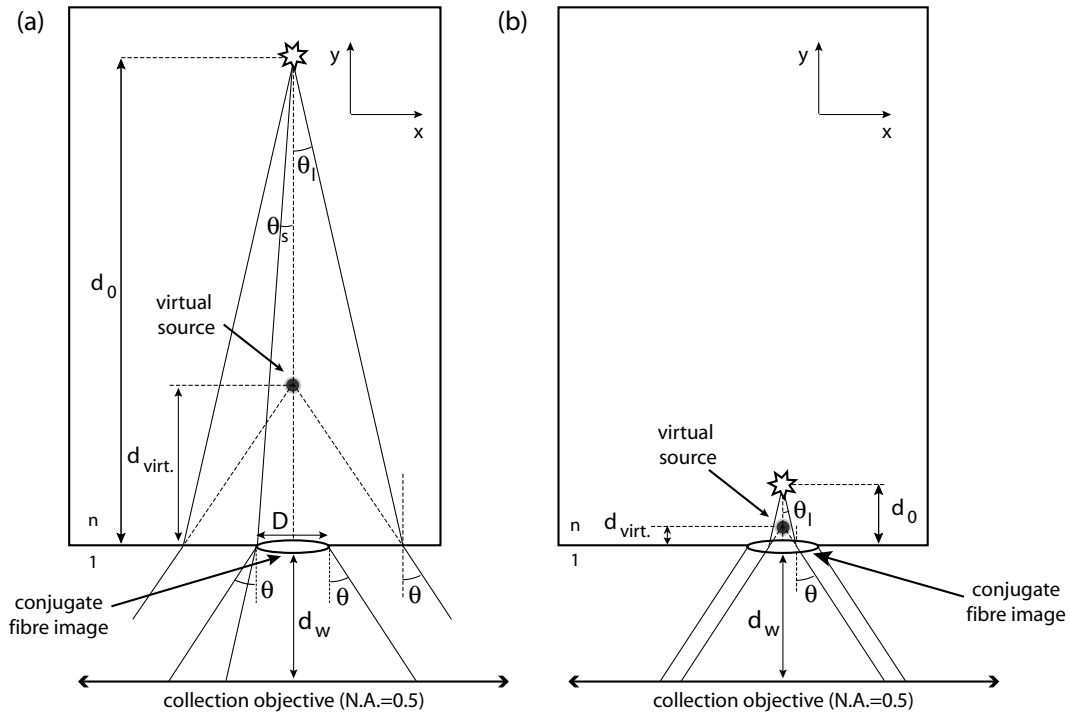
Figure 3.4: Measurement of a reference spectrum: PL is emitted at a distance d_0 from the facet and is collected by an objective with a collection angle $\theta = 30°$ and injected into a fibre with a conjugate image of diameter D. Two different regimes exist: a) The source is placed far from the facet. b) Excitation close to the facet.
[*Mesure d'un spectre de référence: PL est émise à une distance d_0 de la facette puis est collectée par un objectif avec un angle de collection $\theta = 30°$ pour être injectée dans une fibre avec un image conjugé de diamètre D. Deux différents régimes existent: a) La source est placée loin de la facette. b) Excitation proche de la facette.*]

light can be performed by imaging the edge signal [49].

3.1.5 Sample structure

3.1.5.1 Vertical waveguide

As stated above, the useful light for the measurement is the one guided by the vertical heterostructure. The mode profiles inside the guiding layer for both InP and GaAs are shown in Fig. 3.5(a) and (b), respectively.
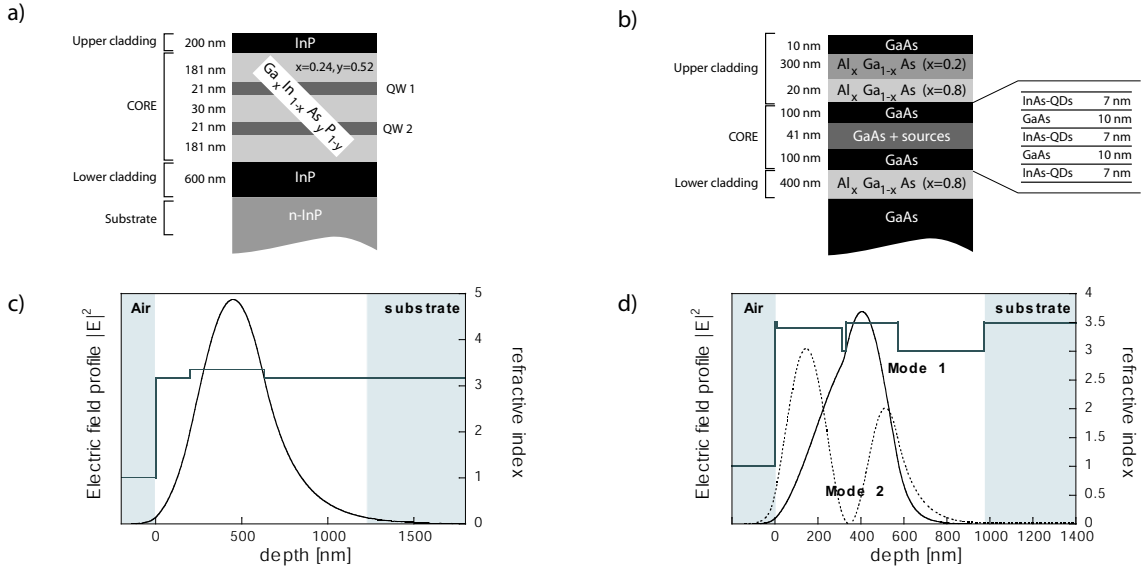

Figure 3.5: a) Vertical structure of the InP samples containing 2 QWs. b) Vertical structure of the GaAs samples containing 3 QD layers. c) Guided mode profile InP case: the guide is monomode in TE-polarisation with $n_{eff} = 3.24$. d) Guided mode profile GaAs case: there exist two guided TE-polarised modes with $n_{eff} = 3.36$ and 3.13, respectively.

[*a) Structure verticale des échantillons GaAs qui contiennent 2 puits quantiques. b) Structure verticale des échantillons InP qui contiennent 3 couches de boîtes quantiques. c) Profiles des modes guidés, cas InP : le guide est monomode en polarisation TE avec $n_{eff} = 3.24$. d) Profiles des modes guidés, cas GaAs : Deux modes guidés polarisés TE avec $n_{eff} = 3.36$ et 3.15 existent.*]

The vertical structure in InP supports a single mode with effective index $n_{eff} = 3.24$. This is the case for the InP structure where a TE-polarised mode with an effective index given by $n_{eff} = 3.24$ is supported. The maximum of the squared electric field profile $|E^{(}z)|^2$ is slightly shifted from the centre of the core layer, while it decays exponentially in the cladding layers (see Fig. 3.5(a)). The shift between the profile peak and the location of the QWs slightly reduces the QW reabsorption on the propagating mode. We note that, due to the material dispersion, n_{eff} is a function of λ and, for a PL emission spectrum centred at 1500 nm, the effective index dispersion of the guided mode is $\partial n/\partial\lambda = 2.5 \cdot 10^{-4}$ nm. Then, since for a single ILS measurement a spectral interval of $\Delta\lambda = 100$ nm is probed and $\Delta n = \Delta\lambda \cdot (\partial n/\partial\lambda)$, dispersion-corrected n_{eff} values are found to range from 3.23 to 3.255.

In the case of GaAs the vertical structure supports two TE-polarised modes (see Fig. 3.5(b)) and the effective indices of the even-like mode *1* and the odd-like mode *2* are $n_{\text{eff}} = 3.36$ and 3.15, respectively. As in the previous case, n_{eff} is a function of λ and, for a PL emission spectrum centred at 1050 nm, the effective index dispersion of the guided mode is $\partial n / \partial \lambda = 5 \cdot 10^{-4}$ nm. Mode *2* has its field mainly concentrated in the upper cladding and it can be assumed to leak more into air and therefore to be more lossy than mode *1*. According to a transfer-matrix calculation [60,61], the extinction length of the cladding mode (mode *2*) is of the order of 40 μm compared to 725 μm of the fundamental mode (see Table 3.1).

mode	symmetry	n_{eff}	extinction length [μm]
1	even	3.36	725
2	odd	3.13	42

Table 3.1: Vertical modes in the GaAs heterostructure as described in Table 2.2: the extinction length includes both tunnelling into air and absorption of the core at the central wavelength $\lambda = 1050$ nm. The angles θ and α are defined in Fig. 3.6.
[Modes verticaux dans l'hétérostructure GaAs décrite dans le tableau 2.2: la longueur d'extinction prend en compte la fuite dans le substrat et dans l'air et l'absorption dans le coeur à la longueur d'onde centrale $\lambda = 1050$ nm. Les angles θ et α sont définie dans la Fig. 3.6.]

The effective index can be translated into a internal reflection angle θ by using the relation $n_{\text{eff}} = n_{\text{core}} \cdot \sin \theta$, yielding $\theta = 73.5\,^\circ$, $\theta = 63.6\,^\circ$ for mode 1 and 2, respectively. Only mode 1 ($\alpha = 16.5\,^\circ$) impinges on the facet with an angle below the critical angle $\alpha_c = 16.6\,^\circ$ and can couple-out (see Fig. 3.6).
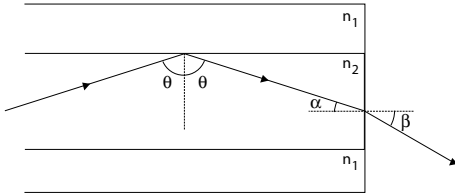

Figure 3.6: Geometrical picture of out-coupling at the facet.
[Image géometrique du couplage à l'exterieur.]

3.1.5.2   Embedded light source

InP samples: Quantum wells   Typical guided PL spectra of the InP samples taken at room temperature with the excitation spot at distance $d = 70$ μm from the cleaved facet are presented in Fig. 3.7(a) for the TE polarization (black solid line). The structure is designed to have the two quantum well emission wavelengths centred at $\lambda_1 = 1565$nm and $\lambda_2 = 1460$nm, respectively. The feature evidenced at $\lambda_{\text{GAP}} = 1220$nm is attributed to the $Ga_{0.24}In_{0.76}As_{0.52}P_{0.48}$ band gap emission. The guided PL spectrum is strongly modified with respect to the frontal PL due to the QW reabsorption. A steep flanc can be observed in the guided PL spectrum at $\lambda = 1475$ nm due to reabsorption which is mainly due to the TE-polarized electron-heavy-holes recombination in QW1 and QW2, respectively [62]. The convolution of the QW1 and QW2 PL peaks yields a guided signal with an overall spectral window of $\Delta \lambda \approx 100$ nm. The value for the lateral PL can be further increased by performing measurements at high pumping power
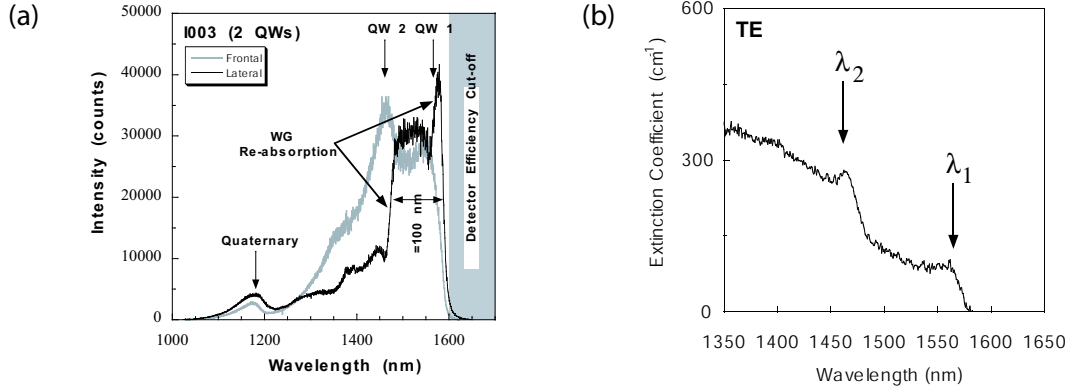
Figure 3.7: a) Typical guided TE-polarised photoluminescence (PL) signal of InP heterostructure (black curve) is collected by placing the excitation spot in an unetched region of the sample at a distance $d = 70\,\mu\text{m}$ from the cleaved edge. Arrows indicate the QW1 and QW2 contributions from the two GaInAsP QWs and the sharp low-wavelength absorption edge due to the QW reabsorption inside the guide. The low-intensity PL emission at $\lambda_{GAP} = 1.18\,\mu\text{m}$ from the quaternary GaInAsP guide core is evidenced. For comparison, the frontal PL is shown in grey. b) Modal losses (TE) of the InP/GaInAsP step-index waveguide. Vertical arrows indicate the emission wavelength of QW1 and QW2.

[a) Le signal de photoluminescence (PL) typique (polarisé en TE) d'une hétérostructure InP est collecté en excitant à une distance de $d = 70\,\mu m$ du bord clivé. Les flèches indiquent les contributions des 2 puits quantiques GaInAsP (QW1 et QW2) et le flanc d'absorption à haute énergie dû à la réabsorption des puits quantiques dans le guide. La PL de basse intensité à $\lambda_{GAP} = 1.18\,\mu m$ du quaternaire GaInAsP est visible. Pour permettre la comparaison la PL frontale est affichée en gris. b) Pertes modales mesurées en TE d'un guide InP/GaInAsP. Les flèches verticales indiquent la longueur d'onde d'émission des puits quantique 1 et 2.]

($\approx 340\,\text{kWcm}^{-2}$). This intrinsic limit could be overcome by substituting QWs with QDs) as already done for ILS measurements on GaAs-based structures [48].

The absorption coefficient plotted in Fig. 3.7(b) was obtained by measuring the bare guided signal $I_0(\lambda, d)$ for different d values between 50 and 100 μm and using a Lambert-Beer-type formula modified to take into account the variation of the collection angle with d [49], i.e.,

$$I_1(\lambda, d) = \frac{A}{d} I_0(\lambda) T_{air} e^{-\alpha(\lambda)d} \tag{3.2}$$

where A is a constant, $I_0(\lambda)$ is the total intensity emitted at the excitation point, and T_{air} is the transmission coefficient at the interface with air. The extinction curve features two steep edges corresponding to the absorption due to QW1 and QW2. The two arrows indicate the nominal emission wavelengths of QW1 and QW2.

GaAs samples: Quantum dots Fig. 3.8(a) presents the frontal PL of a GaAs sample containing three layers of QDs. The spectral width of the frontal emission spectrum amounts to 112 nm. The small peak around 923 nm corresponds to the wetting layer with high InAs content. The lateral PL of QDs is not polarised, but due to different coupling with respect to TE and TM modes, the guided TE-polarised signal

measured at the facet is more than twice as big [31] as the TM-polarised signal. This fact fits well with the exploration of the TE-gap of our PhCs. The guided TE-polarised PL signal features a relatively flat band centred around $\lambda = 1050\,\text{nm}$ and an exploitable width of $\Delta\lambda = 150\,\text{nm}$ (see Fig 3.8(b)). The lateral guided signal is indeed very different from the frontal PL. The strong GaAs peak is completely missing due to the strong absorption for wavelengths smaller than 930 nm, the band gap energy of GaAs.
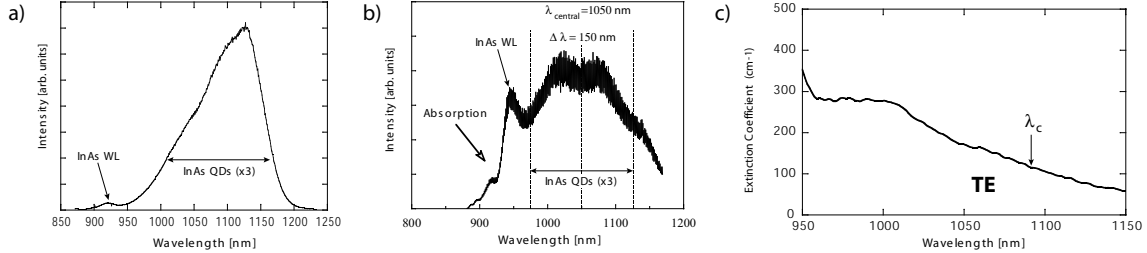

Figure 3.8: Photoluminescence (PL) spectra of GaAs heterostructure containing 3 layers of self-organised InAs QDs: a) front PL. b) TE guided PL. c) modal losses (extinction coefficient).
[*Spectre de photoluminescence (PL) de la structure* GaAs *contenant 3 couches de boîtes quantiques InAs: a) PL frontale. b) PL guidée en TE. c) Pertes modales (coefficient d'extinction).*]

The overall modal losses due to the vertical mode confinement and the reabsorption of the active layer, is smaller in the case of QDs in GaAs than for QWs in InP . They are of the order of $120\,\text{cm}^{-1}$ for three layers of QDs (see Fig. 3.8(c)), whereas they are of the order of $200\,\text{cm}^{-1}$ in the case of two QWs in InP (see Fig. 3.7(b)).

3.2 Setup

Our setup (sketched in Fig 3.9) is based on the same principle as the original setup developed at EPP [49], but allows ILS measurements on both GaAs -based ($\lambda = 1\,\mu\text{m}$) and InP -based ($\lambda = 1.55\,\mu\text{m}$) PhC samples [41]. A 17-mW He-Ne laser ($\lambda = 633\,\text{nm}$) is used to excite spontaneous emission inside the active layer. The laser beam is spatially filtered and expanded in order to arrive with the adapted diameter at the final focusing microscope lens.

A 200 mm focal length IR microscope lens with numerical aperture N.A. = 0.4 focuses the beam onto the sample surface. The achieved excitation spot diameter ($\varnothing = 2.5\,\mu\text{m}$) yields a maximum pumping density of $340\,\text{kWcm}^{-2}$. When focusing the laser beam, the use of a dichroïc mirror along with an Si-CCD camera provides the simultaneous imaging of the sample front surface and the excited PL spot.

The light beam escaping from the cleaved facet is collected by a perfectly achromatic 36 x Cassegrain lens with an 8.6 mm working distance. The achromaticity is crucial for utilising the setup in two different wavelength ranges of InP and GaAs. The limited numerical aperture (N.A. = 0.5) corresponds to an internal in-plane collection angle $\theta < 9\,^\circ$ and ensures the directionality of the measurement [49]. A polariser after the reflecting microscop lens allows one to select the TE- (or TM-) polarised component of the signal. Finally a beamsplitter is used to split the collected signal into two
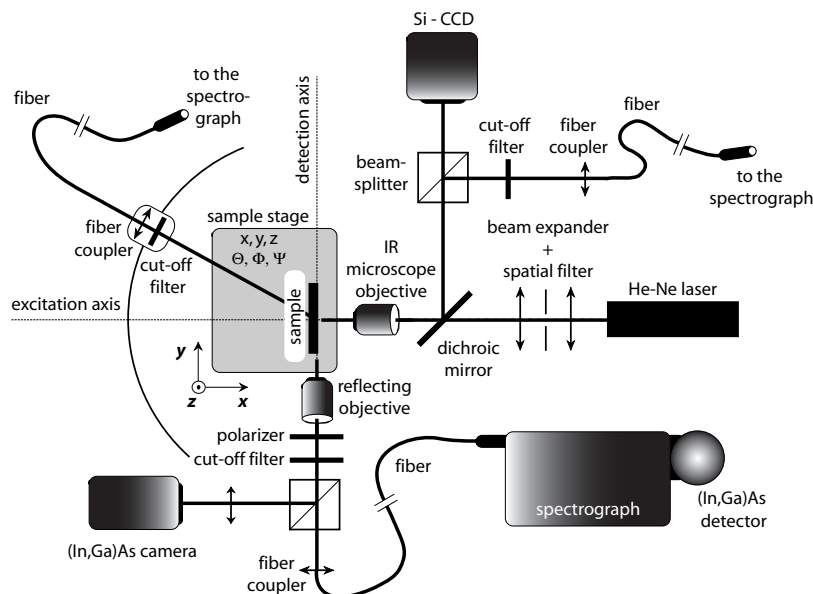
Figure 3.9: Scheme of the experimental setup operating at both 1.55 μm and 1 μm.
[*Schéma expérimental qui fonctionne à 1.55 μm et 1 μm.*]

beams. The first is focused by a long-focal length lens ($f = 40$ cm) onto the $In_xGa_{1-x}As$ near-infrared area camera to image the facet signal. The second beam is coupled into a multi-mode fibre and fed into a 46-cm flat-field imaging spectrograph for spectral analysis. The spectrometer is equipped with a liquid nitrogen-cooled $In_xGa_{1-x}As$ photon counting array detector. The cut-off filters is tuned to block the light from the HeNe-laser (633 nm).

The key components of the setup and its respective performances are:

The spectrometer: It is of the imaging type with a focal length of $f = 46$ cm and is fabricated by Jobin Yvon. Depending on the resolution and spectral coverage requested, either a grating with 150 gr/mm blazed at 1200 nm or a 900 gr/mm blazed at 850 nm can be used. At 1500 nm the resolution of the spectrometer with a slit aperture of 10 μm is 0.04 nm and 0.05 nm for the 150 gr/mm and the 900 gr/mm grating, respectively. When used with the CCD detector array, the resolution for the two gratings at 1500 nm are 0.7 nm/pxl and 0.08 nm/pxl for respective spectral ranges of 360 nm and 40 nm.

The detector array: is manufactured by Sensors Unlimited and consists of two interlaced bars of 256 pixels providing a total of 512 pixels sized 50×500 μm. The pixels are constructed from individual photodiodes arranged in a linear array with a silicon CMOS readout multiplexer circuit. The small gain asymmetry between the two bars respectively between even and odd pixels leads to an interlacing problem which can, however, be corrected by software.

The detector array is in contact with a liquid nitrogen-cooled reservoir (T=77 K), leading to excellent signal-to-noise ratios. The detector can be operated either in a high-sensitivity (HS) mode or in a high-dynamical-range (HDR) mode. In the HS mode the gain is 75 $e^-/$ count with a fixed pattern noise [1] of 280 e^-/s and a read-out noise of

----

[1]Each individual InGaAs photodiode pixel in an array is connected to its own capacitive trans-
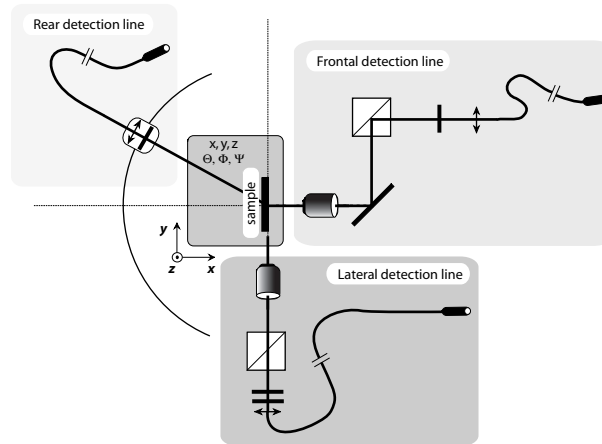
Figure 3.10: Scheme with focus on the different collection lines provided by the setup.
[*Schéma montrant les différentes lignes de collection.*]

640 e^- rms. In the HDR mode the sensitivity is 2000 e^-/ count with a fixed pattern noise of 390 e^-/s and a read-out noise of 6100 e^- rms. As a rule of thumb one should switch from HS mode (shorter integration time) to HDR mode when the integration time exceeds 80 s, in order not to saturate the dark count.

The infrared camera: is produced by Sensors Unlimited and is based on a similar technology to that of the detector array. The chip area measures 320×240 pixels with a pixel pitch of 40 μm. The quantum efficiency is larger than 75 % from 1 to 6 μm.

The sample stage: The sample is fixed on a sample stage which includes translations in all three spatial directions (x,y,z) and three rotations (Θ, Φ, Ψ). The x-y-translators are equipped by differential micrometers with a resolution of 0.07 μm.

Detection lines: The setup comprises three different detection lines: frontal, lateral and angle-resolved rear detection (see Fig. 3.10)

3.3 Characterisation of test structures

The basic characterisation sample contains simple crystal slabs (4 and 8 rows both ΓM and ΓK orientation) and 1D-Fabry-Pérot cavities. Fig. 3.11 sketches a typical layout of a test sample. These structures allow to assess the fabrication quality and the main parameters (gap position, filling-factor, loss).

---

impedance preamplifier circuit. As a result, the bias voltages are often slightly different from pixel to pixel. These minute differences in the output of each element lead to a predictable and repeatable noise signal known as **fixed pattern response**. It depends greatly on both the integration time and the array operating temperature, and can be reduced by thermoelectric or liquid nitrogen cooling. Fortunately, the fixed pattern response is highly repeatable and can almost be eliminated by subtracting a dark acquisition of the same integration time as the illuminated spectrum of interest (from Jobin Yvon).
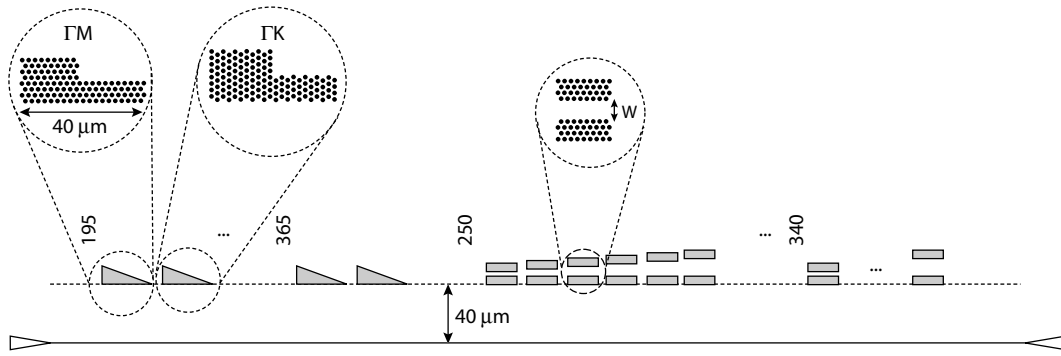
Figure 3.11: Typical test sample for basic characterisation containing simple slabs and 1D-cavities.
[Echantillon de test typique contenant des cristaux simples et des cavités Fabry-Pérot.]

3.3.1 PhC slabs

The experimental configuration for PhC slab transmission measurements is illustrated in Fig. 3.1. The measurement of simple PhC samples provides primarily the energy location of the gap, the gap width, the residual transmission within the gap, the band-edge transmission levels, which are closely related to the out-of plane losses (see section 3.4). In order to investigate the optical properties of the triangular PhC structures, it is sufficient to measure the optical coefficients in the two main crystallographic directions ΓM and ΓK [49]. Fig. 3.12 shows a typical image of a simple crystal slab as seen by the frontal detection line.
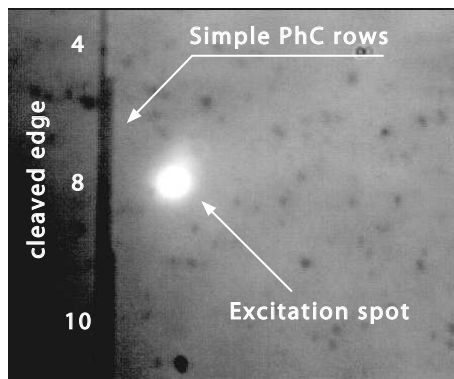

Figure 3.12: Front image of a ΓM -oriented PhC slab consisting of three blocks of 4, 8 and 10 air-holes rows, respectively. The arrow shows the typical excitation spot ($\varnothing = 4\,\mu$m).
[Image frontale du cristal photonique orienté direction ΓM et composé de trois blocks de 4, 8 et 10 rangées de trous. La flèche indique le spot d'excitation typique ($\varnothing = 4\,\mu$m).]

Transmission spectra through 4 and 8-row-thick GaAs -based PhC slabs along both ΓM and ΓK orientations and for TE polarization are shown in Fig. 3.13. Well-defined stop-gaps appear in the spectra in both orientations.

A standard 2D plane wave expansion (PWE) method as described in chapter 4 was used to calculate the positions of the bandedges as a function of the fill factor f which allows to deduce f from the experimental spectrum. It is worth noting that, because of its simplicity and precision, the PWE method constitutes a fast characterisation tool enabling us to determine the effective f value from the position of the band edges. Being complementary, the spectra were fitted in the framework of a 2D FDTD model.
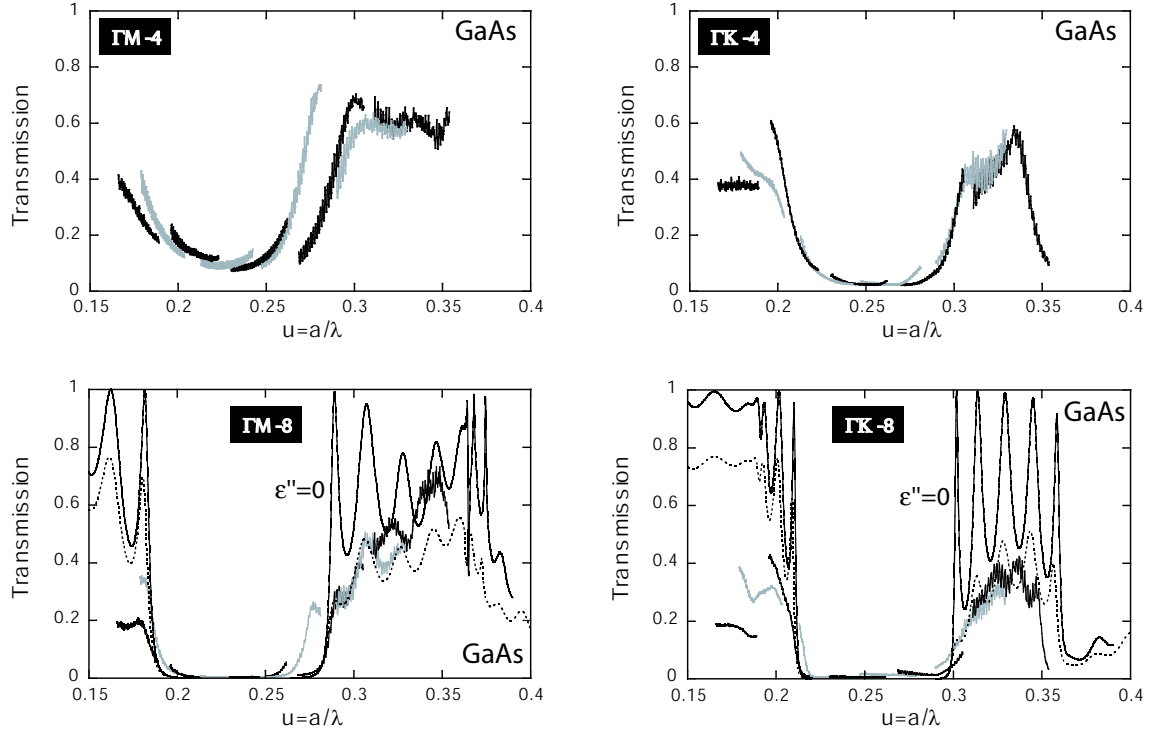
Figure 3.13: Transmission spectra of 4 and 8 rows of simple crystals oriented in ΓM - and
ΓK -direction, respectively. The thin black line corresponds to the 2D FDTD
fit without loss ($f = 33\%$, $\varepsilon'' = 0$) and the dotted line to the case with loss
($\varepsilon'' = 0.08$) (the loss parameter ε'' will be introduced in detail in section 3.4).
[Spectre de transmission de 4 et 8 rangées de cristaux simples en direction
ΓM et ΓK . La ligne noire mince correspond au calcul FDTD 2D sans pertes
($f = 33\%$, $\varepsilon'' = 0$) et la ligne pointillée au cas avec pertes ($\varepsilon'' = 0.08$) (le
paramètre de perte ε'' sera introduit en détail dans la section 3.4).]

The comparison between the experimental spectrum and a 2D lossless FDTD calcu-
lation yields the conclusion that the purely 2D FDTD is missing an important physical
parameter. As noted in section 1.3, the third dimension plays an important role in
2D PhC slab structures. Due to the fact that the guided modes in low vertical index-
contrast structures are situated above the light line, they are inherently lossy and the
transmission drops below the theoretical predictions of the purely 2D calculation with-
out out-of-plane losses ($\varepsilon'' = 0$). Generally the air-band edge is more sensitive to losses
than the dielectric band-edge since the field is mainly concentrated in the air holes [48].
The discrepancy between theory and experiment can be resolved by the ε''-model which
takes losses into account by means of a complex dielectric constant ε'' in the holes (see
section 3.4).

As expected [48], ΓK edges are located at higher energies than the ΓM corresponding
ones: due to the higher k value at the Brillouin zone edge, the ΓK stopband is centered at
a higher energy than the ΓM stopband but has a similar width. As widely demonstrated
by purely 2D band structure calculations [48], when triangular lattices of air holes in
a dielectric matrix are considered, the TE gap width increases with f as well as the
dielectric and air band edge energies (see section 1.3.4). Interference-like features appear
outside the stopgaps. These oscillations originate from interferences between Bloch

waves which propagate inside the PhC. The Bloch waves are reflected at the PhC slab boundaries, leading to standing waves and Fabry-Pérot-like transmission peaks. The wavelength spacing of the peaks scales with N^{-1}, where N is the number of rows [52].

The higher in-plane diffraction efficiency for ΓK than for ΓM [51] lowers T values at the ΓK air band edge with respect to the ΓM one. Both in the case of 8 rows along ΓM and ΓK the transmission at the dielectric band edge is very weak, which is probably due to the fabrication quality for the very small periods ($a = 195, 210\,\text{nm}$). Finally, an average residual transmission of 0.4 % is observed inside the gap for 8 rows. While the energy of the dielectric band edge is roughly independent of f for values lower than 0.50, the opposite behaviour holds for the air band edge. In the latter case, since the electric field is located mostly in the air holes, the energy of the band edge grows rapidly with f [48]. Thus, by fitting the location of the air band edge in the experimental spectrum, the effective f values reported in Table 3.2 were deduced. Additionally to f, the FDTD fit yields the loss parameter ε'', which will be explained in detail in section 3.4.

PhC slabs	band gap	PWE	FDTD	
(8 rows)	($u = a/\lambda$)	f_{PWE} (air)	f_{FDTD} (air)	f_{FDTD} (air)
ΓM	0.18 - 0.28	0.333	0.33	0.08
ΓK	0.21-0.29	0.333	0.33	0.08

Table 3.2: Overview of the fit results (f, ε'') for simple GaAs -based PhC slabs.
[*Aperçu des paramètres du calcul théorique (f, ε'') pour des cristaux simples basés sur GaAs.*]

3.3.2   1D-Fabry Pérot PhC cavities

The measurement of simple slabs yielded the transmission but not the reflection. For the existence of the band gap, one should prove that not only the transmission vanishes, but that simultaneously a high reflection (and/or diffraction) appears, *i.e.* the light is not only absorbed or scattered. The obtainment of reflection data from the PhC slab spectra $T(\lambda)$ is not straightforward and the obtained values are strongly affected by experimental uncertainties [50]. However, it is well known that the extraction of high R values from measurements on high finesse planar 1D Fabry Pérot (FP) cavities is a more accurate technique [63]. As shown in Fig. 3.14, such cavities can easily be created by introducing a spacer (*i.e.*, a line defect) between two PhC slabs etched parallel to the cleaved edge [64,53]. Single slab optical properties can be accurately deduced from the analysis of the FP resonance peaks appearing in the transmission spectrum [65]. According to the theory, both T_{max} and Q are functions of T and R values for each mirror [66,67], so that the optical properties of the PhC-like mirrors can be deduced indirectly.

3.3.2.1   Fabry Pérot transmission without absorption

FP peaks were best-fitted with the Airys formula. A typical experimental spectrum is shown in Fig. 3.17(a). Two different types of loss may occur, mirror losses due to out-of-plane scattering at the holes and intra-cavity loss due to reabsorption by the

active layer. For the case with no intra-cavity losses, the FP transmission is given by [67]:

$$T_{FP}(\lambda) = \frac{T^2}{|1 - Re^{j2\phi}|^2} = \frac{T^2}{1 + R^2 - 2R\cos 2\phi} \tag{3.3}$$

where $T = \sqrt{T_1 T_2}$ and $R = \sqrt{R_1 R_2}$ are the transmission and reflection coefficients for a single PhC mirror (*i.e.*, for a 4 row-thick ΓM slab) and 2ϕ is the normal incidence round-trip phase including the two mirror reflection. The round-trip phase can be broken down into a propagation-dependent phase $2\phi_0(u) = 2kW = 4\pi\frac{W}{a}n_{\text{eff}}u$ and the 2 phase-shifts $2\varphi(u)$ due to the mirror reflections (*i.e.* $r = |r| \cdot e^{j\varphi}$), where W is the geometrical mirror spacing and $k = 2\pi n_{\text{eff}}/\lambda$ the propagation constant in a medium with effective index n_{eff}:

$$2\phi(u) = 2\phi_0(u) + 2\varphi(u) \tag{3.4}$$

The peak transmission is obtained from Eq. (3.3) by setting the roundtrip phase to a multiple of 2π:

$$T_{\text{FP}}^{(\text{peak})} = \left(\frac{T}{1-R}\right)^2 \tag{3.5}$$

The mirror loss L is taken into account by the relation $T + R + L = 1$ and thus the peak transmission writes:

$$T_{\text{FP}}^{(\text{peak})} = \left(\frac{T}{1-R}\right)^2 = \left(1 - \frac{L}{1-R}\right)^2 \tag{3.6}$$

3.3.2.2 Fabry Pérot transmission including absorption

When intra cavity absorption, described by the waveguide absorption coefficient α is introduced, the single round trip absorption becomes $R^2 e^{-2\alpha W}$ [66] (the absorption inside the mirror is neglected). By replacing R by $R \cdot e^{-\alpha W}$ in Eq. (3.3), one obtains:

$$T_{FP}(\lambda) = \frac{T^2}{|1 - Re^{-\alpha W}e^{j2\phi}|^2} = \frac{T^2}{1 + R^2 e^{-2\alpha W} - 2Re^{-\alpha W}\cos 2\phi} \tag{3.7}$$
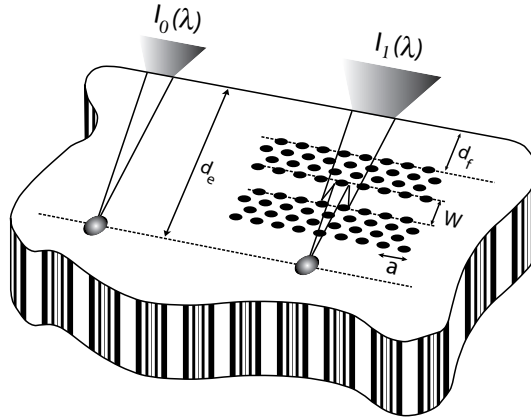

Figure 3.14: Experimental configuration for the measurement of FP cavities.
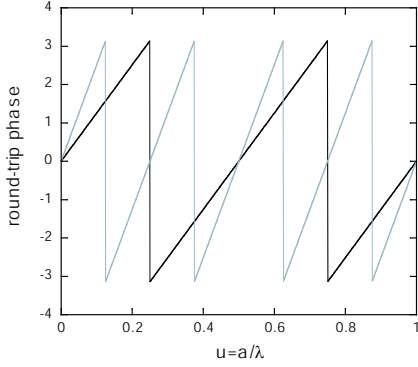*[Configuration expérimentale pour la mesure des cavités FP.]*

Figure 3.15: Roundtrip phase $\phi(u)$ in the case of a metallic mirror FP cavity. The black and the grey lines depict a cavity of width $2a$ and $4a$, respectively.
[*Déphasage pour un aller-retour dans une cavité FP de miroirs métalliques. Les courbes noire et grise représentent une cavité de largeur $2a$ et $4a$ respectivement.*]

for the FP transmission and

$$T_{\text{FP}}^{(\text{peak})} = \left(\frac{T}{1 - Re^{-\alpha W}}\right)^2 = \left(1 - \frac{L}{1 - Re^{-\alpha W}}\right)^2 \tag{3.8}$$

for the peak transmission. The finesse of a cavity is given by:

$$\mathcal{F} = \frac{\pi\sqrt{R}e^{-\alpha\frac{W}{2}}}{1 - Re^{-\alpha W}} \tag{3.9}$$

3.3.2.3   Metallic mirror phase

The physics of a metallic FP cavity and a PhC cavity is basically the same. The only difference lies in the frequency dependence of the phase shift upon reflection at the mirror. In the case of a metallic mirror, the phase shift is $\phi = \pi = const$ and thus $\phi(u) = \phi_0(u) = 2\pi\frac{W}{a}n_{\text{eff}}u$. Fig. (3.15) shows the round-trip phase of a metallic mirror cavity for two different cavity widths.

The slope in the phase diagram is proportional to the cavity width.

3.3.2.4   PhC mirror phase

In the case of a Bragg reflector or a PhC mirror, the mirror reflection phase depends on the wavelength. In the case of PhCs the exact phase relation can be calculated by means of the Sakoda method (see chapter 4, section 4.2). The result of the calculation is depicted in Fig. 3.16.

The precision of the Sakoda calculation is given by the number N and M of Fourier components parallel and perpendicular to the mirror plane.

In the literature, when dealing with Bragg FP cavities, many authors introduce an effective cavity width $W' = W + 2L_p$, taking into account the penetration of the field into the mirror. In this notation the round-trip phase writes:

$$2\phi(u) = 4\pi(\frac{W}{a} + 2\frac{L_p}{a})n_{\text{eff}}u \tag{3.10}$$

The introduction of a penetration depth is a bit awkward since its actual value depends on the considered quantity (*e.g.* FP peak position or angular emission distribution) and furthermore it is usually a function of wavelength. However it is possible

to linearise Eq. (3.4) around the energy of the FP peak, where $2\varphi(u_{\mathrm{FP}}) = 0 + n \cdot 2\pi$:

$$2\phi(u) = \underbrace{2\phi(u_{\mathrm{FP}})}_{=0} + 2\left.\frac{d\phi}{du}\right|_{u_{\mathrm{FP}}} (u - u_{\mathrm{FP}}) = 2\left.\frac{d\phi_0}{du}\right|_{u_{\mathrm{FP}}} (u - u_{\mathrm{FP}}) + 2\left.\frac{d\varphi}{du}\right|_{u_{\mathrm{FP}}} (u - u_{\mathrm{FP}})$$

$$= 4\pi\frac{W}{a}n_{\mathrm{eff}}(u - u_{\mathrm{FP}}) + 2\left.\frac{d\varphi}{du}\right|_{u_{\mathrm{FP}}} (u - u_{\mathrm{FP}}) \quad (3.11)$$

On the other hand, the approach with the penetration depth (Eq. (3.10)) yields:

$$2\phi(u) = \underbrace{2\phi}_{=0}(u_{\mathrm{FP}}) + 4\pi\left(\frac{W}{a} + \frac{2L_p}{a}\right)n_{\mathrm{eff}}(u - u_{\mathrm{FP}})$$

$$= 4\pi\frac{W}{a}n_{\mathrm{eff}}(u - u_{\mathrm{FP}}) + 8\pi\frac{L_p}{a}n_{\mathrm{eff}}(u - u_{\mathrm{FP}}) \quad (3.12)$$

The comparison between Eq. (3.11) and Eq. (3.12) yields:

$$\frac{L_p}{a} = \frac{1}{4\pi n_{\mathrm{eff}}}\left.\frac{d\varphi}{du}\right|_{u_{\mathrm{FP}}} \quad (3.13)$$

, *i.e.* the mirror penetration length is a function of the derivative of the mirror phase and the effective index.
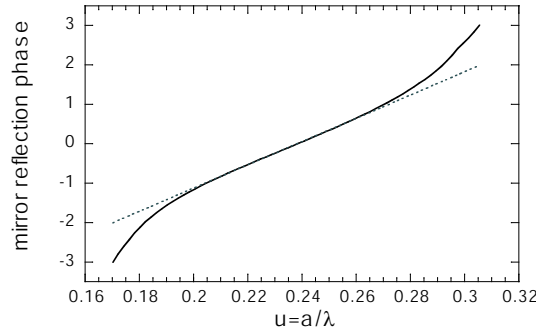

Figure 3.16: The calculation of the complex reflection coefficient of a 4-row ΓM slab by Sakoda's method yields the mirror reflection phase (solid line). The slope of the linear fit (dotted line) around u_0 is $d\varphi/du = 29.5$. (Parameters: $f = 0.33$, $\varepsilon_{\mathrm{sub}} = 11.4$, $N = 10$, $M = 100$)
[Le calcul du coefficient de réflexion complexe d'un miroir de cristal photonique de 4 rangées donne la phase de réflexion du miroir. La courbe peut être linéarisée autour de u_0 avec une pente de $d\varphi/du = 29.5$ (Paramètres: $f = 0.33$, $\varepsilon_{sub} = 11.4$, $N = 10$, $M = 100$).]

3.3.2.5   The cavity order

The cavity order m of an FP peak is given by the condition $2\phi(u_{\mathrm{FP}}) = m \cdot 2\pi$, where m denotes the cavity order. Evaluating the latter expression yields [67]:

$$m \cdot 2\pi = 2\phi(u_{\mathrm{FP}}) = 4\pi\left(\frac{W}{a} + 2\frac{L_p}{a}\right)u_{\mathrm{FP}} \quad \longrightarrow \quad m = 2n_{\mathrm{eff}}u_{\mathrm{FP}}\left(\frac{W}{a} + 2\frac{L_p}{a}\right) \quad (3.14)$$

Making use of Eq. (3.13) one can express the cavity order in terms of the mirror phase:

$$m = 2n_{\text{eff}}u_{\text{FP}}\frac{W}{a} + \frac{u_{\text{FP}}}{\pi}\frac{d\phi}{du} \qquad (3.15)$$

The round-trip phase factor 2ϕ can also be expressed in terms of m:

$$2\phi(u) = 4\pi n_{\text{eff}}\left(\frac{W}{a} + 2\frac{L_p}{a}\right)u = 2\pi\left[2n_{\text{eff}}\left(\frac{W}{a} + 2\frac{L_p}{a}\right)u_{\text{FP}}\right]\frac{u}{u_{FP}} = 2\pi m\frac{\lambda_{\text{FP}}}{\lambda} \quad (3.16)$$

3.3.2.6 The quality factor

The quality factor of a cavity is given by the full width at half maximum value of the resonance and the central peak energy, *i.e.* $Q = \frac{\lambda_0}{\delta\lambda}$.

3.3.2.7 Experimental FP spectra

Determining λ_{FP} from the spectrum and inserting Eq. (3.16) into Airy's formula (Eq. (3.7)) allows one to fit R, T and m. The FP peaks measured on the GaAs sample GWW5-2/part B are listed for different cavity widths in Table 3.3, including the peak wavelength and the intra-cavity absorption coefficient at the specific wavelength.

$\frac{W}{a}$	a	λ_{FP} [nm]	u_{FP}	α $[cm^{-1}]$
1.6	290	1102	0.263	103
1.7	270	1099	0.246	107
1.8	270	1139	0.237	66
1.9	250	1131	0.221	70

Table 3.3: Classification of the FP peaks for different cavity widths (from sample GWW5-2, part B).
[Classification des pics FP pour différentes largeurs de cavités (de l'échantillon GWW5-2, partie B).]

The summary of the fitted parameters is listed in Table 3.4. In a next step the quality factors of the different peaks are determined.

$\frac{W}{a}$	R	T	m	$\mathcal{F}$	$Q \approx m \cdot \mathcal{F}$	$Q = \frac{\lambda_0}{\delta\lambda}$
1.6	0.829	0.063	4.00	16.3	65.2	65 ± 3
1.7	0.843	0.066	4.00	17.9	71.6	73 ± 3
1.8	0.851	0.057	4.00	19.1	76.4	75 ± 3
1.9	0.831	0.089	4.00	16.6	66.4	67 ± 3

Table 3.4: Results from the Airy-fit. In the last column the $\delta\lambda$ was taken at full width at half maximum (from sample GWW5-2, part B).
[Résultats du calcul théorique Airy. Pour la dernière colonne le $\delta\lambda$ correspond à la largeur totale à demi-hauteur (de l'échantillon GWW5-2, partie B).]

The fit yields for all peaks $m = 4.00$. An alternative method to determine m and L_p/a of the mirror is to fit the FP peak positions as a function of different physical

cavity widths W/a (see Fig. 3.17(b)), *i.e.*,

$$\frac{1}{u_{\text{FP}}} = \frac{2n_{\text{eff}}}{m} \left(\frac{W}{a} + \frac{2L_p}{a} \right) \tag{3.17}$$

This procedure assumes that the penetration depths for the different cavities are equal. By inserting m and the appropriate W into Eq. (3.14), one obtains the corresponding penetration depths (see Table 3.5).

$\frac{W}{a}$	$\frac{L_p}{a}$
1.6	0.325
1.7	0.354
1.8	0.350
1.9	0.390

Table 3.5: Penetration depths for the different FP peak wavelengths.
[*Longueur de pénétration pour les différentes longueurs d'onde des pics FP.*]

The L_p values found are quite different, especially for $W/a = 1.6$ and 1.9. The main reason is that the FP peaks of the different cavity widths are situated at different energies and that the mirror phase and therefore the penetration depth is energy dependent. A second minor reason is that the FP peaks correspond to different lattice periods, which may have slightly different air-filling factors. This is especially true for small periods. A small influence could stem from dispersion effects, which, however, have been minimized by selecting peaks with similar peak wavelengths. Because of these reasons, the experimental points in Fig. 3.17(b) cannot be fitted with a constant penetration depth as described by Eq. (3.17). The figure shows a fit with constant (grey) and with variable (black) penetration depth.
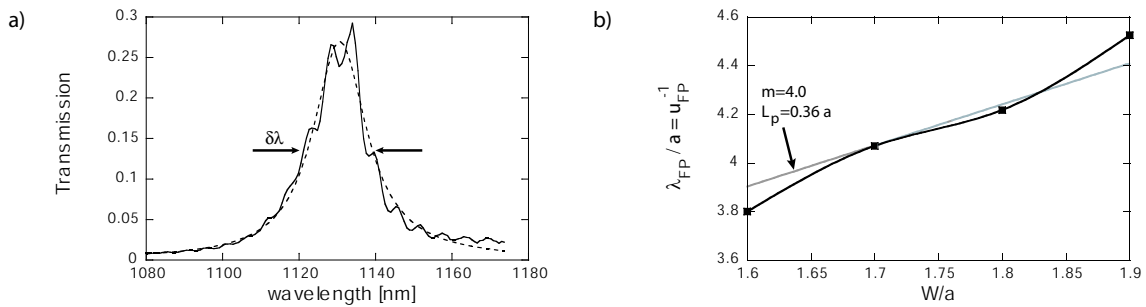

Figure 3.17: a) Typical transmission spectra of a 1D FP cavity of width $W/a = 1.9$ in GaAs . The solid line and the dotted line correspond to measurement and fit, respectively. b) Fit allowing one to determine the cavity order and the penetration length.
[*a) Spectre de transmission d'une cavité FP en GaAs d'une largeur $W/a = 1.9$. La ligne solide et la ligne pointillée correspondent respectivement à la mesure et à la courbe théorique. b) Détermination de l'ordre de la cavité et de la longueur de pénétration.*]

3.4 Out-of-plane loss-model

To the key properties T and R of PhCs one should add also the losses (L), since they will essentially affect the performance of future PhC components. Loss may originate from different sources, *e.g.* waveguide losses (property of the quasi-2D PhC) and out-of-plane scattering towards the substrate and air). Out-of-plane losses can be broken down into intrinsic loss and losses due to the hole characteristics (hole depth, hole form, hole surface rugosity), *i.e.*

$$\varepsilon'' = \varepsilon''_{\text{intr}} + \varepsilon''_{\text{hole}} \tag{3.18}$$

The intrinsic losses correspond to a structure with infinitely deep holes. They are defined by the vertical heterostructure (index-contrast between core and cladding layer, layer thickness) and f. In a simplistic picture the intrinsic losses can be attributed to the fact that the light is not guided inside the holes, *i.e.* the vertical confinement is missing (see Fig. 3.18). Decreasing the fill factor reduces the intrinsic losses since the percentage of the non-guiding part of the heterostructure becomes smaller. The width of the band gap on the other hand will decrease also. A moderate f of around 30 % is a good compromise for a sufficient gap width and acceptable losses.
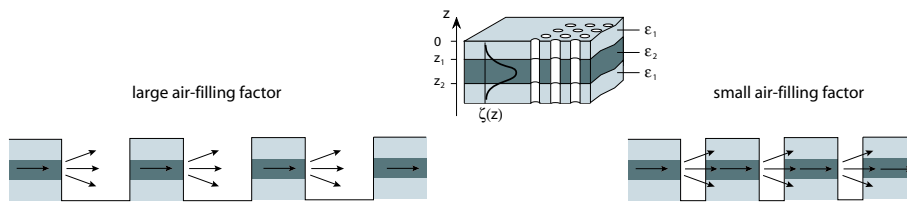

Figure 3.18: In a simplistic picture the out-of-plane losses are due to the absence of vertical confinement in the holes.
[Dans un modèle simplifié les pertes hors plan sont dues à l'absence de confinement dans les trous.]

A shape contribution is introduced to take into account losses due to the finite etch depth (see section 3.4.2) and to the non-cylindrical hole-shape (see section 3.4.3). A different form of imperfections is the perturbation of the periodicity by *disorder*. This includes the deviation of the individual hole shapes from the circular shape and fluctuations of the origin of individual holes with respect to the perfect lattice.

Experimentally it is possible to determine the loss $L = 1 - (T + R + D)$ by measuring the full set of parameters T, R and D [31], where T and R have the usual meaning and D is in-plane diffraction. However, the latter procedure is time-consuming and delicate.

The idea of the ε''-model is to introduce phenomenologically an imaginary dielectric constant ε'' in the air-holes in order to account for scattering losses. Loss, inherently linked to the full 3D structure, can in this way be taken into account in simpler 2D models. This procedure is very useful for modelling, where heavy and complex 3D calculations can be approximated by 2D calculations including the loss parameter ε''. For finite difference time domain (FDTD) calculations, the ε'' is technically introduced as a conductivity parameter $\sigma(\lambda) = (c/2\lambda)\varepsilon''$ [68].

The total loss can be determined experimentally by fitting the simple slab transmission spectrum with the FDTD method. Fig. 3.19 shows the dependence of the

transmission spectra on the loss parameter ε'' for the case of InP. Note that the air-band is more sensitive to losses than the dielectric band since more field energy is stored in the air holes.
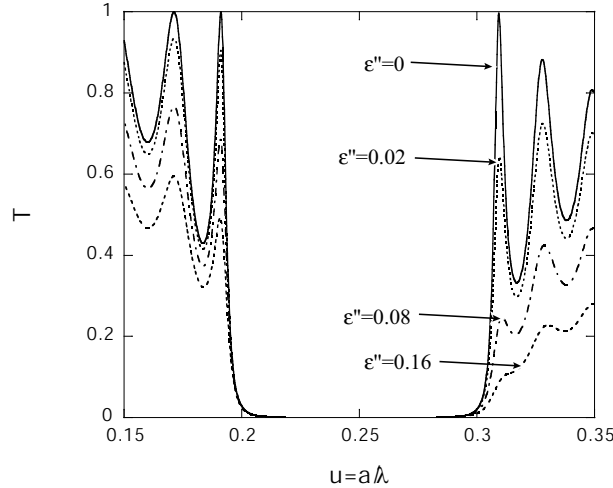

Figure 3.19: Transmission spectra of 8 rows ΓM PhC calculated by FDTD for different values of ε'' (parameters: InP, TE-pol., $f = 0.35$). The calculation has been performed with the toolbox by M. Qiu, KTH, Sweden.
[Spectres de transmission de 8 rangées ΓM calculés par FDTD pour différentes valeurs de ε'' (paramètres: InP, TE-pol., $f = 0.35$). Le calcul a été effectué avec la toolbox de M. Qiu, KTH, Sweden.]

3.4.1 Intrinsic losses

The intrinsic losses are independent of fabrication quality of the holes. They represent the ultimate loss limit that can be reached with a perfect fabrication. H. Benisty *et al.* have developed a model for the calculation of the intrinsic losses based on a perturbation approach.

Let us consider the wave equation of an inhomogeneous medium with the three-dimensional dispersion-less dielectric constant $\varepsilon(\mathbf{r})$:

$$\nabla^2 \mathbf{E}(\mathbf{r}, \omega) + k_0^2 \varepsilon(\mathbf{r}) \mathbf{E}(\mathbf{r}, \omega) = 0 \tag{3.19}$$

In a scalar field approximation Eq. (3.19) writes:

$$\nabla^2 U(\mathbf{r}, \omega) + k_0^2 \varepsilon(\mathbf{r}) U(\mathbf{r}, \omega) = 0 \tag{3.20}$$

where $U(\mathbf{r})$ describes a scalar field. Assuming that the dielectric map is separable into the horizontal and the vertical direction, *i.e.* $\varepsilon_{\mathrm{v+h}}(x, y, z) = \varepsilon_{\mathrm{h}}(x, y) + \varepsilon_{\mathrm{v}}(z) - A$, the resulting wave equation is solved by the separable field $U(x, y, z, \omega) = \Psi(x, y)\xi(z)e^{j\omega t}$ [69]:

$$\nabla^2 \Psi\xi + k_0^2[\varepsilon_h(x, y) + \varepsilon_v(z) - A]\Psi\xi = 0 \tag{3.21}$$

with $k_0 = \omega^2/c^2$ and A a constant to be determined in the following. By applying the identity $\nabla^2(\Psi\xi) = (\nabla^2\Psi) \cdot \xi + \Psi \cdot (\nabla^2\xi)$ Eq. (3.21) can be separated into two equations

which have to be fulfilled simultaneously:

$$\nabla^2 \Psi + k_0^2 \varepsilon_h(x, y) = 0 \tag{3.22}$$

$$\nabla^2 \xi + k_0^2 [\varepsilon_v(z) - A]\xi = 0 \tag{3.23}$$

From Eq. (3.23) and $k_z^2 = k_0^2 \varepsilon_v - k_0^2 n_{\text{eff}}^2$ it follows that $A = n_{\text{eff}}^2$, *i.e.* the effective index of the first guided mode of the unpatterned vertical waveguide structure.

The real 3D PhC described by $\varepsilon_{3D}(x, y, z)$ can be broken down into the so-called separable map ε_{v+h} and a perturbation consisting of an array of dielectric plugs in air with dielectric constant $\Delta \varepsilon = \varepsilon_2 - \varepsilon_1$ inside the core (see Fig. 3.20) [69].
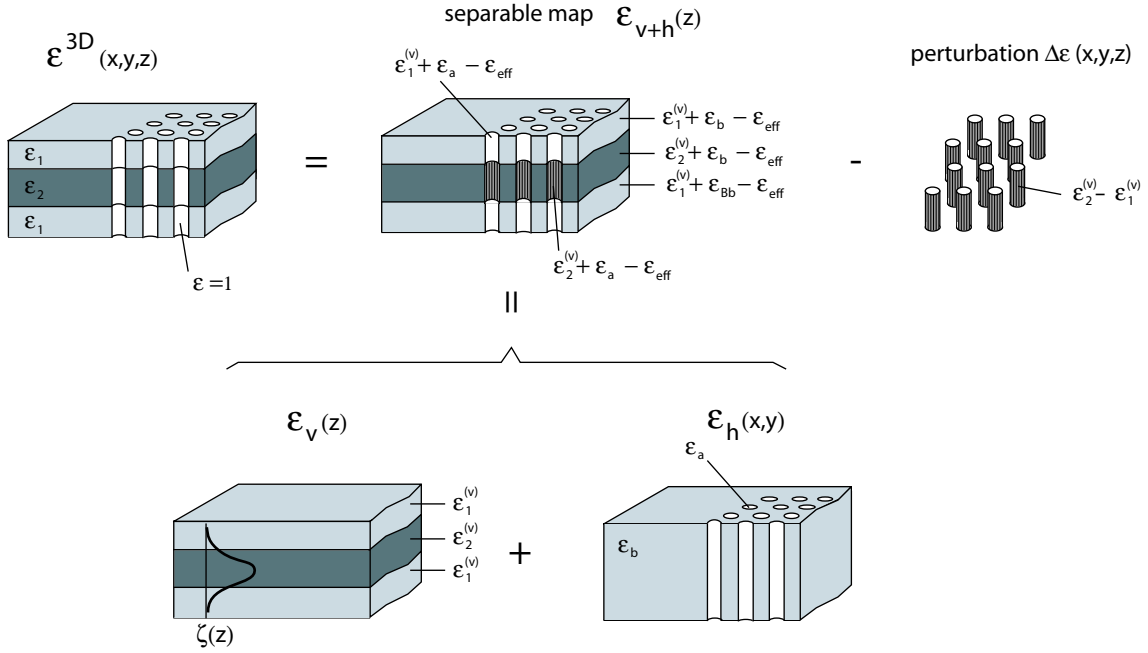

Figure 3.20: The real three-dimensional dielectric map $\varepsilon_{3D}(x, y, z)$ cannot be separated, but it can be written as the superposition of a planar waveguide ($\varepsilon_v(z)$), a 2D PhC ($\varepsilon_h(x, y)$) and a perturbation $\Delta \epsilon(x, y, z)$.

[Le vrai cristal photonique complet (guide plan + cristal photonique bidimensionnel) ne peut pas être décomposé, mais il peut être décrit comme superposition de la carte diélectrique verticale ($\varepsilon_v(z)$), horizontale ($\varepsilon_h(x, y)$) et d'une perturbation $\Delta \varepsilon(x, y, z)$.]

It should, however, be noted that the decomposition of the separable map is not unique. The problem amounts to fit the four distinct values in the separable map $\varepsilon_{v+h}(z)$ to the three actual dielectric constant (ε_1, ε_2, 1) of the non-separable map $\varepsilon^{3D}(x, y, z)$ [69], yielding a linear equation system with 3 equations and 4 unknowns ($\varepsilon_1^{(v)}$, $\varepsilon_2^{(v)}$, ε_a, ε_b):

$$\begin{aligned}
\varepsilon_1^{(v)} + \varepsilon_b - \varepsilon_{\text{eff}} &= \varepsilon_1 \\
\varepsilon_2^{(v)} + \varepsilon_b - \varepsilon_{\text{eff}} &= \varepsilon_2 \\
\varepsilon_1^{(v)} + \varepsilon_a - \varepsilon_{\text{eff}} &= 1
\end{aligned} \tag{3.24}$$

This is in contrast to the calculation of $\varepsilon_{\text{hole}}''$ in the next section which renders the calculation of $\varepsilon_{\text{intr}}''$ less reliable than $\varepsilon_{\text{hole}}''$. The correct decomposition is still an open question and additional physics is required to find the significant one.

In the first Born approximation [2], the perturbation $\Delta\varepsilon(\boldsymbol{r})$ induces a spatially periodic polarisation $\Delta P(\boldsymbol{r}) = \Psi(x,y)\xi(z)\Delta\varepsilon(\boldsymbol{r})$. Each dielectric plug can be considered as a radiating electric dipole source which emits light into the air, the substrate and the core. Although the dipoles are embedded in a complicated heterostucture one may approximate that they emit in a bulk medium with index $n_2 = \sqrt{\varepsilon_2}$ [69].

For radiation from a periodic lattice of holes, one may expect coherent Bragg scattering such that only a fraction η of the total emission is coupled to radiation modes. There exist however several arguments that justify to focus on a single hole, *i.e.* to neglect coherence effects: In the case of a two-dimensional lattice the the scattered light is mainly directed in the horizontal plane and the integral over the vertical half space leads to constant values, independently of the number of scatterers. On the other hand, the disorder also helps to destroy the coherence. Additionally when taking into account finite crystal effects stemming from the few physical rows or the short light penetration depth, one may assume that the individual scatterers emit incoherently [69]. If not, one would have to take into account the modification of the isotropic dipole emission by the vertical heterostructure by using the extraction efficiency of η of a multi-layer stack.

The dissipated energy in each hole by the electric field can be described by an imaginary dielectric constant ϵ''_{int} is given by [59]

$$dP_{diss} = \frac{1}{2}\,\epsilon_0\,\omega_0\,\epsilon''_{\text{int}}\boldsymbol{E}^2(x,y,z)\,dV \tag{3.25}$$

where the 3D electrical field $\boldsymbol{E}^2(x,y,z)$ can conveniently be separated into a vertical and a lateral field profile in a scalar way:

$$E(x,y,z) = |\boldsymbol{E}(x,y,z)| = E_0\Psi(x,y)\xi(z) \tag{3.26}$$

$$\iint |\Psi(x,y)|^2 dx\,dy = 1 \tag{3.27}$$

$$\int |\xi(z)|dz = 1 \tag{3.28}$$

assigning E_0 the electrical field unit Vm^{-1} and keeping the vertical and horizontal mode profiles as unitary densities with units m^{-1} and m^{-2}, respectively. According to Refs. [69,59] the ε'' value in Eq. (3.25) can be expressed by:

$$\varepsilon''_{\text{int}} \propto V_{\text{core}}(\Delta\varepsilon)^2\eta\Gamma_{\text{core}} = \frac{w}{\lambda/n_2}(u^2 f)(\Delta\varepsilon)^2\eta\Gamma_{\text{core}} \tag{3.29}$$

where w is the core thickness, η is the extraction efficiency of the dipole in each hole and Γ_{core} is the confinement factor of the mode in the core. Thus for low-index-contrast, the intrinsic scattering losses scale with the square of the dielectric contrast between core and cladding. For higher contrasts this relationship breaks down and the losses level out [20].

When looking at Eq. (3.29) it seems evident that the losses may be reduced by lowering the vertical index contrast. However, by decreasing $\Delta\varepsilon$ the vertical confinement

---

[2]It is usually not possible to obtain a closed solution to the integral equation of scattering. For weak scattering ($\Delta\varepsilon$ close to unity), it is sufficient to consider the first term of the perturbation expansion (first Born approximation)

is reduced and the mode shape extends more into the cladding and thus samples more the bottom of the holes. As becomes clear in the next section, there is a trade-off between reducing the intrinsic losses and the losses due to finite hole depth, the actual optimum depending on the achievable etch depth.

It is sometimes convenient to write Eq. (3.29) in the form:

$$\varepsilon''_{\text{int}} \propto u^2 f \tag{3.30}$$

Eq. (3.30) represents a scaling law which allows one to rescale $\varepsilon''_{\text{int}}$ for a different filling factor value or material system. Exact 3D calculations inspired by grating-Fourier analysis yield for the GaAs -based heterostructure intrinsic losses in the range of $0.024 - 0.048$ [70]. For the InP case according to Eq. (3.30) a smaller value can be deduced, *i.e.* $0.01 - 0.02$ [59] due to the smaller vertical index contrast $\Delta\varepsilon$.

3.4.2 Losses due to finite hole depth

Similarly to the case of intrinsic losses, the 3D dielectric map is not separable in the case of PhCs with a finite hole depth. The actual PhC structure is considered as the sum of the ideal system with infinitely deep holes (*i.e.* the intrinsic loss case) plus a dielectric perturbation at the bottom of the holes. This perturbation consists of plugs with dielectric constant $\tilde{\varepsilon} = 1 - \varepsilon_1$ that extend from $z = d$ to $z = -\infty$ (see Fig. 3.21) [59]. The fact that the perturbation extends to infinity is not problematic since the system is probed by guided modes with finite extent into the cladding.
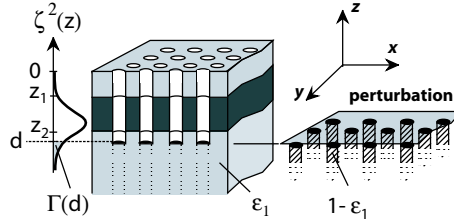

Figure 3.21: The PhC with finite hole depth can be regarded as superposition of a PhC with infinitely deep holes and a perturbation with dielectric constant $\Delta\epsilon = 1 - \epsilon_1$ in the missing part of the hole. The partial confinement factor $\Gamma(d)$, *i.e.* the overlap between the squared field profile with the missing air column region, is sketched.

[Le cristal photonique avec des trous finis peut être considéré comme super-position d'un cristal avec des trous infinis et d'une perturbation $\Delta\epsilon = 1 - \epsilon_1$ dans la partie manquante des trous. Le facteur de confinement partiel $\Gamma(d)$, i.e. le recouvrement du profil de champ carré avec la partie de la colonne d'air manquante est indiqué.]

In contrast to the case of intrinsic losses, the dipole radiates in a homogeneous medium with the cladding index. The influence of the nearby waveguide compared with that of the cladding radiation modes is neglected [59]. It can be assumed that all the power of the dipole radiation is lost (no extraction efficiency). The imaginary dielectric constant accounting for the finite hole depth of perfectly cylindrical holes is given by [59]:

$$\varepsilon''_{\text{hole}}{}^{(\text{cyl})} = \tilde{\varepsilon}^2 \frac{8\pi^2}{3\lambda^3} n_{\text{clad}} \Gamma(d) L_d S_{\text{hole}} \tag{3.31}$$

where

$$\Gamma(d) = \frac{\int\limits_{-\infty}^{d} \zeta^2(z)dz}{\int\limits_{-\infty}^{+\infty} \zeta^2(z)dz} \tag{3.32}$$

is the partial confinement factor, [70] *i.e.* the overlap integral of the squared field profile $\zeta^2(z)$ with the missing air column region, $n_{\mathrm{clad}} = \sqrt{\varepsilon_1}$ is the refractive index of the bottom cladding and L_d is defined as the decay length of the exponential decay of $\zeta(z)$ into the bottom cladding, *i.e.*,

$$\zeta(z) \propto \exp(+z/L_d) \qquad z < 0 \tag{3.33}$$

$\Gamma(d)$ as well as $\varepsilon''_{\mathrm{hole}}{}^{(\mathrm{cyl})}$ have been plotted for different material systems, where one of them is the $\mathrm{Al}_x\mathrm{Ga}_{1-x}\mathrm{As}/\mathrm{GaAs}$ system mainly used in this thesis (see Fig. 3.22). The dotted line represents a typical loss value of $\varepsilon = 0.08$ that is been measured in the GWW5-2 GaAs sample.
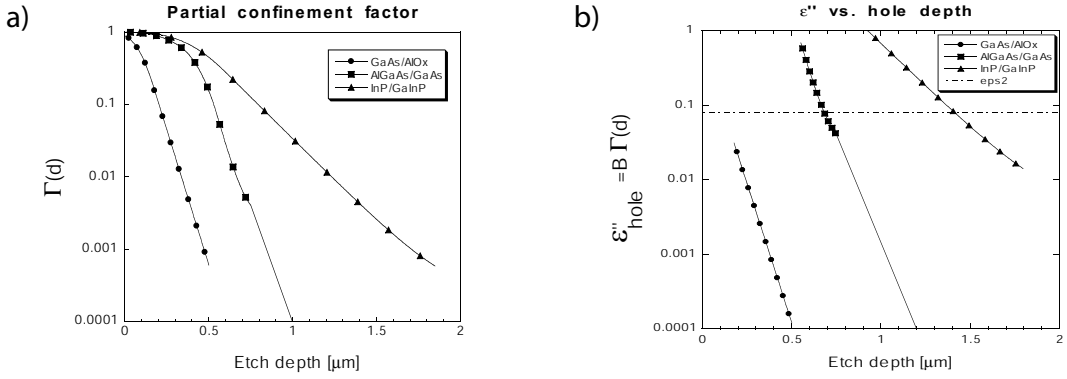

Figure 3.22: a) Partial confinement factor $\Gamma(d)$ plotted for three different cases: (i) a typical GaAs/AlO$_x$-based 2D PhC, (ii) an $\mathrm{Al}_x\mathrm{Ga}_{1-x}\mathrm{As}/\mathrm{GaAs}$ structure, (iii) an InP/GaInAsP system. b) Estimate of the loss parameter $\varepsilon''_{\mathrm{hole}} = B\Gamma(d)$ as a function of the etch depth d for the three cases for hole diameters that correspond to the typical air-filling factor values of $f = 0.2 - 0.3$. The curves are shown only for d values in the bottom cladding (*i.e.* $|d| > |z_2|$; see Fig. 3.21). *[a) Facteur de confinement partiel $\Gamma(d)$ en fonction de d pour trois différents cas: (i) un cristal photonique 2D typique basé sur GaAs/AlO$_x$, (ii) une structure $\mathrm{Al}_x\mathrm{Ga}_{1-x}\mathrm{As}/\mathrm{GaAs}$, (iii) un système InP/GaInAsP. b) Estimation des pertes $\varepsilon''_{\mathrm{hole}} = B\Gamma(d)$ en fonction de la profondeur de gravure d pour les trois cas pour des diamètres de trous correspondant à des facteurs de remplissage typiques de $f = 0.2 - 0.3$. Les courbes sont montrées seulement pour des valeurs de d dans la gaine inférieure (i.e. $|d| > |z_2|$; voir Fig. 3.21).]*

3.4.3 Losses due to the hole shape

Unfortunately the picture of perfectly cylindrical holes with a flat bottom does not correspond to reality (see, for example, section 2.2). Often the holes etched in InP by ECR and CAIBE are cylindrical in the upper part and conical in the lower part (compare section 2.2). In some cases the conical part is additionally truncated.

3.4.3.1 Cylindroconical holes

In general, vertical sidewalls can be achieved only in the top part of etched holes, whereas oblique walls tend to occur at the bottom. A conical hole-shape can frequently be found in PhCs etched by ECR-RIE as well as CAIBE. For simplicity it is assumed that the conical portion of the hole is located entirely inside the bottom cladding, which is the case for state-of-the-art etching technology. The parameter z_b indicates the base of the conical part and the angle α the sidewall inclination (see Fig. 3.23).
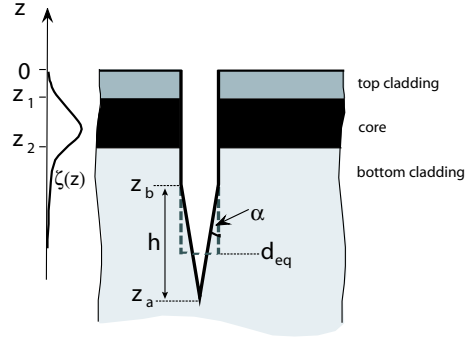
Figure 3.23: Sketch of the cylindroconical hole shape model. The main geometric parameters and the guided field profile $\zeta(z)$ are shown. z_{eq} is defined as the equivalent depth of a cylindrical hole that gives the same amount of losses as the tapered-bottom hole.

[Schéma du modèle pour les trous de type cylindre conique. Les paramètres géométriques principaux et le profile du mode guidé $\zeta(z)$ sont indiqués. z_{eq} est défini comme la profondeur équivalente d'un trou cylindrique de pertes indentiques.]

Formally, the calculation differs from the cylindrical shape regime only in the evaluation of the partial confinement factor. It is sufficient to replace [59]

$$\int_{-\infty}^{d} \zeta(z)dz \quad \text{by} \quad \int_{-\infty}^{z_b} g(z)\zeta(z)dz \tag{3.34}$$

where $g(z)$ is a form factor that accounts for the fractional amount of material left as a perturbation at depth z and that can be applied, in principle, to an arbitrary hole shape. In the case of cylindroconical holes, this form factor is given by:

$$g(z) = \begin{cases} 1 & |z| > |z_a| \\ 1 - \frac{r(z)^2}{r_0^2} & |z_b| < |z| < |z_a| \end{cases} \tag{3.35}$$

where $r(z) = (z - z_a)\tan\alpha$ is the local cone radius and r_0 is the cylindrical hole radius.

In principle, Eqns. (3.34) and (3.35) could be used to directly evaluate Eq. (3.31), but it is more instructive to attempt a comparison between the ideal flat bottom case and the conical bottom case. For this reason we introduce an equivalent hole depth d_{eq} [59], that corresponds to the depth of a perfectly cylindrical hole with the same amount of loss, *i.e.*,

$$d_{eq} = d_{eq}(L_d, \underbrace{r, \alpha}_{h}) \equiv z_b + L_d \cdot \ln\left[2\left(\frac{1}{h/L_d} - \frac{1 - \exp(-h/L_d)}{(h/L_d)^2}\right)\right] \tag{3.36}$$

where z_b is the location of the cone base and $h \equiv z_b - z_a$ is the cone height (see Fig. 3.23). By replacing d in Eq. (3.31) by d_{eq}, one obtains the conical shape factor $\varepsilon_{hole}''^{(con.)}$.

The following analysis has been performed on a InP sample, but the same approach could also be applied to GaAs. The experimental spectra are compared with theoretical spectra calculated with a 2D FDTD model (see Fig. 3.24). The air fill factor f and ε'' were chosen as the only free parameters of the fit [3] that Different ε'' values have been used in order to fit either the dielectric or the air band. This discrepancy is du to the general scaling law reported in Eq. (3.30). From the fit of the air transmission band, the total loss parameter value $\varepsilon = 0.32 \pm 0.020$ is obtained. By subtracting from this value the intrinsic losses $\varepsilon_{int}'' \approx 0.01 - 0.02$, a hole shape loss of $\varepsilon_{hole}'' = 0.305 \pm 0.025$ can be deduced.
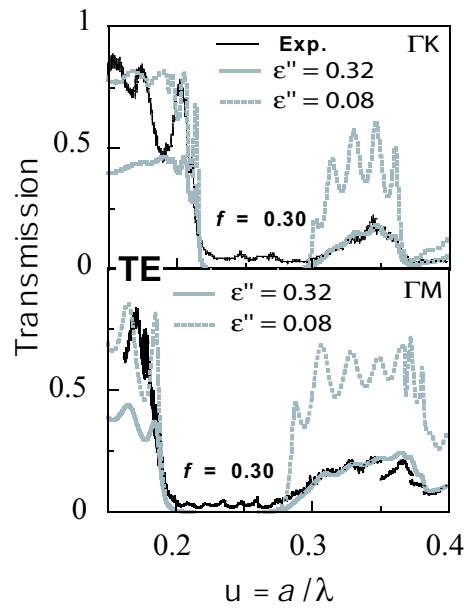

Figure 3.24: TE transmission spectra through 8 rows of ΓM and ΓK oriented PhC slabs for the sample in Fig. 3.25. Experimental spectra (boldface curves) are compared with 2D FDTD calculated spectra (lightface curves)
[Spectre de transmission en TE de 8 rangées de cristal photonique orienté ΓM et ΓK de l'échantillon de la figure 3.25. Les spectres expérimentaux (lignes noires) sont comparés avec des spectres calculés par FDTD 2D (lignes grisées).]

On the other hand, from the SEM micrograph analysis the cone slope α in the first L_{decay} can be determined. One notices that the holes in Fig. in Fig. 3.25(a) are not perfectly conical and that α varies along z. Nevertheless , because of the exponential decay of the perturbation with depth, losses depend mostly on the hole shape, *i.e.* the angle, in the first decay length. Thus taking into account $L_d \approx 360$ nm, the value $\alpha \approx 2.5° \pm 0.5°$ is deduced. This angle translates into a loss-factor $\varepsilon_{hole}''^{(con.)} = 0.3$ (see Fig. 3.25b)). This value is in perfect agreement with the experimental data.

---

[3]The effective air fill factor value obtained from the fit is checked to fall within the range set by the lateral SEM analysis that is influenced by the local hole shape fluctuations. These are due to the uncertainty in cleaving through the centres of the holes, the average on a limited number of holes and by the cylindroconical hole shape.
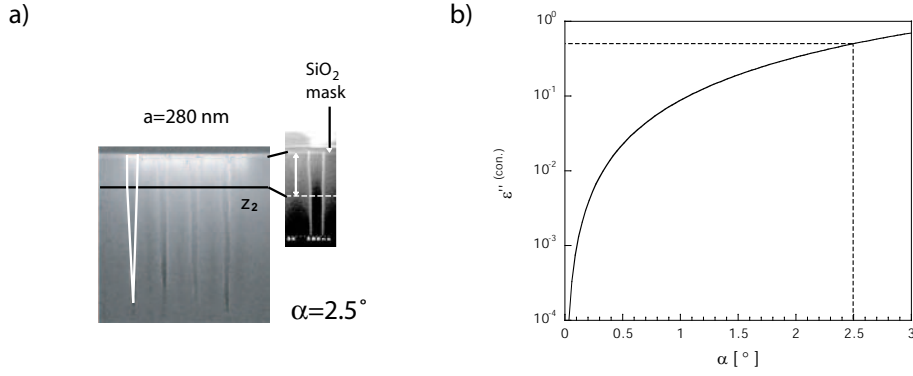
Figure 3.25: a) SEM micrograph of an InP sample with the conical hole-shape, typical for ECR-RIE and CAIBE ($R_{\text{hole}} = 200nm$, $f = 0.3$). The cone angle is $\alpha = 2.5°$. b) Angular dependance of hole-shape induced losses for strictly conical holes. [a) Image MEB d'un échantillon InP avec la forme conique, typique pour ECR-RIE et CAIBE ($R_{hole} = 200nm$, $f = 0.3$). b) Dépendance angulaire des pertes induites par la forme pour des trous strictement coniques.]

Based on Fig.3.25(b), the following conclusions can be made: For angles $\alpha < 0.5°$, i.e. for holes with almost straight walls in some L_{decay} inside the lower cladding, the conical hole-shape losses could reach the level of the intrinsic losses (i.e. 0.01-0.02 for InP). A second important message is that the ILS characterisation together with the 'FDTD+ε''' form a precise analysis tool: 1° of conicity translates into an ε'' value that can be measured optically. The upper loss limit for IO applications with good performance (e.g. [70] corresponds to $\alpha < 1.5°$, a value that has already been outreached by now.

3.4.3.2   Truncated cones

In the case of ICP etching, the holes are still conical, but the bottom of the cone is truncated (see Fig. 3.26).
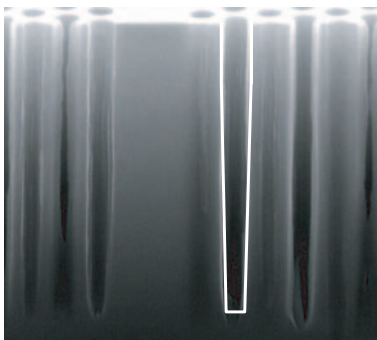

Figure 3.26: SEM micrograph of an InP sample etched by ICP ($R_{\text{hole}} = 120\,\text{nm}$, $f \approx 0.5$). Note the truncated cone hole shape.
[Image MEB d'un échantillon InP gravé par ICP ($R_{hole} = 120nm$, $f \approx 0.5$). Notez la forme en trou conique tronqué.]

As done for the conical case the hole shape losses could be calculated analytically by introducing a form factor that accounts for the fractional amount of material left as a perturbation at a given depth z. The goal is, however, not to calculate more and more complicated hole shapes but rather to decouple hole depth and angle and determine the influence of both parameters on losses. This more analytic approach gives more insight into the weight of each parameter, e.g. whether for a certain hole depth it is

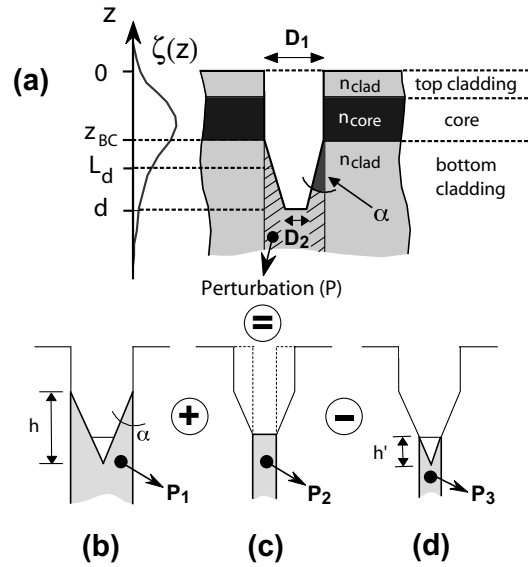**Figure 3.27:** (a) Sketch of the truncated-cone hole shape model. The main geometrical parameters are shown as well as the guided field profile $\zeta(z)$ and its decay length L_d in the bottom cladding. The shaded region represents the dielectric perturbation P complementary to the air hole. (b)-(d) Sketch of the three partial perturbations P_1, P_2, and P_3 into which each radiating plug P can be broken down.

[(a) Schéma du model trou conique tronqué. Les principaux paramètres géométriques, le profile du mode guidé $\zeta(z)$ ainsi que sa longueur de décroisement L_d dans la gaine inférieure sont indiqués. La région ombrée représente la perturbation diélectrique par rapport à un trou cylindrique infini. (b)-(d) Schéma des trois perturbations partielles dans lesquelles chaque pilier radiatif peut être décomposé.]

more effective to reduce the angle than etching deeper holes. As shown in Fig. 3.27, the complicated plug at the hole bottom can be broken down into the three contributions (b), (c) and (d) [58].

In Fig. 3.28 $\varepsilon''_{\text{hole}}$ is plotted as a function of α for different d-values. The curve calculated using Eqs. 3.31 and 3.36 for the case of simple conical holes with the same angle values is reported for comparison (thick gray line). Three regimes can be identified: For *small* α values (*i.e.,* $\alpha \leq 0.03°$) the shape contribution to losses is negligible and $\varepsilon''_{\text{hole}}$ is a function of hole depth d (*cylindrical shape regime*). On the other hand, for *large* angles (*i.e.,* $\alpha > 1°$) $D_2 \ll D_1$ for all d values, and the hole shape tends to the cone limit (*conical shape regime*). Therefore, $\varepsilon''_{\text{hole}}$ is almost independent of the hole depth and all the curves approach the simple cone line. Finally, in the *intermediate* case the *truncated-cone regime* is obtained and both d and α have to be considered to analyse the influence of hole morphology on out-of-plane losses.

One notes that very quickly hole angle becomes more important than depth. This is especially true for $\varepsilon''_{\text{hole}} > \varepsilon''_{\text{intr}}$. A typical value for the intrinsic losses, $\varepsilon''_{\text{intr}} = 0.015$, is indicated in Fig. 3.28.

The following analysis has been performed on a InP sample, but the same approach could also be applied to GaAs. Fig. 3.29 shows the experimental transmission through 8 rows of ΓM-oriented PhC of an ICP-etched InP sample. The experimental curve

has been fitted by 2D FDTD calculation with f and ε'' as free fitting parameters. Two different sets of parameters [*i.e.* (i) $f = 0.52$ and $\varepsilon'' = 0.045$; (ii) $f = 0.49$ and $\varepsilon'' = 0.09$] were used to fit the dielectric and air bands, respectively [58]. Using the scaling law (Eq. 3.30) the intrinsic losses account for $\varepsilon_{\mathrm{int}} = 0.02 - 0.03$, so that $\varepsilon''_{\mathrm{hole}} = 0.06 - 0.07$ for the air band.

This value translates into an average cone angle $\alpha = 0.7° - 0.8°$ with $d > 2\,\mu\mathrm{m}$. These values agree with the local SEM analysis, which yields a hole diameter $D_1 = 200 - 500\,\mathrm{nm}$, an aspect ratio of 14, and a total depth $d \geq 3\,\mu\mathrm{m}$. Comparing with Fig. 3.28, one notes that the sample is situated still in a regime where contributions to losses are mainly due to the sidewall verticality, while the effect of increasing the hole depth is almost negligible.

Thus the model constitutes a valuable tool for deciding to which parameter (*e.g.* hole depth and/or inclination angle) priority has to be given. For example, in a strongly conical regime it is not worth increasing hole depth without correcting the angle in the first decay length.
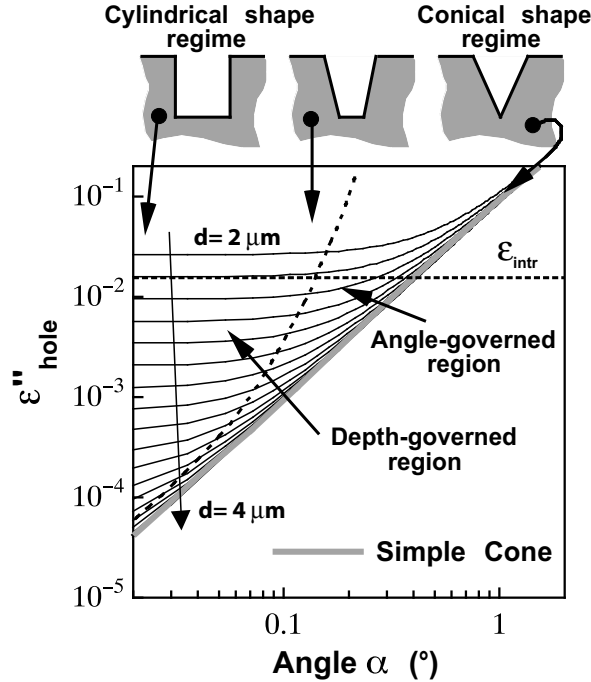

Figure 3.28: Plot of the shape term ϵ''_{hole} as a function of the cone angle α. Calculations were performed for an InP -based PhC with an air filling factor $f = 0.5$ and $D_1 = 460\,\mathrm{nm}$. The total depth d ranges from 2 to 4 $\mu\mathrm{m}$ (with steps $\Delta d = 0.1\,\mu\mathrm{m}$). Cylindrical and conical hole shape regimes are indicated, while the curve obtained for a simple conical hole is reported as reference (thick gray line).

[Graphique du terme de forme ϵ''_{hole} en fonction de l'angle α du cône. Les calculs ont été effectués pour un cristal photonique InP avec un facteur de remplissage $f = 0.5$ et $D_1 = 460\,\mathrm{nm}$. La profondeur totale s'étale de 2 à 4 $\mu\mathrm{m}$ (avec un pas $\Delta d = 0.1\,\mu\mathrm{m}$). Pour les formes des trous, les régimes cylindriques et les régimes coniques sont indiqués. La courbe obtenu pour un trou conique simple est indiquée comme référence (ligne grise épaisse).]
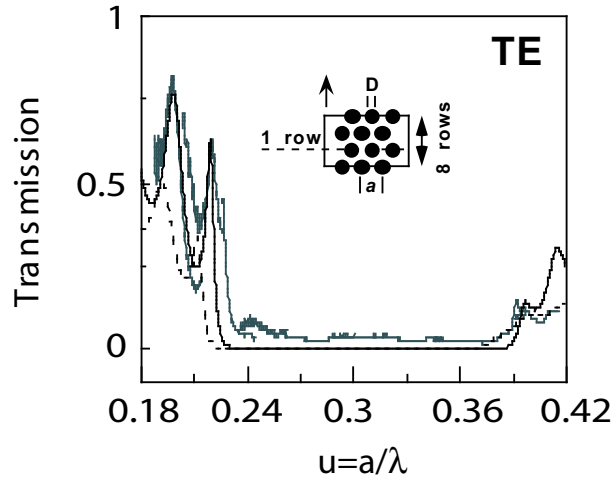
Figure 3.29: Transmission spectra through eight rows thick ΓM -oriented PhC slabs as sketched in the inset. The experimental spectrum is compared to 2D FDTD calculations (solid line: $f = 0.52$, $\varepsilon'' = 0.045$, dotted line: $f = 0.49$, $\varepsilon'' = 0.09$). *[Spectres de transmission de 8 rangées de cristal photonique orientées ΓM . Le spectre expérimental est comparé au calcul FDTD 2D (ligne solide: $f = 0.52$, $\varepsilon'' = 0.045$, ligne pointillée: $f = 0.49$, $\varepsilon'' = 0.09$).]*

3.4.4 Application of the loss model on GaAs

The etch depth of the GaAs samples in this thesis is typically $d = 1.1$ μm (see Fig. 3.30). The SEM image shows perfectly cylindrical holes. Rescaling the intrinsic losses for the GaAs -based heterostructure to the correct fill-factor f and the energy of the air-band edge for which the f was determined yields $\varepsilon''_{\text{intr}} = 0.06 \pm 0.01$. Subtracting this value from the ε'' value from the air-band edge provides $\varepsilon''_{\text{hole}} = 0.02 \pm 0.01$. Applying the model for cylindrical holes (Eq. (3.31)) yields an hole depth between 950 nm and 1150 nm, which agrees completely with the SEM image.
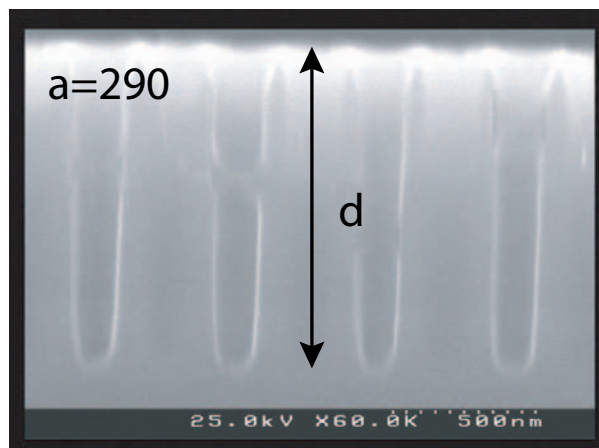

Figure 3.30: Lateral view of the SEM micrograph of GaAs sample cleaved through a row of holes. The etch depth is $d = 1.1$ μm.
[Vue latérale d'une image MEB d'un échantillon GaAs clivé à travers une rangée de trous.]

3.5   Conclusion and outlook

In conclusion, the ILS technique is a powerful characterisation tool, yielding quantitative results of the main optical parameters (*e.g.* R, T, D, L). It proved to be a versatile method for PhC characterisation of both GaAs ($\lambda = 1\,\mu\mathrm{m}$) and InP ($\lambda = 1.5\,\mu\mathrm{m}$) samples, thus covering a huge wavelength range. The ILS technique eliminates difficulties and uncertainties arising in standard optical techniques (*e.g.*, the end-fire method [71]). These uncertainties are mainly due to unknown fibre-to-chip coupling efficiencies and fibre polarisation issues. A drawback of the method is the strong reabsorption in the active layer which limits the size and complexity of the structures that can be investigated. Thus the ILS technique remains up to now the method of choice for the assessment of fabrication quality in general and especially of etching performance. It is also suitable to test new ideas and building blocks, but would not be appropriate to test large integrated optical circuits.

The ε''-model proved to be a valuable tool to assess fabrication quality and to split the total loss into the different contributions originating from finite hole depth or non-cylindrical hole shapes. There exists a perfect interplay between the ε''-model, which has been validated by 3D FDTD simulations, SEM-images and 2D FDTD simulations. However the model is not only suitable to extract the losses from the measurements, but also to understand the physical origin of losses (depth vs. angle), which is pretty difficult with 3D models.

Both in GaAs and InP the etching technology has now reached a level where the hole shape losses are similar to the intrinsic losses. Once the total losses are comparable to the intrinsic losses, one has to optimise the vertical heterostructure, *i.e.* one has to find the structure that optimises losses for the achievable hole depth d. The optimal structure is an interplay between the intrinsic and etch-depth or hole-form-induced losses: By increasing the confinement, $\Gamma(d)$ and therefore $\varepsilon''_{\mathrm{hole}}$ is reduced, but the intrinsic losses are likely to increase [70]. In InP, reabsorption could be reduced by moving the QWs inside the core towards the cladding layer.

It should be stressed that $1°$ of sidewall inclination is not a small angle and translates into a ε'' value that can be precisely measured optically.

Chapter 4

The plane wave expansion method

Among the various computational methods, the plane wave expansion (PWE) approach has become *de facto* the standard for band structure calculations in PhCs. This chapter describes in detail the PWE method that has been used to validate a large part of the experimental results in this thesis.

4.1   2D plane wave expansion method

PWE stands for a simple and straightforward method to represent periodic fields using classical Fourier expansion in terms of harmonic functions defined by the reciprocal lattice vectors. In this section, a detailed derivation of the master equation and its implementation into an algebraic eigenvalue problem is provided for the case of 2D PhCs.

The macroscopic Maxwell-equations in an electric polarisable and magnetisable material in MKS units are [72]:

$$\nabla \cdot \mathbf{D} = \rho \tag{4.1}$$

$$\nabla \times \mathbf{H} - \frac{\partial \mathbf{D}}{\partial t} = \mathbf{J} \tag{4.2}$$

$$\nabla \cdot \mathbf{B} = 0 \tag{4.3}$$

$$\nabla \times \mathbf{E} + \frac{\partial \mathbf{B}}{\partial t} = 0 \tag{4.4}$$

where $\mathbf{E}$ and $\mathbf{B}$ are the mean values for the electric field and the magnetic induction in the case of the microscopic Maxwell equations for the vacuum. For the case of a homogeneous dielectric medium, the relationship between the macroscopic quantities, *i.e.* the displacement $\mathbf{D}$ and the magnetic field $\mathbf{H}$, and the microscopic quantities $\mathbf{E}$ and $\mathbf{B}$ is given by the equations:

$$\mathbf{D} = \varepsilon_0 \varepsilon \mathbf{E} \qquad \varepsilon = 1 + \chi_e \tag{4.5}$$

$$\mathbf{H} = \frac{1}{\mu_0} \frac{1}{\mu} \mathbf{B} \qquad \mu = 1 + \chi_m \tag{4.6}$$

where the fields are assumed to be weak and spatially and temporally not too fast changing fields and ε and μ denote the relative dielectric constant and the relative magnetic permeability, respectively. Furthermore the following assumptions and simplifications are made:

i. Free charges (ρ) or currents ($\mathbf{J}$) are neglected.

ii. The field strengths are small enough to be in the linear regime.

iii. The material is locally macroscopic and isotropic, *i.e.* the dielectric constant $\varepsilon(\mathbf{r})$ is scalar.

iv. The magnetic permeability is very close or equals to unity ($\mu_r \cong 1$).

v. Only lossless dielectrics are considered for which $\varepsilon(r)$ is a purely real quantity.

Taking these assumptions into account, Eqs. (4.2)-(4.4) can be written as:

$$\nabla \cdot \mathbf{E} = 0 \tag{4.7}$$

$$\nabla \times \mathbf{H} - \varepsilon_0 \varepsilon(\mathbf{r}) \frac{\partial \mathbf{E}}{\partial t} = \mathbf{J} \tag{4.8}$$

$$\nabla \cdot \mathbf{H} = 0 \tag{4.9}$$

$$\nabla \times \mathbf{E} + \frac{\partial \mathbf{H}}{\partial t} = 0 \tag{4.10}$$

Assuming plane waves for the electrical and magnetic fields, *e.g.* $\mathbf{H}(\mathbf{r}) = \mathbf{a}e^{j\mathbf{kr}}$ and $\mathbf{E}(\mathbf{r}) = \mathbf{a}e^{j\mathbf{kr}}$, Eq. (4.7) and (4.9) become:

$$\nabla \cdot \mathbf{H} = (\nabla \cdot \mathbf{a})e^{j\mathbf{kr}} + \mathbf{a}(\nabla e^{j\mathbf{kr}}) = j\mathbf{a} \cdot \mathbf{k}e^{j\mathbf{kr}} = 0 \quad \longrightarrow \quad \mathbf{a} \cdot \mathbf{k} = 0 \tag{4.11}$$

, thus ensuring transversality: one can focus on the other two equations as long as the transversality requirement is fulfilled. For the time-dependence of the fields, a harmonic oscillation can be assumed, *i.e.* $\mathbf{H}(\mathbf{r}, t) = \mathbf{H}(\mathbf{r})e^{j\omega t}$ and $\mathbf{E}(\mathbf{r}, t) = \mathbf{E}(\mathbf{r})e^{j\omega t}$. This is of no restriction, since Maxwell's equations are linear and a more complex time-dependence can be built up as a superimposition of the harmonic modes. Plugging the harmonic fields into Eqs. (4.8) and (4.10), one obtains:

$$\nabla \times \mathbf{H}(\mathbf{r}) - j\omega\varepsilon_0\varepsilon(\mathbf{r})\mathbf{E}(\mathbf{r}) = 0 \tag{4.12}$$

$$\nabla \times \mathbf{E}(\mathbf{r}) + j\omega\mu_0\mathbf{H}(\mathbf{r}) = 0 \tag{4.13}$$

Dividing Eq. (4.12) by $\varepsilon(\mathbf{r})$, taking the curl and plugging Eq. (4.13) into it, one finally obtains the *master equation* for the $\mathbf{H}$-field:

$$\hat{\Theta}\mathbf{H}_\omega(\mathbf{r}) = \left(\frac{\omega}{c}\right)^2 \mathbf{H}_\omega(\mathbf{r}) \quad \text{with} \quad \hat{\Theta} = \nabla \times \left[\frac{1}{\varepsilon(\mathbf{r})}\nabla\times\right] \tag{4.14}$$

On the other hand, taking the rotational of Eq. (4.13), inserting Eq. (4.12) into it and dividing by $\varepsilon(\mathbf{r})$, yields the *master equation* for the $\mathbf{E}$-field:

$$\hat{\Xi}\,\mathbf{E}_\omega(\mathbf{r}) = \left(\frac{\omega}{c}\right)^2 \mathbf{E}_\omega(\mathbf{r}) \quad \text{with} \quad \hat{\Xi} = \frac{1}{\varepsilon(\mathbf{r})}\nabla \times \nabla\times \tag{4.15}$$

The operator $\hat{\Theta}$ has the convenient properties of being both linear and hermitian. A detailed proof of hermicity can be found in appendix A. However, the operator $\hat{\Xi}$ is

not hermitian. The latter problem could be solved defining a new field $\mathbf{F}(\mathbf{r}) = \sqrt{\varepsilon(\mathbf{r})}\mathbf{E}$, which transforms Eq. (4.15) into

$$\hat{\Pi}\,\mathbf{F}_\omega(\mathbf{r}) = \left(\frac{\omega}{c}\right)^2 \mathbf{F}_\omega(\mathbf{r}) \quad \text{with} \quad \hat{\Pi} = \frac{1}{\sqrt{\varepsilon(\mathbf{r})}}\nabla \times \nabla \times \frac{1}{\sqrt{\varepsilon(\mathbf{r})}} \tag{4.16}$$

leading to a hermitian operator $\hat{\Pi}$, with the drawback that the field $\mathbf{F}$ is not transverse any more ($\mathbf{k} \cdot \mathbf{F} \neq 0$).

The dimensionality (1D, 2D, 3D) has not been explicitly defined yet. However, since the samples in this thesis are *quasi*-2D we restrict ourselves to the pure 2D case. When considering a symmetric PhC slab waveguide the eigenvalue problem can be split into the two distinct TE ($H_x = H_y = E_z = 0$) and TM ($E_x = E_y = H_z = 0$) polarisations.

$$\frac{\partial}{\partial x}\left[\frac{1}{\varepsilon(\mathbf{r})}\frac{\partial}{\partial x}H_z\right] + \frac{\partial}{\partial y}\left[\frac{1}{\varepsilon(\mathbf{r})}\frac{\partial}{\partial x}H_z\right] + \frac{\omega^2}{c^2}H_z = 0 \qquad \text{'TE'} \tag{4.17}$$

$$\frac{1}{\varepsilon(\mathbf{r})}\left[\frac{\partial^2}{\partial x^2} + \frac{\partial^2}{\partial y^2}\right]E_z + \frac{\omega^2}{c^2}E_z = 0 \qquad \text{'TM'} \tag{4.18}$$

So far, periodicity has not been taken into account. The modes in a periodic medium are of the Bloch form (see section 1.5.2), *i.e.*

$$\mathbf{H}_\mathbf{k}(\mathbf{r}) = e^{j\mathbf{k}\mathbf{r}}\mathbf{u}_\mathbf{k}(\mathbf{r}) \tag{4.19}$$

where $\mathbf{u}_\mathbf{k}(\mathbf{r})$ is a periodic function in $\mathbf{r}$, *i.e.* $\mathbf{u}_\mathbf{k}(\mathbf{r} + \mathbf{R}) = \mathbf{u}_\mathbf{k}(\mathbf{r})$. An obvious step is to expand $\mathbf{u}_\mathbf{k}(\mathbf{r})$ into a Fourier series over the reciprocal lattice vectors. In the following all reciprocal and real-space vectors are 2D in-plane vectors. Thus, one way to solve Eqs. (4.17) and (4.18) is to expand both the inverse dielectric map and the magnetic field into a plane wave basis:

$$\frac{1}{\varepsilon(\mathbf{r})} = \sum_{m=1}^{N}\hat{\kappa}(\mathbf{G}_m)e^{j\mathbf{G}_m\mathbf{r}} \tag{4.20}$$

$$H_z(\mathbf{r},\omega) = e^{j\mathbf{k}\mathbf{r}}\underbrace{\sum_{m=1}^{N}A_m(\mathbf{k})e^{j\mathbf{G}_m\mathbf{r}}}_{\mathbf{u}_\mathbf{k}(\mathbf{r})} = \sum_{m=1}^{N}A_m(\mathbf{k})e^{j(\mathbf{k}+\mathbf{G}_m)\mathbf{r}} \tag{4.21}$$

$$E_z(\mathbf{r},\omega) = \sum_{m=1}^{N}B_m(\mathbf{k})e^{j(\mathbf{k}+\mathbf{G}_m)\mathbf{r}} \tag{4.22}$$

where $\mathbf{G}_m$ denote the reciprocal lattice vectors and $\mathbf{k}$ is a reciprocal vector inside the first Brillouin zone. The Bloch modes can be labelled by their respective k-value. Substituting these expansions into Eqs. (4.17) and (4.18) leads to a hermitian positive-definite eigenvalue problem in matrix form [73] [1]:

---

[1]Sözüer *et al.* [74] suggest that the eigenvalue problem for the TM polarisation should rather be put in the form of a generalised hermitian eigenvalue problem of the form $A \cdot x = \lambda B \cdot x$ with A and B being hermitian rather than in the form $(B^{-1}A)x = \lambda x$. The fact that $B^{-1}A$ is no longer hermitian adds unnecessary computational complexity to the problem (symmetric eigenvalue problems can be handled much more efficiently than unsymmetric ones). However, the substitution done by Maradudin *et al.* in Eq. (4.25) allows one to write the master equation as a normal hermitian eigenvalue problem of the form $Ax = \lambda x$ even for TM polarisation.

$$\sum_{m=1}^{N} (\mathbf{k} + \mathbf{G}_n) \cdot (\mathbf{k} + \mathbf{G}_m) \cdot \hat{\kappa}(\mathbf{G}_n - \mathbf{G}_m) \cdot A_m(\mathbf{k}) = \frac{\omega^2}{c^2} A_n(\mathbf{k}) \qquad \text{`TE'} \qquad (4.23)$$

$$\sum_{m=1}^{N} |\mathbf{k} + \mathbf{G}_n| \cdot \hat{\kappa}(\mathbf{G}_n - \mathbf{G}_m) \cdot |\mathbf{k} + \mathbf{G}_m| \cdot C_m(\mathbf{k}) = \frac{\omega^2}{c^2} C_n(\mathbf{k}) \qquad \text{`TM'} \qquad (4.24)$$

$$\text{where} \quad C_n(\mathbf{k}) = |\mathbf{k} + \mathbf{G}_n| \cdot B_n(\mathbf{k}) \qquad (4.25)$$

For the TE polarisation the full matrix form reads:

$$
\begin{aligned}
&\left[\begin{pmatrix} (\mathbf{k}+\mathbf{G}_1)\cdot(\mathbf{k}+\mathbf{G}_1) & \cdots & (\mathbf{k}+\mathbf{G}_1)\cdot(\mathbf{k}+\mathbf{G}_m) & \cdots & (\mathbf{k}+\mathbf{G}_1)\cdot(\mathbf{k}+\mathbf{G}_N) \\ \vdots & \ddots & \vdots & & \vdots \\ (\mathbf{k}+\mathbf{G}_n)\cdot(\mathbf{k}+\mathbf{G}_1) & \cdots & (\mathbf{k}+\mathbf{G}_n)\cdot(\mathbf{k}+\mathbf{G}_m) & \cdots & (\mathbf{k}+\mathbf{G}_n)\cdot(\mathbf{k}+\mathbf{G}_N) \\ \vdots & & \vdots & \ddots & \vdots \\ (\mathbf{k}+\mathbf{G}_N)\cdot(\mathbf{k}+\mathbf{G}_1) & \cdots & (\mathbf{k}+\mathbf{G}_N)\cdot(\mathbf{k}+\mathbf{G}_m) & \cdots & (\mathbf{k}+\mathbf{G}_N)\cdot(\mathbf{k}+\mathbf{G}_N) \end{pmatrix} \right. \qquad \text{`TE'} \\
&\left. \cdot \begin{pmatrix} \hat{\kappa}(\mathbf{G}_1-\mathbf{G}_1) & \cdots & \hat{\kappa}(\mathbf{G}_1-\mathbf{G}_m) & \cdots & \hat{\kappa}(\mathbf{G}_1-\mathbf{G}_N) \\ \vdots & \ddots & \vdots & & \vdots \\ \hat{\kappa}(\mathbf{G}_n-\mathbf{G}_1) & \cdots & \hat{\kappa}(\mathbf{G}_n-\mathbf{G}_m) & \cdots & \hat{\kappa}(\mathbf{G}_n-\mathbf{G}_N) \\ \vdots & & \vdots & \ddots & \vdots \\ \hat{\kappa}(\mathbf{G}_N-\mathbf{G}_1) & \cdots & \hat{\kappa}(\mathbf{G}_N-\mathbf{G}_m) & \cdots & \hat{\kappa}(\mathbf{G}_N-\mathbf{G}_N) \end{pmatrix} \right] \cdot \begin{pmatrix} A_1 \\ \vdots \\ A_n \\ \vdots \\ A_N \end{pmatrix} = \frac{\omega^2}{c^2} \begin{pmatrix} A_1 \\ \vdots \\ A_n \\ \vdots \\ A_N \end{pmatrix}
\end{aligned}
\qquad (4.26)
$$

whereas for TM polarisation one has:

$$
\begin{aligned}
&\left[\begin{pmatrix} |\mathbf{k}+\mathbf{G}_1|\cdot|\mathbf{k}+\mathbf{G}_1| & \cdots & |\mathbf{k}+\mathbf{G}_1|\cdot|\mathbf{k}+\mathbf{G}_m| & \cdots & |\mathbf{k}+\mathbf{G}_1|\cdot|\mathbf{k}+\mathbf{G}_N| \\ \vdots & \ddots & \vdots & & \vdots \\ |\mathbf{k}+\mathbf{G}_n|\cdot|\mathbf{k}+\mathbf{G}_1| & \cdots & |\mathbf{k}+\mathbf{G}_n|\cdot|\mathbf{k}+\mathbf{G}_m| & \cdots & |\mathbf{k}+\mathbf{G}_n|\cdot|\mathbf{k}+\mathbf{G}_N| \\ \vdots & & \vdots & \ddots & \vdots \\ |\mathbf{k}+\mathbf{G}_N|\cdot|\mathbf{k}+\mathbf{G}_1| & \cdots & |\mathbf{k}+\mathbf{G}_N|\cdot|\mathbf{k}+\mathbf{G}_m| & \cdots & |\mathbf{k}+\mathbf{G}_N|\cdot|\mathbf{k}+\mathbf{G}_N| \end{pmatrix} \right. \qquad \text{`TM'} \\
&\left. \cdot \begin{pmatrix} \hat{\kappa}(\mathbf{G}_1-\mathbf{G}_1) & \cdots & \hat{\kappa}(\mathbf{G}_1-\mathbf{G}_m) & \cdots & \hat{\kappa}(\mathbf{G}_1-\mathbf{G}_N) \\ \vdots & \ddots & \vdots & & \vdots \\ \hat{\kappa}(\mathbf{G}_n-\mathbf{G}_1) & \cdots & \hat{\kappa}(\mathbf{G}_n-\mathbf{G}_m) & \cdots & \hat{\kappa}(\mathbf{G}_n-\mathbf{G}_N) \\ \vdots & & \vdots & \ddots & \vdots \\ \hat{\kappa}(\mathbf{G}_N-\mathbf{G}_1) & \cdots & \hat{\kappa}(\mathbf{G}_N-\mathbf{G}_m) & \cdots & \hat{\kappa}(\mathbf{G}_N-\mathbf{G}_N) \end{pmatrix} \right] \cdot \begin{pmatrix} C_1 \\ \vdots \\ C_n \\ \vdots \\ C_N \end{pmatrix} = \frac{\omega^2}{c^2} \begin{pmatrix} C_1 \\ \vdots \\ C_n \\ \vdots \\ C_N \end{pmatrix}
\end{aligned}
\qquad (4.27)
$$

4.1.1 2D Lattices of holes

The lattice parameters of the two most common 2D lattice geometries including their Brillouin zones have been sketched in section 1.3.2. Due to the rotational symmetry of the lattice, $\hat{\theta}$ commutes, for example, in the case of the triangular lattice with the rotational operator $\Re_{\frac{\pi}{3}}$ (see B) leading to redundant zones in the Brillouin zone and allowing one to focus on the irreducible part of the Brillouin zone (shaded region) which comprises the three symmetry points (see Fig. 1.6). The in-plane **k**-vector is very easily introduced into the calculation allowing one to calculate band structures in a straightforward way: Once the reciprocal dielectric map is expanded into a Fourier-series, the actual diagonalisation can be looped over **k**. One calculates the eigenvalues for the different **k**-values along the symmetry directions of the Brillouin zone, *i.e.* it is sufficient to follow a path in k-space on the border of the irreducible Brillouin zone which is spanned, in the case of the triangular lattice, by the three symmetry points Γ, M and K.

The lattice parameters (*e.g.* filling factor, dielectric contrast, lattice geometry) enter the calculation by means of the $\hat{\kappa}$-array (defined in Eq. 4.20). Where this is possible one should calculate the $\hat{\kappa}$ coefficients analytically rather than numerically [74]. A limitation of this specific analytical implementation of the PWE lies in the maximum f. Since the κ-matrix is calculated analytically by performing the Fourier integral over the circular aperture inside the unit cell, it has been assumed that the holes are not overlapping. This reduces the useful f-range to the touching limit of the holes, *i.e.* to $f = 0.785$ and to $f = 0.907$ for the square and triangular lattice, respectively.

On the other hand, the determination of the $\hat{\kappa}$-elements by Fast Fourier Transform (FFT) offers a higher degree of freedom with respect to arbitrary non-circular hole shapes or to structures with extremely high f-values, such that the holes are overlapping. However, EM fields tend to be singular near sharp edges and corners. The FFT rounds these and may cause additional inaccuracies if the sampling mesh is not fine enough.

The Fourier coefficients $\hat{\kappa}(\mathbf{G})$ are determined by the integral over the surface a_c of the unit cell (see Table 1.1) [73]:

$$\hat{\kappa}(\mathbf{G}) = \frac{1}{a_c} \int\limits_{a_c} d\mathbf{r} e^{-j\mathbf{Gr}} \frac{1}{\varepsilon(\mathbf{r})} = \begin{cases} \frac{1}{\varepsilon_a} f + \frac{1}{\varepsilon_b}(1-f) & \mathbf{G} = 0 \\ \left(\frac{1}{\varepsilon_a} - \frac{1}{\varepsilon_b}\right) f \frac{2J_1(Gr)}{Gr} & \mathbf{G} \neq 0 \end{cases} \tag{4.28}$$

where J_1 denotes a first-order Bessel function. This method of taking directly the Fourier transform of the reciprocal dielectric function is usually referred to as the **inverse method**. In order to get finite summations, the expansion series of the fields and of the inverse dielectric map has to be truncated. The number of reciprocal vectors, equal to the number of plane waves, determines the precision of the calculation. The reciprocal lattice is given by all possible linear combinations of the reciprocal vectors, *i.e.*

$$\mathbf{G} = h_1 \cdot \mathbf{b}_1 + h_2 \cdot \mathbf{b}_2 \tag{4.29}$$

with h_1, h_2 being integers between $-\infty$ and $+\infty$. An approved way to truncate is to define a maximal norm $G_{\max}$ and select the reciprocal vectors that meet the condition $|\mathbf{G}| \leq G_{\max}$ [75]. In this way the reciprocal space is truncated isotropically.

When $\varepsilon(\mathbf{r})$ has a jump discontinuity, as it is the case at the hole interface, its discrete Fourier transform will have a long tail due to Gibbs phenomenon [2] [76]. Thus, although the Fourier series yields convergence in the mean, the series overshoots the actual values at the simple discontinuities. At the discontinuity in $\varepsilon(\mathbf{r})$ the EM fields $\mathbf{E}$, $\mathbf{D}$, $\mathbf{B}$ or $\mathbf{H}$ will in general themselves be discontinuous and feature slowly decreasing Fourier components even for very large values of $|\mathbf{G}|$. A possible way to reduce the Gibbs phenomenon may be to approximate the step function in the spatial representation of the dielectric function by a continuous function, *e.g.* a high-order Gaussian.

An additional error in the finite matrix representation of $\kappa(\mathbf{G}_n - \mathbf{G}_m)$ comes from the asymmetric truncation in the $\mathbf{G}_n \neq 0$ rows [74]. The additional error introduced by the asymmetric truncation gets worse for the components where $|\mathbf{G}_n| \rightarrow G_{\max}$.

---

[2]Near a point, where a function $f(x)$ has a jump discontinuity, the partial sums $S_n(x)$ of a Fourier series exhibit a substantial overshoot near these endpoints, and an increase in n will not diminish the amplitude of the overshoot, although with increasing n the overshoot occurs over smaller and smaller intervals. This phenomenon is called Gibbs phenomenon.

4.1.2   The Ho method

In the inverse method the reciprocal dielectric map $1/\varepsilon(\mathbf{r})$, on which the calculation is based, is directly Fourier-transformed ($\kappa \equiv [[1/\varepsilon]]$) and then truncated ($\kappa^{(N)} = [[1/\varepsilon]]^{(N)}$). In this notation the double squared brackets of $[[1/\varepsilon]]$ denote the Toeplitz matrix generated by the Fourier coefficients of $1/\varepsilon$ and the subscript $^{(N)}$ indicates the truncation to a $N \times N$ matrix, where N is the number of wavevectors below cut-off. The idea of taking the Fourier transform of the dielectric map $\varepsilon(\mathbf{r})$, truncating it and then inverting it to improve convergence was first used by K. M. Ho *et al.* [21], and improved by L. Li [77] (see Table 4.1). When $[[\varepsilon]]$, the Fourier transform of $\varepsilon(\mathbf{r})$ is first truncated at $N \times N$, and then inverted, the matrix $[[\varepsilon]]^{(N)^{-1}}$ obtained can be quite different from the $N \times N$ matrix $\kappa^{(N)}$, especially when $\varepsilon(\mathbf{r})$ is discontinuous [74]. However L. Li [77] notes that contrary to intuition and contrary to Ref. [74] even as
$$N \to \infty, \quad \kappa^{(N)} \neq [[\varepsilon]]^{(N)^{-1}}.$$

The differences between Ho's method and the inverse method are summarised in Table 4.1.

	step	inverse method	Ho's method
1.	evaluation of Fourier integrals	$\hat{\kappa}_{\text{inv}} = [[\frac{1}{\varepsilon(\mathbf{r})}]]$	$\hat{\sigma} = [[\varepsilon(\mathbf{r})]]$
2.	matrix truncation	$\hat{\kappa}_{\text{inv}}^{(N)} = [[\frac{1}{\varepsilon(\mathbf{r})}]]^{(N)}$	$\hat{\sigma} = [[\varepsilon(\mathbf{r})]]^{(N)}$
3.	matrix inversion	$-$	$\hat{\kappa}_{\text{Ho}}^{(N)} = \{\hat{\sigma}\}^{-1}$

Table 4.1: Comparison between the inverse method and Ho's method (the double brackets mean 'Fourier transform of'). Even as $N \to \infty$, $\hat{\kappa}_{\text{inv}}^{(N)} \neq \hat{\kappa}_{\text{Ho}}^{(N)}$.
  [Comparaison entre la méthode inverse et la méthode de Ho (les double parenthèses signifient 'transformé de Fourier de'). Même quand $N \to \infty$, $\hat{\kappa}_{\text{inv}}^{(N)} \neq \hat{\kappa}_{\text{Ho}}^{(N)}$.]

The size of the band gap is highly sensitive to the volume fraction of each component (*i.e.* the effective filling factor f_{eff}). By changing the numerical representation of the dielectric function or the number of expansion terms, the truncated dielectric map is affected such that f_{eff} changes, which in turn affects the size of the band gaps [78]. Therefore the gap width is a good criterion to test convergence. Two different convergence tests have been performed for the 1st- and 2nd order TE gap in a triangular lattice of air-holes for an effective index that lies in the middle of the one for GaAs and InP. For the 1st order gap situated around $u = 0.24$ (see Fig. 4.2 (a)), Ho's method shows clearly a better convergence than the inverse method, especially for small N. The convergence of the second-order gap situated around $u = 0.61$ is slightly worse than the first-order one (see Fig. 4.2 (b)). This is inherently related to the PWE method where accuracy decreases with increasing energy.
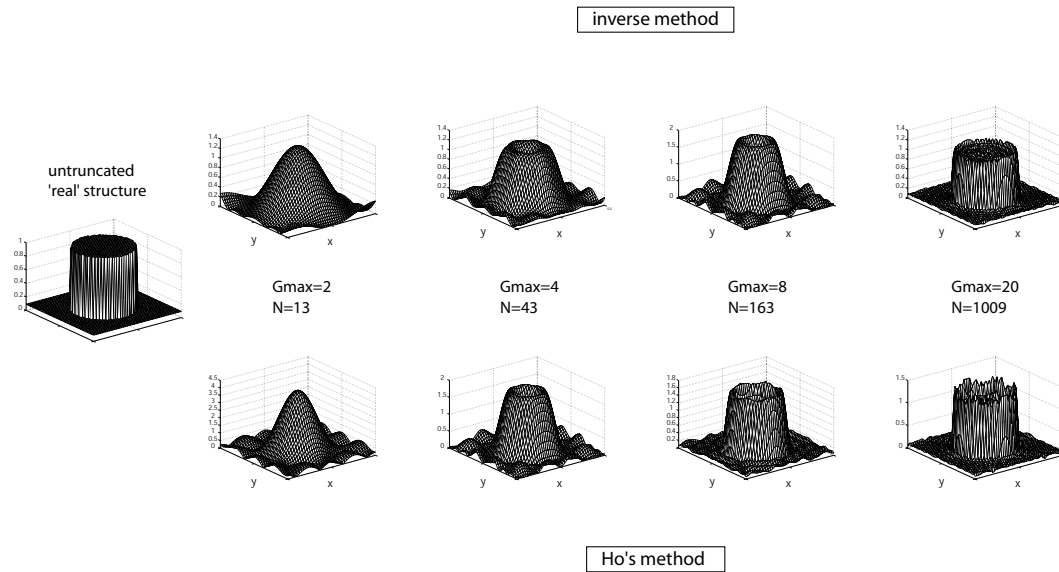
Figure 4.1: Representation of the truncated reciprocal dielectric map as a function of the number of plane waves both for the 'inverse' and 'Ho's method'. In comparison on the left side the 'real', untruncated map.

[Représentation de la carte diélectrique réciproque en fonction du nombre d'ondes planes pour la 'méthode inverse' et la 'méthode de Ho'.]
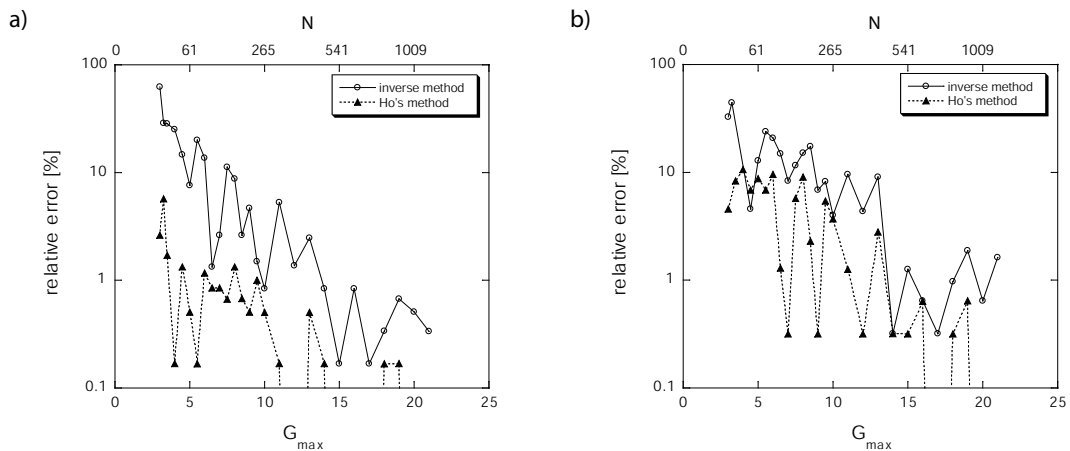

Figure 4.2: Convergence of the inverse method and Ho's method for the computation of the gap width as a function of G_{max} or N, respectively (Parameters: triangular lattice, $f = 0.3$, $\varepsilon_{hole} = 1$, $\varepsilon_{sub} = 11$). a) First-order TE gap, b) Second order TE gap.

[Convergence de la méthode inverse et de la méthode de Ho pour le calcul de la largeur du gap en fonction de G_{max} ou N (Paramètres: réseau triangulaire, $f = 0.3$, $\varepsilon_{hole} = 1$, $\varepsilon_{sub} = 11$). a) Première bande interdite TE, b) Deuxième bande interdite TE.]

The fast convergence of Ho's method implies that a small number of plane waves is sufficient to yield accurate results, even if the truncated dielectric function has large fluctuations and overshoots. [3].

---

[3]Note that the convergence of the eigenvectors is normally one order of magnitude slower than for

4.1.3 The supercell approach

The standard PWE method is restricted to the calculation of band structure calculation of bulk PhC. For the calculation of more complicated structures, *e.g.* cavities and waveguides, a super-periodicity has to be introduced by means of a supercell, containing many unit cells (see Fig. 4.3).
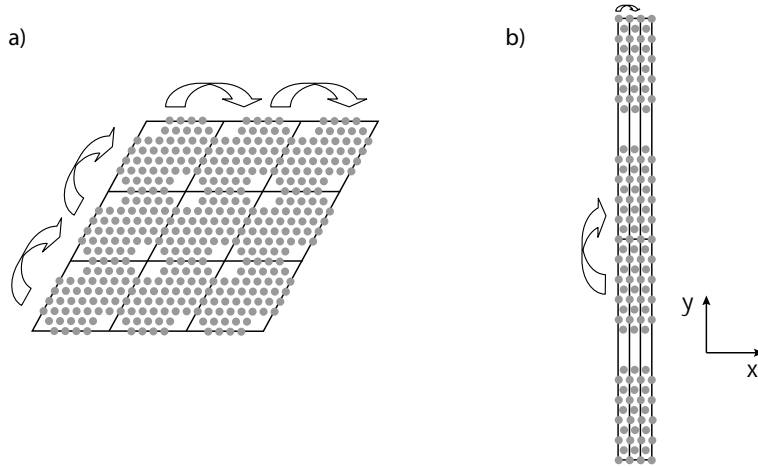
Figure 4.3: Two different supercell configurations: a) parallelogram-like supercell: suitable for cavity modes; b) rectangular-like supercell: suitable for straight guides and 1D-cavities.
[*Deux différents types d'une supercellule: a) type losange: adapté aux modes de cavités; b) type rectangle: adapté aux guides droits, et aux cavités 1D.*]

In the case of the supercell containing a defect (*e.g.* a cavity), this defect is repeated periodically in space (periodic boundary conditions). The Fourier coefficients describing this superperiodicity are given by the Fourier integral over the area A_{sc} of the supercell and the wavevectors are the reciprocal vectors with respect to the direct vectors spanning the supercell. When considering the parallelogram-like supercell with αa sidelength, the reciprocal vectors of the supercell are just those of the unit cell divided by the factor α, *i.e.* $\mathbf{b}_1^{(sc)} = \frac{1}{\alpha}\mathbf{b}_1$ and $\mathbf{b}_2^{(sc)} = \frac{1}{\alpha}\mathbf{b}_2$. This supercell is well adapted to the study of isolated cavity defects. The superperiodicity leads to the formation of an infinite number of 'ghost defects' that are separated from each other by the supercell length. It must be ensured that the coupling between two neighbouring defects is negligible, *i.e.* that the localised cavity field has sufficiently decreased before it hits the neighbouring cavity. In practice, the number of surrounding rows of holes has to be steadily increased until the cavity energy eigenvalues converge to a stable value.

When taking a rectangular supercell of width a and height αa then the reciprocal lattice is likewise rectangular with reciprocal vectors $\mathbf{b}_1^{(sc)} = \frac{2\pi}{a}(1,0)$ and $\mathbf{b}_2^{(sc)} = \frac{2\pi}{a}(0,\frac{1}{\alpha})$. When truncating at constant $G_{\max}$, this signifies that the expansion along the longer side of the supercell contains more terms than along the short side. This second type of supercell is well suited for the calculation of the modes and the dispersion of straight waveguides and also coupled cavity waveguides (CCWs) (see chapter 8.

---

the eigenvalues

The $\hat{\kappa}$ of a supercell containing α^2 unit cells writes:

$$\hat{\kappa}(\mathbf{G}) = \frac{1}{A_{sc}} \int\limits_{A_{sc}} d\mathbf{r} e^{-j\mathbf{Gr}} \frac{1}{\varepsilon(\mathbf{r})} = \frac{1}{\varepsilon_b} \delta_{G,0} + \left(\frac{1}{\varepsilon_a} - \frac{1}{\varepsilon_b}\right) \frac{1}{A_{sc}} \int\limits_{A_{sc}} d\mathbf{r} e^{-j\mathbf{Gr}} \cdot \mathbf{S}(\mathbf{r}) \qquad (4.30)$$

where $\mathbf{S}(\mathbf{r})$ is a binary function which is 1 inside the holes and 0 elsewhere. The surface of the supercell can be expressed as $A_{sc} = \alpha^2 a_c$. The integral over the supercell can be replaced by a sum of integrals over the individual holes, making it convenient to define a local spatial variable $\mathbf{r}' \doteq \mathbf{r} - \mathbf{R}_i$ leading to identical integrals for each hole:

$$
\begin{aligned}
\hat{\kappa}(\mathbf{G}) &= \frac{1}{\varepsilon_b} \delta_{G,0} + \left(\frac{1}{\varepsilon_a} - \frac{1}{\varepsilon_b}\right) \frac{1}{A_{sc}} \sum_{\text{holes i}} \left[\int\limits_{1 \text{ hole}} d\mathbf{r}' e^{-j\mathbf{G}(\mathbf{R}_i + \mathbf{r}')} \right] \\
&= \frac{1}{\varepsilon_b} \delta_{G,0} + \underbrace{\left[\left(\frac{1}{\varepsilon_a} - \frac{1}{\varepsilon_b}\right) \frac{1}{a_c} \int\limits_{1 \text{ hole}} d\mathbf{r}' e^{-j\mathbf{Gr}'} \right]}_{F(\varepsilon_a, \varepsilon_b, G, R)} \cdot \underbrace{\left[\frac{1}{\alpha^2} \sum_{\text{holes i}} e^{-j\mathbf{GR}_i} \right]}_{S(\mathbf{G}, \{\mathbf{R}_i\})} \qquad (4.31)
\end{aligned}
$$

Similar to x-ray diffraction in solid state physics, the complete structure can be separated into a form factor F describing the geometry and material properties of a single hole and a structure factor S taking into account the lattice structure. As in the case of the simple band structure calculation, the Fourier transform of a circular aperture yields a first-order Bessel-function.

$$\hat{\kappa}(\mathbf{G}) = \begin{cases} \frac{1}{\varepsilon_b} + \left(\frac{1}{\varepsilon_a} - \frac{1}{\varepsilon_b}\right) f \frac{N_{\text{holes}}}{\alpha^2} & \mathbf{G} = 0 \\[3mm] \left(\frac{1}{\varepsilon_a} - \frac{1}{\varepsilon_b}\right) f \frac{2 J_1(Gr)}{Gr} \cdot \frac{1}{\alpha^2} \sum\limits_{\text{holes i}} e^{-j\mathbf{GR}_i} & \mathbf{G} \neq 0 \end{cases} \qquad (4.32)$$

where the filling factor was introduced as $f = a_{\text{hole}}/a_c$. For supercell calculations, Ho's method is of essential importance, since the number of plane waves involved scales with $N \propto \alpha^2 \cdot G_{\max}^2$. Thus using Ho's method Eq. (4.32) translates into:

$$
\begin{aligned}
\hat{\sigma}(\mathbf{G}) &= \begin{cases} \varepsilon_b + (\varepsilon_a - \varepsilon_b) f \frac{N_{\text{holes}}}{\alpha^2} & \mathbf{G} = 0 \\[3mm] (\varepsilon_a - \varepsilon_b) f \frac{2 J_1(Gr)}{Gr} \cdot \frac{1}{\alpha^2} \sum\limits_{\text{holes i}} e^{-j\mathbf{GR}_i} & \mathbf{G} \neq 0 \end{cases} \\[3mm]
\hat{\kappa} &= (\hat{\sigma})^{-1}
\end{aligned}
\qquad (4.33)
$$

The precision of the supercell calculation is given by the truncation value $G_{\max}$ of the reciprocal lattice. Assuming a supercell containing α times β unit cells, the number of necessary plane waves is given by the division of the circle area with radius $G_{\max}$ by the area occupied in reciprocal space by a single vector, $i.e.$

$$N = \frac{G_{\max}^2 \pi}{\left(\frac{2\pi}{\alpha a}\right) \left(\frac{2\pi}{\beta a}\right)} = \alpha \beta N_0 \qquad (4.34)$$

In order to have the same precision as in the calculation of the bulk crystal, one needs $\alpha \cdot \beta$ times more reciprocal vectors. In consequence for a big supercell it is only feasible to go up to the third order approximation with respect to a single hole.

4.1.4 Variable hole sizes

In this section the case of a supercell containing holes at positions $\{\mathbf{R}_i\}$ with various radii $\{r_i\}$ is considered. In this case the calculation of the $\hat{\kappa}$-matrix is slightly more complex (compare with Eq. 4.35), *i.e.*

$$
\hat{\sigma}(\mathbf{G}) =
\begin{cases}
\varepsilon_b + (\varepsilon_a - \varepsilon_b)\frac{1}{\alpha^2}\frac{\pi}{a_c}\sum_{\text{holes i}} r_i^2 & \mathbf{G} = 0 \\[2em]
(\varepsilon_a - \varepsilon_b) \cdot \frac{1}{\alpha^2}\frac{\pi}{a_c}\sum_{\text{holes i}} r_i^2 \frac{2J_1(Gr_i)}{Gr_i}e^{-j\mathbf{G}\mathbf{R}_i} &
\end{cases}
\tag{4.35}
$$
$$
\hat{\kappa} = (\hat{\sigma})^{-1}
$$

where a_c denotes the unit cell area and r_i the radius of the i-th hole of the supercell.

The extension to variable holes will be used for the calculation of the coupling length in directional couplers as a function of the radius of the barrier holes between the two waveguides (see chapter 7).

Another example of the PWE with variable holes is the existence of a monopole mode inside a modified H1 cavity. The original H1 cavity possesses only two degenerate dipole modes. By reducing the diameter of the boundary holes to 60 %, a monopole mode appears amongst other modes (see Fig. 4.4).
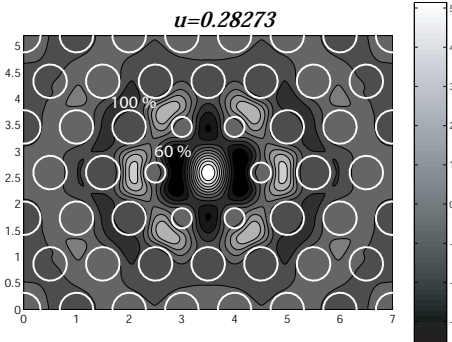
Figure 4.4: This example shows the norm of the H_z field of a monopole mode ($f = 0.37$, $\varepsilon_{\text{sub}} = 11$, $G_{\max} = 4.5$, $N = 2325$).
[Cet exemple montre le module du champ H_z d'un mode monopole ($f = 0.37$, $\varepsilon_{sub} = 11$, $G_{max} = 4.5$, $N = 2325$).]

4.1.5 The limits of the plane wave method

The Gibbs phenomenon becomes a problem particularly when structures with very different index contrasts are incorporated into the same supercell. Let us consider the case of a shallow ridge waveguide bordered by a PhC structure as it may be considered for an active device. The parameters of the structure are the effective indices of the ridge ($n_2 = 3.1909$) and the cladding region ($n_1 = 3.1836$), the ridge width d_1 and the separation d_2 between the ridge and the PhC (see Fig. 4.5).

The oscillations in the index profile, caused by the strong discontinuity at the holes, penetrate far into the hole-free zone of the waveguide (see Fig. 4.6).

For a weak index contrast between the ridge and the cladding region, these oscillations can be one order of magnitude larger than the actual index difference. One may test the reliability of the results as long as the average indices in the two regions remain correct. Fig. 4.7 shows the difference between the averaged ridge and cladding indices as a function of the intended index contrast Δn. The linear fit shows a good agreement

down to an index contrast of $\Delta n = 0.05$. It should, however, be emphasised that what is problematic is not low index contrast *per se* but the combination of low index and high index structures in proximity of each other.

Another issue is the distance between the ridge and the PhC structure. The Gibbs oscillations decrease with increasing distance from the PhC. Fig. 4.8 investigates how the absolute mean index of the ridge is influenced by the spacing d_1 to the PhC. The agreement becomes good only for distances greater than one lattice constant.

The role of the PhC in the structure sketched in Fig. 4.5 is not to guide (the light is already guided by the ridge) but rather to provide feedback. This can be achieved at the third-order Bragg condition that couples the two counter-propagating fundamental modes. The relative width $\Delta u/u$ of the stopband as a function of the horizontal index contrast between the ridge and the cladding is provided in Fig. 4.9.

For small index contrast the field is less confined in ridge and interacts more with the PhC, increasing the feedback.

In conclusion it can be said that the smaller the index contrast is within the low-contrast structure, the greater the distance has to be from the high-index contrast PhC structure.
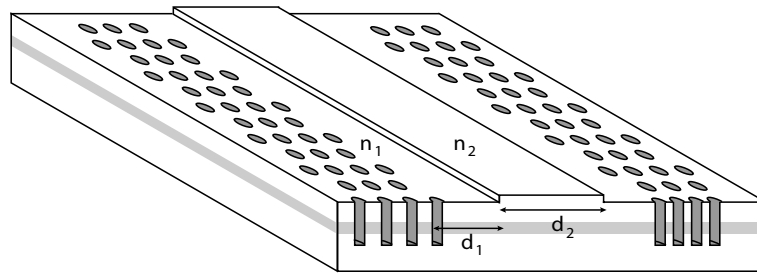
Figure 4.5: Schematic representation of a ridge waveguide embedded into a 2D PhC. The ridge locally leads to an increased effective index.
[Schéma d'un guide ruban incorporé dans un cristal photonique 2D. Le guide ruban provoque localement une augmentation de l'indice effectif.]
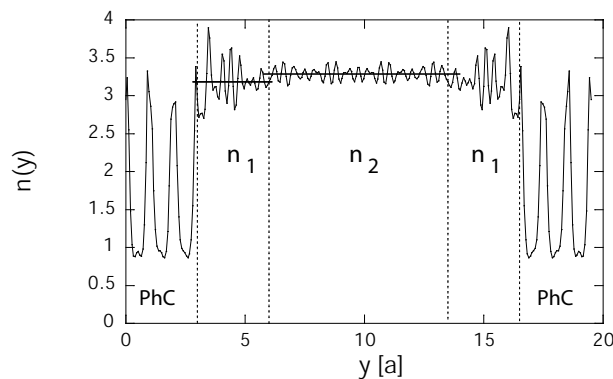
Figure 4.6: Vertical cross-section through the reconstructed refractive index map ($N = 1095$) of the structure described in Fig. 4.5 (Parameters: $d_1 = 3$, $d_2 = 7.5$, $n_1 = 3.1836$, $\Delta n = 0.1$ and $G_{\max} = 3.2$).
[Coupe vertical à travers la carte du profil d'indice reconstruit ($N = 1095$) de la structure présentée dans la figure 4.5 (Paramètres: $d_1 = 3a$, $d_2 = 7.5a$, $n_1 = 3.1836$, $\Delta_n = 0.1$ and $G_{max} = 3.2$).]

The present PWE implementation proved to be quite memory hungry. This is the case especially for the eigenmode calculation, more precisely when the Matlab® command $[V, D] = eig(B)$ is evoked (see Fig. 4.10). When, for example, working with $N = 4000$ plane waves, the maximum memory load mounts up to 640 MB and 1.2 GB for the band structure and the eigenmode calculation, respectively. These numbers are, however, optimistic values since they take only the big matrices into account that scale with N^2 and neglect memory temporarily allocated by Matlab® routines. When imposing inversion symmetry of the super periodic structure such that $\varepsilon(\mathbf{r}) = \varepsilon(-\mathbf{r})$, the κ-array and thus the eigenvalue equation become real. This leads to a considerable
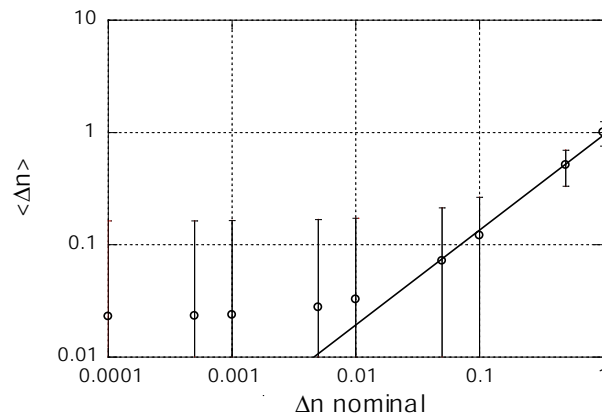
Figure 4.7: The graph plots the approximated index contrast, obtained by averaging the index profile as in Fig. 4.6 for the ridge and cladding region, versus the *a priori* index contrast (Parameters: $f = 0.35$, $n_1 = 3.1836$, $G_{\max} = 4.5$, $N = 2025$).
[Contraste d'indice approximé en fonction du contraste d'indice nominal, obtenu en moyennant le profil d'indice comme dans la figure 4.6 pour la région du ruban et du cladding (Paramètres: $f = 0.35$, $n_1 = 3.1836$, $G_{max} = 4.5$, $N = 2025$).]
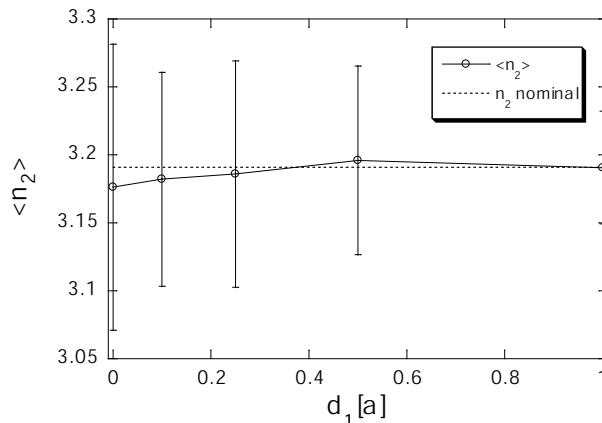
Figure 4.8: This graph shows the influence of the distance d_1 between ridge and PhC on the average ridge index. The pointed line represents the nominal index ($n_2 = 3.1909$). (Parameters: $n_1 = 3.1836$, $n_2 = 3.1909$, $d_2 = 7.5$, $f = 0.35$, $G_{\max} = 4.5$).
[Ce graphique montre l'influence de la largeur du cladding sur l'indice moyen du guide ruban. La ligne pointillée représente l'indice nominal ($n_2 = 3.1909$). (Paramètres: $n_1 = 3.1836$, $n_2 = 3.1909$, $d_2 = 7.5$, $f = 0.35$, $G_{\max} = 4.5$).]

reduction of the memory load. This reduces the memory load by a factor of 1.25 and 2.25 for the band structure and eigenmode calculation respectively.

Assuming an $\alpha \times \alpha$ supercell, the number of plane waves grows quadratically with α and $G_{\max}$. Thus the memory requirement grows with $N^2 \propto \alpha^4$.

So far we have been limited by memory rather than by computation time. For small N ($< \approx 500$) the biggest part of the time is consumed by the construction of the κ-matrix and neither by the matrix inversion (Ho's method) nor the diagonalisation process. This may, however, change rapidly with increasing N, since the classical diagonalisation algorithms scale with $N^3 \propto \alpha^6$, which is not very appealing.
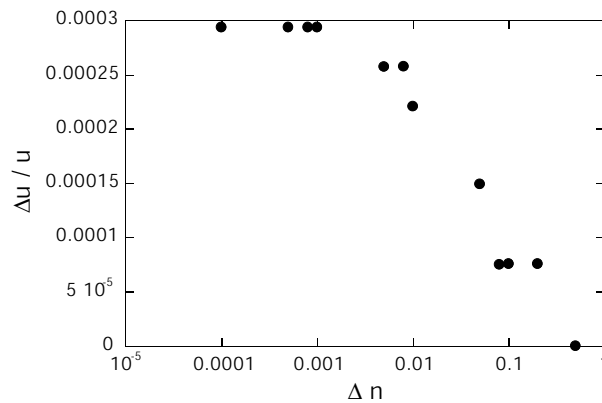
Figure 4.9: Relative width of the third-order Bragg stopband as a function of index contrast Δn (Parameters: TE-pol, $f = 0.35$, $d_1 = 1$ a, $d_2 = 7.5$ a, $G_{\max} = 1.6$).
[Largeur relative du mini-stopband à la condition de Bragg d'ordre 3 en fonction du contraste d'indice Δn (Paramètres: TE-pol, $f = 0.35$, $d_1 = 1$ a, $d_2 = 7.5$ a, $G_{max} = 1.6$).]
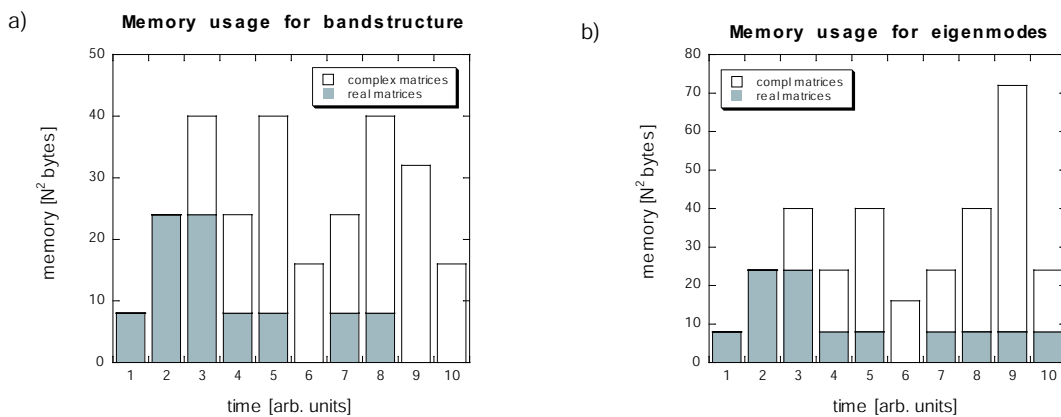
Figure 4.10: The graph shows schematically the memory usage of Matlab[®] implementation during different program phases (only variables that scale with $O(N^2)$ have been included).
[Le graph montre schématiquement la consomation de mémoire vife dans différents stade de l'execution (seules les variable grandissant en $O(N^2)$ ont été incluses.]

4.1.6   Extension to the third dimension

An extension of the PWE model to the third dimension has been done in the literature [79] but is practically limited to the computation of bandstructures of 3D bulk crystal. A supercell could, in principle, be added, but would practically be very restricted in size: Assuming a cubic supercell with $\alpha \cdot a$ unit cells in each direction, then the number of plane waves would scale with α^3 and G_{max}^3. Thus memory would grow with $N^2 \propto \alpha^6$ and computing time would scale with $N^3 \propto \alpha^9$. An additional memory requirement would be linked to the fact that polarisation cannot be separated in 'TE' and 'TM' any more. For the 3D case a variational method would probably be preferable to the matrix diagonalisation method.

4.2   The Sakoda method

4.2.1   Basic principles

In 1995 K. Sakoda presented a new original method for the calculation of the transmittance and Bragg reflectivity of 2D photonic lattices [80,81]. The method is based on the plane wave expansion of the electromagnetic field and the inverse dielectric constant and is applicable to any 2D photonic lattice, *e.g.* square, triangular. Instead of directly developing the electric field, a pseudo field is introduced and developed: By subtracting a boundary value function $f_E(x, y)$ from the electrical field in region II (inside the PhC), a pseudo-field $\psi_E(x, y)$ is defined. This field cancels the incoming wave on the PhC boundary and allows one to rewrite the problem in the form *operator* $\times \psi_E = 0$ without any second members. In order to satisfy the m cancellation of the pseudo-field at the PhC boundary, the method uses a development in sines and cosines rather than in complex exponentials. The computational domain is divided into three regions, the incoming plane (I), the actual PhC (II) and the back plane (III). Note that the actual PhC boundary is spaced by the distance d from the outer hole boundary (see Fig. 4.11).

The main advantage of Sakoda's method over the standard PWE is the ability to calculate the complex reflection and transmission coefficients. The model takes into account interference phenomena and the coupling of the external field to the PhC. By analysing experimental transmission spectra, K. Sakoda noted that the transmission spectrum is not only governed by the density of states (DOS), but that the spectrum is modified by finite size effects and the external coupling strength [81].

Besides the transmission, reflection and diffraction spectra Sakoda's method allows to calculate the field inside the PhC. A typical field distribution inside a 4-row ΓM mirror (see Fig. 4.12) is depicted in Fig. 4.13.

4.2.2   Application to Fabry-Pérot cavities between PhC mirrors

In this section the Fabry-Pérot (FP) transmission is calculated by plugging the complex reflection and transmission coefficients $r_0(u)$ and $t_0(u)$, obtained by Sakoda's method, into Airy's formula. This procedure, in the following referred to as 'Sakoda+FP' model,
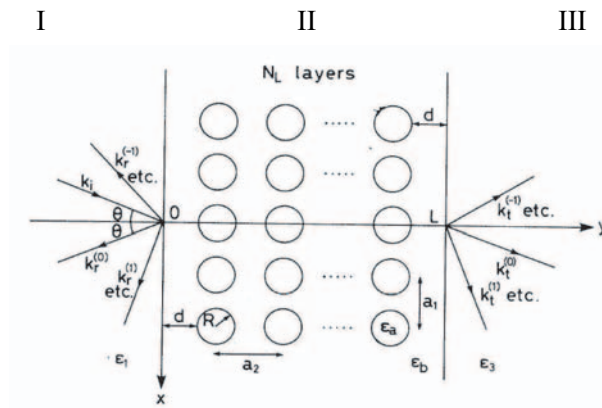
Figure 4.11: Configuration for the calculation of the transmission and the Bragg reflection spectra for the case of a rectangular lattice defined by the lattice constants a_1 and a_2 (top view) (from Sakoda [81]).
[Configuration pour le calcul de la transmission et de la réflexion de Bragg pour le cas d'un réseau rectangulaire donné par les constantes de réseau a_1 et a_2 (d'après Sakoda [81]).]
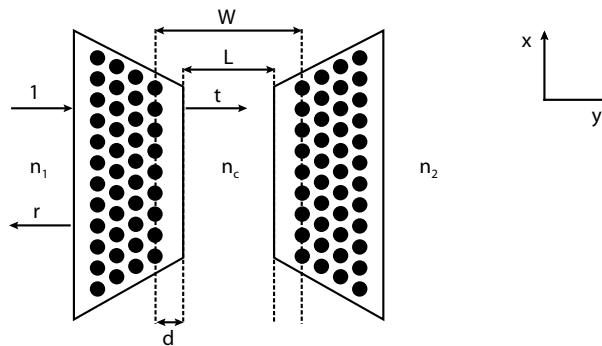

Figure 4.12: Schematic diagram for the transmission calculation of a FP cavity.
[Schéma pour le calcul de la transmission d'une cavité Fabry-Pérot.]
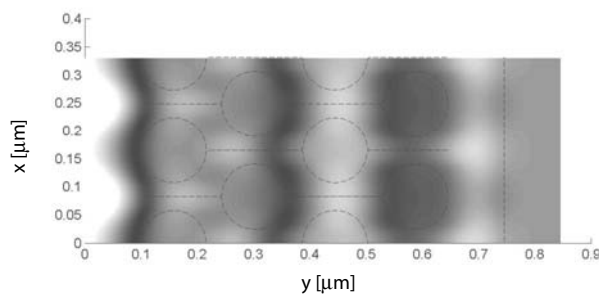
Figure 4.13: Map of the magnetic field ($|H_z|$) inside the 4-row ΓM mirror, calculated with Sakoda's method.
[Image du champ magnétique ($|H_z|$) à l'intérieur d'un block de 4 rangées ΓM , calculé avec la méthode de Sakoda.]

has the advantage that after having calculated the frequency-dependent coefficients for given mirror parameters (f, ε_{sub}), the FP transmission can easily be evaluated for cavities of arbitrary width. Similar to the FDTD model the out-of-plane losses are included in the Sakoda method by means of a complex dielectric constant ε'' inside the holes. Although the FDTD fit of simple crystal transmission spectra yields information about f and ε'' in the region of the dielectric and the air-band, the important frequency region of the band gap is lacking. In order to get the loss value inside the bandgap, one would have to fit FP transmission spectra. However, the experience showed that apart from the energy position, the FP peak height is not reliably fitted by FDTD [82].

This deficiency may be overcome by the proposed 'Sakoda+FP' model. The model is based on exact transmission and reflection values and the only free-fitting parameters in Airy's formula are the basic mirror parameters f and ε''.

The FP transmission, defined by the single mirror properties r and t, the effectiv index n_{eff} in the cavity, the intra-cavity absorption α and the effective cavity length L (see Fig. 4.12), is given by Airy's formula:

$$t_{\text{FP}} = \frac{t_1 t_2 v \cdot e^{jk_y L}}{1 - r_1 r_2 v^2 e^{j2k_y L}} = \frac{t^2 v \cdot e^{jk_y L}}{1 - r^2 v^2 e^{j2k_y L}} \tag{4.36}$$

where $k_y = \frac{2\pi}{\lambda} n_{\text{eff}} = \frac{2\pi}{a} n_{\text{eff}} \cdot u$ and $u = a/\lambda$. The propagation loss inside the cavity is introduced by means of the loss factor v, where $v \cdot v^* = V = e^{-\alpha L}$ and $V = 1$ means loss-free.

For r and t the 0th-order coefficients r_0 and t_0 are inserted from the Sakoda calculation. Since the coefficients are defined not with reference to the last row of PhC but to the reference plane shifted by the distance d with respect to the *extremity* of the holes, the following correction has to be made to the cavity length:

$$\frac{L}{a} = \frac{W}{a} - 2 \cdot \frac{d}{a} - 2 \cdot \frac{R}{a} \tag{4.37}$$

In our case the refractive index inside and on both sides of the cavity are all equal to n_{eff}, thus:

$$T_{\text{FP}} = \frac{n_2}{n_1} |t_{\text{FP}}|^2 = |t_{\text{FP}}|^2 \tag{4.38}$$

In order to check the definition of the cavity length given in Eq. (4.37), the following test was performed. By choosing $\frac{W}{a} = \frac{\sqrt{3}}{2}$, the FP cavity defined by two four-row mirrors transforms actually in a defect-free block of eight rows of PhC. The result of the Sakoda calculation for the '4+4' FP transmission and the 8 row simple crystal transmission is shown in Fig. 4.14.

The agreement in the dielectric band and in the band gap is perfect whereas the air band transmission is significantly different.

An example of an experimental peak measured by the experimental technique described in chapter 3 and fitted by the 'Sakoda+FP' model is depicted in Fig. 4.15. The fit of the peak yields $f = 0.3$ and $\varepsilon'' = 0.0475$ which has to be compared to $\varepsilon'' = 0.06$, a value that has been deduced from the FDTD fit of the air-band and the scaling law (Eq. (3.30)). The difference lies in the error bars of the ε''-model.

Another test is to check the agreement of the FP peak position between experimental and calculation for different cavity widths (see Fig. 4.16). Experimental values are

available for $W/a = 1.6$, 1.7, 1.8 and 1.9 (see Fig. 4.16(left)). For larger cavity widths the 'Sakoda+FP' model is compared with different numerical techniques (PWE and FDTD). Fluctuations of the experimental peak positions may be due to small variations in f and dispersion effects due to different peak wavelengths.

There is not only a difference in peak position between experiment and calculation, but also within the different numerical methods (Sakoda, PWE, FDTD). For the bigger cavities supporting multiple modes, the selection criterion was to keep the mode order constant. One notes that the agreement between Sakoda and FDTD gets better for increasing cavity sizes. A possible reason could be that when plane wave impinges on the first block it is on projected on the Bloch modes inside the slab, at the inner interface the mode is projected again on a plane wave basis and propagates to the
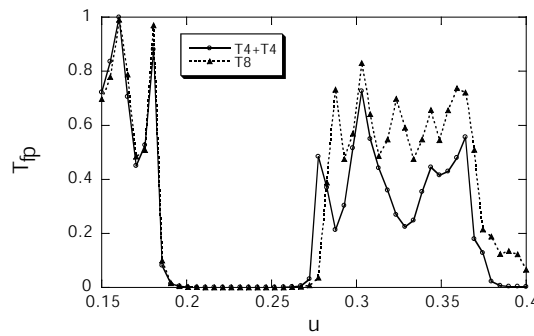
Figure 4.14: When taking the two 4-row mirrors in the Sakoda+FP-model closer to the limiting distance of $W/a = \sqrt{3}/2$, the resulting transmission should approximately agree with the transmission of an 8-row mirror (parameters: $f = 0.33$, $\varepsilon_{\mathrm{sub}} = 11.4$, $\varepsilon'' = 0$, N=15, M=150, 50 points).
[En rapprochant les deux miroirs à 4 rangées du model Sakoda+FP à la distance limite de $W/a = \sqrt{3}/2$, la transmission devrait approximativement être conforme à la transmission d'un miroir à 8 rangées (paramètres: $f = 0.33$, $\varepsilon_{sub} = 11.4$, $\varepsilon'' = 0$, N=15, M=150, 50 points)]
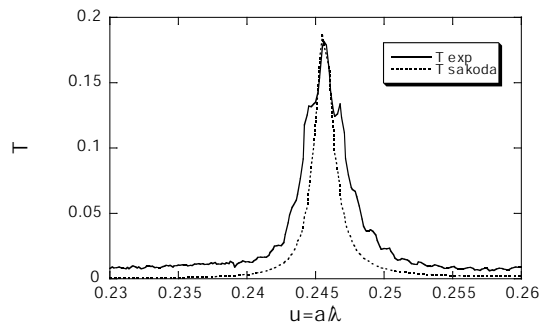
Figure 4.15: The experimental spectrum (solid line) of an FP cavity ($W/a = 1.7$, $a = 270$ nm) is fitted with Airy's function (dotted line) using the complex reflection and transmission coefficient calculated with Sakoda's method (parameters: $f = 0.3$, $\varepsilon_{\mathrm{sub}} = 11.4$, $\varepsilon'' = 0.0475$, N=15, M=150, 50 points)
[Comparaison entre le spectre expérimental (trait solide) d'une cavité FP et la courbe théorique de la fonction d'Airy (ligne pointillée) en utilisant les coefficients complexes de réflexion et transmission calculé avec la méthode de Sakoda (paramètres: $f = 0.3$, $\varepsilon_{sub} = 11.4$, $\varepsilon'' = 0.0475$, N=15, M=150, 50 points).]

second block where it is again converted into a Bloch mode and so on. In the case of a large mirror separation this picture may work well. However for small cavity widths the Bloch modes couple with each other by means of evanescent field coupling. These interference effects are taken into account by the FDTD and the PWE calculation, but not by Sakoda+FP model. The coupling between the two mirrors decreases for increasing cavity widths, reducing the error of the model. Additionally to the cavity width there is another degree of freedom, the cavity symmetry. The cavity can be mirror symmetric (A-type) or glide symmetric (B-type). The PWE and FDTD model take the symmetry into account, whereas the Sakoda model assumes uniform r_0, t_0 over the whole plane. The relative difference in peak energy for the two symmetries is about 0.16% (see Fig. 4.17) and thus in most cases negligible.

In overall terms, the 'Sakoda+FP' model has met our expectations. The energy
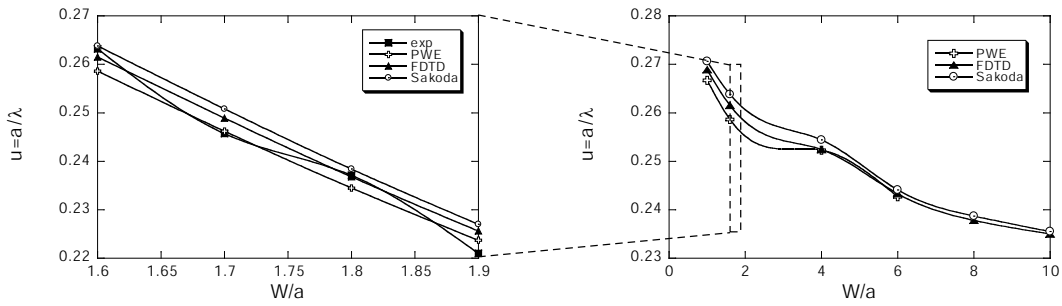
Figure 4.16: Comparison of the experimental FP peak position with Sakoda's method. In order to cross-check, the energies are also calculated by PWE and FDTD. The Sakoda method converges towards the values of alternative modelling techniques, *i.e.* PWE and FDTD, for large cavity sizes.
[Comparaison de la position expérimentale du pic FP avec la méthode de Sakoda. Les énergies ont été calculées en plus avec PWE et FDTD. La méthode de Sakoda converge vers des valeurs des techniques alternatives pour des tailles de cavité élevées.]
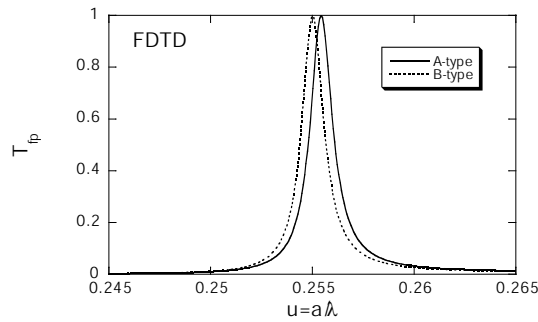
Figure 4.17: In the FDTD calculation there exists a small difference in FP peak position whether the structure is mirror symmetric (A-type, solid line) or glide symmetric (B-type, dotted line). The FP cavities on the sample are B-type (parameters: $W/a = 1.6$, $f = 0.3$, $\varepsilon_{\mathrm{sub}} = 11.4$, $\varepsilon'' = 0$).
[Dans le calcul FDTD il existe une différence mineure dans l'énergie centrale du pic FP selon que la structure a une symétrie miroir (type A, trait solide) ou une symétrie décalée (type B, trait pointillé). Les cavités FP sur l'échantillon sont de type B (paramètres: $W/a = 1.6$, $f = 0.3$, $\varepsilon_{sub} = 11.4$, $\varepsilon'' = 0$).]

position as well as the FP transmission fit are satisfactory. However, for the necessary precision the number of plane waves had to be boosted and the method lost a lot of its flexibility and speed.

4.3 Conclusions

The PWE method is probably the most widely used tool for simple band structure calculations. It has been shown that Ho's method features indeed an improved convergence with respect to the inverse method. The improved convergence rate more than makes up the additional effort needed to invert the matrix $[[\varepsilon]]^{(N)}$. This is especially important when working with a supercell, where, for a given precision, the number of plane waves scales quadratically with the supercell dimensions α and thus the memory usage scales with α^4. In contrast to time domain methods (*e.g.* FDTD), the procedure directly yields the fields and the corresponding mode energies, not requiring post-processing of the data in order to extract the physical data.

There are a few restrictions to the PWE method in general and to the chosen implementation in particular. The chosen analytical Fourier transformation as described in this section does not allow for intersecting holes, thus limiting the maximum possible f value. This limitation could, however, be overcome by a numerical Fourier transformation. Furthermore, mainly due to Gibbs phenomenon, it is practically impossible to have high-index and low-index contrast features inside the same structure.

Chapter 5

Hybrid waveguides

One of the most important components inside a PhC integrated circuit is the channel waveguide which provides the connection between different building blocks. The waveguide should be low loss and provide a broad bandwidth. One phenomenon limiting the bandwidth is the mini-stopband (MSB) [83] (see section 5.1.2). The initial goal of this work was to test a waveguide design that could in principle have been MSB free. We have seen that in a PhC waveguide the MSB stems from the periodic corrugation of the PhC waveguide border. The original idea was to eliminate the MSBs by breaking the translational symmetry. This can be achieved by making a waveguide with different crystal orientation at the two borders, *i.e.* ΓM and ΓK , respectively (see Fig. 5.1). This new type of waveguide is called a 'hybrid waveguide'.
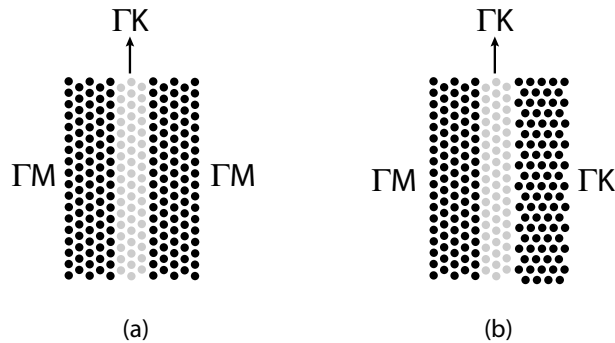
Figure 5.1: (a) Sketch of a (standard) W3 waveguide with 3 missing rows along ΓM direction. (b) Sketch of a hybrid waveguide with one border ΓM and teh other ΓK . *[Schéma d'un guide (standard) W3 avec trois rangées manquantes selon la direction ΓM . (b) Schéma d'un guide hybrid avec un bord ΓM et l'autre ΓK .]*

For completeness we should mention that in some cases the existence of the MSB is desired. For example due to its sensitivity with respect to the PhC parameters (*e.g.* air-filling factor, propagation losses) it can be utilised as a local probe for PhC parameters inside the waveguide. Another application is in the size reduction of directional couplers due to the MSB effect (see chapter 7).

5.1 The standard W3 waveguide

The standard Wn PhC waveguide is a line defect consisting of n missing rows of holes along the ΓK direction. The structures investigated in this thesis are W3 waveguides (see 5.1).

5.1.1 Transmission measurement

5.1.1.1 Modal selectivity (excitation)

Experimentally when measuring straight waveguides by the ILS technique, the source is positioned at about $d_e = 20\,\mu$m from the guide entry. This ensures that the waveguide is excited by a quasi-plane wave. In this case only modes with even parity can be excited. However, due to the wavevector mismatch between the plane wave and higher-order modes only the fundamental mode is effectively excited.

5.1.1.2 Collection

Let us focus first on the case where there is no structure, the case when taking a reference. The useful signal, the one that is guided in the core of the heterostructure is astigmatic, because it is only confined in the vertical direction. In the horizontal plane it propagates freely with n_{eff} of the guided mode. As discussed in section 3.1.4 the refraction at the facet creates a virtual source situated at the distance d_0/n_{eff}, where d_0 is the distance between the real source and the facet (see Fig. 5.2).

When considering a straight waveguide exited at the same distance d_0, it appears that the guide exit at the distance d_f from the facet constitutes a new point source whose light is again distributed into the three different channels (air, substrate, guided mode) towards the microscope objective. Its corresponding virtual source is situated at d_f/n_{eff}.

Fig. 5.2 illustrates the case where the collection objective (N.A.=0.5, spotsize=4μm) is focused on the facet. In this case the guided signal appears as elongated ellipse in the plane. Both in case (a) and (b) the amount of collected signal is limited by the spotsize ($D = 4\,\mu$m) of the collection objective.

In the case (b) one may choose the focal plane at the virtual source instead of at the facet. By moving the focus inside the semiconductor the form of the collected signal changes. Due to the astigmatism the long axis of the ellipse is now turned by 90 ° and points perpendicularly to the plane. According to Refs. [49,54] this allows one to make sure that the collected has travelled indeed through the guide. When the signal is clearly visible on the screen the focus on the virtual guide exit image gives reliable results.

Additional selectivity is provided by the lateral collection objective. The higher order modes either leave the facet with an angle that is superior to 30 °, and are thus not collected by the $N.A. = 0.5$ objective, or impinge on the GaAs air interface with an angle greater than the critical angle $\alpha_c = 17$ ° and are totally internally reflected.

5.1.1.3 Normalisation of the guide transmission

In contrast to simple crystal structures the waveguide transmission cannot be simply normalised with respect to a reference spectrum measured in an un-patterned region. This would eliminate the spectral form of the source but would not yield the absolute transmission:

  i. The in- and out-coupling efficiency of the guide is not known.

  ii. In the case of the waveguide the relevant source is situated at the guide exit and therefore closer to the facet than in the case of the reference.

The correct way to normalise the waveguide transmission is to measure guides of different lengths and to deduce from them the extinction coefficient [54]. The entries of the different waveguides have to be excited at constant distance d_e (see Fig. 5.3).

The ratio of the intensities corresponding to two different lengths yields the total extinction coefficient:

$$\frac{I_2(\lambda)}{I_1(\lambda)} = e^{-\alpha_{\mathrm{tot}}(\lambda)\cdot(L_2-L_1)} \tag{5.1}$$

The total extinction coefficient can be separated into material absorption and the modal loss, *i.e.* $\alpha_{\mathrm{tot}} = \alpha_{\mathrm{mat}} + \alpha_{\mathrm{guide}}$. The material absorption can be measured independently by measuring $I(d,\lambda)$ in an un-patterned region for different distances d between the
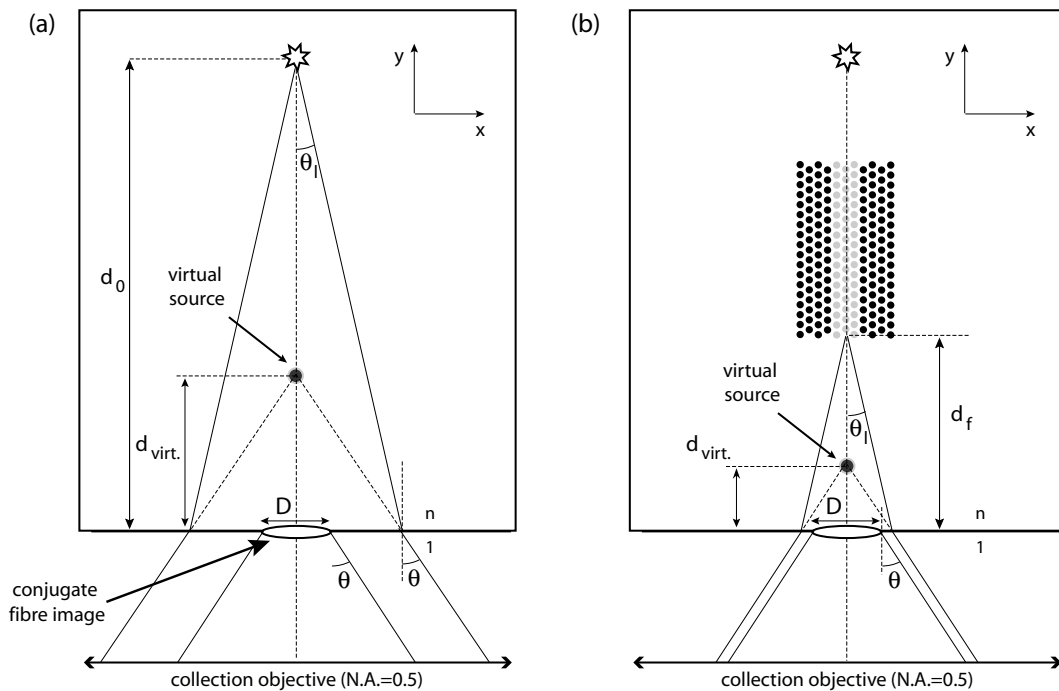
Figure 5.2: Sketch of the collection geometry for the measurement of: a) a reference signal, b) a channel waveguide transmission. Note the different distance $d_{\mathrm{virt.}}$ between the virtual source and the facet for the two cases.
[Géométrie de collection pour la mesure: a) d'un signal de référence, b) du signal transmis par le guide. Noter la différente distance $d_{\mathrm{virt.}}$ entre la source virtuelle et la facette pour les deux cas.]

spot and the facet:

$$I(d,\lambda) = I_0 \frac{e^{-\alpha_{\mathrm{mat}}(\lambda)d}}{d} \qquad \longrightarrow \qquad \frac{I(d_1,\lambda)}{I(d_2,\lambda)} = \frac{d_2}{d_1} e^{-\alpha_{\mathrm{mat}}(d_1-d_2)}$$

$$\longrightarrow \alpha_{\mathrm{mat}}(\lambda) = -\frac{1}{d_1-d_2}\ln\left(\frac{I(d_1,\lambda)}{I(d_1,\lambda)}\frac{d_1}{d_2}\right) \tag{5.2}$$

An example of a normalised W3 waveguide extinction spectrum is shown in sect. 5.1.1.4.
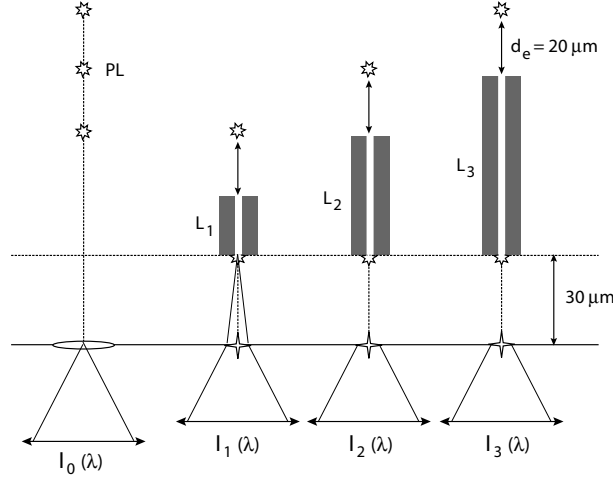
Figure 5.3: The straight guides are excited at a fixed distance $d_e = 20\ \mu$m. The lateral objective is focused on the in plane image of the PhC waveguide exit. The reference spectrum has been collected in an un-patterned region at the same excitation distances.

[Les guides droits sont excités à une distance fixe $d_e = 20\ \mu$m. L'objectif latéral est focalisé sur l'image horizontale virtuelle à l'extrémité du guide. Le spectre de référence est pris à partir d'une région sans structures aux mêmes distances d'excitation que les guides.]

5.1.1.4   W3 transmission spectra

Fig. 5.4 shows the transmission spectra of a W3 waveguide of different lengths (30 a, 60 a, 90 a. One notes a clear transmission dip around $u = 0.255$.

The application of the normalisation procedure discussed before yields a material absorption of $\alpha_{\mathrm{mat}} = 60 - 100\ \mathrm{cm}^{-1}$, a modal loss of $\alpha_{\mathrm{guide}} = 60 - 95\ \mathrm{cm}^{-1}$ (see Fig. 5.5).

5.1.1.5   The projected band structure of waveguides

When considering, for example, a channel waveguide in ΓK direction, *i.e.* a line defect obtained by omitting a row of holes along ΓK , the translation symmetry in ΓM direction is broken whereas the periodicity in propagation direction is maintained. Thus the waveguide modes can be classified by the Bloch-vector $k_\parallel$ inside the first Brillouin-zone $[-\pi/a, \pi/a]$ of the waveguide (see Fig. 5.6(a)).

It is convenient to project both the band structure of the waveguide modes and the bulk modes on $k_{\parallel}$ in order to visualize the position of the band gap. In fact the bulk modes $\omega(k_{\parallel}, k_{\perp})$ of the irreducible Brillouin zone spanned by Γ, K and M are first folded and then projected on $k_{\parallel}$ as sketched in Fig. 5.6(b). The Brillouin zone of the waveguide which, even though the basic lattice is triangular, is only a line interval in ΓK -direction and should not be confused with the Brillouin zone of the bulk crystal.

The projection of the continuum (*i.e.* the bulk modes) on $k_{\parallel}$ leads to the formation of spurious bands outside the band gap in the dielectric and the air-band (see Fig. 5.6(c)). This phenomenon is more important for supercells with large heights in y-direction because then the reciprocal lattice vectors are denser spaced (see Fig. 5.7).

Since the number of eigenvalues equals the number N of reciprocal vectors one obtains more bulk bands $\omega^{(\text{bulk})}(k_{\parallel}, k_y)$, where $k_y \epsilon \left[-\frac{\pi}{\beta a}, +\frac{\pi}{\beta a} \right]$. In a few words the spacing between the individual folded bulk bands is only linked to the size of the supercell in y-direction and tends towards a continuum for the case of an infinitely high supercell. Often, this continuum is represented in band diagrams by a shaded area.

The W1 (width=$\sqrt{3}a$) is not monomode for the chosen parameters. In order to get a monomode waveguide for the air-hole (membrane-)structure, the width has to be reduced to 0.7 W, where W is the width of a standard W1 waveguide [84].
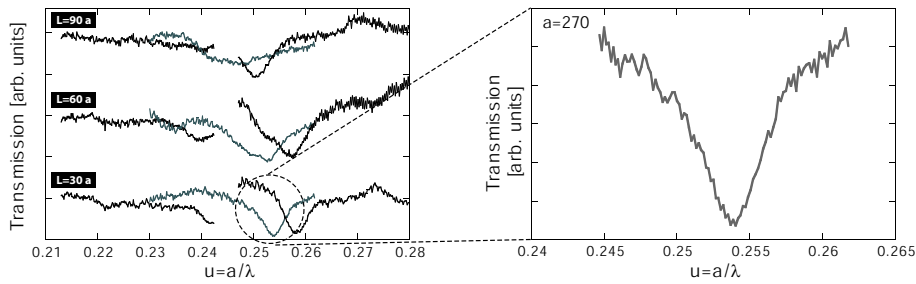
Figure 5.4: Transmission spectra of W3 waveguides with $L = 30$ a, 60 a and 90 a. The mini-stopband (MSB) is clearly visible at $u = 0.254$.
[*Spectre de transmission des guides W3 avec $L = 30$a, 60a et 90a. La mini-bande est clairement visible à la fréquence $u = 0.254$.*]
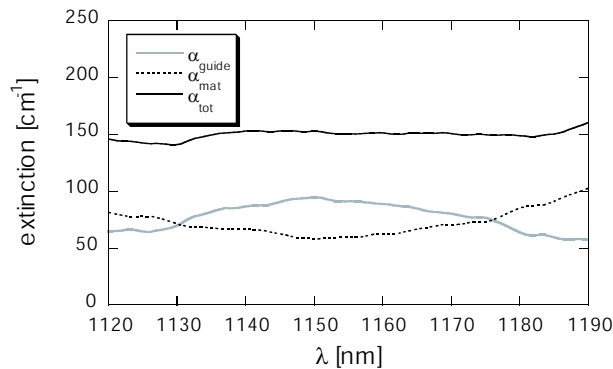
Figure 5.5: The total extinction coefficient (black solid line) of a W3 waveguide can be separated into material absorption (dotted line) and modal loss of the guide (grey line).
[*Le coefficient d'extinction total (ligne noire) peut être séparé en l'absorption du matériau (ligne pointillée) et les pertes modales du guide (ligne grise).*]
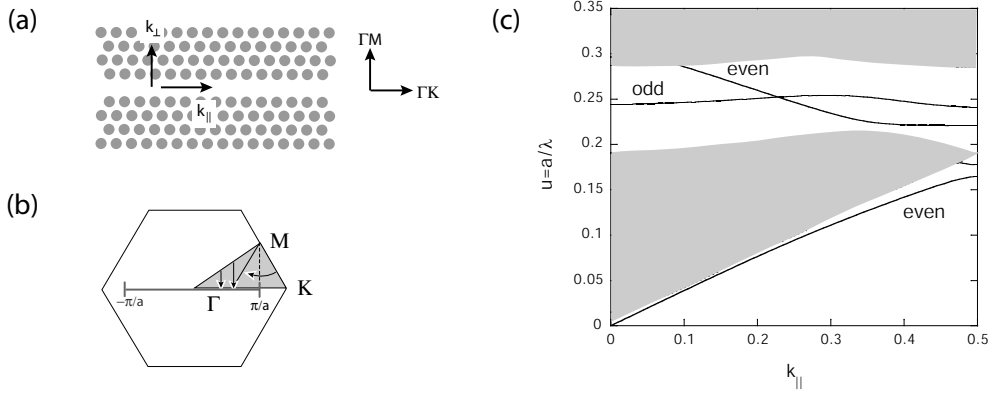
Figure 5.6: ((a) Schematic representation of a W1 waveguide (1 missing row in ΓK -
direction). (b) Brillouin zone of triangular bulk structure, not to be confused
with the rectangular Brillouin zone of the waveguide. The bulk bands are folded
and projected on $k_∥$ (ΓK) into the interval $[-\pi/a, \pi/a]$. (c) Dispersion rela-
tion of the W1 waveguide which is not monomode for the chosen parameters
(TE-pol., $f = 0.35$, $\varepsilon_{sub} = 11.4$, $\varepsilon_{cyl} = 1$, $G_{max} = 3.2$). The shaded region
corresponds to the projected bulk bands.

*[a) Représentation schématique du guide W1 (une rangée de trous manquants
en direction ΓK). b) Zone de Brillouin d'un cristal à réseau triangulaire. Ne pas
confondre avec la zone de Brillouin rectangulaire du guide. Les bands du cristal
massive sont repliées et projetée sur $k_∥$ (ΓK) dans l'interval $[-\pi/a, \pi/a]$. c) Re-
lation de dispersion du guide W1 qui n'est pas monomode pour les paramètres
choisis (TE-pol., $f = 0.35$, $\varepsilon_{sub} = 11.4$, $\varepsilon_{cyl} = 1$, $G_{max} = 3.2$). La région en gris
correspond aux bandes projetées du cristal massif.]*
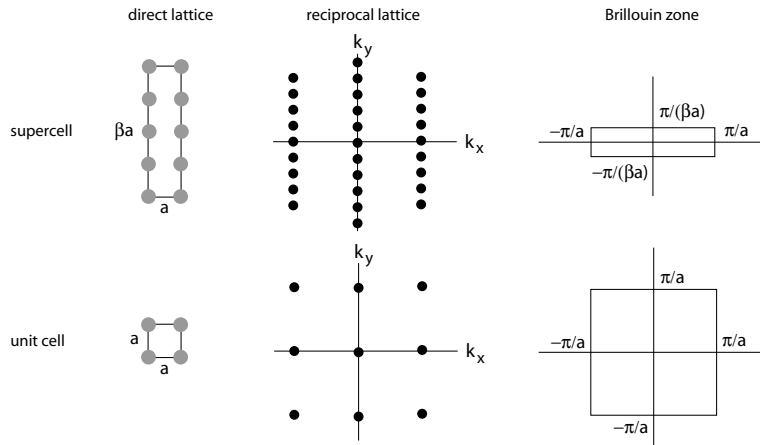
Figure 5.7: The spacing of the reciprocal vectors and the height of the Brillouin zone are
squeezed along the k_y direction (example shows a square lattice).
*[L'espacement des vecteurs réciproques et la zone de Brillouin sont comprimés
selon la direction k_y (l'exemple montre un réseau carré).]*

5.1.2 The mini-stopband (MSB)

Fig. 5.8(a) shows the ideal case of a perfect metal waveguide which supports a defined
number of modes for each polarisation for a given thickness. In Fig. 5.8(b) a periodic
perturbation is introduced along the propagation direction (*e.g.* a thickness variation

of period a). Generally speaking, mode coupling between modes i and j will occur whenever the two wavevectors along the direction of propagation differ by an integer number of reciprocal lattice vectors [83], *i.e.*

$$\beta_1 - G = -\beta_2 \tag{5.3}$$

Diagonal couplings ($1 \Leftrightarrow 1$, $2 \Leftrightarrow 2$) occur at the zone boundaries ($k_\| = \pi/a$) leading to a Bragg-like reflection. There are however off-diagonal couplings, $i \neq j$ which do not occur at the zone boundaries. They originate from the band-folding at the zone boundary, leading to an anti-crossing between mode 1 and 2 (see 5.8(b)).
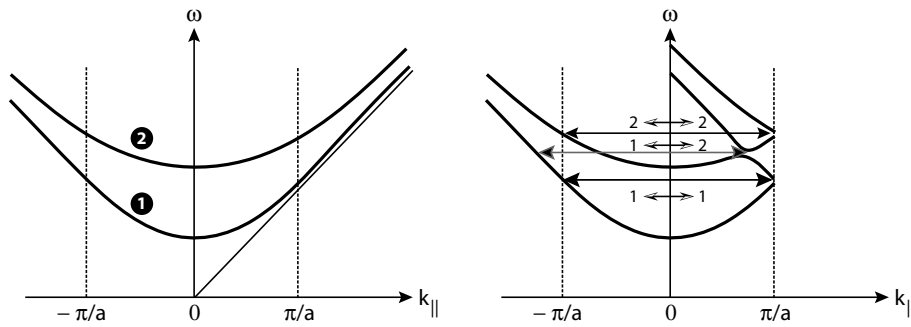
Figure 5.8: a) Dispersion relation for an ideal metal waveguide. b) In the case of a corrugation with period a, the bands are folded back into the first Brillouin zone. Apart from the Bragg stopband there occurs a MSB due to the coupling between mode 1 and 2 (from S. Olivier *et al.* [83]).

[a) Relation de dispersion d'un guide métallique idéal. b) Dans le cas d'une corrugation avec période a, les bandes sont repliées dans la première zone de Brillouin. A part des mini-bandes de Bragg il y a une mini-bande due au couplage entre le mode 1 et 2 (d'après S. Olivier et al. [83]).]

The same coupling phenomenon can also be observed in PhC waveguides. Fig. 5.9 shows the relevant part of the dispersion relation of a *W3* waveguide where the anti-crossing occurs between the mode of order five and the folded fundamental mode.

A direct visualisation of the phase-matching condition in Eq. (5.3) is provided by the extended Brillouin zone scheme (see Fig. 5.10). By translating the second order Brillouin zone by a reciprocal lattice vector, the fundamental mode is folded back into the first Brillouin zone and one obtains again the reduced Brillouin zone scheme.

5.1.3 Determination of the fill factor by means of the MSB

The 2D FDTD fit of the simple slab transmission spectra (as described in section 3.3.1) yields the fill factor f of the dielectric and the air band, which may be transferred only with greatest care to periods within the band gap. However, the fill factor for periods within the gap can be determined from the experimental mini-stopband (MSB) position [83], which depends sensitively on f (see Fig. 5.11).

Generally the transmission dips in the measured straight waveguide spectra (see for example Fig. 5.4) have a larger full width at half maximum value than calculated by PWE. There are two factors potentially contributing to the enlargement of the MSB
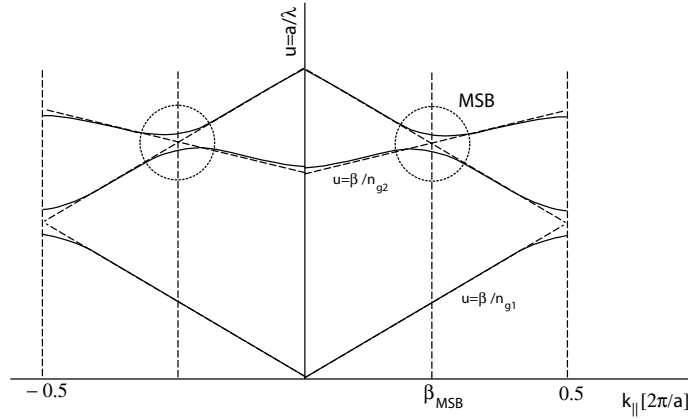
Figure 5.9: In the reduced zone scheme the W3 dispersion curves are folded back into the first Brillouin zone: The MSB appears as an anti-crossing between the two modes.

[Dans le schéma de zone réduite les courbes de dispersion du W3 sont repliées dans la première zone de Brillouin: Le mini band se manifeste comme anti-croisement entre les deux modes.]
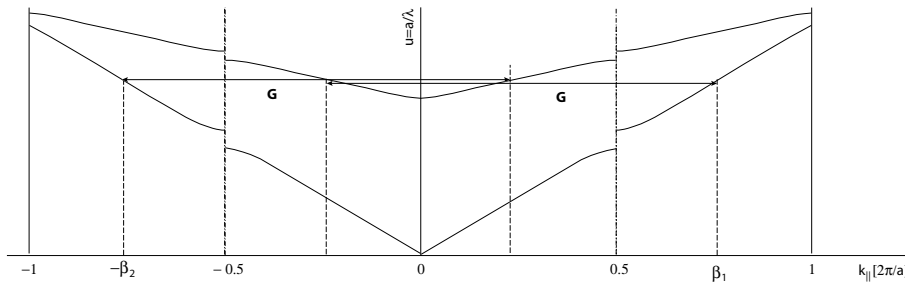

Figure 5.10: Dispersion relation of mode 1 (fundamental mode) and mode 5 of the W3 waveguide represented in the extended zone scheme: The forward propagating mode 1 is coupled with the backward propagating mode 5 by the inverse lattice vector **G**.

*[Relation de dispersion du mode 1 (mode fondamental) et mode 5 du guide W3 dans le schéma de la zone de Brillouin étendue: Le mode 1 se couple par le vecteur réciproque **G** avec le mode 5, qui se propage en contresens.]*
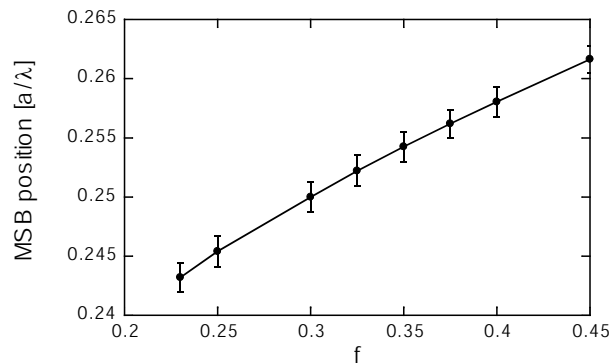
Figure 5.11: Mini-stopband position and width as a function of air-filling factor. (parameters for the PWE: $\varepsilon_{\text{sub}} = 11.4$, $G_{\text{max}} = 3.2$).

[Position de la mini-bande et sa largeur en fonction du facteur de remplissage (paramètres du calcul d'ondes planes: $\varepsilon_{sub} = 11.4$, $G_{max} = 3.2$).]

dip. Firstly, the PWE does not include losses, thus the energy splitting at the anti-crossing point agrees only with the full width at half maximum of the transmission dip if waveguide losses are zero. The presence of losses leads to a broadening which increases with the guide length (see Fig. 5.16(b) in section 5.1.4.2). Secondly, the exact MSB position is smoothed by fluctuations of f within the same guide. In this way the MSBs corresponding to different f would fall at slightly different energies and superimpose each other, leading to an effective broadening of the MSB.

When studying the MSB of the guides of different length one notes that the MSB is often more pronounced for short guides ($L = 30 - 60$ a) than for very long guides ($L = 400$ a). Since the MSB is a interference effect where the scattered wave amplitudes of each period add up constructively, one would expect the effect to become more and more distinct. However, this is only true as long as the losses are negligible (see Fig. 5.16(a) in section 5.1.4.2).

5.1.4 The mini-stopband in the framework of coupled mode theory

5.1.4.1 Contra-directional coupling

Firstly, the case of a single waveguide with a perturbation $\Delta\varepsilon$ and an absorption coefficient α is considered. The unperturbed modes $\mathbf{E}_m(x,y)e^{j(\omega t - \beta_m z)}$ are solutions of the unperturbed wave equation:

$$\left[\nabla_T^2 - \beta_m^2 + \frac{\omega^2}{c^2}\varepsilon_u \right] \mathbf{E}_m = 0 \qquad m = 1, .., N \tag{5.4}$$

where $\nabla_T^2 \doteq \frac{\partial^2}{\partial x^2} + \frac{\partial^2}{\partial y^2}$ is the transverse Laplacian and ε_u is the unperturbed index map. The total electric field inside a single waveguide can be expressed as the superposition of the unperturbed states, forming a complete orthogonal basis:

$$\mathbf{E}(x,y,z,t) = \sum C_m(z)E_m(x,y)e^{j(\omega t - \beta_m z)} \tag{5.5}$$

where the β_m are negative for modes propagating in the negative z-direction. The total electric field $\mathbf{E}(x,y,z,t)$ is now inserted into the wave equation of the perturbed structure:

$$\left[\nabla^2 + \frac{\omega^2}{c^2}[\varepsilon_u + \Delta\varepsilon(x,y,z)] \right] \mathbf{E}(x,y,z,t) = 0 \tag{5.6}$$

where $\Delta\varepsilon$ is the perturbation. To evaluate (5.6), the double derivative with respect to z has to be taken:

$$\frac{\partial^2}{\partial z^2} \sum C_m(z)\mathbf{E}_m e^{j(\omega t - \beta_m z)} = \sum \left[-\beta_m^2 C_m(z) - j2\beta_m \frac{dC_m}{dz} + \frac{d^2 C_m(z)}{dz^2} \right] \mathbf{E}_m e^{j(\omega t - \beta_m z)} \tag{5.7}$$

By assuming 'weak' dielectric perturbation such that the variation of the mode amplitudes over z is slow, *i.e.* $\left(\frac{d^2 C_m}{dz^2} = 0 \right)$, the last term in (5.7) can be neglected. With Eq.

(5.7), Eq. (5.6) writes:

$$\sum_m C_m \underbrace{\left[\nabla_T^2 - \beta_m^2 + \frac{\omega^2}{c^2}\varepsilon_u\right] \mathbf{E}_m}_{=0} e^{j(\omega t - \beta_m z)}$$

$$+ \sum_m \left[-j2\beta_m \frac{dC_m}{dz} + \frac{\omega^2}{c^2}\Delta\varepsilon C_m\right] \mathbf{E}_m e^{j(\omega t - \beta_m z)} \quad = \quad 0 \tag{5.8}$$

Taking the scalar product with $\mathbf{E}_k$ leads to:

$$\sum_m \frac{dC_m}{dz}\langle \mathbf{E}_k | \mathbf{E}_m \rangle e^{-j\beta_m z} = \sum_m \frac{-j\omega^2}{2\beta_m c^2}\langle \mathbf{E}_k | \Delta\varepsilon | \mathbf{E}_m \rangle C_m \cdot e^{-j\beta_m z} \tag{5.9}$$

For $N = 2$ this reads:

$$k = 1: \quad \frac{dC_1}{dz}\langle \mathbf{E}_1 | \mathbf{E}_1 \rangle e^{-j\beta_1 z} = -\frac{j\omega^2}{2\beta_1 c^2}\langle \mathbf{E}_1 | \Delta\varepsilon | \mathbf{E}_1 \rangle C_1 e^{-j\beta_1 z} - \frac{j\omega^2}{2\beta_2 c^2}\langle \mathbf{E}_1 | \Delta\varepsilon | \mathbf{E}_2 \rangle C_2 e^{-j\beta_2 z}$$

$$k = 2: \quad \frac{dC_2}{dz}\langle \mathbf{E}_2 | \mathbf{E}_2 \rangle e^{-j\beta_2 z} = -\frac{j\omega^2}{2\beta_2 c^2}\langle \mathbf{E}_2 | \Delta\varepsilon | \mathbf{E}_2 \rangle C_2 e^{-j\beta_2 z} - \frac{j\omega^2}{2\beta_1 c^2}\langle \mathbf{E}_2 | \Delta\varepsilon | \mathbf{E}_1 \rangle C_1 e^{-j\beta_1 z}$$

$$\tag{5.10}$$

which simplifies to:

$$\frac{dC_1}{dz} = -j \underbrace{\frac{1}{2\beta_1}\frac{\omega^2}{c^2}\frac{\langle \mathbf{E}_1 | \Delta\varepsilon | \mathbf{E}_1 \rangle}{\langle \mathbf{E}_1 | \mathbf{E}_1 \rangle}}_{\Delta\beta_1} C_1 - j \underbrace{\frac{\omega^2}{2\beta_2 c^2}\frac{\langle \mathbf{E}_1 | \Delta\varepsilon | \mathbf{E}_2 \rangle}{\langle \mathbf{E}_1 | \mathbf{E}_1 \rangle}}_{\kappa_{12}} C_2 e^{j(\beta_1 - \beta_2)z}$$

$$\frac{dC_1}{dz} = -j \underbrace{\frac{1}{2\beta_2}\frac{\omega^2}{c^2}\frac{\langle \mathbf{E}_2 | \Delta\varepsilon | \mathbf{E}_2 \rangle}{\langle \mathbf{E}_2 | \mathbf{E}_2 \rangle}}_{\Delta\beta_2} C_2 - j \underbrace{\frac{\omega^2}{2\beta_1 c^2}\frac{\langle \mathbf{E}_2 | \Delta\varepsilon | \mathbf{E}_1 \rangle}{\langle \mathbf{E}_2 | \mathbf{E}_2 \rangle}}_{\kappa_{21}} C_1 e^{-j(\beta_1 - \beta_2)z} \tag{5.11}$$

where the terms $\Delta\beta_1$, $\Delta\beta_2$ result from the dielectric perturbation on mode 1 and 2, respectively and represent a small change in the propagation constants β_1 and β_2 of the unperturbed modes [85]. Thus by accounting for the modified propagation constants in the total field

$$\mathbf{E}(x, y, z, t) = \sum C_m(z) E_m(x, y) e^{j(\omega t - (\beta_m + \Delta\beta_m)z)} \tag{5.12}$$

the CME for contra-directional coupling write [85]:

$$\frac{dC_1}{dz} = -j\kappa_{12}C_2 e^{j2\delta\beta_{12}z}$$

$$\frac{dC_2}{dz} = -j\kappa_{21}C_1 e^{-j2\delta\beta_{12}z} \tag{5.13}$$

where $\delta\beta_{12} = \frac{1}{2}(\beta_1 + \Delta\beta_1 - \beta_2 - \Delta\beta_2)$. By substituting $C_1 = \tilde{C}_1 e^{+j\delta\beta_{12}\cdot z}$ and $C_2 = \tilde{C}_2 e^{-j\delta\beta_{12}\cdot z}$ as in Ref. [86] one gets rid of the exponentials and Eq. (5.13) becomes

$$\frac{d}{dz}\begin{pmatrix} \tilde{C}_1 \\ \tilde{C}_2 \end{pmatrix} = \begin{pmatrix} -j\delta\beta_{12} & -j\kappa_{12} \\ -j\kappa_{21} & j\delta\beta_{12} \end{pmatrix} \cdot \begin{pmatrix} \tilde{C}_1 \\ \tilde{C}_2 \end{pmatrix} \tag{5.14}$$

Losses may be introduced in the usual way by means of a complex propagation constant. The total loss is the sum of material absorption and waveguide losses.

i.e. $\alpha = \alpha_{QD} + \alpha_{WG}$ and may depend on the specific mode. Thus introducing the modal loss coefficients α_1, α_2 and assuming that mode 1 is forward-propagating and mode 2 is backward-propagating turns Eq. (5.14) into:

$$\frac{d}{dz}\begin{pmatrix}\tilde{C}_1 \\ \tilde{C}_2\end{pmatrix} = \begin{pmatrix}-j\delta\beta_{12} - \alpha_1 & -j\kappa_{12} \\ -j\kappa_{21} & j\delta\beta_{12} + \alpha_2\end{pmatrix} \cdot \begin{pmatrix}\tilde{C}_1 \\ \tilde{C}_2\end{pmatrix} \tag{5.15}$$

$$\text{with} \quad \kappa_{12} = \frac{\omega^2}{2\beta_2 c^2}\frac{\langle\mathbf{E}_1|\Delta\varepsilon|\mathbf{E}_2\rangle}{\langle\mathbf{E}_1|\mathbf{E}_1\rangle} \tag{5.16}$$

where $\alpha_1, \alpha_2 > 0$ and furthermore $\kappa_{21} = -\kappa_{12}^*$ is imposed by energy conservation [87]: The coefficients C_i can be normalized such that the net power is:

$$P = p_1|C_1|^2 + p_2|C_2|^2 \tag{5.17}$$

where $p_{1,2}$ is +1 for flow in positive and -1 for flow in negative direction. For contra-directional coupling $P = |C_1|^2 - |C_2|^2$, which leads to the result $\kappa_{12} = -\kappa_{21}^*$ [87] .

For the application of the CMEs to PhC waveguides, one is interested in *periodic* perturbations along z. In this section the contra-directional coupling induced by a periodic dielectric perturbation is studied. The single W3-waveguide is inherently multimode and the periodic corrugation of the PhC guide leads to the formation of a MSB (see section 5.1.2). Since the problem can be considered as *quasi*-2D, the integration in direction vertical to the plane can be omitted in the calculation of the coupled mode parameters. However, to take the periodicity into account, we have to integrate in z-direction over the width of the supercell (see Fig. 5.14). The dielectric map can be written as a Fourier series where usually only the first-order is considered:

$$\varepsilon(x, z) = \varepsilon_u + \Delta\varepsilon \approx g_1(x)e^{-jGz} + g_1^\star(x)e^{jGz} \quad \text{with} \quad G = \frac{2\pi}{a}$$

$$\text{where} \quad g_1(x) = \frac{1}{a}\int_0^a e^{jGz}\varepsilon(x, z)\,dz \tag{5.18}$$

Putting (5.18) into Eq. (5.15) leads to:

$$\frac{d}{dz}\begin{pmatrix}\tilde{C}_1 \\ \tilde{C}_2\end{pmatrix} = \begin{pmatrix}-j\delta\beta_{12} - \alpha_1 & -j\kappa_{12} \\ -j\kappa_{21} & j\delta\beta_{12} + \alpha_2\end{pmatrix} \cdot \begin{pmatrix}\tilde{C}_1 \\ \tilde{C}_2\end{pmatrix} \tag{5.19}$$

$$\text{with} \quad \delta\beta_{12} = \frac{1}{2}(\beta_1 + \Delta\beta_1 - \beta_2 - \Delta\beta_2 - G) \tag{5.20}$$

$$\text{and} \quad \kappa_{12} = \frac{\omega^2}{2\beta_2 c^2}\frac{\langle\mathbf{E}_1|g_1(x)|\mathbf{E}_2\rangle}{\langle\mathbf{E}_1|\mathbf{E}_1\rangle} \qquad \kappa_{21} = \frac{\omega^2}{2\beta_1 c^2}\frac{\langle\mathbf{E}_2|g_1^\star(x)|\mathbf{E}_1\rangle}{\langle\mathbf{E}_2|\mathbf{E}_2\rangle} \tag{5.21}$$

The coupling is only significant when the phase-matching condition is fulfilled, *i.e.* $\delta\beta_{12} \approx 0$. This is the case, for example, at the Bragg condition ($\beta_1 = -\beta_2 = \frac{\pi}{a}$) or at the MSB position (see Fig. 5.12):
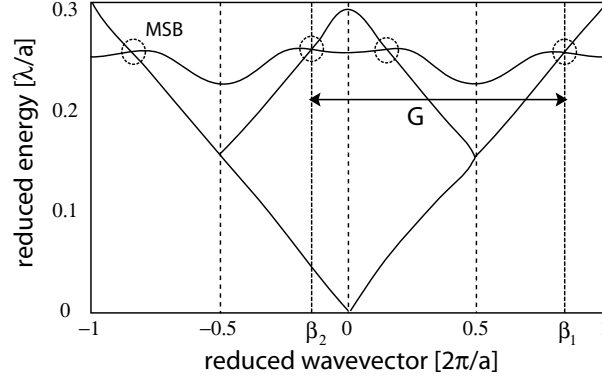
Figure 5.12: Sketch of the simplified band structure over two Brillouin zones showing the
fundamental mode both folded and unfolded and the higher-order mode.
[*Schéma de la structure de bande étendue sur deux zones de Brillouin simplifié.
On voit le mode fondamental replié et déplié et un mode supérieure.*]

In order to fulfil the requirement $\kappa_{12} = -\kappa_{21}^{\star}$, the coupling coefficient has to be made
symmetric:

$$\kappa_{12} = \frac{\omega^2}{2\sqrt{|\beta_1||\beta_2|}c^2} \frac{\langle \mathbf{E}_1|g_1(x)|\mathbf{E}_2\rangle}{\sqrt{\langle \mathbf{E}_1|\mathbf{E}_1\rangle\langle \mathbf{E}_2|\mathbf{E}_2\rangle}} \tag{5.22}$$

If all quantities are expressed in reduced units, distances in a, frequencies in $u = a/\lambda$
and wavevectors in $2\pi/a$, we can write:

$$\kappa_{12} = \frac{\pi u^2}{a\sqrt{|\beta_1||\beta_2|}} \frac{\langle \mathbf{E}_1|g_1(x)|\mathbf{E}_2\rangle}{\sqrt{\langle \mathbf{E}_1|\mathbf{E}_1\rangle\langle \mathbf{E}_2|\mathbf{E}_2\rangle}} \tag{5.23}$$

For perfect phase-matching ($\delta\beta_{12} = 0$), the CME system (5.19) has a compact analytical
solution. Assuming as boundary condition that for the forward wave $\tilde{C}_1(z = 0) = 1$ and
for the backward wave the amplitude at the end of the interaction region $\tilde{C}_2(z = L) = 0$.
The amplitudes as a function of the interaction length L is then given by [86]:

$$\tilde{C}_1(L) = 1/\cosh(\kappa_{12}L) \tag{5.24}$$

$$\tilde{C}_2(0) = -j \cdot \tanh(\kappa_{12}L) \tag{5.25}$$

An example depicting the squared amplitudes is shown in Fig. 5.13.

Eq. (5.23) allows one to directly calculate the coupling coefficient. Fig. 5.14 (a) and
(b) show the modulus of the magnetic field H_z of the fundamental and the fifth-order
mode, respectively. For the calculation of the overlap integral in Eq. (5.23), these fields
have to be converted in to electrical fields.

On the other hand, it can also be extracted from the dispersion relation of a single
W3 waveguide (see Fig. 5.15).

The relation between coupling coefficient and energy splitting (MSB width) is given
by [85]:

$$\Delta\omega = 2\left(\underbrace{\frac{c}{(n_{g1} + n_{g2})/2} \cdot \Delta\beta}_{\kappa_{12}}\right) \longrightarrow \kappa_{12} = \frac{1}{2}\Delta u_{12}\pi(n_{g1} + n_{g2}) = 0.154 \tag{5.26}$$

where the group indices of fundamental mode ($n_{g1} = 3.42$) and higher-order mode ($n_{g2} = 36$) can be extracted from the dispersion relation of a single W3 guide. The results of both methods are summarised in Table 5.1.

	by overlap integral	by dispersion relation
Δu_{12}	–	0.003
κ_{12}	0.128	0.154

Table 5.1: Contra-directional coupling coefficients explicitly calculated from the overlap integral on the one hand and extracted from the dispersion relation on the other hand.

[Coefficient de couplage contra-directionel calculé explicitement à partir de l'intégrale de recouvrement d'une côté et extrait de la relation de dispersion de l'autre côté.]
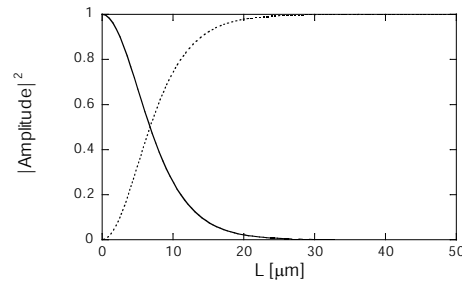
Figure 5.13: Example of contra-directional coupling without losses ($\kappa_{12} = 0.13 \, \mu\text{m}^{-1}$, $\delta\beta = 0$). The solid line and the dotted line depict $|\tilde{C}_1(L)|^2$ and $|\tilde{C}_2(0)|^2$, respectively.

[Exemple du couplage contra-directionnel sans pertes ($\kappa_{12} = 0.13 \, \mu\text{m}^{-1}$, $\delta\beta = 0$). La ligne solide et la ligne pointillée représentent respectivement $|\tilde{C}_1(L)|^2$ et $|\tilde{C}_2(0)|^2$.]
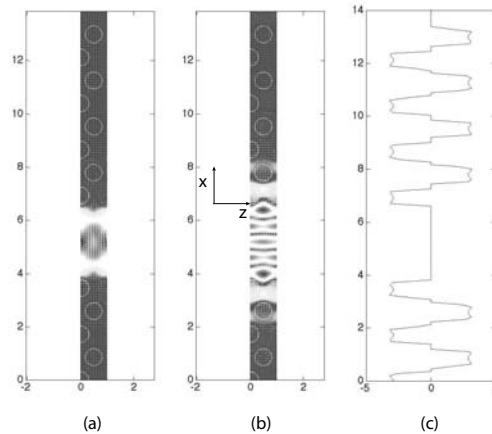
Figure 5.14: Explicit evaluation of the contra-directional coupling coefficient κ_{12} using Eq. (5.23): a) Modulus of the H_z field of the fundamental mode, b) of the higher-order mode (with 5 lobes), c) First Fourier component $g_1(x)$ of the dielectric map as defined in Eq. (5.18).

[Calcul explicit du coefficient de couplage contra-directionel κ_{12} en utilisant l'Eq. (5.23): a) Module du champ H_z du mode fondamental, b) du mode d'ordre supérieur (avec 5 lobes), c) Première composante de Fourier $g_1(x)$ de la carte diélectrique (comme définie dans l'Eq. (5.18).]

The overlap integral slightly underestimates the coupling coefficient κ_{12} with respect to the value extracted from the dispersion relation.

5.1.4.2   MSB-Transmission fit

An elegant way to determine experimentally the contra-directional coupling coefficient κ_{12} as well as the modal propagation losses has been proposed by S. Olivier *et al.* [88]. The method is based on the CME and considers the transmission spectrum around the MSB energy and fits the typical transmission dip. In order to perform the fit of the MSB-transmission dip, one just takes the formulae from section 5.1.4.1, *i.e.*

$$\begin{pmatrix} \frac{d\tilde{C}_1}{dz} \\ \frac{d\tilde{C}_2}{dz} \end{pmatrix} = \begin{pmatrix} -j\delta\beta_{12} - \alpha_1 & -j\kappa_{12} \\ +j\kappa_{12}^{\star} & j\delta\beta_{12} + \alpha_2 \end{pmatrix} \cdot \begin{pmatrix} \tilde{C}_1 \\ \tilde{C}_2 \end{pmatrix} \tag{5.27}$$

$$\tag{5.28}$$

At the MSB-position the phase-matching is perfectly fulfilled.

$$\delta\beta_{12} = \frac{1}{2}(\tilde{\beta}_1 - \tilde{\beta}_2 - G) = 0 \tag{5.29}$$

where $\tilde{\beta}_1 = \beta_1 + \Delta\beta_1 > 0$ and $\tilde{\beta}_2 = \beta_2 + \Delta\beta_2 < 0$. In order to model the transmission-dip, the CMEs have to be solved for different energy values around u_{MSB}, which means that β_1 and β_2 and the detuning parameter $\delta\beta_{12}$ vary as a function of Δu (see Fig. 5.15)

$$\tilde{\beta}_1 = \beta_1^{MSB} + \Delta u \cdot n_{g1}$$
$$\tilde{\beta}_2 = \beta_2^{MSB} + \Delta u \cdot n_{g2} \tag{5.30}$$
$$\delta\beta_{12} = \frac{1}{2}\Delta u \cdot (n_{g1} - n_{g2}) \tag{5.31}$$
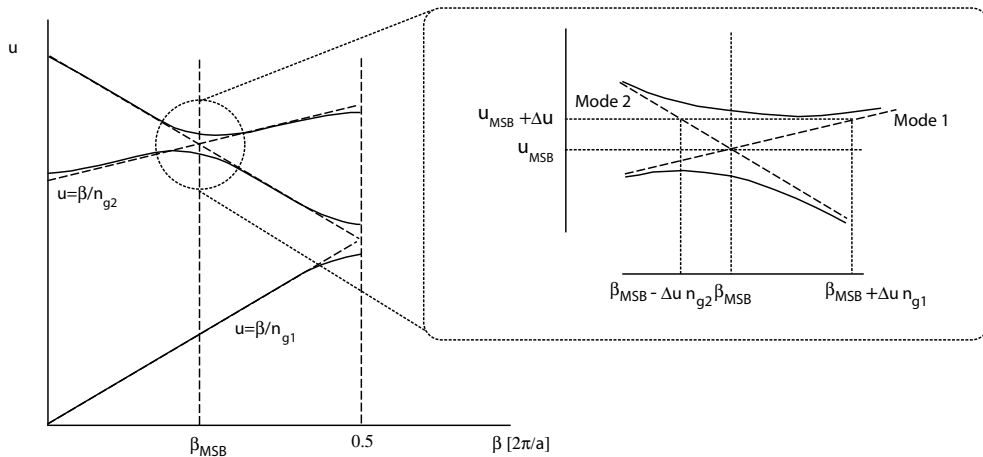
Figure 5.15: Sketch of the dispersion relation of a W3 waveguide, showing the relationship between Δu and $\Delta\beta$ [56].
[Schéma des relations de dispersion d'un guide W3, montrant la relation entre Δu et $\Delta\beta$ [56].]

Thus for each individual u value, a linear differential equation system of the form $\frac{d}{dz}\Phi(z) = [M(u)]\Phi(z)$ with constant coefficients has to be solved. This system is usually solved by diagonalisation, *i.e.*

$$\frac{d}{dz}\phi(z) = VDV^{-1}\phi(z) \qquad \rightarrow \qquad \frac{d}{dz}V^{-1}\phi(z) = DV^{-1}\phi(z)$$

$$\rightarrow \qquad \frac{d}{dz}\rho(z) = D\rho(z) \quad \text{with} \quad \rho = V^{-1}\phi(z) \tag{5.32}$$

where D is a diagonal matrix. This leads to a decoupled system which can easily be solved:

$$\rho(z) = \begin{pmatrix} r_1 e^{d_{11}\cdot z} \\ r_2 e^{d_{22}\cdot z} \end{pmatrix} \qquad \text{and} \quad r = \begin{pmatrix} r_1 \\ r_2 \end{pmatrix} = V^{-1}\phi_0 \tag{5.33}$$

The solution $\rho(z)$ can then be back-transformed to $\phi(z) = V\rho(z)$. The experimental transmission dip due to the MSB is usually more pronounced for shorter guides (30 a) than for longer guides (90a) (see section 5.1.1.4). Since the MSB is an interference effect where the contributions from each period add up constructively, it should get stronger with increasing guide length. However, this is only the case when absorption is zero (see Fig 5.16(a)). But as soon as absorption comes into play this the MSB broadens and the transmission falls, especially for very large guides (see Fig 5.16(b)). Additionally the MSB may be sensitive to fluctuations in the hole size, which are more developed in longer waveguides.
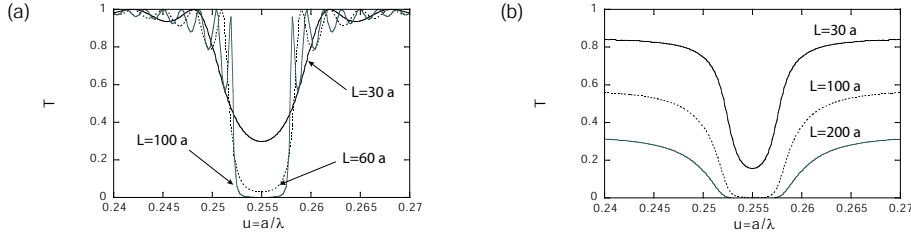
Figure 5.16: Calculated MSB transmission for guides of different length. a) no propagation losses (parameters: $\kappa_{12} = 0.15\ \mu\text{m}^{-1}$, $\alpha_1 = 0$, $\alpha_2 = 0$, $a = 270\ \text{nm}$), b) with propagation losses (parameters: $\kappa_{12} = 0.15\ \mu\text{m}^{-1}$, $\alpha_1 = 0.01$, $\alpha_2 = 0.1$, $a = 270\ \text{nm}$).

[Transmission de la mini-bande calculée pour des guides de différentes longeurs. a) sans pertes (paramètres: $\kappa_{12} = 0.15\ \mu\text{m}^{-1}$, $\alpha_1 = 0$, $\alpha_2 = 0$, $a = 270\ \text{nm}$), b) avec pertes (paramètres: $\kappa_{12} = 0.15\ \mu\text{m}^{-1}$, $\alpha_1 = 0.01$, $\alpha_2 = 0.1$, $a = 270\ \text{nm}$).]

	$L = 100$ a	$L = 200$ a
u_{MSB}	0.255	0.253
κ_{12} $[\mu\text{m}^{-1}]$	0.127	0.100
α_1 $[\mu\text{m}^{-1}]$	0.0369	0.0147
α_2 $[\mu\text{m}^{-1}]$	0.266	0.473

Table 5.2: Fit parameters of the coupled mode fit in Fig. 5.17

[Paramètres de la courbe théorique dans la Fig. 5.17 calculés avec la théorie des modes couplés.]

The fit works well for both waveguide lengths. One notes that the MSB position is slightly shifted in energy, which is due to a variation in the air-filling factor. The
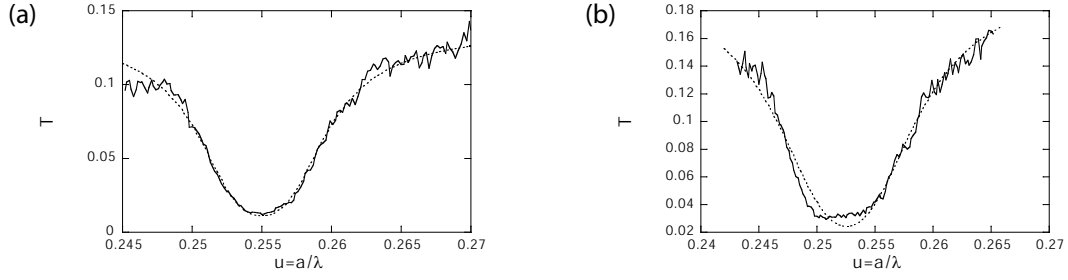
Figure 5.17: Example of the coupled mode fit of the MSB transmission dip of the W3
normalisation guides (The fitted values are listed in Table 5.2). a) $L = 100$ a,
b) $L = 200$ a.

*[Exemple de la transmission du MSB des guides de normalisation (W3) avec la
courbe théorique calculée selon la théorie des modes couplés (Les paramètres
sont énumérés dans le tableau 5.2). a) $L = 100$ a, b) $L = 200$ a.]*

coupling strength in the case of $L = 100$ a is about 30 % higher than in the case of
$L = 200$ a. The losses of the fundamental mode are about 7-30 times smaller than those
of the order five mode, depending on the guide length. The value $\kappa_{12} = 0.127\,\mu\text{m}^{-1}$ for
the 100-row-long W3 waveguide agrees well with the value $\kappa_{12} = 0.128$ calculated by
the overlap integral and $\kappa_{12} = 0.154$ from the dispersion relation (see Table 5.1). The
fit procedure seems to be more robust for κ_{12} than for the absorption coefficients. The
absorption of the fundamental mode for the guide with $L = 100$ a is $\alpha_1 = 147\ \text{cm}^{-1}$,
which is very close to the usual absorption value of $150\ \text{cm}^{-1}$ for a W3 waveguide
including the waveguide and the QD absorption.

5.2 The hybride waveguide

5.2.1 Description of the structure

The hybrid waveguides have been fabricated with different widths which correspond approximately to the widths of the normal waveguides W1, W2 and W3 (see Fig. 5.18). The hybrid guides, labelled HY1, HY2 and HY3 according to 1, 2 and 3 missing ΓM rows of holes are fabricated in three different lengths (30 a, 60 a and 90 a) in order to allow for loss measurements.
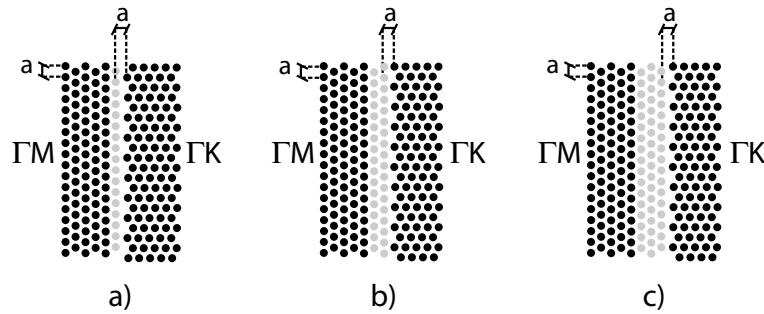
Figure 5.18: Sketch of hybrid waveguides of different widths: a) 1 row ΓK (HY1), b) 2 rows ΓK (HY2), c) 3 rows ΓK (HY3)
[Aperçu des guides hybrides de largeur différentes: a) 1 rangée ΓK (HY1), b) 2 rangées ΓK (HY2), c) 3 rangées ΓK (HY3)]

The actuals widths of for HY1, HY2 and HY3 are $(1+\frac{\sqrt{3}}{2})a$, $(1+\sqrt{3})a$ and $(1+3\frac{\sqrt{3}}{2})a$, respectively.

Fig. 5.19 shows a scanning electron micrograph of an HY1 guide of length 30 a. The measurements in this chapter have been performed on the sample labelled GWW5-2/part A.

5.2.2 Measurement results

Fig. 5.20 shows the transmission of a HY1 waveguide for three different lengths.

Similar to the standard W1 the transmitted signal by the HY1 is weak, which is due to the small coupling efficiency from the plane wave into the waveguide mode on
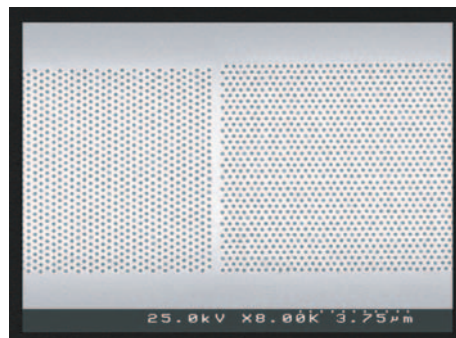
Figure 5.19: Scanning-electron microscopy (SEM) micrograph of a hybrid guide of width 1 row (HY1) and a length of 30 periods
[Image MEB d'un guide hybride HY1 de 30 périodes de longueur.]

the one hand and due to higher propagation losses, related to the high confinement, on
the other hand. The shaded region indicates the position of the air-band of the bulk
PhC for the ΓM direction. The occurrence of transmission above the ΓM air-band at
$u = 0.285$ is due to the fact that the wavevector of the lower-order propagating modes
is rather directed in the ΓK direction for which the air-band edge is situated at $u = 0.3$
and the mode is still guided. Furthermore the low-order modes also experience the
effect of index-guiding.

Figs. 5.21 and 5.22 show that in opposition to the expectation that the transmission
of hybrid guides should be MSB-free, there are plenty of dips and features in the spectra.

The HY2 features some transmission dips with the typical MSB form.
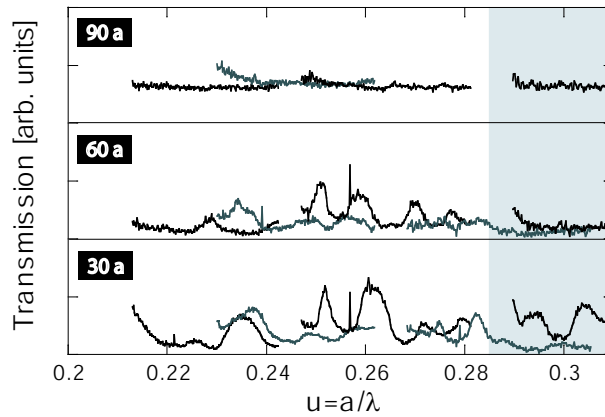
Figure 5.20: Transmission spectra of a HY1 hybrid waveguide of length 30 a, 60 a and 90 a.
The shaded region indicates the position of the air-band in ΓM direction.
*[Spectres de transmission d'un guide hybride HY1 de longueur 30 a, 60 a et
90 a. La région ombrée indique la position de la bande air direction ΓM .]*
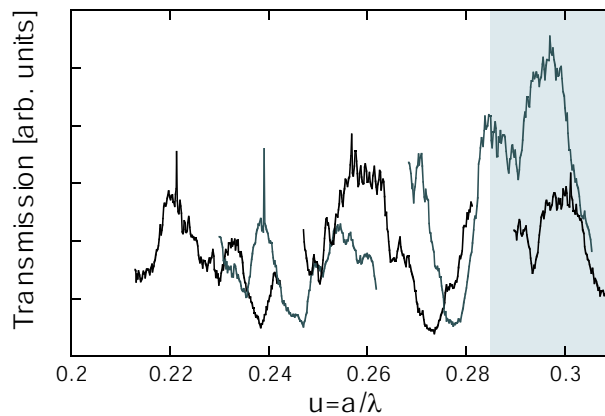
Figure 5.21: Transmission spectrum of a HY2 hybrid waveguide of length 60 a. The shaded
region indicates the position of the air-band in ΓM direction.
*[Spectre de transmission d'un guide hybride HY2 de longueur 60 a. La région
ombrée indique la position de la bande air direction ΓM .]*
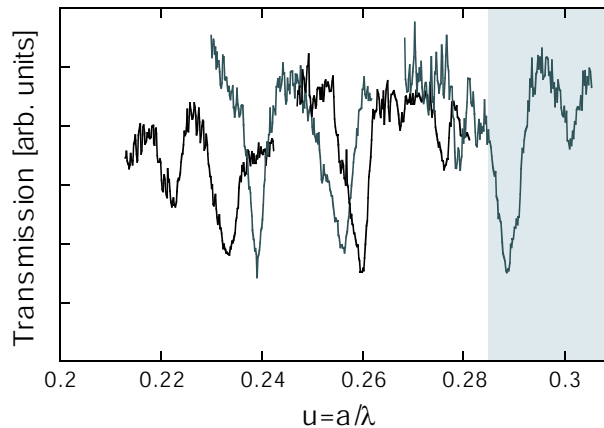
Figure 5.22: Transmission spectrum of a HY3 hybrid waveguide of length 60 a. The shaded region indicates the position of the air-band in ΓM direction.
[*Spectre de transmission d'un guide hybride HY3 de longueur* 60 a. *La région ombrée indique la position de la bande air direction* ΓM *.*]

However, the HY3 features the largest transmission the most pronounced transmission dips and we will therefore concentrate on this structure in the following sections.

As can be seen in the experimental spectra of HY1, HY2 and HY3 (see Figs. 5.20, 5.21, 5.22), the transmission of hybrid guides is not MSB free and features a great number of transmission dips. When normalising waveguides of different length, the energy region around MSBs should be excluded or analysed only with greatest care. The first reason is that the size of the MSB dip does not scale linearly with length. The second is that the normalisation procedure divides *intensity* spectra and the MSB is an interference effect, thus depending on the *amplitude*.

Therefore the usual way of normalisation, by deducing the extinction coefficient from the measurement of guides of different length (see section 5.1.1.3), cannot be applied in this case. The spectra presented in this section are normalised only by the PL of the un-patterned region and are therefore in arbitrary units.

5.2.3 Discussion

In order to provide accurate modelling of the hybrid waveguides, knowledge about the local filling factor is required which fluctuates between different periods and sample positions. The f values, deduced from the fit of the MSB position of W3 waveguides (see section 5.1.3) that are located in the vicinity of the hybrid waveguides, yields the values in Table 5.3.

a	$L = 30$ a	$L = 60$ a	$L = 90$ a
270	0.35	0.31	–
290	0.4	0.39	0.31

Table 5.3: Air-filling factor of different periods and different guide lengths deduced from the MSB position.
[*Facteur de remplissage des périodes et de guides de longueurs différentes déduit de la position de la mini-bande.*]
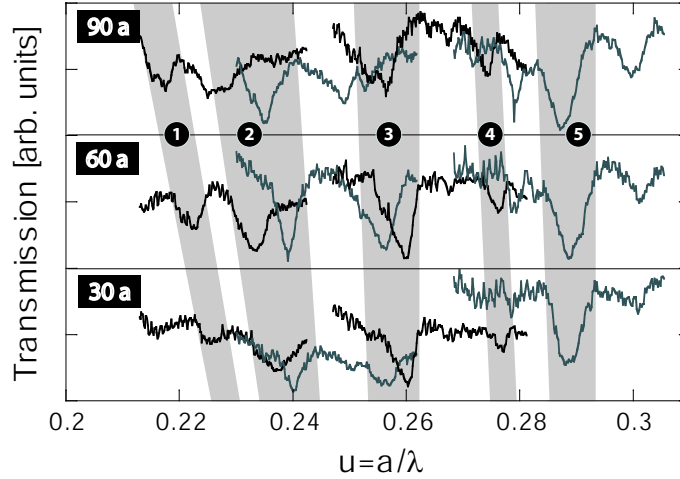
Figure 5.23: There are five major MSB dips in the transmission spectra of the HY3 guides
which are labelled from 1 to 5.
*[Il existe cinq mini-bandes dans les spectres de transmission du guide HY3 qui
sont numérotées de 1 à 5.]*

All simulations for hybrid guides have been performed with an air-filling factor of
$f = 0.35 \pm 0.04$.

In this section we will analyse the experimental results in order to understand the
physical reason for the occurrence and position of the MSB-like transmission dips.

In the case of HY3 five main transmission dips can be identified (see Fig. 5.23).
Their energy position and form fluctuates between different periods and lengths. The
energy shift between different periods is due to fluctuations in the air-filling factor and
to dispersion effects. The difference between different guide lengths might stem from
proximity effects during the e-beam patterning.

		Transmission dip n°				
a	L [a]	1.	2.	3.	4.	5.
250	30	0.226	0.237	–	–	–
	60	0.222	0.233	–	–	–
	90	0.217	–	–	–	–
270	30	–	0.240	0.257	–	–
	60	–	0.239	0.256	–	–
	90	–	0.235	–	–	–
290	30	–	–	0.260	0.277	–
	60	–	–	0.260	0.276	–
	90	–	–	0.256	0.274	–
315	30	–	–	–	–	0.289
	60	–	–	–	–	0.289
	90	–	–	–	–	0.288
Average [a/λ]		0.222 ± 0.005	0.237 ± 0.003	0.258 ± 0.002	0.276 ± 0.002	0.289 ± 0.001

Table 5.4: Experimental transmission dip positions deduced from Fig. 5.23
[Liste des positions des creux de transmission déduit de la Fig. 5.23.]

The dip positions have been extracted from Fig. 5.23 and been listed for different periods and lengths. For each transmission dip the arithmetic average energy position has been calculated (see Table 5.4).

MSB positions calculated by FDTD One tool for verification of the experimental results is to perform a numerical experiment by means of the 2D finite difference time domain (FDTD) method. This method provides transmission spectra for the direct comparison (see Fig. 5.24) as well as images of the field distribution.
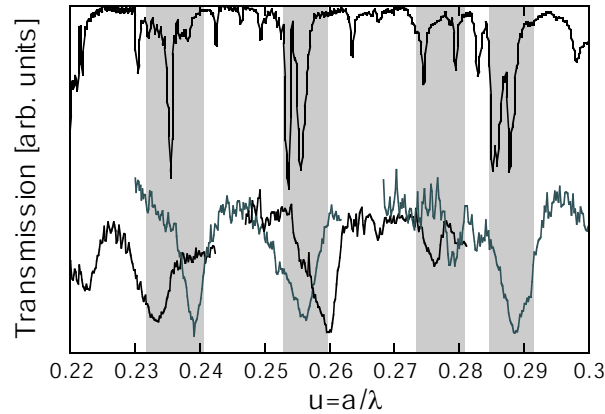
Figure 5.24: Comparison between experiment (lower curve) and FDTD (upper curve) for the HY3 guide. The FDTD spectrum has been calculated for $L = 60$ a.
[Comparaison entre l'expérience (courbe du bas) et le calcul FDTD (courbe du haut) pour le guide HY3. Le spectre FDTD a été calculé pour $L = 60$ a.]

The FDTD calculations showed the existence of transmission dips for all types of hybrid guides. Fig. 5.24 shows a good agreement between the experimental spectrum (lower curve) and the FDTD calculation (upper curve). The shaded regions depict the experimentally observable MSBs.

Table 5.5 provides a comparison between the experimentally deduced MSB position and the FDTD calculation. All five peaks agree within the error bars.

Transmission dip n°	Exp.	FDTD
1	0.222 ± 0.005	0.220 ± 0.001
2	0.237 ± 0.003	0.236 ± 0.0004
3	0.258 ± 0.002	0.256 ± 0.001
4	0.276 ± 0.002	0.275 ± 0.001
5	0.289 ± 0.001	0.287 ± 0.001

Table 5.5: Comparison between the experimental MSB position (result from Table 5.4) and the FDTD calculation (see Fig. 5.24 shows a good agreement.
[La comparaison entre la position expérimentale de la mini-bande (résultat de la Table 5.4) et le calcul FDTD montre une bonne correspondance.]

The magnetic field maps inside a HY3 waveguide are depicted in Fig. 5.25 for two different excitation energies, one lying outside and one inside a transmission dip. In the latter case one can clearly see that a part from the fundamental mode is converted into higher-order modes.
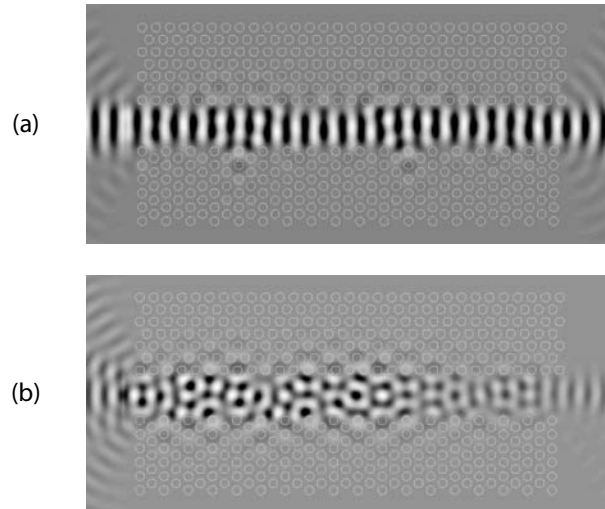
Figure 5.25: Magnetic field distribution inside HY3 waveguide calculated by FDTD. a) outside MSBs ($u = 0.226$), b) inside an MSB ($u = 0.256$).
[*Champ magnétique à l'intérieur du guide HY3. a) en dehors des mini-bandes ($u = 0.226$), b) à l'intérieur d'une mini-bande.*]

The FDTD calculation can prove the existence of transmission dips but does not explain the underlying physics. In the next section the positions of the MSBs are investigated in detail with the PWE method.

MSB positions calculated by PWE As discussed in section 5.1.2, the MSBs appear in the dispersion relation as anti-crossing between different bands. Due to the incommensurable periods a and $\sqrt{3}a$ in propagation direction the hybrid waveguides cannot be described by a supercell.

One possible explication of the persistence of MSB dips is to say that the feedback and thus the MSB is exclusively due to the periodicity of one side of the guide and that the PhC on the other side behaves as a mirror which provides waveguiding. This can be incorporated into a supercell approach by defining a guide which is half PhC (either ΓM or ΓK) and half ridge waveguide (see Fig. 5.26). This makes even more sense since the fundamental mode in the considered air-hole structure is anyway index-guided, and thus the PhC and the ridge border behave similarly.

Presumably the penetration depth for a PhC border and a ridge border are different, thus one does not exactly know the position of this virtual ridge interface and in addition the position is likely to vary as a function of energy. Therefore the MSB positions for both ΓM and ΓK symmetry are plotted as a function of the geometrical width as adjustable parameter (see Fig. 5.27). The shaded regions correspond to the experimental MSB positions according to Table 5.4.

Due to the approximations discussed above, the model is not able to yield the exact energy positions of the MSBs. However, the model helps to test the physical idea and to understand occurrence of the additional MSBs and can predict their number and relative widths quite well.

An alternative approach is to simulate the real hybrid waveguide without ridge by exploiting the superperiodicity, *i.e.* by taking a supercell that is larger than one unit cell in propagation direction one can approximate the ΓK period by a rational number.

Due to the limitations on the number of plane waves, the supercell width has been chosen 7 periods and the ΓK period of $\sqrt{3}a$ has thus been approximated by $7/4 \cdot a$, which corresponds to a relative error of 1 %. This superperiodicity has the drawback that the whole band structure is projected on a Brillouin zone that is several times smaller thus leading to a dense artificial bandfolding. Fig. 5.28(a) and (b) show the supercell for the calculation of this approximated hybrid waveguide. The corresponding banddiagram is shown in part in Fig. 5.28(c). The fundamental mode is marked by a thick grey line and the anti-crossings are evidenced by circles.

In Fig. 5.29 the MSB position deduced from the approximated calculation as described above is compared with the experimental spectrum (lowest curve) and the 2D FDTD calculation (middle curve). Each square corresponds to a MSB predicted by the PWE and the lengths of the stems are proportional to the widths of the MSBs. The
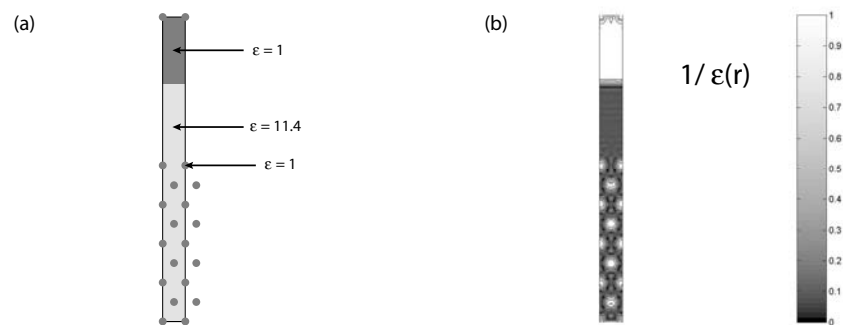
Figure 5.26: Dielectric map of a guide of PhC type on one side and of ridge type on the other side. a) sketch of the supercell b) Reconstruction of the inverted and truncated dielectric map.
[Carte diélectrique d'un guide de type cristal photonique d'une côté et du type ruban de l'autre côte. a)Aperçu de la supercellule, b) Reconstruction de la carte diélectrique inversée et tronquée.]
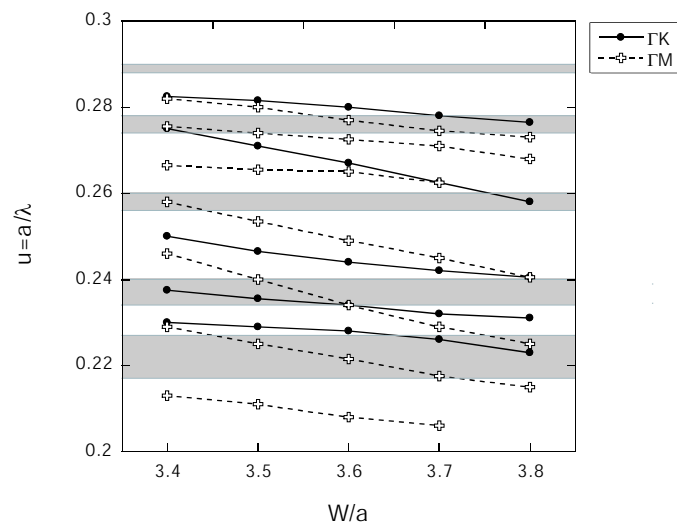
Figure 5.27: MSB position as a function of the guide width for the structure described in Fig. 5.26.
[Position de la mini-bande en fonction de la largeur du guide pour la structure décrite dans la Fig. 5.26.]
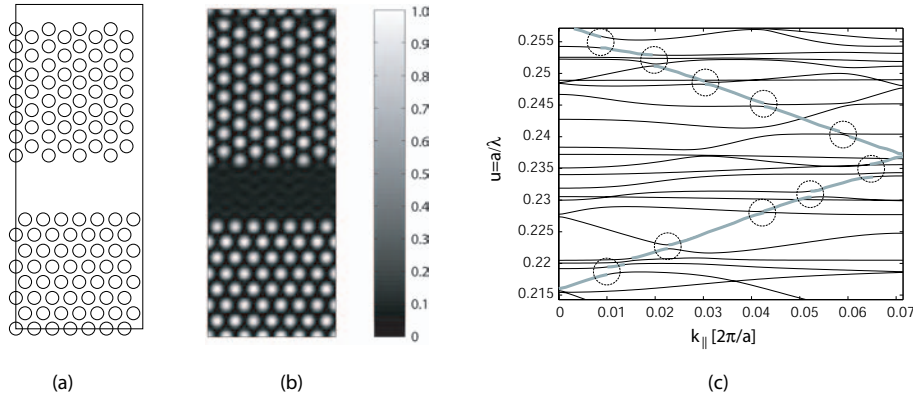
Figure 5.28: PWE calculation of the periodically approximated HY3 waveguide. a)
Schematic representation of the supercell, b) Representation of the truncated
reciprocal dielectric map, c) Part from the band structure.
*[Calcul d'ondes planes du guide HY3 avec une périodicité approximée. a)
Schéma de la supercellule, b) Représentation de la carte diélectrique tronquée,
c) Section de la structure de bande.]*

overall agreement for the main MSBs is good.
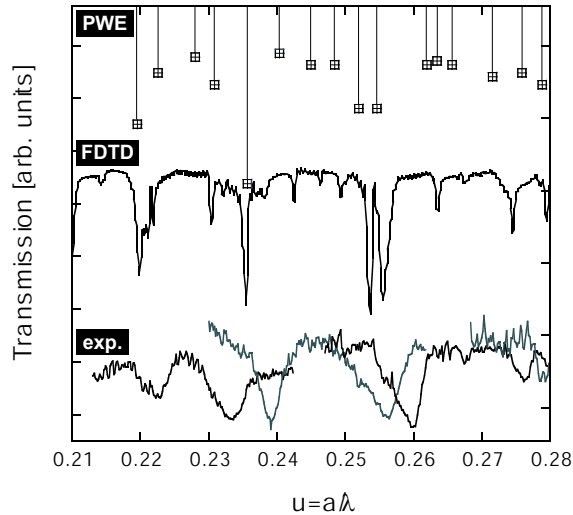
Figure 5.29: MSB positions calculated by PWE in comparison with FDTD calculation and
experiment. The length of the stems are proportional to the MSB widths.
*[Mini-bandes calculées par la méthode des ondes planes en comparaison avec
le calcul FDTD et l'expérience (longueur des barres est proportionnelle à la
largeur des mini-bandes).]*

By considering the eigenmodes calculated by PWE one finds a similar behaviour in
the fields as in the FDTD calculation. The field for both cases have been calculated at
exactly the same energies (compare Fig. 5.25). In the case of Fig. 5.30(b) the actual
field at $u = 0.254$ is a superposition of the fields from the lower and upper branch.

In conclusion the PWE calculation with the superperiodicity reproduces very well
the MSB positions in the experiment.

It is worth pointing out that the various modeling techniques (especially the FDTD
method) have not been available at the moment of the sample design and that the
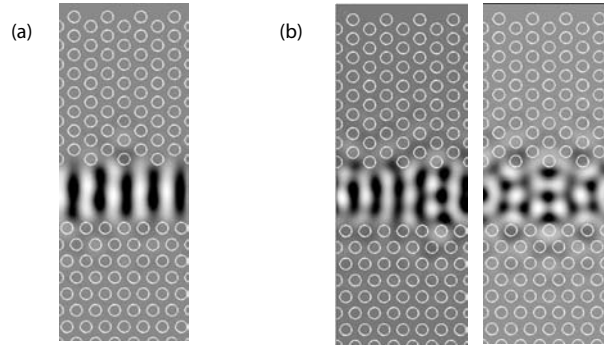
Figure 5.30: Eigenmodes of the supercell of the approximated HY3 waveguide (parameters: $f = 0.35$, $\varepsilon_{\text{sub}} = 11.4$). a) fundamental mode far from anti-crossing ($k = 0.0348$, $u = 0.226$), b) lower and upper branch of anti-crossing ($k = 0.001$, $u = 0.254$ and 0.256).
[Modes propres de la supercellule du guide HY3 approximée (paramètres: $f = 0.35$, $\varepsilon_{sub} = 11.4$). a) mode fondamental loin de l'anti-croisement ($k = 0.0348$, $u = 0.226$), b) branche inférieure et supérieure de l'anti-croisement ($k = 0.001$, $u = 0.254$ et 0.256).]

structure has been fabricated with the aim to test a conceptual idea rather than to have a specific application in view.

5.3 Conclusion on hybrid waveguides

Hybrid waveguides consisting of a ΓM and a ΓK border of different widths and lengths have been measured by means of the ILS technique. The original expectation of MSB-free PhC waveguides has not been met. On the contrary, the transmission spectra feature an unexpected variety of transmission dips. The occurrence of these MSB-like features has been validated by FDTD and a deeper understanding could be gained by applying the PWE method. From the practical point of view there is no obvious direct application of hybrid guides. However, they may be considered as a first step in exploiting multiple periodicity.

Chapter 6

Bends and splitters based on low symmetry-order (LSO) cavities

In the context of dense optical integration, especially for an 'all PhC' approach, PhC-based bends and splitters play a key role in linking the different building blocks on a monolithically integrated optical chip. In a triangular lattice the canonical bend deflects the light by an angle of 60 degrees. The main requirements on a bend are low-loss, low-reflection and broad-bandwidth. The state-of-the-art in transmission of W3-based waveguide bends is $70\,\%$, within a bandwidth of $3\,\%$, *e.g.*, $30\,\mathrm{nm}$ at $1\,\mu\mathrm{m}$ [89]. Ideas to improve the bend transmission, like the introduction of corner mirrors or open low quality factor cavities, have been extensively studied in classical integrated optics [90] and have been adopted to PhCs and studied as well as cavity resonant bends [91]. The generic cavity resonant bend (CRB) or cavity resonant splitter (CRS) consists of a cavity that is connected to a set of input and output waveguides supporting a single transmission band for the case of a single mode waveguide or multiple transmission bands as, for example, is the case for the W3 waveguide. The resonant cavity is usually multi-mode. The coupling strength can be modified by varying the thickness of the barrier between cavity and waveguide, thus modifying the coupling and the quality factor of the cavity.
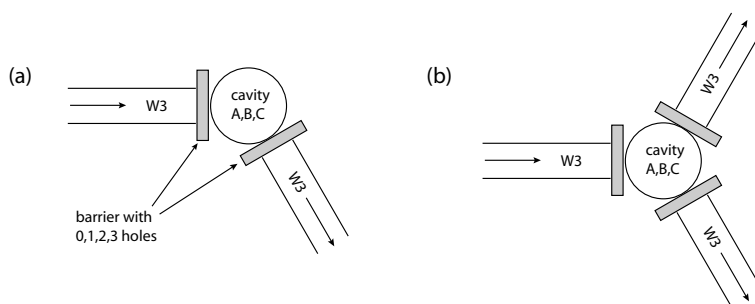
Figure 6.1: Basic illustration of the bend and splitter configuration. Different combinations of cavity types (A, B, C) and coupling coefficients between waveguides and cavity (# holes per barrier) have been tested.
[Schéma des différentes configurations de virage et diviseur basé sur des cavités. Différentes combinaisons de types de cavités (A, B, C) et différents coefficients de couplage entre les guides et la cavité (# trous dans la barrière) ont été testés.]

In this chapter CRBs and CRSs based on low-symmetry-order (LSO) cavities are studied both experimentally and theoretically.

6.1   Structure layout

In this study we have considered bends and splitters based on three different types of asymmetric cavities denominated as A, B and C. For each cavity there is a sub-design depending on the number of holes (n) in the barrier between cavity and waveguide ranging from three to zero with decreasing confinement (X-Sn) (see Fig. 6.2).

The waveguides consist of three missing rows of holes (W3) and each arm is 30 periods (ΓK rows) long.
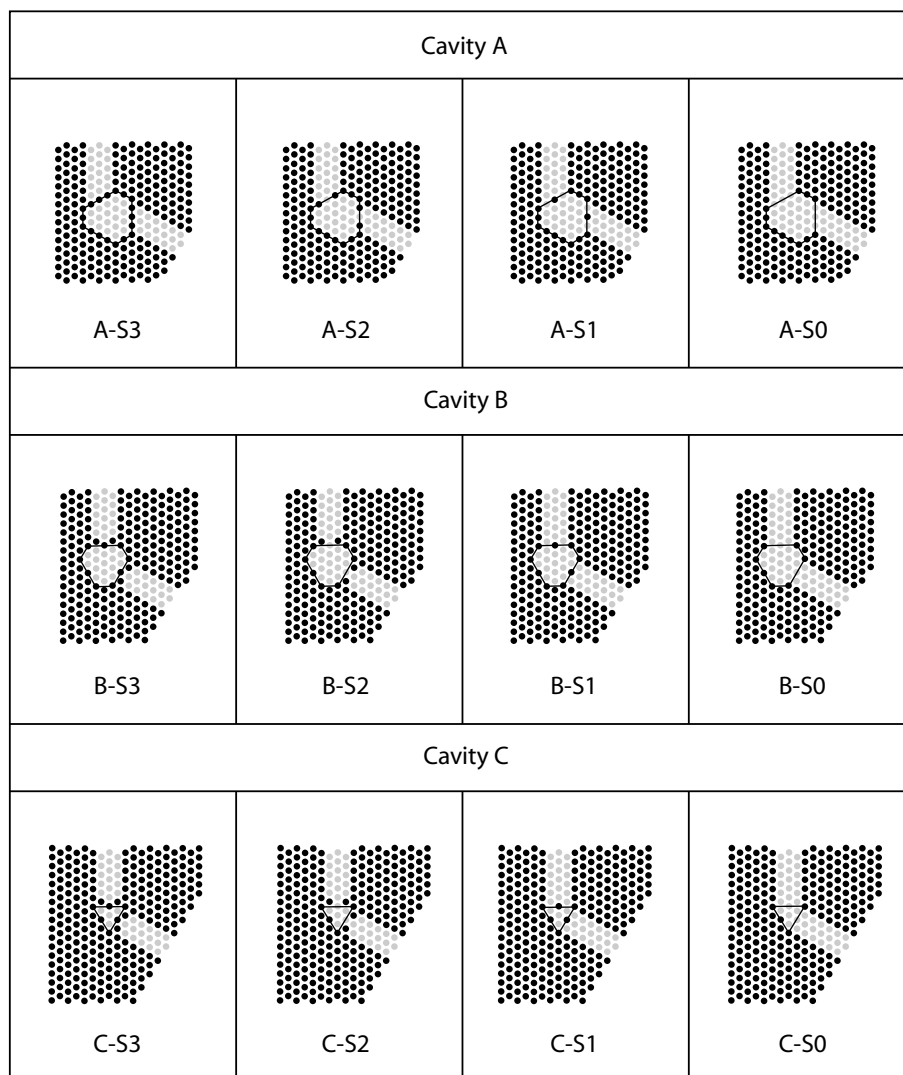
Figure 6.2: Sketch of the different bend designs based on three different asymmetric cavity types with varying coupling coefficient.
[Aperçu des différents virages basés sur trois différents types de cavités asymmetriques avec un coefficient de couplage variable.]

For each bend design there exists the corresponding symmetric splitter with a 120°

angle between the three connecting arms (see Figs. 6.3 and 6.4).
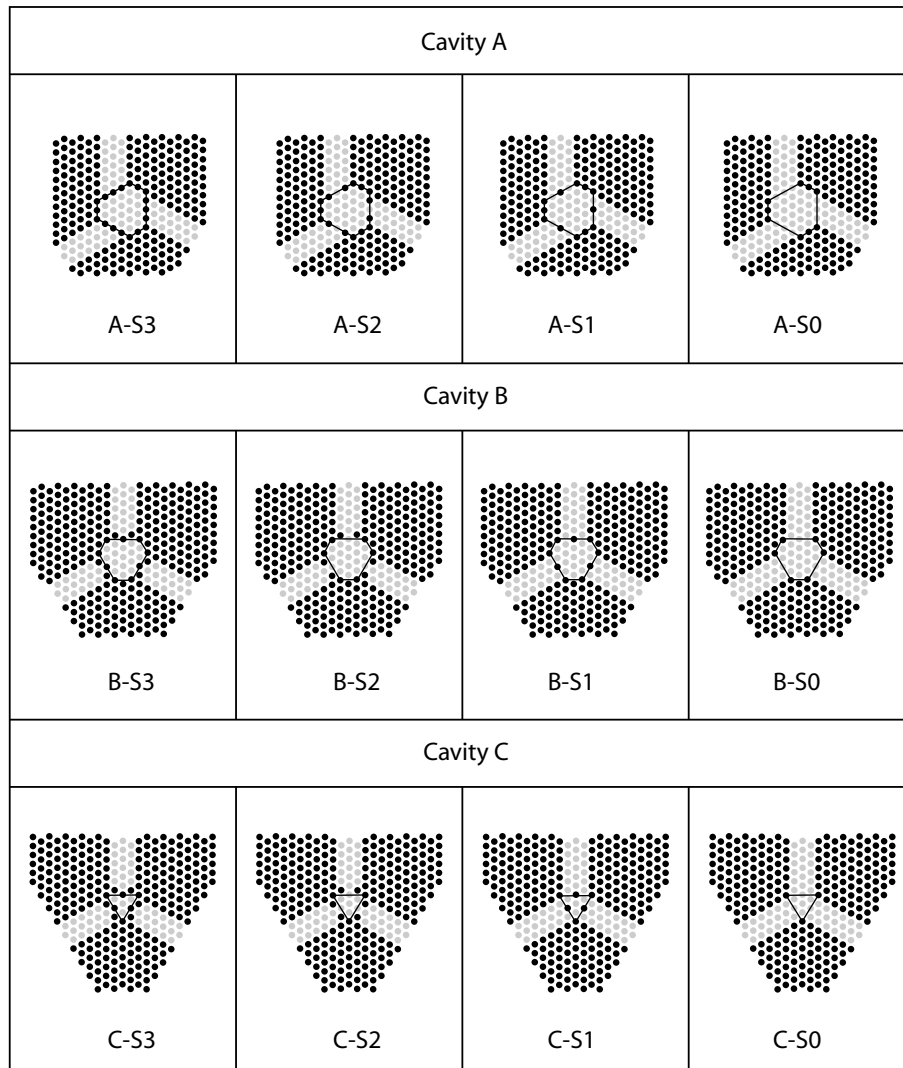
Figure 6.3: Sketch of the different splitter designs based on three different asymmetric cavity types with varying coupling coefficient.
[Aperçu des différents diviseurs basés sur trois différents types de cavités asymmetriques avec un coefficient de couplage variable.]
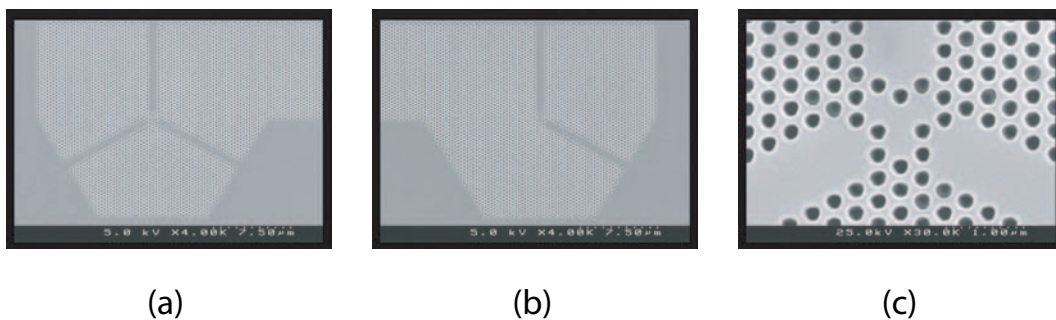
Figure 6.4: Scanning-electron microscopy (SEM) micrograph of design C: a) splitter, b) bend, c) close-up of cavity C-S3.
[Image MEB de structure C: a) diviseur, b) virage, c) zoom de la cavité C-S3.]

The straight guides are 30 lattice periods long. All the splitter designs have perfect threefold rotational symmetry and therefore should have equal splitting ratios. The cavity A is a bit different from the other two cavities regarding the fact that the centre of rotation does not coincide with the crossing point of the three waveguide axes. The waveguides impinge at an angle of 30° on the cavity, which might lead to an asymmetric splitting ratio between the two output ports.

6.2   Experimental results

The measurements in this chapter have been performed on the sample labelled 'GWW5-2/part B'.

6.2.1   Principle of measurement

Different kinds of measurements can be carried out on cavity bend and cavity splitter structures in principle. One may be interested in the total transmission of the structure, including the coupling at the waveguide ends, the two straight waveguide transmissions and the bend transmission. It is difficult to get the normalised total transmission out of a single bend structure, because there are too many unknown parameters: First of all the coupling efficiency in and out-of the waveguide is not known, then one should have identified the wavelength dependence of the source $S(\lambda)$ and the collection efficiency at the facet. The spectral form of the source can be eliminated by dividing the total spectra by a reference spectrum (Ref 1) taken in an unpatterned region at the distance D from the facet(see Fig 6.5). This reference has a different collection efficiency than a signal having travelled through a waveguide (e.g. Ref 1) since their respective virtual sources are situated at different distances from the facet. After the normalisation with Ref 1, however, the total transmission is still in arbitrary units.

If one is interested in bend transmission (without waveguide transmission) the best way is to normalise the total transmitted spectrum by the signal of a straight reference guide which has twice the length of the single arm. By keeping the excitation distance from the guide entry and the distance from the structure to the facet constant, almost all unknown parameters can be eliminated and one obtains the bend transmission in absolute units:

$$\frac{T_{\text{tot}}}{T_{\text{straight}}} = \frac{T_{30}T_{\text{bend}}T_{30}}{T_{60}} \approx \frac{T_{30}T_{30}T_{\text{bend}}}{T_{60}} \approx \frac{T_{60}T_{\text{bend}}}{T_{60}} = T_{bend} \qquad (6.1)$$

As already noted in section 5.2.2, the normalisation based on the division of intensity spectra may neglect phenomena that depend on the phase. For the wavelength regions where the losses scale linearly with the length of the waveguide, the transmission of a 60-row straight section is the square of the 30-row transmission. However, in the frequency region where mode-conversion and strong scattering occurs (e.g. near the mini-stopband (MSB)) the signal is sensitive to symmetry breaking. For example, the insertion of a cavity into a straight waveguide may cause a mode conversion at the bend from the fundamental mode to higher order modes that possess higher propagation losses and different coupling strengths.

The normalisation of the splitter transmission is totally analogous to the normalisation of the bend transmission.

Since there are no light blockers between the structures a rather large excitation distance of $d_e = 39\,\mu$m from the waveguide entry has been chosen in order to prevent direct light bypassing the structure and arriving below the critical angle of $\alpha_c = 17.2\,^\circ$ on the facet (see Fig. 6.5).
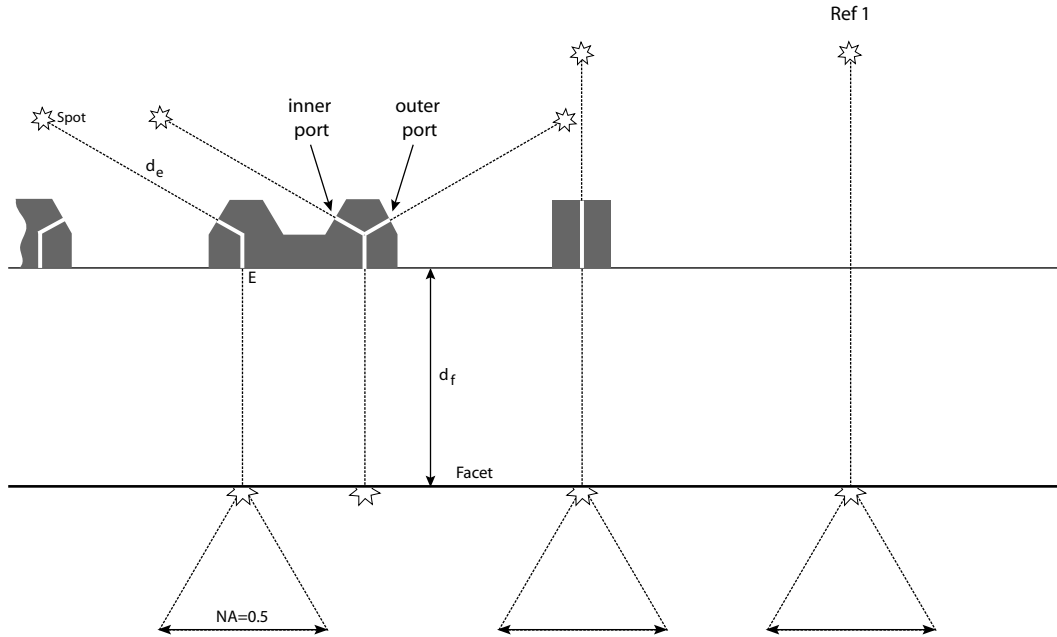

Figure 6.5: Sketch of the measurement setup (to scale). The total transmission through the bends and splitters can be normalised by the straight waveguide transmission of 60 rows in order to obtain the isolated bend and splitter transmission, respectively.

[Aperçu de la méthode de mesure (à l'échelle). La transmission totale à travers le virage ou le diviseur peut être normalisée par la transmission d'un guide droit de longeur 60 rangées pour obtenir la transmission isolée du guide ou du diviseur.]

For the focalisation and light collection the standard procedure for waveguides was applied (see section 5.1.1).

The measured transmission value proved to be independent whether the splitter was excited from the inner port or the outer port as expected from theory. The splitter measurement was performed on the inner port since the parasitic light was shielded by the structure itself and the splitter signal was therefore more visible (see Fig. 6.6).

6.2.2 Bend transmission

The first thing to do when normalising bend and splitter transmissions is to determine position and width of the MSB of the 60-row straight waveguide, since this frequency region has to be excluded or interpreted only with great care (see section 5.2.2). The MSB is situated at $u = 0.254$ and has a width, taking into account dispersion effects between different periods, of $\Delta u = 0.1$.
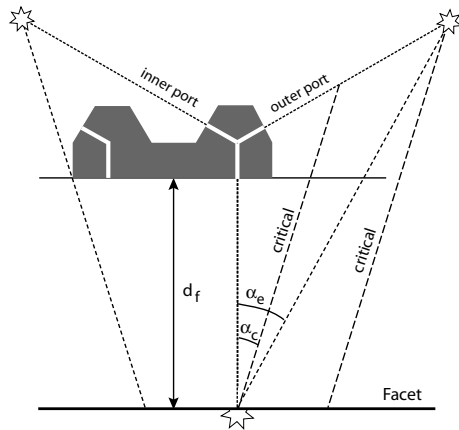
Figure 6.6: The splitter structure (in scale) can either be excited from the inner or the outer part. In the former case the structure acts as an additional shield to block parasitic light.
[Le diviseur (à l'échelle) peut être excité soit du port intérieur soit du port extérieur. Dans le premier cas la structure fonctionne comme bloqueur additionnel de lumière parasite.]

Let us consider now the experimental bend transmission. For all the A-cavity bends the transmission is between 10 % and 20 %. Transmission is very flat for the design A-S0 whereas the resonances are more accentuated for A-S3. At the right end of the spectra at $u = 0.285$ the air-band corresponding to the ΓM -direction starts and the bend transmission therefore becomes meaningless for higher frequencies (see Fig. 6.8).

For the design B the average transmission level is 20 % and consequently higher than for design A. The peak-transmissions exceed 30 %.

The transmission level for C-cavity-based bends is between 10 % and 20 % and attains 30% peak transmission for design C-S1. The experimental transmission values for the A, B and C-cavity do not differ a lot, but for all of them the design with a single present hole in the barrier (-S1) shows the best performance.
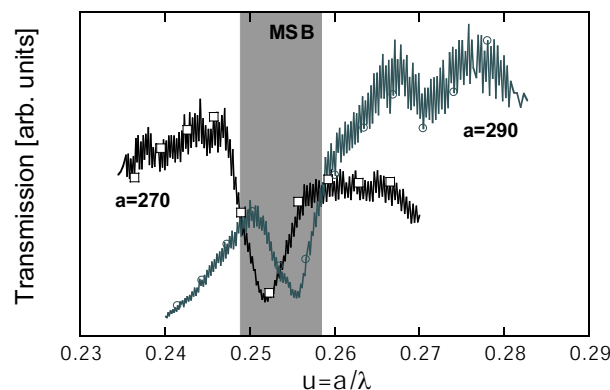
Figure 6.7: Transmission spectrum of the straight waveguide with the mini-stopband (MSB) clearly visible at $u = 0.254$
[Spectre de transmission du guide droit de normalisation à 60 rangées avec la mini-bande clairement visible à la fréquence $u = 0.254$]
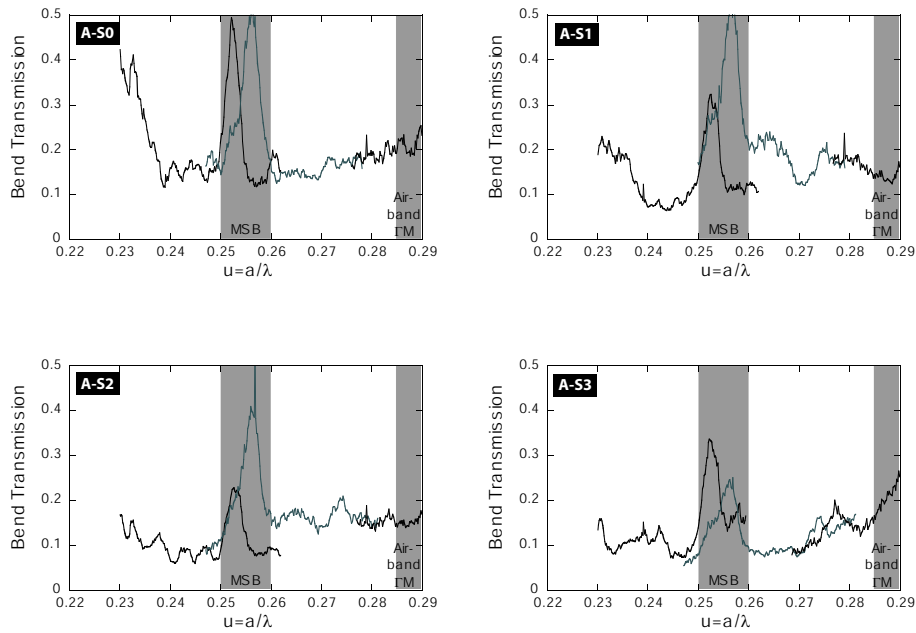
Figure 6.8: Absolute bend transmission of design A. The frequency region of the MSB of the straight waveguide and the beginning of the air-band have been shaded.
[Transmission absolue du virage basé sur la cavité A. Les régions de fréquence de la mini-bande du guide droit et le début de la bande air ont été ombrées.]
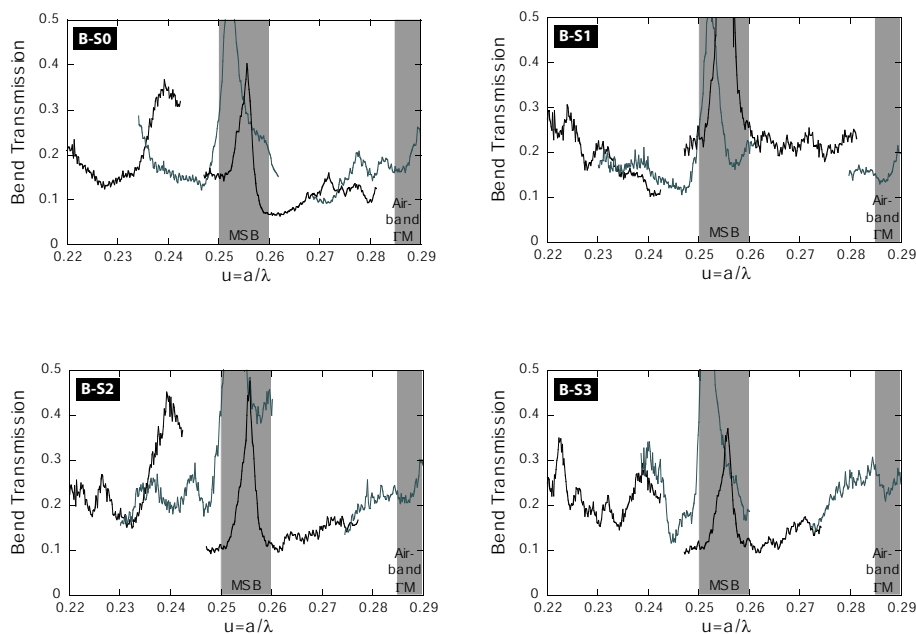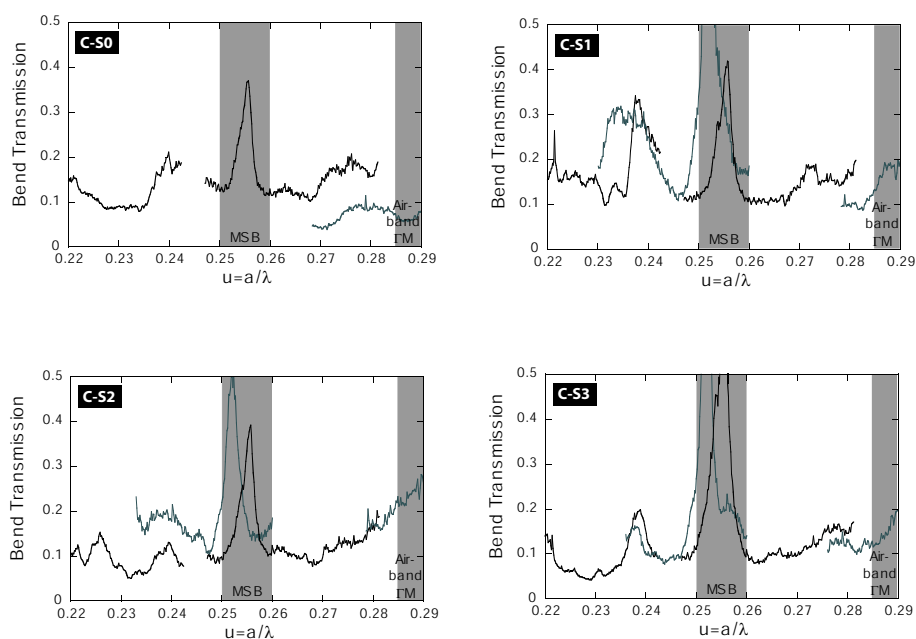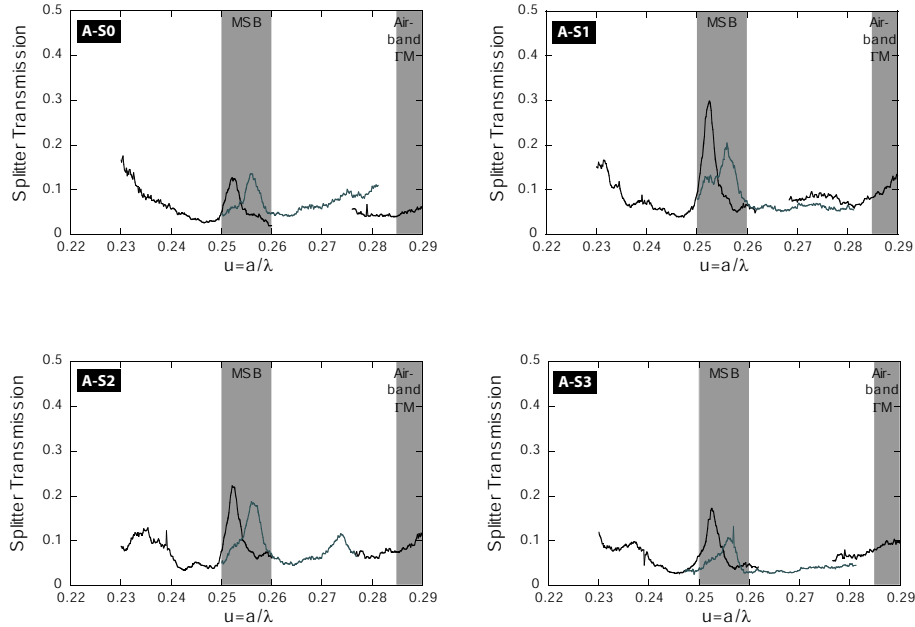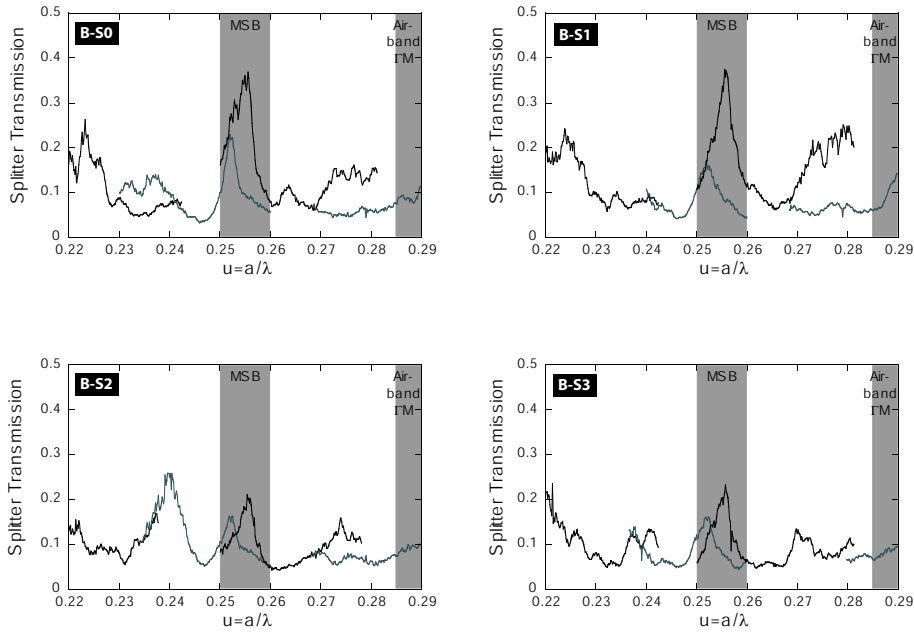

Figure 6.9: Absolute bend transmission of design B. The frequency region of the MSB of the straight waveguide and the beginning of the air-band have been shaded.
[Transmission absolue du virage basé sur la cavité B. Les régions de fréquence de la mini-bande du guide droit et le début de la bande air ont été ombrées.]
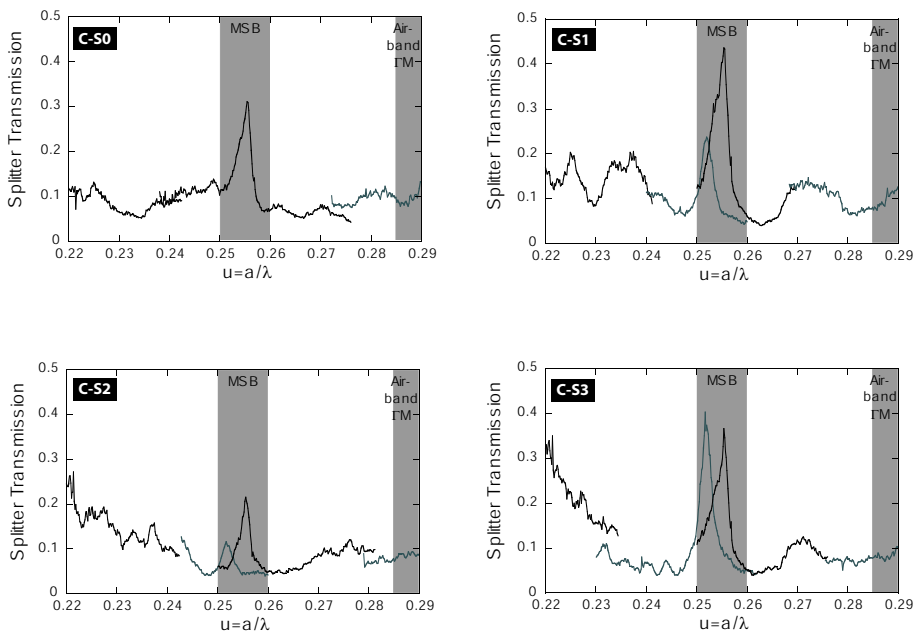
Figure 6.10: Absolute bend transmission of design C. The frequency region of the MSB of the straight waveguide and the beginning of the air-band have been shaded. [*Transmission absolue du virage basé sur la cavité C. Les régions de fréquence de la mini-bande du guide droit et le début de la bande air ont été ombrées.*]

6.2.3 Splitter transmission

For the cavity A the splitter transmissions (see Fig. 6.11) are about half of the bend transmissions (see Fig. 6.8), *i.e.* $5 - 10\%$, and even for the case of three barrier holes (A-S3) the transmission is very flat and no clear peaks can be identified.

Figure 6.11: Absolute splitter transmission of design A. The frequency region of the MSB of the straight waveguide and the beginning of the air-band have been shaded. *[Transmission absolue du diviseur basé sur la cavité A. Les régions de fréquence de la mini-bande du guide droit et le début de la bande air ont été ombrées.]*

The average transmission for cavity B is slightly higher than for cavity A, *e.g.* 15% for B-S2.

For design C, the average transmission is 15% and in the case of C-S1 there is a strong cavity peak which cannot be attributed to one of the cavity modes.

Figure 6.12: Absolute splitter transmission of design B. The frequency region of the MSB of the straight waveguide and the beginning of the air-band have been shaded. *[Transmission absolue du diviseur basé sur la cavité B. Les régions de fréquence de la mini-bande du guide droit et le début de la bande air ont été ombrées.]*

Figure 6.13: Absolute splitter transmission of design C. The frequency region of the MSB of the straight waveguide and the beginning of the air-band have been shaded. *[Transmission absolue du diviseur basé sur la cavité C. Les régions de fréquence de la mini-bande du guide droit et le début de la bande air ont été ombrées.]*

6.3 Data analysis and discussion

6.3.1 Advantages of LSO cavities

In a hexagonal lattice the natural cavity possesses hexagonal symmetry and its spectral properties have been investigated both theoretically and experimentally [92,93]. Hexagonal cavities Hn can be classified by an integer number n, indicating the side length in number of ΓM periods. Although these cavities support non-degenerate modes with hexagonal symmetry, they account for a large number of doubly-degenerate modes, which are not suitable for symmetric 60° bends or splitters. The reason is that a cavity with a degenerate mode usually has a good coupling with *one* of the input or output waveguides, but a weak coupling with the others (see Fig. 6.15(a)). Alternatively one may construct from the degenerate basis modes kind of a rotational symmetric mode (see Fig. 6.15(b)). In this case, the phase between two lobes is not a multiple of π, but a multiple of $\pi/3$. This additional phase shift may perturb the phase relation between input and output port and introduce Fabry Perot like spikes in the bend transmission.

The objective of this chapter is to use low-symmetry order cavities so as to increase the density of regularly spaced non-degenerate modes with threefold rotational symmetry and a frequency within the transmission band of the W3 waveguide. Symmetric modes (monopole, trigonal, hexapole) provide equal branching ratios and the criterion of spectral isolation reduces the mode-mixing between the cavity modes that may lead to undesired excitation of higher-order modes in the exit guide. The occurrence of double degeneracy due to the six-fold rotational symmetry of the cavity can be lowered by breaking the strict six-fold cavity geometry (see Fig. 6.14). Apart from this basic rule, the optimal cavity form was probably only found by heuristic methods.
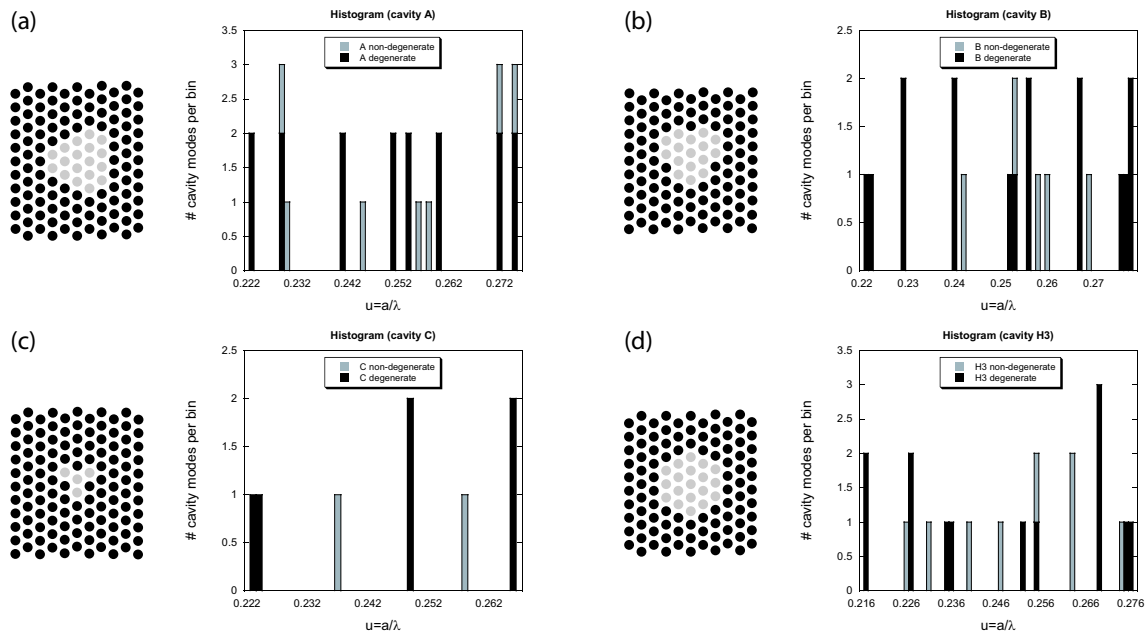

Figure 6.14: Histogram of the energy distribution of the non-degenerate and degenerate cavity modes for the case a) A-cavity, b) B-cavity, c) C-cavity, d) H3-cavity. *[Histogramme de la distribution des modes de cavité non-dégénérés et dégénérés pour le cas de a) cavité A, b) cavité B, c) cavité C, d) cavité H3.]*
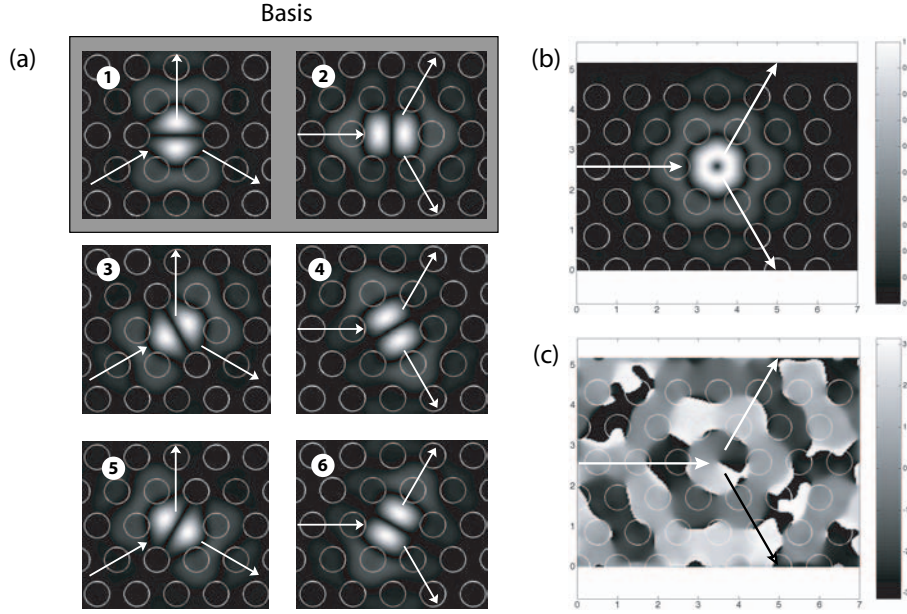
Figure 6.15: a) The H1 cavity (one missing hole) is a typical example supporting two degenerate dipole modes. Taking the modes 1 and 2 as basis, modes 3-6 can be constructed as a superposition. From modes 1,3,5 one may also construct a mode with hexagonal rotation symmetry: b) norm of magnetic field H_z, c) phase of magnetic field H_z.

[La cavité H1 (un trou manquant) est un exemple typique qui supporte deux modes dégénérés du type dipôle. Si les modes 1 et 2 forment une base, les modes 3-6 peuvent être construits comme superposition. A partir des modes 1,3,5 on peut construire un mode avec une symétrie de rotation hexagonale: b) norme du champs magnétique H_z, c) phase du champs magnétique H_z.]

6.3.2 Mode calculation of isolated cavities

Since the transmission of the bend and the splitter is provided by the coupling between the input and output waveguides and the cavity modes, their frequency and symmetry properties should be considered. Although an in-depth classification of the resonant-modes would imperatively require group theory as proposed in [94], a simpler classification by degeneracy, symmetry and frequency is sufficient for our purpose.

The measured frequency peak is often shifted in frequency with respect to the calculated cavity peak. This is due to the fact that the cavity modes are calculated for an uncoupled, isolated cavity, completely surrounded by PhC. The thin barrier of maximum one complete row of ΓK PhC reduces the confinement leading to a shift towards smaller frequencies.
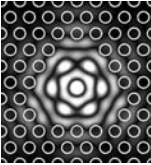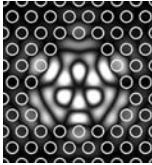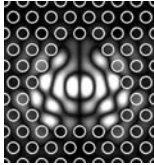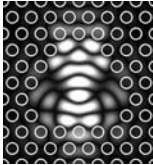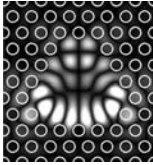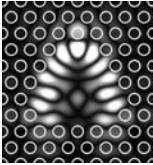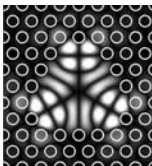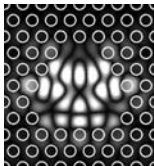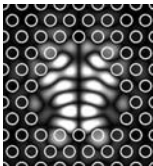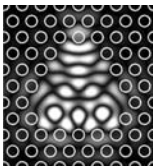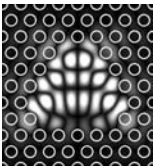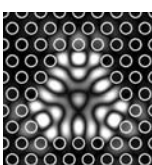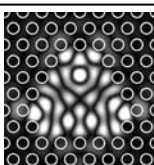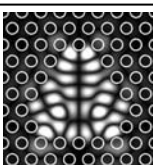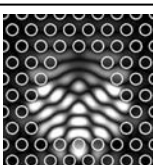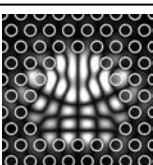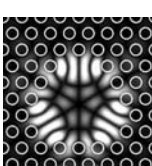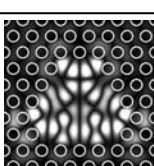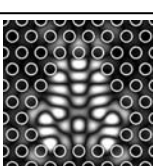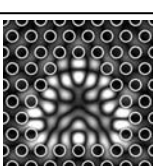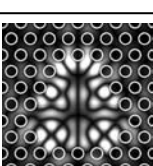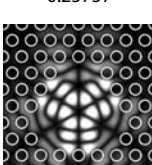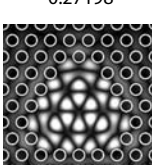
Non-degenerate modes	Degenerate modes				
Monopole		Others			
0.25569	0.22872	0.22917	0.22929	0.22335	0.22336
	0.22956	0.24066	0.24073	0.25126	0.25131
	0.24517	0.25367	0.25368	0.26019	0.26019
	0.25757	0.27224	0.27224	0.27453	0.27454
	0.27198				
	0.27503				

Figure 6.16: Classification of the isolated cavity modes for the cavity A by degeneracy, symmetry and frequency. Within the non-degenerate modes it can be distinguished between monopole and trigonal modes.
[*Classification par dégénérescence, symétrie et fréquence des modes de la cavité A. A l'intérieur des modes non-dégénérés on peut distinguer entre les modes monopôle et ternaire.*]
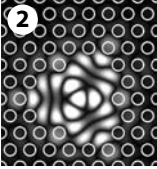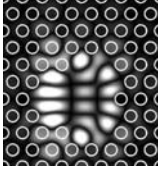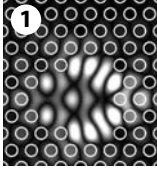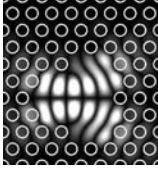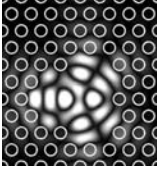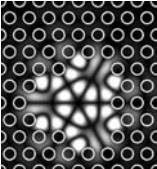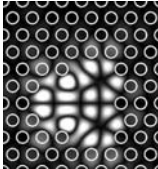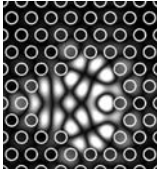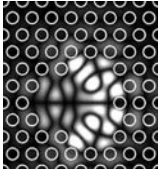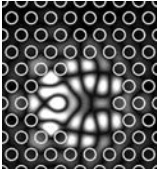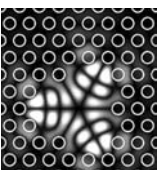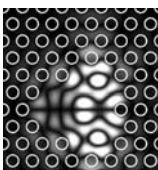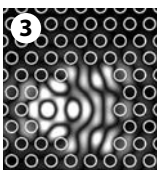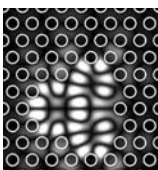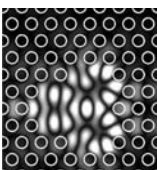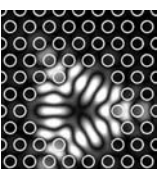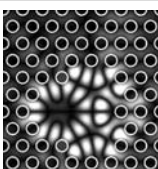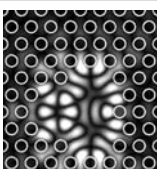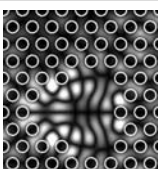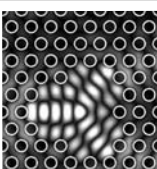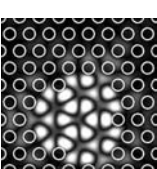
Non-degenerate modes	Degenerate modes			
Trigonal	Others			

Figure 6.17: Classification of the isolated cavity modes for the cavity B by degeneracy, symmetry and frequency. Only the modes with trigonal symmetry are non-degenerate. The peaks labelled 1-3 correspond to the transmission peaks in Fig. 6.19.

[*Classification par dégénérescence, symétrie et fréquence des modes de la cavité B. Seuls les modes avec la symétrie ternaire sont non-dégénérés. Les pics 1-3 correspondent aux pics de transmission dans la Fig. 6.19.*]

Figure 6.18: Classification of the isolated cavity modes for the cavity C by degeneracy, symmetry and frequency. Within the non-degenerate modes there are only modes with trigonal symmetry
[Classification par dégénérescence, symétrie et fréquence des modes de la cavité C. A l'intérieur des modes non dégénérés il y a seulement des modes de symétrie ternaire.]

In general, the transmission peaks in the experimental spectra in section 6.2.2 show a rather flat transmission. This might be related to a low quality factor of the cavity or to high losses. The goal of the next section is to estimate the quality factors and relate them to the bend and splitter transmission.

6.3.3 Transmission calculation by FDTD

Finite Difference Time Domain (FDTD) simulations have been performed in order to reproduce in a theoretical model the ILS experiment. The normalised bend transmission is obtained analogously to the ILS experiment by normalising with respect to a reference waveguide (see Fig. 6.20).

Four main peaks may be identified in the calculated transmission spectrum (see Fig. 6.19). The correspondence for the peak position is good whereas the peak heights and linewidths do not agree.

Peaks 1 and 2 can be clearly identified in the experimental spectrum. Peak 3 is visible but falls in the range of the MSB position where the transmission spectrum is to be taken with the greatest care. Peak n°4, based on the parasitic cavity, is experimentally non-existent. It might be argued that this kind of local resonance is very sensitive to fabrication imperfections and thus only observable theoretically.

The source pulse is spatially and temporally a Gaussian centred at the energy $u = 0.26$. The Gaussian pulse has a spatial width (spotsize) of 1 period (half width at
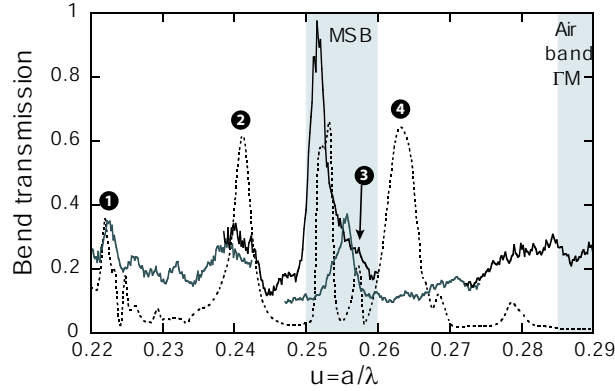
Figure 6.19: Comparison between the bend transmission of the B-S3 cavity measured experimentally and calculated by FDTD.
[Comparaison entre la transmission du virage de la cavité B-S3 mesurée expérimentalement et calculée par FDTD.]
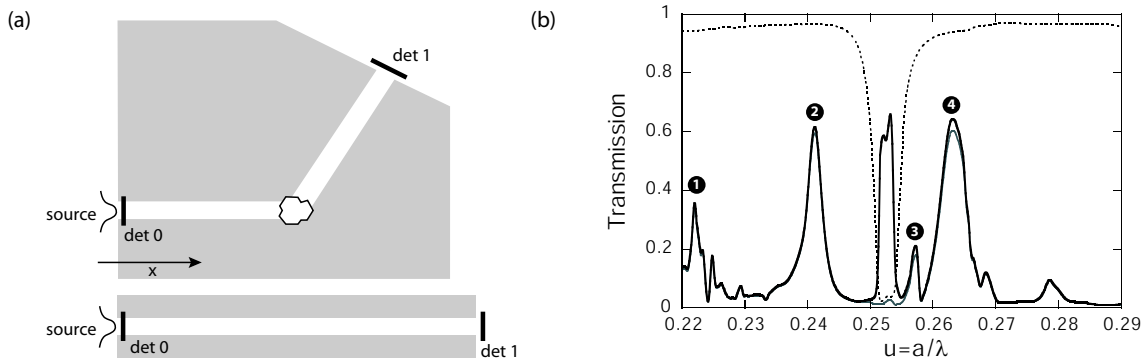
Figure 6.20: (a) Scheme for the FDTD calculation: the total transmission of the bend structure is normalised by the straight waveguide transmission as in the ILS experiment. (b) B-S3 bend: The dotted curve corresponds to the straight waveguide transmission and the solid gray curve to the total transmission of the structure. The solid black curve represents the normalised bend transmission ($f = 0.33$, $\varepsilon_{\mathrm{sub}} = 11.4$, $\varepsilon'' = 0.69$).
[(a) Schéma du calcul FDTD: la transmission totale de la structure virage est normalisée par la transmission du guide droit comme dans l'expérience de source interne. (b) La courbe pointillée correspond à la transmission du guide droit et la ligne grise solide à la transmission totale de la structure. La ligne solide noire représente la transmission normalisée du virage ($f = 0.33$, $\varepsilon_{sub} = 11.4$, $\varepsilon'' = 0.69$).]

half maximum). Losses have been taken into account by a conductivity parameter corresponding to the re-scaled ε'' value. the source is positioned directly at the guide entry ($x = 0$) and emits a Gaussian pulse in time which is detected at the reference detector (det 0 at $x = 1$). After travelling through the structure, the light is detected at detector det 1. As in the experiment, the bend transmission is obtained by dividing the total transmission by the straight guide transmission.

The peak energies plus the corresponding re-scaled loss parameters used afterwards for the field calculation (Fig. 6.21) are listed in Table 6.1.

The peaks 1-3 can easily be attributed to the cavity modes calculated by PWE,

Peak n°	$u = a/\lambda$	ε''
1	0.2219	0.0502
2	0.2411	0.0593
3	0.2573	0.0676
4	0.2633	0.0707

Table 6.1: Peak values read out from the bend transmission spectrum shown in Fig. 6.20 and the corresponding re-scaled ε'' values used for the field calculations in Fig. 6.21

[Valeurs des énergies de résonance dans le spectre de transmission de virage de la Fig. 6.20 et les valeurs rééchelonnées de ε'' pour le calcul de champs dans la Fig. 6.21]
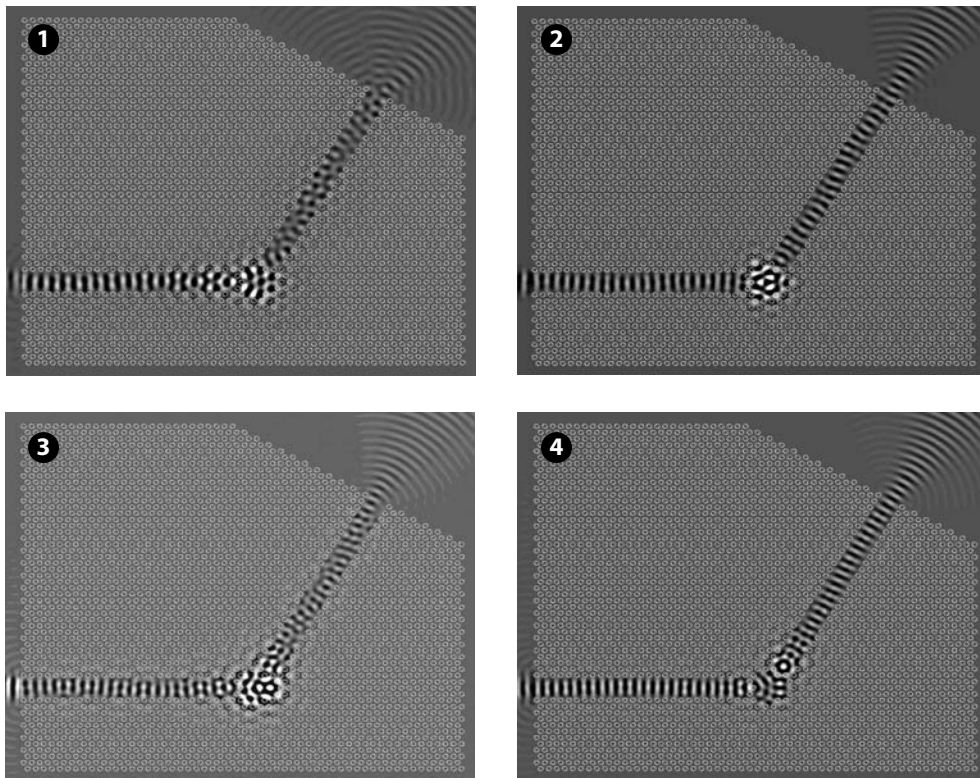
Figure 6.21: Magnetic field distribution inside the bend structure (B-S3 cavity) for the four peaks specified in Table 6.1 and calculated by 2D FDTD.

[Distribution du champ magnétique à l'intérieur de la structure de virage (cavité B-S3) calculée par FDTD 2D pour les quatre résonances spécifiées dans le Tableau 6.1.]

as marked in Fig. 6.17. We note that the bend transmission is based both on non-degenerate and degenerate modes. In the case of the two degenerate cavity modes (peaks n° 1 and 3) the waveguide field after the cavity contains also higher-order modes, whereas in the case of peak n° 2 the non-degenerate cavity mode couples exclusively to the fundamental mode. Peak n° 4 has a very high field intensity *outside* the actual cavity in a parasitic cavity formed at the waveguide-cavity corner.

Figure 6.22 confronts the experimental spectrum of the B-S3 splitter with the FDTD calculation. The agreement between the experiment and the FDTD calculation is good,
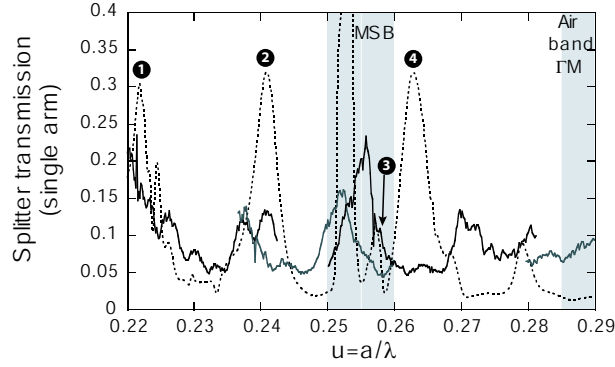
Figure 6.22: Comparison between the transmission spectrum of a B-S3 cavity-based splitter measured experimentally and calculated by FDTD.
[Comparaison entre le spectre de transmission du diviseur basé sur la cavité B-S3, mesuré expérimentalement et calculé par FDTD.]
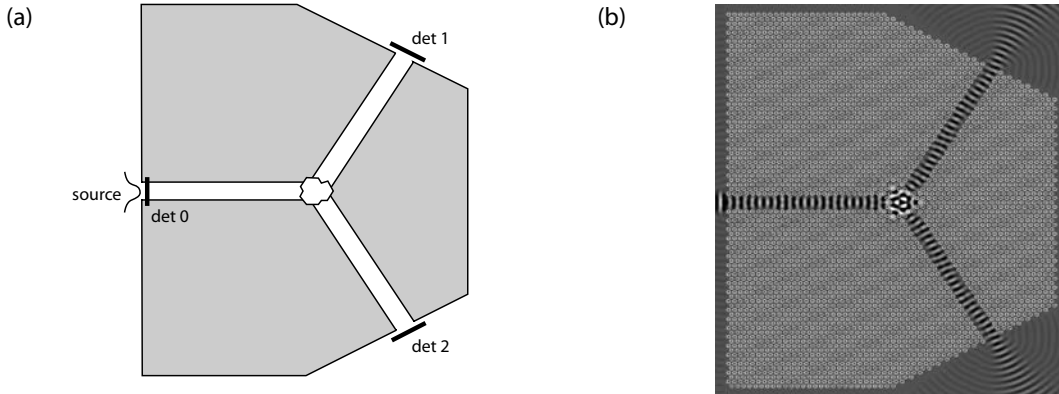
Figure 6.23: a) Sketch of the FDTD configuration. The source pulse ($u_0 = 0.26$) is released into port 1 of the splitter structure and detected at the beginning of port 1 (reference detector det 0) and at the exit of port 2 (det 1) and port 3 (det 2). b) Magnetic field pattern corresponding to the non-degenerate mode n° 2.
[a) Aperçu du domaine de calcul FDTD. L'impulsion de source est lancée dans le port 1 du diviseur et détectée à l'entrée du port 1 (détecteur de référence (det 0) et à la sortie du port 2 et port 3 (détecteurs det 1 et det 2). b) Distribution du champ magnétique correspondant au mode non-dégénéré n° 2.]

especially for the range to the left of the MSB. As in the case of the bend, the peak at $u = 0.263$ is not experimentally observable.

The calculation of splitter transmission by FDTD is very similar to bend transmission with the only difference that an additional detector is positioned at the guide exit of the second arm (see Fig. 6.23(a)). The detected signals at *det 1* and *det 2* proved to be identical, showing symmetric splitting. As in the experiment and in the case of the bend, the FDTD splitter transmission is obtained by dividing the total transmission by the straight guide transmission. When comparing bend transmission (Fig. 6.20) with splitter transmission (Fig. 6.22) one notes that the form of the spectrum is almost identical. Concerning the signal levels, total splitter transmission (both arms together) is consistently equal to bend transmission. The theoretical ratio of 8/9 between total bend and total splitter transmission (sum of both arms) is not obtained because losses are included.

6.3.4 The time-dependent coupled mode model

6.3.4.1 Definition of the quality factor

The quality factor of a cavity is usually defined as:

$$Q_0 = 2\pi \frac{\text{energy stored in the cavity}}{\text{energy lost per cycle}} = 2\pi \frac{W_{\text{cav}}}{P_{\text{diss}}T} = \frac{\omega_0 W_{\text{cav}}}{P_{\text{diss}}} \qquad (6.2)$$

where P_{diss} denotes the energy loss rate, W_{cav} the total energy stored inside the cavity and ω_0 the resonance frequency of the cavity. This definition is very common in the domain of electronic or microwave oscillators whereas in optics the quality factor is usually defined by the resonance linewidth, *i.e.* $Q = \omega_0/\delta\omega$. These two definitions are equivalent: The differential equation for the cavity energy writes:

$$\frac{dW_{\text{cav}}}{dt} = -P_{\text{diss}} \quad \rightarrow \quad \frac{dW_{\text{cav}}}{dt} = -\frac{P_{\text{diss}}\omega_0 W_{\text{cav}}}{\omega_0 W_{\text{cav}}} \quad \rightarrow \quad \frac{dW_{\text{cav}}}{dt} = -\frac{\omega_0}{Q}W_{\text{cav}} \qquad (6.3)$$

Where the solution is given by:

$$W_{\text{cav}}(t) = W_0 e^{-\frac{\omega_0}{Q}t} \qquad (6.4)$$

and for the electrical field inside the cavity ($W_{\text{cav}} \propto |\mathbf{E}|^2$) the time dependence notes:

$$\mathbf{E}(t) = \mathbf{E}_0 e^{-\frac{\omega_0}{2Q}t} e^{j\omega_0 t} \qquad (6.5)$$

The frequency dependence of the electric field is obtained by a Fourier transformation:

$$\mathbf{E}(\omega) = \int\limits_0^\infty dt\, e^{-j\omega t}\mathbf{E}(t) = \mathbf{E}_0 \int\limits_0^\infty dt\, e^{j\left[(\omega-\omega_0)-\frac{\omega_0}{2Q}\right]t} = \frac{1}{\frac{\omega_0}{2Q} - j(\omega_0 - \omega)}\mathbf{E} \qquad (6.6)$$

The frequency power spectrum is given by:

$$I(\omega) = \frac{1}{2}\varepsilon_0 nc\mathbf{E}(\omega)\mathbf{E}^*(\omega) \propto \frac{1}{\left(\frac{\omega_0}{2Q}\right)^2 + (\omega_0 - \omega)^2} \qquad (6.7)$$

This Lorentzian lineshape function has a full width at half maximum value of $\delta\omega = \omega_0/Q$, yielding $Q = \frac{\omega_0}{\delta\omega}$.

Sometimes it is useful to express the quality factor in terms of lifetime and vice versa:

$$\text{Plugging} \quad P_{\text{diss}} = -\frac{dW}{dt} = \frac{2W_{\text{cav}}}{\tau} \quad \text{into Eq. (6.2)} \quad \longrightarrow \quad \frac{1}{Q} = \frac{2}{\omega_0\tau} \qquad (6.8)$$

6.3.4.2 Introduction of the formalism

In this section we will use the time-dependent coupled-mode theory (CMT), which was introduced by H.A. Haus [87], and apply it to our cavity bends and splitter. The model focuses on a single-mode cavity with a resonance frequency ω_0 and is characterised by an intrinsic and an external quality factor. The intrinsic quality factor Q_0, also called

unloaded quality factor, accounts for the losses inside the cavity (absorption and out-of-plane scattering). It describes the coupling of the cavity modes to the leaky modes above the light line. Its actual value depends on the field overlap with the holes, *i.e.* on the confinement of the mode inside the cavity. The external coupling factor Q_e accounts for the energy leakage of the cavity due to the coupling with the waveguide. The value for Q_e is very much dependent on the symmetry of the cavity mode with respect to the waveguide modes and is thus very different for each cavity mode.

Let us consider first a single-mode cavity coupled to a single waveguide (see Fig. 6.24).
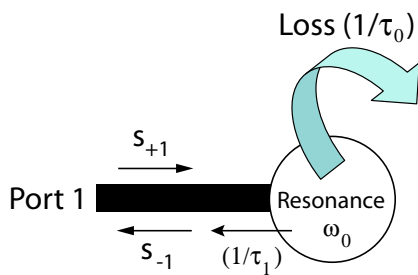
Figure 6.24: Sketch of a cavity coupled to a single waveguide and the corresponding CMT parameters.
[Schéma d'une cavité couplée avec un guide d'onde et les paramètres principaux du modèle des modes couplés.]

The temporal coupled mode theory (CMT) is actually based on a temporal differential equation describing the balance between incoming and outgoing field fluxes. In the ideal case with no losses, it is assumed that inside the cavity the field-amplitude oscillates with frequency ω_0 $(a(t) = e^{j\omega_0 t})$ and is normalised such that $W = |a|^2$ corresponds to the field energy stored inside the cavity. The cavity may lose energy due to intrinsic losses $(\sim 1/\tau_0)$ or due to the coupling to the waveguide $(\sim 1/\tau_1)$. Thus in the case where no external wave impinges on the cavity, the amplitude inside the cavity writes:

$$a(t) \propto e^{j\omega_0 t} e^{-\frac{t}{\tau_0}} e^{-\frac{t}{\tau_1}} \tag{6.9}$$

The power inside the cavity may be increased by an impinging wave with amplitude s_{+1} coupled to the cavity by a coupling constant κ_1 and normalised such that $|S_{+1}|^2$ equals the power carried by the incident wave. Taking the time derivative of from Eq. (6.9) and accounting for an incident wave s_{+1} yields:

$$\frac{da(t)}{dt} = j\omega_0 a(t) - \left(\frac{1}{\tau_0} + \frac{1}{\tau_1}\right)a(t) + \kappa_1 s_{+1} \tag{6.10}$$

The coupling coefficient κ_1 is depends on the external cavity lifetime τ_1. The relationship between the two quantities is found using the time-reversed symmetry of Maxwell's equations for lossless media $(\tau_0 = \infty)$: If there is no external source, the mode amplitude decays at the rate $1/\tau_1$ and thus the cavity mode energy with $2/\tau_1$ and the energy is transported by the outgoing wave:

$$\frac{d|a|^2}{dt} = -\frac{2}{\tau_1}|a|^2 = -|s_{-1}|^2 \tag{6.11}$$

In the time-reversed situation, the cavity mode energy is driven by the incident wave s_{+1} at frequency ω_0 and grows exponentially with $1/\tau_1$:

$$\frac{d|\tilde{a}|^2}{dt} = \frac{2}{\tau_1}|\tilde{a}|^2 \tag{6.12}$$

The time-reversed solution is given by:

$$\tilde{a} = \tilde{a}_0 e^{j\omega_0 t} e^{\frac{t}{\tau_1}} = e^{j\underbrace{(\omega_0 - j/\tau_1)}_{\omega}t} \tag{6.13}$$

and the driving frequency is $\omega = \omega_0 - j/\tau_1$. Inserting this frequency into Eq. (6.18) yields:

$$\tilde{a} = \frac{\kappa_1 \tilde{s}_{+1}}{2/\tau_1} \tag{6.14}$$

On the other hand, it follows from Eq. (6.11):

$$\frac{d|\tilde{a}|^2}{dt} = +\frac{2}{\tau_1}|\tilde{a}|^2 = +|\tilde{s}_{+1}|^2 \quad \longrightarrow \quad \tilde{a} = \sqrt{\frac{\tau_1}{2}}\tilde{s}_{+1} \tag{6.15}$$

The comparison between Eq. (6.14) and Eq. (6.15) finally yields:

$$\kappa_1 = \sqrt{\frac{2}{\tau_1}} \tag{6.16}$$

and Eq. (6.10) can be rewritten as

$$\frac{da(t)}{dt} = j\omega_0 a(t) - (\frac{1}{\tau_0} + \frac{1}{\tau_1})a(t) + \sqrt{\frac{2}{\tau_1}}s_{+1} \tag{6.17}$$

Let us assume that at $t = 0$ no energy is stored inside the cavity. If the system is excited by a source emitting at frequency ω, i.e. $s_{+1} = |s_{+1}|e^{j\omega t}$, the response of the system will be at the same frequency, i.e. $a = a_0 e^{j\omega t} \rightarrow \frac{da}{dt} = j\omega a_0 e^{j\omega t} = j\omega a$ and Eq. (6.10) becomes:

$$a(\omega) = \frac{\kappa_1 s_{+1}}{j(\omega - \omega_0) + \frac{1}{\tau_0} + \frac{1}{\tau_1}} \tag{6.18}$$

When a wave impinges on the cavity it is partly coupled into the cavity field and partly reflected. Since the system is linear it can be assumed that s_{-1} is the superposition of a term proportional to s_{+1} and a term proportional to the cavity amplitude a:

$$s_{-1} = c_{+1}s_{+1} + c_a a \tag{6.19}$$

The coefficient c_a corresponds to the case where $s_{+1} = 0$ and has already been evaluated in Eq. (6.11):

$$s_{-1} = \sqrt{\frac{2}{\tau_1}}a = c_a a \quad \rightarrow \quad c_a = \sqrt{\frac{2}{\tau_1}} = \kappa_1 \tag{6.20}$$

The coefficient c_{+1} can be deduced from energy conservation, i.e. the net power flowing into the cavity must equal the increase of the cavity mode energy plus the energy dissipation (loss):

$$|s_{+1}|^2 - |s_{-1}|^2 = \frac{d}{dt}|a|^2 + \frac{2}{\tau_0}|a|^2 \tag{6.21}$$

On the other hand from Eq. (6.17) it follows that:

$$
\frac{d}{dt}|a|^2 = \frac{d}{dt}(aa^*) = \frac{da}{dt}a^* + a\frac{da^*}{dt} = \left[j\omega a - \left(\frac{1}{\tau_0} + \frac{1}{\tau_1} \right) a + \sqrt{\frac{2}{\tau_1}}s_{+1} \right] a^*
$$
$$
+ \left[-j\omega a^* - \left(\frac{1}{\tau_0} + \frac{1}{\tau_1} \right) a^* + \sqrt{\frac{2}{\tau_1}}s_{+1}^* \right] a
$$
$$
= -2(\frac{1}{\tau_0} + \frac{1}{\tau_1})|a|^2 + \sqrt{\frac{2}{\tau_1}}(a^*s_{+1} + as_{+1}^*) \qquad (6.22)
$$

The comparison between Eqs. (6.21) and (6.22) yields:

$$
-\frac{2}{\tau_1}|a|^2 + \sqrt{\frac{2}{\tau_1}}(a^*s_{+1} + as_{+1}^*) = |s_{+1}|^2 - |s_{-1}|^2 \qquad (6.23)
$$

By eliminating a and a^* from Eq. (6.23) by insertion of Eq. (6.19) together with Eq. (6.20) and making a comparison by coefficient, one finally obtains: $c_{+1} = -1$ and the complete relation writes:

$$
s_{-1} = \sqrt{\frac{2}{\tau_1}}a - s_{+1} \qquad (6.24)
$$

By inserting Eqs. (6.18) and (6.16) into Eq. (6.24) and taking the square, one immediately obtains the formula for the reflection R:

$$
R \equiv \left| \frac{s_{-1}}{s_{+1}} \right|^2 = \left| \frac{-j(\omega - \omega_0) - \frac{1}{\tau_0} + \frac{1}{\tau_1}}{j(\omega - \omega_0) + \frac{1}{\tau_0} + \frac{1}{\tau_1}} \right|^2 \qquad (6.25)
$$

6.3.4.3   Application of the formalism to resonant cavity bends

The coupled mode scheme for a bend is sketched in Fig. 6.25.
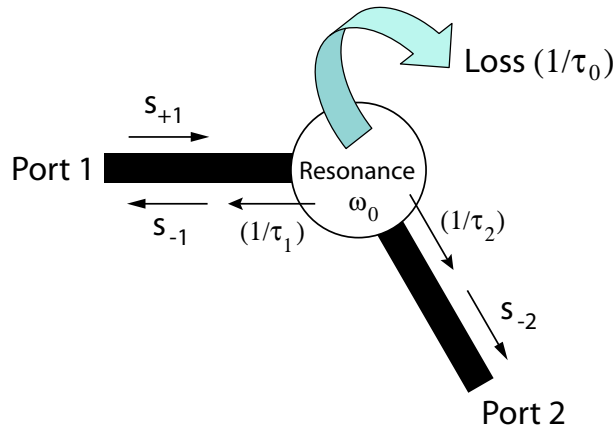
Figure 6.25: Sketch of the coupled mode model for a resonant bend
        [Schéma du modèle des modes couplés pour un virage.]

Extending Eq. (6.17) to the case of a bend we obtain:

$$\frac{da(t)}{dt} = j\omega_0 a(t) - \left(\frac{1}{\tau_0} + \frac{1}{\tau_1} + \frac{1}{\tau_2}\right)a(t) + \sqrt{\frac{2}{\tau_1}}s_{+1} + \sqrt{\frac{2}{\tau_2}}s_{+2} \tag{6.26}$$

For the transmission and reflection calculation, one considers an incoming wave s_{+1} from port 1 and not from port 2. The energy $|a|^2$ in the cavity decays independently into the different channels with the appropriate time constant. Since there is no incoming wave in port 2 the outgoing energy s_{+2} has to stem from the cavity:

$$|s_{-2}|^2 = \frac{2}{\tau_2}|a|^2 \tag{6.27}$$

The solution of Eq. (6.26) for the considered case with $s_{+2} = 0$ reads:

$$a(\omega) = \frac{\kappa_1 s_{+1}}{j(\omega - \omega_0) + \frac{1}{\tau_0} + \frac{1}{\tau_1} + \frac{1}{\tau_2}} \tag{6.28}$$

Eq. (6.28) inserted into Eq. (6.27) yields the formula for the transmitted power (T) from port 1 to port 2:

$$T \equiv \frac{|s_{-2}|^2}{|s_{+1}|^2} = \frac{2}{\tau_2} \left| \frac{\sqrt{\frac{2}{\tau_1}}}{j(\omega - \omega_0) + \frac{1}{\tau_0} + \frac{1}{\tau_1} + \frac{1}{\tau_2}} \right|^2 \tag{6.29}$$

Eq. (6.29) has the form of a Lorentzian lineshape function with a bandwidth (half width at half maximum) $\delta\omega = 1/\tau_{\text{tot}} = 1/\tau_0 + 1/\tau_1 + 1/\tau_2$. For the reflected wave one uses a generalised version of Eq. (6.24) and obtains

$$R \equiv \left| \frac{s_{-1}}{s_{+1}} \right|^2 = \left| \frac{-j(\omega - \omega_0) - \frac{1}{\tau_0} + \frac{1}{\tau_1} - \frac{1}{\tau_2}}{j(\omega - \omega_0) + \frac{1}{\tau_0} + \frac{1}{\tau_1} + \frac{1}{\tau_2}} \right|^2 \tag{6.30}$$

When considering a symmetric bend, *i.e.* a 60°-bend, due to the three-fold rotational symmetry, $\tau_1 = \tau_2$ and by expressing the lifetimes in terms of quality factors (Eq. 6.8), one obtains:

$$R_{\text{max}} = \left| \frac{1}{1 + \frac{2Q_0}{Q_e}} \right|^2 \tag{6.31}$$

$$T_{\text{max}} = \left| \frac{1}{1 + \frac{Q_e}{2Q_0}} \right|^2 \tag{6.32}$$

For the case with zero loss ($\lim_{\frac{Q_e}{Q_0} \to 0}$), this leads to $R = 0$ and $T = 1$. However, for the case where the external coupling equals the internal cavity loss ($Q_e = Q_0$), 1/9 of the power is reflected and the rest is equally distributed into transmission and losses, *i.e.* $T = L = 4/9$.

The model is a simplification with regard to reality in the sense that both the waveguide and the resonant cavity are assumed to be single-mode. The following effects have been neglected:

. *Mode mixing at the corner:* For the case that the cavity features a set of low Q-modes with a great frequency overlap, the incoming fundamental mode excites a distribution of cavity modes which does not necessarily have to couple again into the fundamental mode at the guide exit. [89]

. *Short arm length:* Due to the relatively short arm length of 30 periods, a portion of higher-order modes will also impinge on the cavity.

. *Waveguide properties:* The model does not account for the waveguide dispersion, coupling effects (*e.g.* MSB), back-reflections at the guide exit and the facet.

6.3.4.4   Application of the formalism to resonant cavity splitters

The coupled mode scheme for a splitter is sketched in Fig. 6.26.
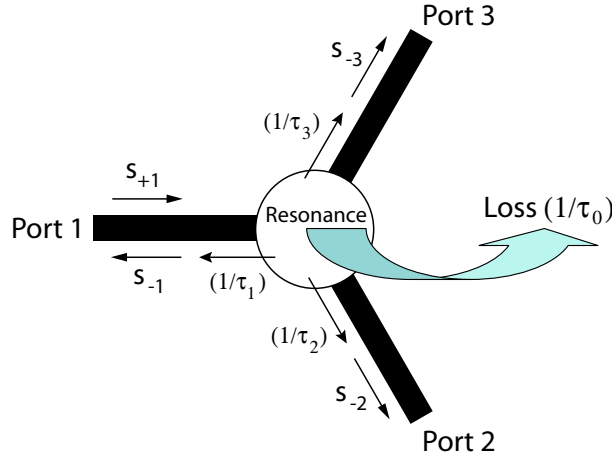
Figure 6.26: Sketch of the coupled-mode model of a resonant cavity splitter
[*Aperçu du modèle des modes couplés pour un diviseur*]

Extending Eq. (6.17) to the case of a splitter we obtain:

$$\frac{da}{dt} = j\omega_0 a - \left(\frac{1}{\tau_0} + \frac{1}{\tau_1} + \frac{1}{\tau_2} + \frac{1}{\tau_3}\right)a + \kappa_1 s_{+1} + \kappa_2 s_{+2} + \kappa_3 s_{+3} \qquad (6.33)$$

By applying the same procedure as for the bend, the input reflection at the input port and the splitter transmission into a single output port are given by [95]

$$R = \left|\frac{s_{-1}}{s_{+1}}\right|^2 = \left|\frac{-j(\omega - \omega_0) - \frac{1}{\tau_0} + \frac{1}{\tau_1} - \frac{1}{\tau_2} - \frac{1}{\tau_3}}{j(\omega - \omega_0) + \frac{1}{\tau_0} + \frac{1}{\tau_1} + \frac{1}{\tau_2} + \frac{1}{\tau_3}}\right|^2 \qquad (6.34)$$

$$T = \left|\frac{s_{-2}}{s_{+1}}\right|^2 = \left|\frac{\frac{2}{\sqrt{\tau_1 \tau_2}}}{j(\omega - \omega_0) + \frac{1}{\tau_0} + \frac{1}{\tau_1} + \frac{1}{\tau_2} + \frac{1}{\tau_3}}\right|^2 \qquad (6.35)$$

For a symmetric splitter ($\tau_1 = \tau_2 = \tau_3$) operated at the resonance frequency $\omega = \omega_0$

and expressed in terms of quality factors Eqs. (6.31-6.32) become:

$$R_{\max} = \left| \frac{1 + \frac{Q_e}{Q_0}}{3 + \frac{Q_e}{Q_0}} \right|^2 \tag{6.36}$$

$$T_{max} = \left| \frac{2}{\frac{Q_e}{Q_0} + 3} \right|^2 \tag{6.37}$$

For the loss-less case ($\lim_{\frac{Q_e}{Q_0} \to 0}$), this leads to the splitting ratio of $T = 4/9$ and $R = 1/9$. The result is well-known in microwave technology [96]. However, for the case where the external coupling equals the internal cavity loss ($Q_e = Q_0$), the power is equally distributed into reflection, transmission and losses, $i.e.$ $R = T = L = 1/4$. In order to overcome the limit of $T = 4/9$ per arm, one has to switch to asymmetric designs where port 1 is slightly different from port 2 and 3.

6.3.5 Calculation of the quality factors

6.3.5.1 Intrinsic quality factor Q_0

In a GaAs sample the absorption by the quantum dots inside the cavity is negligible and Q_0 is dominated by the out-of-plane losses. A first approach to evaluate Q_0 is to combine the field patterns calculated by PWE with the ε''-model formulated in section 3.4.1 and introduce an imaginary dielectric constant ε'' in the holes. The intrinsic cavity loss is mainly given by the overlap of the electric field with the air holes. As already seen in Eq. (3.25) of section 3.4.1, the energy dissipated in a small volume, characterised by an imaginary dielectric constant ϵ'', is given by the dissipated power density:

$$dP_{\text{diss}} = \frac{1}{2} \, \epsilon \, \omega_0 \, \epsilon'' \boldsymbol{E}^2(x, y, z) \, dV \tag{6.38}$$

Integrating Eq. (6.38) over the area of the supercell [1] leads to the total lost power:

$$P_{\text{diss}} = \int_{SC} dP_{\text{diss}} = \frac{1}{2} \varepsilon_0 \, \omega_0 \iint_{SC} dx \, dy \, \varepsilon''(x, y) \mathbf{E}^2 \tag{6.39}$$

The electromagnetic energy is defined as:

$$w_{\text{EM}} = \frac{1}{2} \varepsilon_0 \varepsilon'(\mathbf{r}) \mathbf{E}^2 + \frac{1}{2} \mu_0 \mathbf{H}^2 \tag{6.40}$$

and the total electromagnetic energy stored in the cavity is given by the integral over the supercell (for TE polarisation):

$$W_{\text{cav}} = \int_{SC} dx \, dy \, \frac{1}{2} \varepsilon_0 \varepsilon'(x, y) (|E_x|^2 + |E_y|^2) + \int_{SC} dx \, dy \, \frac{1}{2\mu_0 \omega_0^2} \left| \frac{\partial E_y}{\partial x} - \frac{\partial E_x}{\partial y} \right|^2 \tag{6.41}$$

---

[1] The size should be big enough to include all the evanescent field components.

Since $\varepsilon_0\mu_0 = 1/c^2$ and $u = \omega_0 a/(2\pi c)$, the formula for the intrinsic cavity quality factor writes:

$$Q_0 = \frac{\iint\limits_{SC} dx\, dy\, \epsilon'(x,y)(|E_x|^2 + |E_y|^2) + \frac{1}{4\pi^2 u_0^2}\left|\frac{\partial E_y}{\partial x} - \frac{\partial E_x}{\partial y}\right|^2}{\iint\limits_{SC} dx\, dy\, \epsilon''(x,y)(|E_x|^2 + |E_y|^2)} \tag{6.42}$$

Table 6.2 shows the intrinsic quality factors for the different cavities (A, B, C). The displayed numbers are mean values averaged over the different non-degenerate cavity modes and the corresponding standard deviation.

Design	Q_0
A	277 ± 79
B	234 ± 47
C	173 ± 47

Table 6.2: Intrinsic quality factor of the cavity calculated in a PWE approach. Out-of-plane losses have been taken into account by introducing an imaginary ε'' in the air holes ($\varepsilon'' = 0.08$).
[Facteur de qualité intrinsèque calculé par une approche d'ondes planes. Les pertes hors-plan sont tenues compte par un ε'' imaginaire dans les trous d'air ($\epsilon'' = 0.08$).]

An alternative approach makes use of a 2D FDTD calculation: The computational domain consists of an isolated cavity surrounded by N rows of PhC (see Fig. 6.27). As in the previous method, the scattering losses are taken into account by means of an imaginary ε''. The cavity modes are excited by a dipole source that emits a Gaussian pulse inside the cavity. In order to excite a maximum of different cavity modes, the source is not positioned on a high-symmetry point. The temporal energy decay is monitored by two line detectors positioned along the ΓM and the ΓK direction. The Fourier transform of the time-dependent Poynting vector yields the frequency-dependent power spectrum.
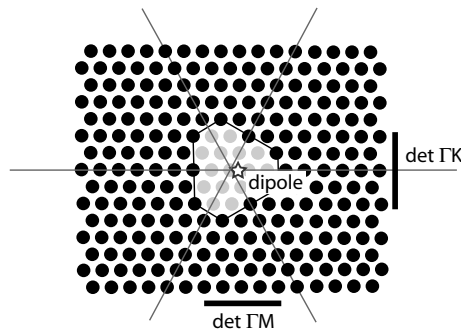
Figure 6.27: For the determination of Q_0 by FDTD, an isolated cavity with N rows around it is excited by a dipole source inside the cavity. The temporal decay of the field is monitored by the weak probes (det ΓM and det ΓK).
[Pour la détermination de Q_0 par FDTD, une cavité isolée est excitée par une source dipolaire à l'intérieur de la cavité. La décroissance temporelle du champ est détectée selon ΓM et ΓK .]

Fig. 6.28 shows the spectra for the cavity B surrounded by 4 and 16 rows, respectively. One may identify four main peaks in the middle of the band gap between $u = 0.22$ and 0.26. There are two other groups of peaks around $u = 0.27$ and 0.28. It is, however, difficult to determine the quality factors of these closely-spaced peaks unambiguously. The signal level decreases exponentially with the number of rows. On
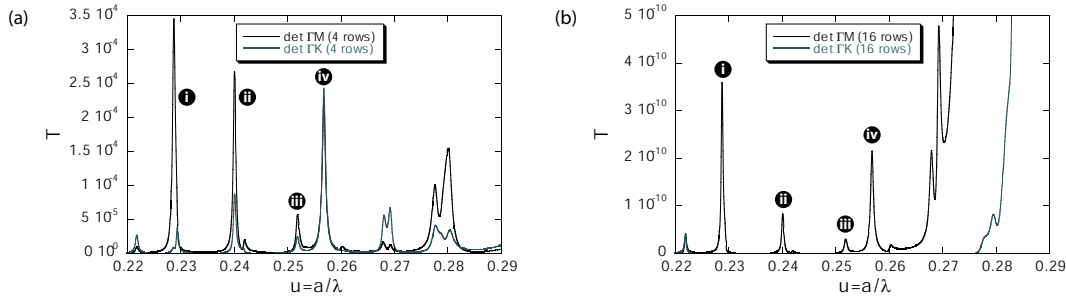
Figure 6.28: FDTD spectrum calculated according to Fig. 6.27 for an isolated B-cavity surrounded by a) 4 rows, b) 16 rows.

[Spectre FDTD calculé d'après Fig. 6.27 pour une cavité isolé de type B entourée de a) 4 rangées, b) 16 rangées.]

the other hand, the effect of additional rows on the cavity confinement decreases with the total number of rows. One expects that the quality factor of the isolated cavity converges towards a constant value, Q_0 (see Fig. 6.29). The two detectors act as weak probes: One is only interested in the temporal decay of the signal and not in absolute intensity levels. A compromise has to be found between having a high enough signal (not a too large number of rows) and still measuring the intrinsic loss of an *isolated* cavity (infinite number of rows).
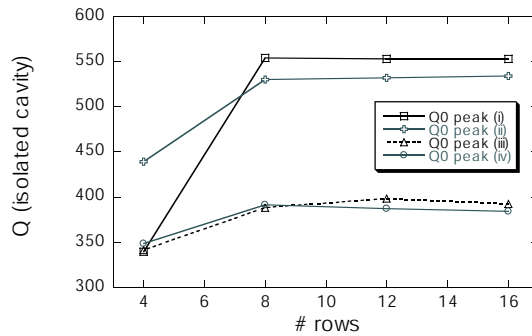
Figure 6.29: Quality factor of the isolated cavity B as a number of surrounding rows (parameters: $f = 0.33$, $\varepsilon_{\text{sub}} = 11.4$, $\varepsilon'' = 0.69@u_0 = 0.26$). The quality factors are converging to constant values that correspond to the intrinsic quality factors Q_0.

[Facteur de qualité pour les différents modes de la cavité B en fonction du nombre de rangées de cristal photonique qui entourent la cavité (paramètres: $f = 0.33$, $\varepsilon_{sub} = 11.4$, $\varepsilon'' = 0.69@u_0 = 0.26$). Les facteurs de qualité convergent vers les valeurs intrinsèques Q_0.]

Table 6.3 summarises the Q_0 values corresponding to the four peaks that have been identified in Fig. 6.28. The values in this table are indicated without error bars since the Q_0 values of the four peaks have not been averaged.

peak n°	u_0	Q_0
i	0.2287	553
ii	0.2401	534
iii	0.2519	392
iv	0.2568	384

Table 6.3: Intrinsic quality factor Q_0 of the four main peaks in Fig. 6.28 calculated by FDTD.
[*Facteur de qualité intrinsèque pour les quatre pics principaux dans la Fig. 6.28 calculé par FDTD.*]

The Q_0 values determined by FDTD are on average bigger by a factor of two than the values deduced from the 'PWE+ε''-model'. Since there is no conclusive sign which method provides more accurate values, and because the external quality factor can only be calculated by FDTD, it is more coherent to choose for both quality factors the FDTD. This is all the more true since the transmission and reflection coefficient in the CMT depend on the ratio between the Q_0 and Q_e.

6.3.5.2   External quality factor Q_e

The external quality factor is affected by the barrier thickness between the cavity and the waveguide as well as by the symmetry of the cavity mode with respect to the waveguide mode, for example, when coupling to the fundamental waveguide mode, at least the parity of the cavity mode should be correct between waveguide and cavity mode. Q_e can be calculated by 2D FDTD in a straight-forward manner. The computational domain includes the complete cavity bend structure. The cavity modes are excited analogously to the intrinsic case by a dipole source inside the cavity. The source is positioned in the first place at the same position as in the intrinsic case and in addition at two other places (see Fig. 6.30), which provides an estimate of the average error of Q_e (see Table 6.4). Since one is not interested in absolute intensities, but only in the temporal decay of the cavity mode into the two waveguides, it is not important to excite the cavity modes equally.

The cavity modes couple to the waveguide modes which propagate towards the guide exit where they are detected by a line detector. The resulting power spectra for the different excitation positions are displayed in Fig. 6.31. For the evaluation of Q_e a lossless structure ($\varepsilon'' = 0$) is assumed.

The values for Q_e corresponding to the different peaks are given directly by their relative linewidths and are listed in Table 6.4. Additionally the total quality factor of the cavity bend

$$\frac{1}{Q_{\text{tot}}} = \frac{2}{Q_e} + \frac{1}{Q_0} \tag{6.43}$$

is listed, which determines the peak width in transmission and which can be directly compared to the experimental spectra.

The values for the external quality factors of the different cavity peaks show a big variance due to the strong symmetry dependence of the coupling between the cavity and the waveguide mode.
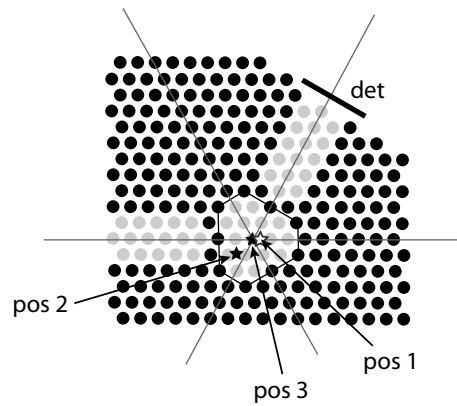
Figure 6.30: For the determination of Q_e by FDTD, the cavity bend is excited by a pulse from a dipole source at different positions inside the cavity. The out-going wave is detected at the guide exit after 30 periods of straight waveguide.
[*Pour la détermination de Q_e par FDTD, le virage à cavité est excité par une impulsion d'une source dipôle à différentes positions à l'intérieur de la cavité. La lumière sortant est détecté à l'extérieur du guide après avoir propagé 30 périodes.*]
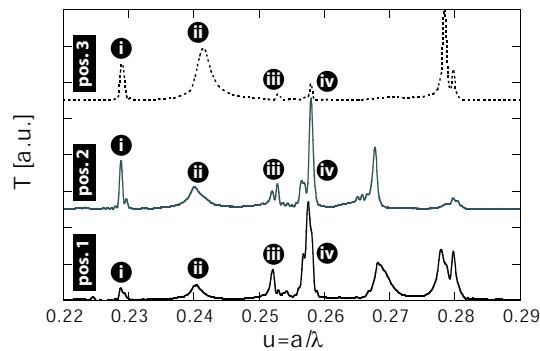
Figure 6.31: FDTD spectrum detected according to Fig. 6.30 with zero loss. The figure shows the spectra corresponding to three different excitation positions inside the cavity (parameters: $f = 0.33$, $\varepsilon_{\mathrm{sub}}$, $\varepsilon'' = 0$, # timesteps $= 10^5$).
[*Spectres FDTD détectés d'après le schéma de la figure 6.30 sans pertes. La figure montre les spectres correspondant à des positions différentes dans la cavité (paramètres: $f = 0.33$, ε_{sub}, $\varepsilon'' = 0$, # pas temporels $= 10^5$).*]

peak n°	u_0	Q_e	Q_0/Q_e	Q_{tot}
i	0.2287	611 ± 179	0.91 ± 0.29	197 ± 38
ii	0.2401	165 ± 70	3.24 ± 1.67	71 ± 26
iii	0.2519	679 ± 16	0.58 ± 0.01	182 ± 2
iv	0.2568	355 ± 128	1.08 ± 0.45	121 ± 30

Table 6.4: External quality factor Q_e extracted from the FDTD power spectra in Fig. 6.31. The error bar in the value for Q_e accounts for the fluctuations between the different excitation positions.
[*Facteur de qualité externe Q_e extrait des spectres de la Fig. 6.31. La barre d'erreur prend en compte les fluctuations entre les différentes positions d'excitations.*]

6.3.6   Application of the CMT model on bend design B-S3

Fig. 6.32 plots the transmission, the reflection and the losses for a bend and a splitter as a function of the ratio Q_0/Q_e. The four peaks of the B-S3 cavity (see Table 6.4) are indicated by vertical lines. In general, if the goal is to have a large bandwidth, the over-coupled regime ($Q_e \ll Q_0$) is advantageous, since even when the cavity is lossy, the light does not stay inside for a long time and thus the losses remain small and the transmission high over a large bandwidth. However, if high frequency selectivity is desired and in order to still have a high peak transmission, both Q_e and Q_0 have to be large. These considerations are based on the simplified assumption of monomode guides connected to a monomode cavity, but qualitatively they remain correct for the multimode case.
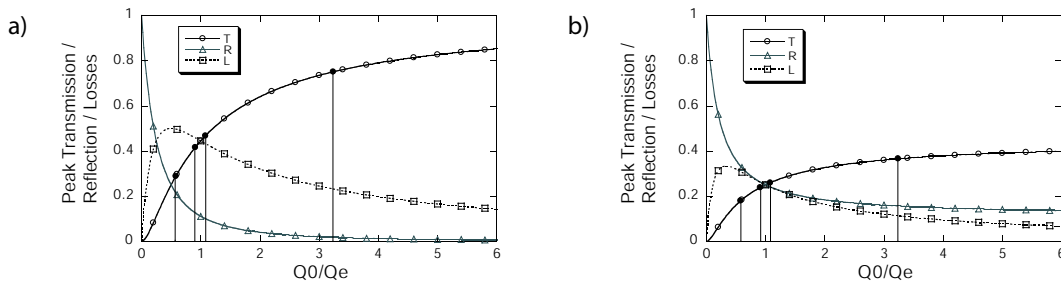
Figure 6.32: Transmission, reflection and losses at resonance as a function of the ratio between the intrinsic and external quality factor: a) for a bend, b) for a splitter. *[Transmission, réflection et pertes à la résonance en fonction du rapport du facteur de qualité intrinseque et externe: a) pour un virage, b) pour un diviseur.]*

The temporal CMT described in section 6.3.4 assumes, in principle, a monomode cavity. For not too closely spaced narrow band resonances, each cavity mode represents an independent transmission channel for the respective frequency sub-range. This is, however, not the case in the present example, where the resonances are overlapping in frequency space. One can help out with an approach based on transmission probability: The probability that a photon is NOT transmitted by the resonances u_1, u_2, ..., u_i is $(1 - T_1)(1 - T_2)\cdots(1 - T_i)$ and the probability of it being transmitted is thus $T_{\text{tot}} = 1 - [(1 - T_1)(1 - T_2)\cdots(1 - T_i)]$. The evaluation of this formula together with Eq. (6.32) for the case of the B-S3 bend, taking into account the four main resonances only, is displayed in Fig. 6.33. The agreement between the CMT and the FDTD spectrum is unsatisfactory. There is a general overestimation of the CMT transmission, which may be partly explained by the fact that the FDTD spectrum in Fig. 6.33 includes the in- and out-coupling and the propagation in the waveguides. Additionally the weighting of the relative resonances peaks does not fully agree. The discrepancy may be explained by the fact that the descibed CMT model is designed as single-mode model and does not include mode conversion at the bend and leaves out the properties of the waveguide.

The total transmission quality factor of the total cavity bend structure can be expressed as a function of Q_0 and the ratio Q_0/Q_e:

$$Q_{\text{tot}} = \left(\frac{1}{Q_0} + \frac{2}{Q_e} \right)^{-1} = \frac{Q_0}{1 + 2\frac{Q_0}{Q_e}} \tag{6.44}$$

This allows to plot Q_{tot} in the same graph as the maximal peak transmission $T_{\max}$ given by Eq. (6.32) (see Fig 6.34). The white circle evidences the parameter space corresponding to the bend design B-S3. It shows that for given intrinsic quality factors $Q_0 = 400 - 550$ and experimental peak transmissions of about $T_{\max} = 0.35$, the total quality factor of the transmission peaks should be in the order of $Q_{\text{tot}} = 200 - 400$. The quality factors that can be deduced from the experimental transmission spectrum are, however, below 100. It seems that this simplified model is not able to provide a complete description of the transmission properties of cavity resonant bends.
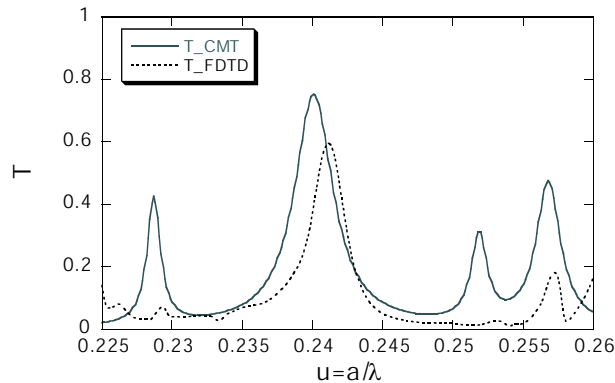
Figure 6.33: Plot of the transmission function of the B-S3 cavity bend calculated by the CMT (gray solid line) (only the 4 modes listed in Table 6.4 are taken into account) and in comparison the FDTD spectrum of the total transmission (dotted line).

[Fonction de transmission du virage à cavité B-S3 calculé avec la théorie des modes couplés (ligne solide grise) (seuls les modes indiqués dans le tableau 6.4 sont considérés) et pour comparaison le spectre FDTD de la transmission totale (ligne pointillée) est donné.]
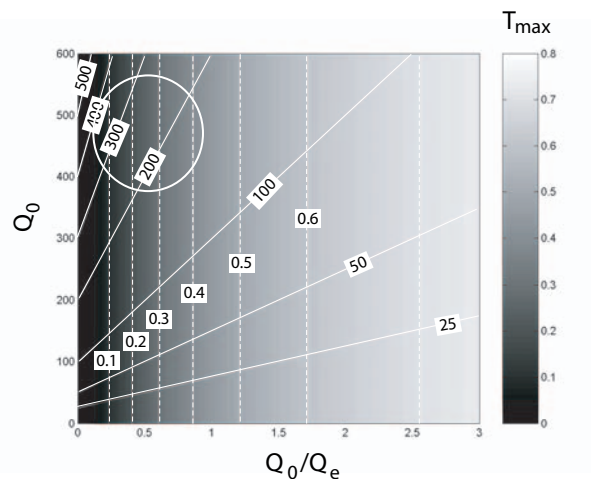
Figure 6.34: Total quality factor (solid lines) and maximum transmission (dotted lines) for a cavity resonant bend as a function of the 2D parameter space Q_0 and Q_0/Q_e. The white circle marks the parameters corresponding to bend design B-S3.

[Facteur de qualité total (lignes solides) et le maximum de transmission (lignes pointillées) pour un virage à cavité résonante en fonction de Q_0 et Q_0/Q_e. Le cercle blanc indique les paramètres correspondant au virage B-S3.]

6.4   Conclusions

The transmission properties of twelve different CRB designs and twelve different cavity resonant splitter designs have been measured and compared. None of the designs features extraordinary transmission levels. The best bend design (B-S3) features an average transmission of 20 % and a peak transmission exceeding 30 %. On the other hand the best splitter design (C-S1) transmits with 15 % on average and reaches 20 % peak transmission.

The experimental transmission spectra have been successfully compared to an FDTD calculation and the main transmission peaks could be attributed to the respective field maps calculated by PWE. The average transmission and the peak positions of the FDTD transmission spectra agree well with the experiment. However, the peak height in the simulation is significantly higher than the experimental values. This may be explained by fabrication imperfections (*e.g.* hole depth fluctuations of the barrier holes), degrading the value of Q_e.

We calculated the intrinsic quality factor with two different methods, the first based on overlap integrals between the field maps calculated by PWE and the holes and the second based on an weak probe FDTD calculation. The external quality factors have been calculated by FDTD.

A temporal coupled mode formalism has been successfully applied to the study of cavity resonant bends and splitters. Although the model is a good approximation, it does not provide a complete description of the transmission properties of cavity resonant bends.

Chapter 7

Linear couplers

Linear or (co-)directional couplers have been used in classical integrated optics for a long time. In its simplest form, a directional coupler consists in two parallel dielectric waveguides placed in close proximity. Energy can be exchanged between the two waveguides by means of evanescent field coupling. In its simplest form the coupler can be considered as coupled two-level system.

The principal parameters of the coupler, *i.e.* the coupling strength and the frequency response, are closely related to the dispersion relation of the coupled waveguides. The functionality of the coupling device can be modified through dispersion engineering. Three regimes can be envisaged (see Fig. 7.1). In regime (a) the waveguide dispersion is linear and the splitting energy is frequency-independent. Such a regime is interesting for broad-band switches or 3dB-couplers. In the regime (b) the splitting in β or the group velocity is frequency dependent. This could be exploited in add-drop filters. The resulting channel spacing is, however, not regular in most cases. The last regime (c) considers a possible decoupling of the PhC waveguides. This may be interesting for reducing cross talk between neighbouring waveguides inside PhC ICs. The density of elements (integration level) might in fact be limited by crosstalk between the waveguides and methods would have to be developed in order to cancel out or at least reduce coupling.
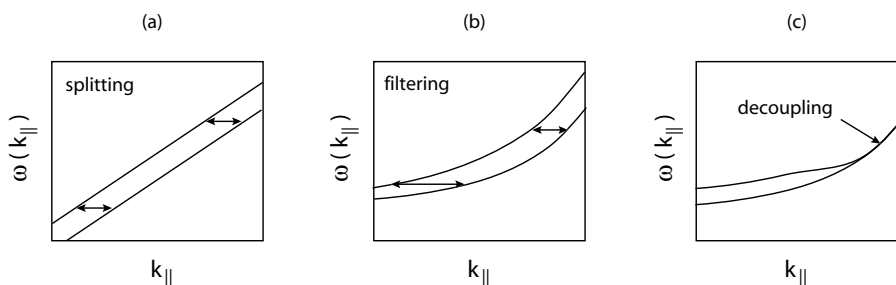
Figure 7.1: Couplers can be used for different applications: a) Linear dispersion leads to frequency-independent intensity splitting. b) Frequency-dependent splitting is useful for filtering application. c) In this regime the waveguides are decoupled from each other.

[Les coupleurs peuvent être utilisés pour différentes applications: a) La dispersion linéaire est utilisé pour la division des intensités. b) La division dépendant de la fréquence peut être utile pour des applications de filtrage. c) Dans ce régime les guides d'ondes sont découplés l'un de l'autre.]

143

The physics of waveguide coupling provides a rich palette of different applications. These include broadband 3-dB intensity splitters [97], active power-switches [98] and wavelength selective add-drops [99]. In the most general case, the system consists of a configuration of N parallel waveguides which may be symmetric or not.

Couplers are of interest since they are important building blocks for integrated optics in general and specifically for PhC ICs. The monolithic combination of this building block with other functionalities has the potential to provide novel applications. PhC-based directional couplers have the potential to provide a significantly shorter coupling length.

7.1 Measurement results

The measurements in this chapter have been performed on the sample labelled 'GWW5-2/part C'.

The couplers are basically two parallel W3 waveguides separated by a spacer of PhC. The coupler structures have been fabricated in three different lengths (100 a, 200 a, 400 a). One structure typically contains a W1-coupler with a single row between the two W1 waveguides (design A), then a W3-coupler with a single row separation (design B) and a W3-coupler with a perforated barrier (a single row with every second hole omitted) (design C) and the corresponding normalisation waveguides (see Fig. 7.2). The idea of design C was to increase the transmissibility of the barrier in order to increase the coupling and reduce the coupling length.
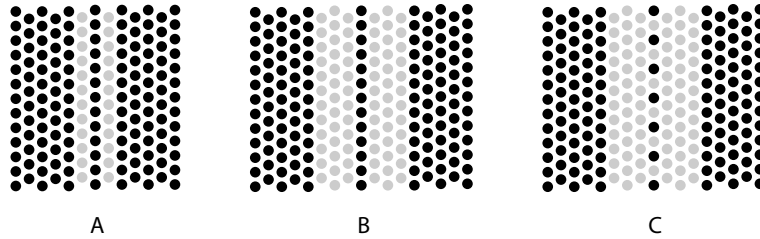
Figure 7.2: Sketch of the different studied coupler designs.
[Représentation schématique des différents types de coupleurs étudiés.]

The SEM micrographs (see Fig. 7.3) show an overview of the structures of a single period ($a = 250$ nm) as well as a close-up of the coupler design B and C.

The values for the air-filling factor deduced from the experimental MSB spectra (as described in section 5.1.3) for the period shown in Fig. 7.5(a) and two additional periods are listed in Table 7.1.

a	L=100 a	L=200 a	L=400 a
250	0.29	0.24	–
270	0.36	0.33	0.33
290	0.40	0.38	–

Table 7.1: Air-filling factor of the different periods deduced from the MSB position.
[Facteur de remplissage des périodes différentes déduit de la position du MSB.]

One notes a large fluctuation between different periods and that for the smallest period the air-filling factor is significantly smaller than the nominal value.

Experimentally, the structures are measured by exciting the different structures at a constant distance $d_e = 20\,\mu$m and the structures are placed at the distance $d_f = 40\,\mu$m (see Fig. 7.4). Light is injected in *port A* of the coupler, couples partly into *port B* and is collected at the facet.

It should be noted that the measurement principle relies on a perfect facet quality. This was not the case for most of the periods and doses, and thus only a very limited set of data was useful. The raw transmission spectra for the period $a = 250\,$nm are depicted in Fig. 7.5.
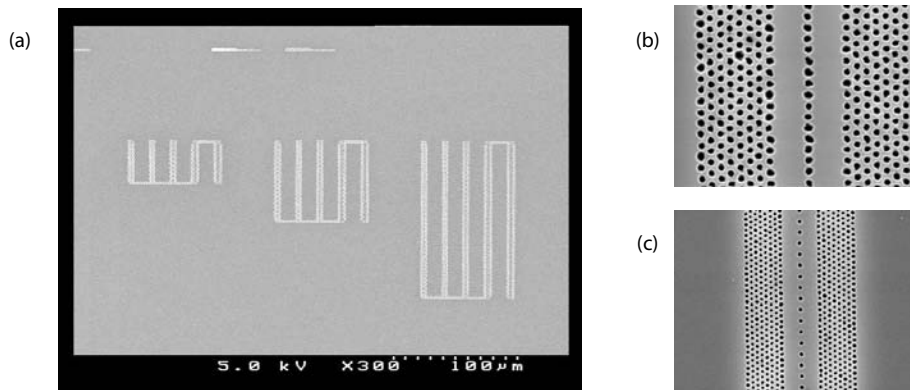
Figure 7.3: SEM images of coupler structures. a) Structures of three different lengths (100 a, 200 a and 400 a) have been fabricated. b) design B (1 row separation) c) design C (1 row separation with every second hole omitted).
[Images MEB des coupleurs. a) Les structures ont été fabriquées en trois longeurs différentes (100 a, 200 a and 400 a). b) structure B (1 rangée de séparation). c) structure C (1 rangée de séparation avec chaque second trous omis.]
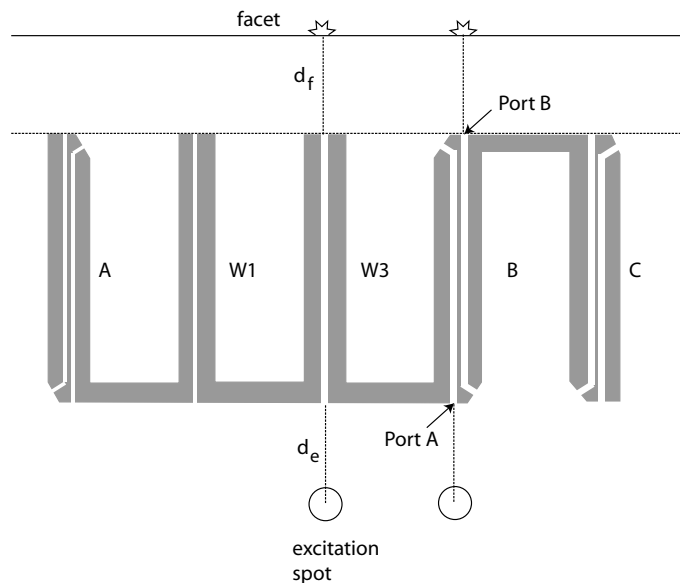
Figure 7.4: Schematic representation of the measurement configuration.
[Schéma de la configuration de mesure.]
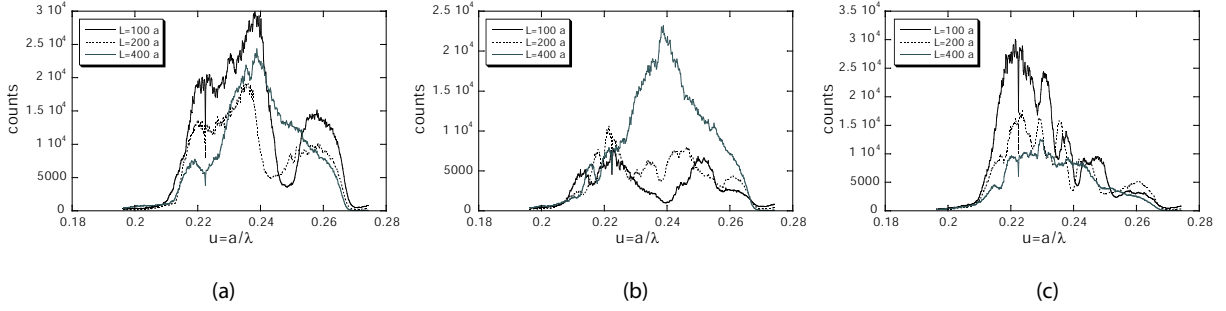
Figure 7.5: Raw spectra from the sample GWW5-2, part E (a=250nm). a) spectra from the normalisation guides, b) coupler transmission design B, c) coupler transmission design C.
[Spectres bruts de l'échantillon GWW5-2, part E (a=250nm). a) spectres des guides de normalisation, b) transmission du coupleur B, c) transmission du coupleur C.]

7.2 Discussion and data analysis

7.2.1 Definition of the coupling length

The coupling length L_c is defined as the distance after which the wave has completely switched form one waveguide to the other. Directional couplers can be analysed either by considering the complete structure consisting of all the guides and their surrounding media (supermode approach) or by considering the coupling and energy exchange between individual waveguides in a perturbative approach (coupled mode approach). Both formulations have their pros and contras.

7.2.1.1 Supermode approach

In the simplest case of two monomode guides, the structure supports two supermodes $|\phi_+\rangle$ and $|\phi_-\rangle$ (also called normal modes) with even and odd parity, respectively (see Fig. 7.6). The supermodes have different propagation constants β_{odd} and β_{even}. They can be expressed by the uncoupled modes $|A\rangle$ and $|B\rangle$ in waveguide A and B, respectively:

$$|\phi_+\rangle = \frac{|A\rangle + |B\rangle}{\sqrt{2}} \qquad |\phi_-\rangle = \frac{|A\rangle - |B\rangle}{\sqrt{2}} \tag{7.1}$$

The total field in the coupler can be expressed as superposition of the two supermodes, *i.e.*

$$|\phi(z) = \frac{1}{\sqrt{2}}|\phi_+\rangle e^{j\beta_+ z} + \frac{1}{\sqrt{2}}|\phi_-\rangle e^{j\beta_- z} = \frac{1}{2}|A\rangle(e^{j\beta_+ z} + e^{j\beta_- z}) + \frac{1}{2}|B\rangle(e^{j\beta_+ z} - e^{j\beta_- z})$$

$$= \frac{e^{j\beta_- z}}{2}\left[\left(e^{j\Delta\beta z} + 1\right)|A\rangle + \left(e^{j\Delta\beta z} - 1\right)|B\rangle\right] \quad \text{with} \quad \Delta\beta = \beta_+ - \beta_- \tag{7.2}$$

At the beginning ($z = 0$) of the coupling section, the field is completely in waveguide A, *i.e.* $|\phi(z = 0)\rangle = |A\rangle$. After the coupling length L_c the field has completely switched
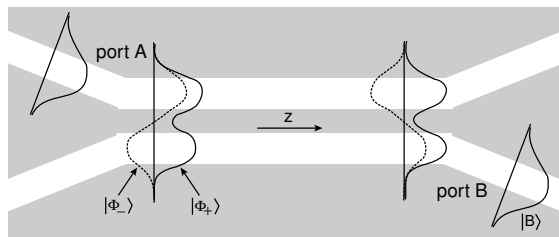
Figure 7.6: Directional coupling in terms of the supermode approach: The input wave at port A excites a superposition of the even and odd mode. At the end of the coupling length the phase shift between the two supermodes is π and the wave leaves the coupler at port B.

[Couplage directionnel dans une description à l'aide de supermodes: L'onde incidente excite une superposition de modes pair et impair. Après la longueur de couplage, le déphasage entre les 2 supermodes est π et l'onde sort du port B.]

to waveguide B, *i.e.* $|\phi(z = L_c\rangle = |B\rangle$. This is only the case if the coupling length (L_c) is an odd multiple of half the beat length, *i.e.*

$$L_c = \frac{1}{2}L_B = \frac{\pi}{\Delta\beta} \equiv \frac{\pi}{|\beta_{\text{odd}} - \beta_{\text{even}}|} \tag{7.3}$$

A schematic dispersion relation of two coupled waveguides is depicted in Fig. 7.7. It shows the uncoupled mode and the even and the odd supermode that have a difference in the propagation constant of $\Delta\beta$. In the case of identical monomode waveguides the power transfer is complete. In the case of two coupled *multimode* waveguides (*e.g.* W3), there are further restrictions with respect to complete transfer (see below).
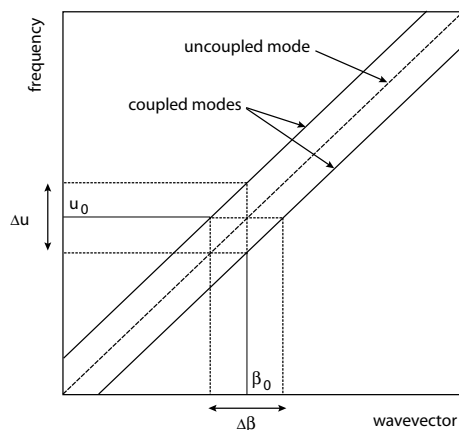
Figure 7.7: Schematic dispersion relation of two coupled waveguides.
[Schéma de la relation de dispersion de deux guides couplés.]

An alternative derivation of the coupling length originates from the *Rabi oscillation* of two coupled oscillators: The coupling between two degenerate states with energy E_A and E_B leads to the formation of two coupled states ϕ_+, ϕ_- with the corresponding energies E_+ and E_-. Since the system is prepared in a state (input mode) that is not an eigenstate of the system (ϕ_+, ϕ_-) the energy now oscillates between state ϕ_+ and ϕ_- with the typical Rabi frequency proportional to the coupling W_{AB} [100]:

$$P_{A \to B}(t) = \frac{4|W_{\text{AB}}|^2}{4|W_{\text{AB}}|^2 + (E_A - E_B)^2} \sin^2\left[\sqrt{4|W_{\text{AB}}|^2 + (E_A - E_B)^2}\,\frac{t}{2\hbar}\right] \tag{7.4}$$

where $2|W_{AB}|$ corresponds to the total splitting (see Fig. 7.8).
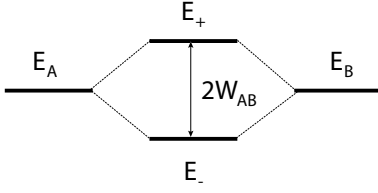
Figure 7.8: Schematic diagram of the Rabi splitting of a two-level system.
[*Schéma du splitting Rabi d'un système à deux niveaux.*]

For $E_A = E_B$ one obtains:

$$P_{A \to B}(t) = \sin^2 \omega t \quad \text{with} \quad \omega = \frac{|W_{AB}|}{\hbar} \quad \text{and} \quad t = \frac{z}{v_G} \tag{7.5}$$

The coupling length defined by complete power switching is given by:

$$\frac{|W_{AB}|}{\hbar} \frac{L_c}{v_G} = \frac{\pi}{2} \quad \longrightarrow \quad L_c = \frac{\pi \hbar v_G}{2|W_{AB}|} \tag{7.6}$$

with $2|W_{AB}| = \hbar|\Delta\omega| = \hbar \left(\frac{2\pi c}{a} \right) |\Delta u|$, one obtains

$$\frac{L_c}{a} = \frac{1}{2n_g |\Delta u|} \tag{7.7}$$

The coupling length is thus inversely proportional to the splitting energy Δu (see Fig. 7.7) and the group index. For the case of a linear dispersion the formulation (7.7) is completely equivalent to (7.3).

In the case the waveguides of a coupler being single mode, a complete power transfer occurs between waveguide A and B. In the more general case of multi mode waveguides a superposition of many supermodes ($N > 2$) may be excited at the coupler entry having different coupling length. Therefor the power transfer is not complete anymore and one concentrates on the supermodes with the biggest weight.

Taking the supermodes of the coupled waveguide as a basis, an arbitrary field distribution propagating inside the coupler can be broken down into the supermodes, *i.e.*

$$E_{\text{tot}}(y, z) = \sum_{n=1}^{N} c_n \cdot B_n(y) \cdot e^{j\beta_n z} \tag{7.8}$$

where $B_n(y)$ is the mode profile of the supermode and β_n its propagation constant. In principle the field distributions are defined in a supercell which is one period wide (Bloch mode), but in order to simplify the numerical calculation only a line profile of the supermodes is considered. The profiles are displayed in Fig. 7.9. At $u = 0.24$ there exist three modes in each W3 waveguide, which leads to six supermodes.

One has to find the correct weighting factors that provide at $z = 0$ a field distribution similar to the fundamental mode in waveguide A and no field at all in Waveguide B, which is equivalent to minimise the following functional:

$$F([c_1, c_2, \ldots c_N]) = \int_{\text{WG B}} |\sum_{n=1}^{N} c_n \cdot B_n(y)|^2 \tag{7.9}$$

The result of the minimization process is depicted in Fig. 7.10. The solid line corresponds to the fundamental mode of waveguide A and the dotted line is the superposition of the six supermodes. The two square markers indicate the interval in which the functional Eq. (7.9) has been minimized.

The weighting factors are $c_1 = -0.75$, $c_2 = -0.66$, $c_3 = -0.03$, $c_4 = -0.04$, $c_5 = -0.05$ and finally $c_6 = -0.04$. One notes that 99 % of the energy is in the first two modes. This means that almost complete power transfer between the two waveguides is possible and that only the $\Delta\beta$ between the first two supermodes has to be considered.
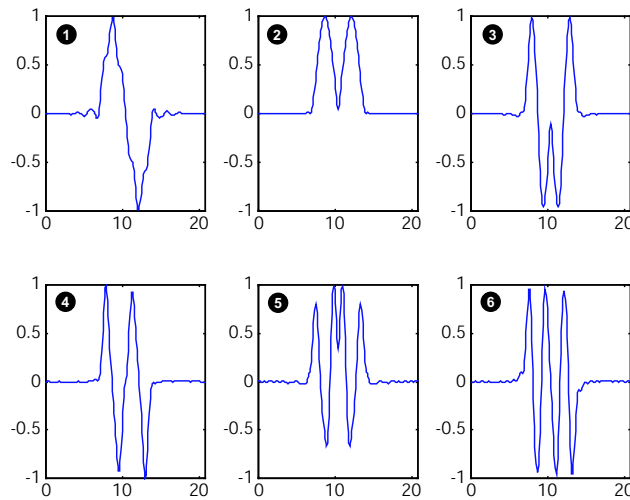
Figure 7.9: Profiles of the supermodes of the coupled waveguide structure. For each single waveguide mode there is an even and an odd supermode (Parameters: $u = 0.24$, $f = 0.33$, $\varepsilon_{\mathrm{sub}} = 11.4$)

[Profiles des supermodes de la structure guides couplés. Pour chaque mode du guide isolé, il existe un supermode pair et impair (Paramètres: $u = 0.24$, $f = 0.33$, $\varepsilon_{sub} = 11.4$).]
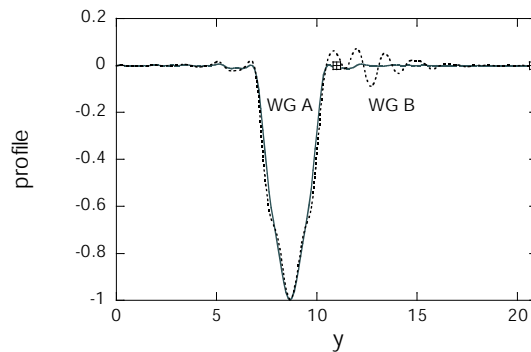
Figure 7.10: Superposition of supermodes in order to minimize the field in waveguide B (dotted line). For comparison, the fundamental mode of waveguide A (solid line) is indicated too.

[Superposition des supermodes en minimisant le champ dans le guide d'onde B (ligne pointillée). Le mode fondamental du guide d'onde A est aussi indiqué pour permettre la comparaison.]

7.2.1.2   Coupled mode approach

In a coupler consisting of two parallel dielectric waveguides usually only co-directional coupling takes place. In the special case of PhC waveguides, where the guide interface is periodically corrugated, however, contra-directional coupling can take place simultaneously. This allows for coupling between the fundamental mode and counter-propagating higher-order modes, leading to the formation of mini-stopbands [83] (see chapter 5). The contra-directional coupling, however, has already been treated in section 5.1.4.1. Therefore we consider here only the co-directional coupling.

Let us start with the general formulation for two parallel dielectric waveguides A and B along the z-direction, which may also include loss. The guides are invariant in z-direction and so the mode profile of the individual modes is constant. For the derivation of the CMEs Ref. [85] is followed. Each individual waveguide mode is a solution of

$$\left[\nabla_T^2 - \beta_i^2 + \frac{\omega^2}{c^2}(\varepsilon_{clad} + \Delta\varepsilon_i)\right]\mathbf{E}_i = 0 \qquad i = a, b \tag{7.10}$$

where ε_{clad} depicts the background dielectric constant and $\Delta\varepsilon_i$ the additional dielectric material forming waveguide i.

The wave equation of the coupled waveguide is given by:

$$\left[\nabla^2 - \frac{\varepsilon(x,y)}{c^2}\frac{\partial^2}{\partial t^2}\right]\mathbf{E} = 0 \tag{7.11}$$

$$\text{with}\quad \varepsilon(x,y) = \varepsilon_{clad}(x,y) + \Delta\varepsilon_a(x,y) + \Delta\varepsilon_b(x,y) \tag{7.12}$$

The total field (supermode) of the coupled structure is expressed on the basis of the unperturbed modes of the single guides:

$$\mathbf{E}(x,y,z,t) = A(z)\mathbf{E}_a(x,y)e^{j(\omega t - \beta_a z)} + B(z)\mathbf{E}_b(x,y)e^{j(\omega t - \beta_b z)} \tag{7.13}$$

and has to satisfy the wave equation of the coupled structure:

$$\left[\nabla^2 + \frac{\omega^2}{c^2}(\varepsilon_{clad} + \Delta\varepsilon_a + \Delta\varepsilon_b)\right]\left[A(z)\mathbf{E}_a(x,y)e^{j(\omega t - \beta_a z)}\right.$$
$$\left. + B(z)\mathbf{E}_b(x,y)e^{j(\omega t - \beta_b z)}\right] = 0 \tag{7.14}$$

To evaluate (7.14), the double derivative with respect to z has to be taken:

$$\frac{\partial^2}{\partial z^2}A(z)\mathbf{E}_a(x,y)e^{i(\omega t - \beta_a z)} = \left[-\beta_a^2 A(z) - 2j\beta_a\frac{dA}{dz} + \frac{d^2A(z)}{dz^2}\right]\mathbf{E}_a(x,y)e^{j(\omega t - \beta_a z)} \tag{7.15}$$

$$\frac{\partial^2}{\partial z^2}B(z)\mathbf{E}_b(x,y)e^{i(\omega t - \beta_b z)} = \left[-\beta_b^2 B(z) - 2j\beta_b\frac{dB}{dz} + \frac{d^2B(z)}{dz^2}\right]\mathbf{E}_b(x,y)e^{j(\omega t - \beta_b z)} \tag{7.16}$$

Plugging (7.13) into (7.14), dropping the terms that form (7.10) and assuming slow

variation of the mode amplitudes over z, *i.e.* $\left(\frac{d^2 A_m}{dz^2} = \frac{d^2 B_m}{dz^2} = 0\right)$, one obtains:

$$-2j\beta_a \frac{dA}{dz}|E_a\rangle e^{-j\beta_a z} - 2j\beta_b \frac{dB}{dz}|E_b\rangle e^{-j\beta_b z} + \frac{\omega^2}{c^2}\Delta\varepsilon_b|E_a\rangle e^{-j\beta_a z}A$$

$$+\frac{\omega^2}{c^2}\Delta\varepsilon_a|E_b\rangle e^{-j\beta_b z}B = 0 \qquad (7.17)$$

$$-2j\beta_b \frac{dB}{dz}|E_b\rangle e^{-j\beta_b z} - 2j\beta_a \frac{dA}{dz}|E_a\rangle e^{-j\beta_a z} + \frac{\omega^2}{c^2}\Delta\varepsilon_a|E_b\rangle e^{-j\beta_b z}B$$

$$+\frac{\omega^2}{c^2}\Delta\varepsilon_b|E_a\rangle e^{-j\beta_a z}A = 0 \qquad (7.18)$$

Multiplying by the complex conjugate of $\mathbf{E}_a$ and $\mathbf{E}_b$, respectively and integrating over the cross-section leads to:

$$-2j\beta_a \frac{dA}{dz}\langle E_a|E_a\rangle e^{-j\beta_a z} - 2j\beta_b \frac{dB}{dz}\underbrace{\langle E_a|E_b\rangle}_{=0} e^{-j\beta_b z}$$

$$+\frac{\omega^2}{c^2}\langle E_a|\Delta\varepsilon_b|E_a\rangle e^{-j\beta_a z}A + \frac{\omega^2}{c^2}\langle E_a|\Delta\varepsilon_a|E_b\rangle e^{-j\beta_b z}B = 0 \qquad (7.19)$$

$$-2j\beta_b \frac{dB}{dz}\langle E_b|E_b\rangle e^{-j\beta_b z} - 2j\beta_a \frac{dA}{dz}\underbrace{\langle E_b|E_a\rangle}_{=0} e^{-j\beta_a z}$$

$$+\frac{\omega^2}{c^2}\langle E_b|\Delta\varepsilon_a|E_b\rangle e^{-j\beta_b z}B + \frac{\omega^2}{c^2}\langle E_b|\Delta\varepsilon_b|E_a\rangle e^{-j\beta_a z}A = 0 \qquad (7.20)$$

which can be simplified to

$$\frac{dA}{dz} = -j\underbrace{\frac{1}{2\beta_a}\frac{\omega^2}{c^2}\frac{\langle E_a|\Delta\varepsilon_b|E_a\rangle}{\langle E_a|E_a\rangle}}_{\Delta\beta_a} - j\underbrace{\frac{1}{2\beta_a}\frac{\omega^2}{c^2}\frac{\langle E_a|\Delta\varepsilon_a|E_b\rangle}{\langle E_a|E_a\rangle}}_{\kappa_{ab}} e^{-j\beta_b z}Be^{j(\beta_a - \beta_b)} = 0 \quad (7.21)$$

$$\frac{dB}{dz} = -j\underbrace{\frac{1}{2\beta_b}\frac{\omega^2}{c^2}\frac{\langle E_b|\Delta\varepsilon_a|E_b\rangle}{\langle E_b|E_b\rangle}}_{\Delta\beta_b} - j\underbrace{\frac{1}{2\beta_b}\frac{\omega^2}{c^2}\frac{\langle E_b|\Delta\varepsilon_b|E_a\rangle}{\langle E_b|E_b\rangle}}_{\kappa_{ba}} e^{-j\beta_a z}Ae^{j(\beta_b - \beta_a)} = 0 \quad (7.22)$$

where the terms $\Delta\beta_a$, $\Delta\beta_b$ result from the dielectric perturbation of waveguide A and B due to the presence of the opposite waveguide B and A, respectively and represent only a small correction to the propagation constants β_a and β_b (see Fig. 7.11).

So by incorporating this small correction of the propagation constant in the total field [85]:

$$\mathbf{E}(x, y, z, t) = A(z)\mathbf{E}_a(x, y)e^{j(\omega t - (\beta_a + \Delta\beta_a)z)} + B(z)\mathbf{E}_b(x, y)e^{j(\omega t - (\beta_b + \Delta\beta_b)z)} \qquad (7.23)$$

the CMEs for directional coupling become:

$$\frac{dA}{dz} = -j\kappa_{ab}Be^{j2\delta\beta_{ab}z}$$

$$\frac{dB}{dz} = -j\kappa_{ba}Ae^{-j2\delta\beta_{ab}z} \qquad (7.24)$$
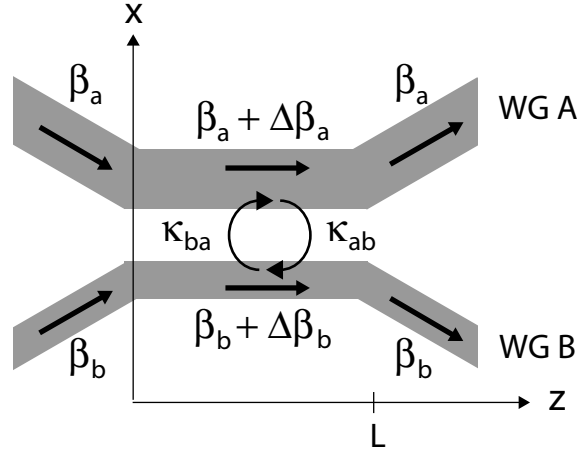
Figure 7.11: Scheme of a directional coupler. The unperturbed propagation constants β_a, β_b of waveguide A and B are modified in the coupling region due to the presence of the additional dielectric material of the opposite waveguide to $\beta_a + \Delta\beta_a$ and $\beta_b + \Delta\beta_b$. The coupling between the 2 waveguides is described by the coupling constant κ_{ab}.

[Schéma du coupleur directionel. Les constantes de propagation non-perturbées β_a, β_b du guide A et B sont modifiées dans la région de couplage à $\beta_a + \Delta\beta_a$ et $\beta_b + \Delta\beta_b$. Le couplage entre les 2 guides est décrit par la constante de couplage κ_{ab}.]

where $\delta\beta_{ab} = \frac{1}{2}(\beta_a + \Delta\beta_a - \beta_b - \Delta\beta_b)$. By introducing the new variables $A = \tilde{A}e^{+j\delta\beta_{ab}\cdot z}$ and $B = \tilde{B}e^{-j\delta\beta_{ab}\cdot z}$ [86], Eq. (7.24) becomes:

$$\frac{d}{dz}\begin{pmatrix} \tilde{A} \\ \tilde{B} \end{pmatrix} = \begin{pmatrix} -j\delta\beta_{ab} & -j\kappa_{ab} \\ -j\kappa_{ba} & j\delta\beta_{ab} \end{pmatrix} \cdot \begin{pmatrix} \tilde{A} \\ \tilde{B} \end{pmatrix} \tag{7.25}$$

Losses can be introduced, as usual, by means of a complex propagation constant. Introducing the modal loss coefficients α_a, α_b for the modes in waveguide A and B, respectively, Eq. (7.25) becomes:

$$\frac{d}{dz}\begin{pmatrix} \tilde{A} \\ \tilde{B} \end{pmatrix} = \begin{pmatrix} -j\delta\beta_{ab} + \alpha_a & -j\kappa_{ab} \\ -j\kappa_{ba} & j\delta\beta_{ab} + \alpha_b \end{pmatrix} \cdot \begin{pmatrix} \tilde{A} \\ \tilde{B} \end{pmatrix} \tag{7.26}$$

$$\text{with} \quad \kappa_{ab} = \frac{\omega^2}{\beta_a c^2} \frac{\langle E_a | \Delta\varepsilon_a | E_b \rangle}{\langle E_a | E_a \rangle} = \kappa_{ba}^{\star} \tag{7.27}$$

Using reduced units and making the coupling coefficient symmetric in β leads to:

$$\kappa_{ab} = \frac{\pi u^2}{\sqrt{\hat{\beta}_a \hat{\beta}_b} a} \frac{\langle E_a | \Delta\varepsilon_a | E_b \rangle}{\langle E_a | E_a \rangle} = \kappa_{ba}^{\star} \qquad \text{with } \beta_{a/b} = \hat{\beta}_{a/b} \frac{2\pi}{a} \tag{7.28}$$

So far, the derivation was general for two dielectric waveguides. In the case of PhC couplers, $\Delta\varepsilon_b$ corresponds by analogy to the additional dielectric material inside the missing holes that form guide B. The discrete translational symmetry of the PhC waveguide is taken into account by integrating over one unit cell in propagation direction. At least for index-guided modes this analogy can be established. In addition, these

considerations affect only the direct calculation of the coupling coefficients with overlap integrals. Alternatively the coupling coefficient can also be evaluated via the splitting energy (see section 7.2.3.1). In this case the supercell calculation of two parallel PhC waveguides supplies exact values for κ_{ab}.

The dielectric perturbation in this case is given by:

$$\Delta\varepsilon_{a/b}(x,y) = \begin{cases} \varepsilon_{sub} - \varepsilon_{air} & \text{inside 'missing' holes of guide A/B} \\ 0 & \text{else} \end{cases} \qquad (7.29)$$

In the case of PhC waveguides we don't average over the cross-section, but over the area of the supercell. When the two waveguides are identical, the wavevectors for equal modes are independent of the waveguide, *i.e.* $\delta\beta_{ab} = 0$.

The coefficient for directional coupling can also be read out directly from the dispersion relation of the coupled waveguide (see Fig. 7.13).

The relation between the directional coupling coefficient and energy splitting between the higher-order supermodes is given by:

$$\text{From Eq. (7.7):} \quad \frac{L_c}{a} = \frac{1}{2n_g\Delta u} \quad \longrightarrow \quad \kappa_{ab} = \frac{\pi}{2L_c} = \pi n_g \Delta u_{ab} \qquad (7.30)$$

where Δu_{ab} can be extracted from the dispersion diagram of two parallel waveguides separated by m rows (see Fig. 7.13). The coupling length L_c is given by

$$L_c = \frac{\pi}{2\kappa_{ab}} \qquad (7.31)$$

The next step is now to test the described coupled mode formalism on some numerical examples. In this case we do not calculate the coupling coefficient for the fundamental mode, but for the fifth order mode. It possesses admittedly a very low group velocity and is therefore difficult to excite from the input waveguide. But, as sketched below, the MSB mechanism allows one to circumvent the problem and to efficiently convert the fundamental mode into the fifth-order mode.

The idea of using an intermediate mode to couple from one waveguide to the next was first adapted to PhC couplers by S. Olivier [101,56] (see Fig. 7.12). The goal would be to have an add-drop with small channel spacing. From the point of view of coupled mode theory there are no limitations on the number of modes involved.
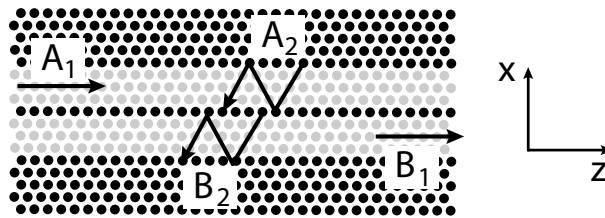
Figure 7.12: Principle: The fundamental mode A_1 is converted into a counter-propagating higher-order mode A_2 at the MSB energy which then easily couples into the corresponding higher-order mode B_2 in the opposite waveguide. This mode is converted back into the forward-propagating fundamental mode B_1.
[*Principe: Le mode fondamental A_1 est converti en un mode d'ordre supérieur qui se propage dans la direction opposée. Celui-ci se couple facilement au mode correspondant B_2 du guide opposé. Ce mode est reconverti en mode fondamental B_1.*]
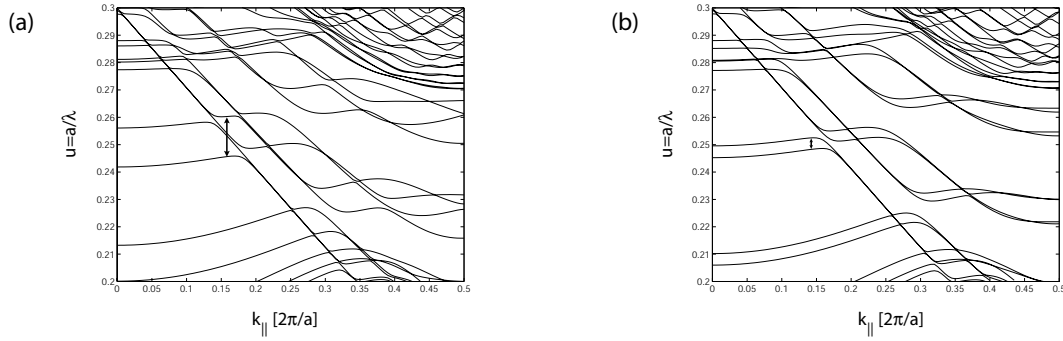
Figure 7.13: Dispersion diagram of two parallel W3 waveguides (parameters: $f = 0.33$, $\varepsilon_{\mathrm{sub}} = 11.4$, $G_{\mathrm{max}} = 1.6$). a) case with 1 row separation. b) case with 3 rows separation.
[Diagramme de dispersion de deux guides W3 parallèles (paramètres: $f = 0.33$, $\varepsilon_{sub} = 11.4$, $G_{max} = 1.6$). a) cas avec 1 rangée de séparation. b) cas avec 3 rangées de séparation.]

Fig. 7.13 shows the dispersion relation of a coupler structure consisting of two W3 waveguides, separated either by one or three rows. The arrow indicates for which energy and propagation constant the calculation has been performed.

The numerical values for the directional coupling coefficients evaluated with the two methods are listed in Table 7.2. The subscripts (1) and (2) denote the fundamental mode and the fifth-order mode, respectively. The analogy with the dielectric waveguide for the calculation of the coupling coefficients by means of overlap integrals seems to work quite well for the considered air-hole structures. One notes that the agreement between the two methods is better for the 'weak' coupling case (m=3). Furthermore the coupling lengths for the fifth-order mode (2) are extremely small.

	by overlap integral		by dispersion relation	
	m=1	m=3	m=1	m=3
$\Delta u_{\mathrm{ab}}^{(1)}$	–	–	≈ 0.0001	≈ 0.0001
$\kappa_{\mathrm{ab}}^{(1)} \quad [a^{-1}]$	0.0017	0.001	≈ 0.001	≈ 0.001
$L_c^{(1)} \quad [a]$	924	1571	≈ 1570	≈ 1570
$\Delta u_{\mathrm{ab}}^{(2)}$	–	–	0.015	0.0032
$\kappa_{\mathrm{ab}}^{(2)} \quad [a^{-1}]$	1.36	0.386	1.69	0.36
$L_c^{(2)} \quad [a]$	1.15	4.07	0.93	4.36

Table 7.2: Co-directional coupling coefficient of the fundamental (1) and the order 5 mode (2) for two different waveguide separations (m equals the number of rows in the barrier). The coefficients have been evaluated both by explicit evaluation of the overlap integral and by extracting the splitting energy from the dispersion relation (Parameters: $f = 0.37$, $\varepsilon_{\mathrm{sub}} = 11$).
[Coefficients de couplage co-directionnel pour le mode fondamental (1) et le mode d'ordre 5 (2) pour deux différentes distances de séparation (m est égal au nombre de rangées dans la barrière). Les coefficients ont été évalués par les intégrales de recouvrement et par la séparation en énergie dans la relation de dispersion (Paramètres: $f = 0.37$, $\varepsilon_{sub} = 11$).]

On the other hand, the numerical agreement between the values extracted from the dispersion relation and the overlap integral is quite satisfactory.

7.2.2 Experimental deduction of the coupling length

By normalising the coupler transmission with the straight waveguide transmission, one can elliminate the propagation losses. With Eq. (7.5) the z-dependence of the transferred power writes:

$$P_{A \to B}(t) \propto \sin^2 \kappa_{ab} z = \sin^2 \frac{\pi}{2L_c} z \qquad (7.32)$$

which allows one to deduce the coupling length from the normalised experimental spectrum. An example of a fit for design B taken around $u = 0.221$ is shown in Fig. 7.14. The fact that the fit curve exceeds unity can be attributed to experimental uncertainties. It yields the coupling length $L_c = 336 \pm 9$ with less than 3 % fit error [1]. The number of three sampling points is quite at the limit of what is allowed by the sampling theorem.
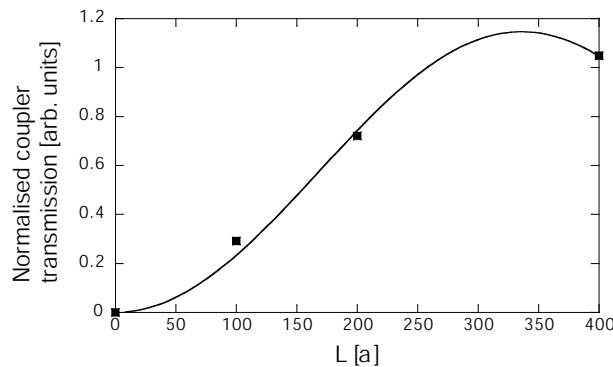
Figure 7.14: Example of a coupling length fit taken at $u = 0.221$: The normalised coupler transmission (square marker) is fitted with a Eq. (7.32) and yields a coupling length $L_c = 336$ a.
[Exemple d'un fit de longueur de couplage prise à l'énergie $u = 0.221$: La courbe théorique (donnée par l'Eq. (7.32) de la transmission normalisée du coupleur passe par les symboles carrés et rend une longueur de couplage $L_c = 336$ a.]

Concerning coupler design A (based on W1 waveguides), no reliable information could be extracted because the collected intensity, especially for the $L = 400$ a structures, was very low.

The fit for design C was less reliable than for design B. Nevertheless the coupling length of design C is, as expected from the better mode overlap, diminished with respect to design B. The fitted coupling length values as a function of frequency and the corresponding fit error for both designs are presented in Fig. 7.15.

---

[1]Defined as the root mean square value of the difference between the measured points and the fit.
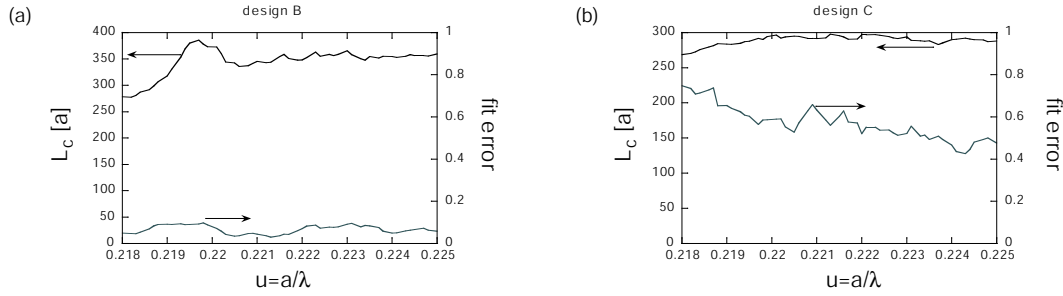
Figure 7.15: Coupling length and fit error extracted from experimental spectra. a) design
B, b) design C.
[Longueur de couplage et son erreur de fit déduit des spectres expérimentaux.]

For design B, the coupling length is of the order of 350 periods and for design C of the
order of 290 periods for an energy range of $u = 0.218 - 0.225$. These values correspond
to absolute lengths of the order of 80 μm. This is significantly below the values of
classical integrated optics (*e.g.* conventional lithium niobate directional couplers have
coupling lengths in the range of $0.1 - 5$ mm [102]), but is rather large for PhC circuits
where the smallest elements, *e.g.* bends are around 1 μm. In section 7.2.3.1 it is shown
that the coupling length can be significantly reduced by tuning the barrier holes.

7.2.3   Calculation of the coupling length

7.2.3.1   Calculation of the coupling length by PWE

By taking a supercell which comprises the two W3 waveguides, one can calculate the
dispersion relation of the coupled structure. The guided mode dispersions correspond
then to the supermodes of the structure. From the splitting Δu, the group-index
$n_g = 3.42$ and Eq. (7.7), one can directly determine the coupling length. The splitting
energy of the fundamental mode is very small, of the order of $\Delta u = 10^{-4}$ (see Fig.
7.16).

This makes the PWE calculation a delicate task and one has to choose the supercell
height and the number of plane waves carefully in order to get good convergence. The
coupling between the fundamental modes is very weak. This is maybe due to the fact
that in the case of air-holes in a high-index dielectric the fundamental mode is index-
guided and thus rather strongly confined. The majority of the publications on PhC
linear couplers investigate the less practical system with dielectric pillars [99,103,98].
The waveguides are defined by one missing row of pillars. In that case the waveguide
is single-mode and the mode is not index-guided and is thus more evanescent into the
neighbouring waveguide, especially for a small number of separating rows. For $u = 0.35$
and $\lambda = 1550$ nm the coupling length can be as short as 28 a $= 9.6\,\lambda$ [98].

The coupling length is mainly determined by the size of the barrier holes and only
secondarily by the overall air-filling factor. The barrier holes play a similar role to that
of the air-spacing between conventional ridge waveguides. The smaller the holes are,
the bigger the overlap is between the fields of neighbouring waveguides, and thus the
stronger the coupling. The dependence of the coupling length on the barrier hole size
has been calculated by PWE and is displayed in Fig. 7.17. For the calculation a filling

factor of $f = 0.28$ (see Table 7.1) has been assumed, which corresponds to a hole radius $R_0 = a\sqrt{\frac{\sqrt{3}}{2\pi}f} = 0.28\,a$. With respect to this hole radius, the radius of the barrier holes has been diminished.

The experimentally found coupling length is indicated in the graph by the dotted line. A value of $L_c \approx 350$ corresponds to a ratio $R_i/R_0 = 0.84$ or $f_i/f_0 = 0.71$ in terms of fill factor. This 30 % smaller fill factor of the barrier holes might be explained by proximity effects that could lead to smaller radii for more isolated holes.

The high sensitivity of the coupling length with respect to certain structural parameters (*e.g.* the size of the barrier holes) allows one to bring the calculation into agreement with the measurements.

This high sensitivity imposes strong restrictions on fabrication tolerance. The same
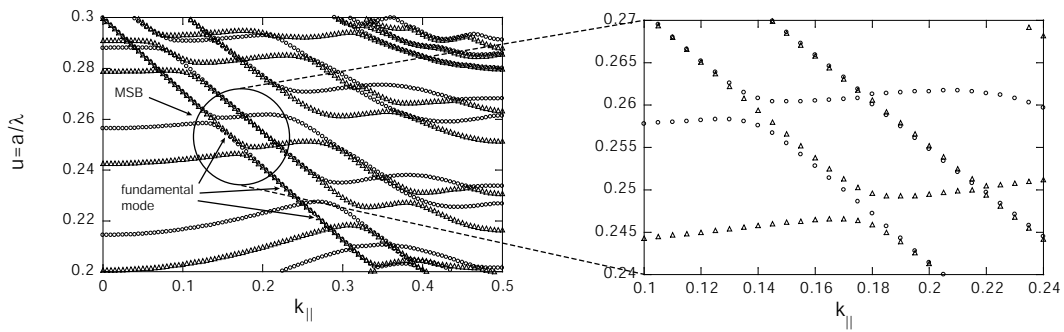
Figure 7.16: Dispersion relation of two coupled W3 waveguides separated by 1 row of holes (design B). One notes that the splitting of the fundamental mode is very weak in comparison to the splitting of the higher order modes. A larger splitting occurs at the MSB energy (Parameters: $f = 0.33$, $\varepsilon_{\mathrm{sub}} = 11.4$, $G_{\mathrm{max}} = 3.2$, number of k-points=101).

[Relation de dispersion de deux W3 guides d'onde couplés séparés par une rangée de trous (design B). On note que l'écart du mode fondamental est très faible en comparaison avec l'écart des modes supérieures. Un écart plus grand se trouve autour de l'énergie de la minibande (Paramètres: $f = 0.33$, $\varepsilon_{sub} = 11.4$, $G_{max} = 3.2$, number of k-points=101).]
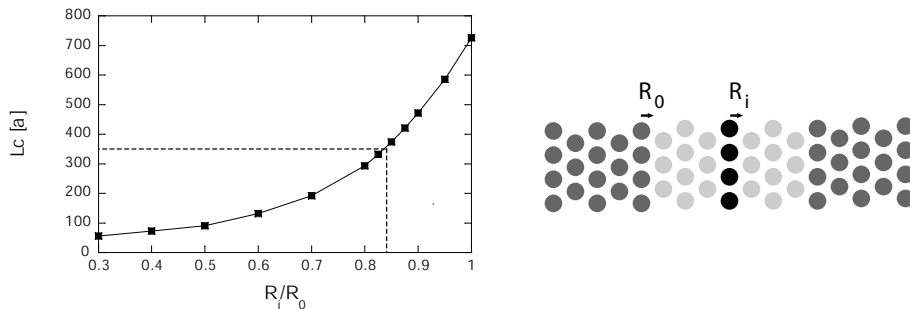
Figure 7.17: Coupling length as a function of the ratio between barrier hole radius to bulk PhC hole radius (parameters: $f = 0.28$, $\varepsilon_{\mathrm{sub}} = 11$, $G_{\mathrm{max}} = 7.2$, $N = 2269$, splitting values are taken at $u = 0.223$).

[Longueur de couplage en fonction du rapport entre les rayons des trous de la barrière et des trous entourants (paramètres: $f = 0.28$, $\varepsilon_{sub} = 11$, $G_{max} = 7.2$, $N = 2269$, l'écart d'énergie a été pris à l'énergie $u = 0.223$).]

sensitivity with respect to the guide separation distance exists also for classical Ti-diffused lithium niobate ridge waveguide couplers: The dependence of the coupling length in Ref. [102] was found to be exponential with a constant decay given by the inverse of the transverse waveguide penetration depth. The problem could be circumvented by introducing a post-fabrication tuning by a local refractive index change by ion implantation or actively by temperature tuning or carrier-injection.

7.2.3.2   Calculation of the coupling length by FDTD

An alternative way to cross-check the PWE calculation is to perform an FDTD calculation. The structure is excited by a plane wave with a spatially Gaussian profile with a spotsize (at half width at half maximum) of $\sigma = 1$ lattice constant positioned directly in front of waveguide A at $x = 0$. Since the structure is extremely long (500 periods) the resolution had to be drastically reduced, *i.e.* the number of grid points in x- and y-direction is only 14 and 12 whereas it is typically 40 and 34 for the simple slab and 1D-cavity calculations. As a consequence, the discretisation becomes coarse, especially for holes reduced in size. Fig. 7.18 shows the magnetic field inside the coupler (design B). For practical reasons the field map had to be cut into four parts (see axis labels). One can clearly observe the energy transfer between the two waveguides.
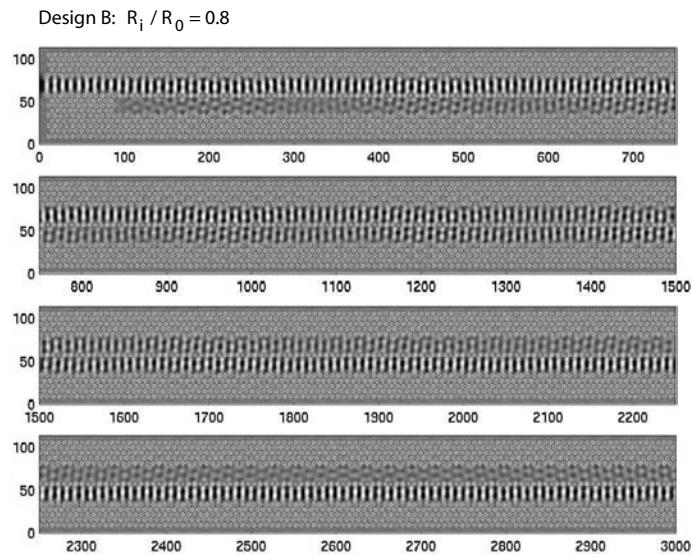
Design B: $R_i / R_0 = 0.8$

Figure 7.18: FDTD calculation of the magnetic field distribution (at $u_0 = 0.223$) of the coupler structure design B allows one to deduce the coupling length. It has been assumed that the holes in the barrier are reduced by a factor $R_i/R_0 = 0.8$ with respect to the surrounding holes (Parameters: $f = 0.28$, $\varepsilon_{\mathrm{sub}} = 11.4$, $\varepsilon'' = 0$, $naccx = 14$, $naccy = 12$).
[*Calcul FDTD de la distribution du champ magnétique (à $u_0 = 0.223$) du coupleur de design B permet de déduire la longueur de couplage. Il était assumé que les trous de la barrière sont réduit d'un facteur $R_i/R_0 = 0.8$ par rapport aux trous environnants (Paramètres: $f = 0.28$, $\varepsilon_{sub} = 11.4$, $\varepsilon'' = 0$, $naccx = 14$, $naccy = 12$).*]

In Fig. 7.19 the vertical field is plotted for the structure C for different size reduction of the barrier holes. For the ratio $R_i/R_0 = 0.8$, a coupling length of 110a can be deduced.
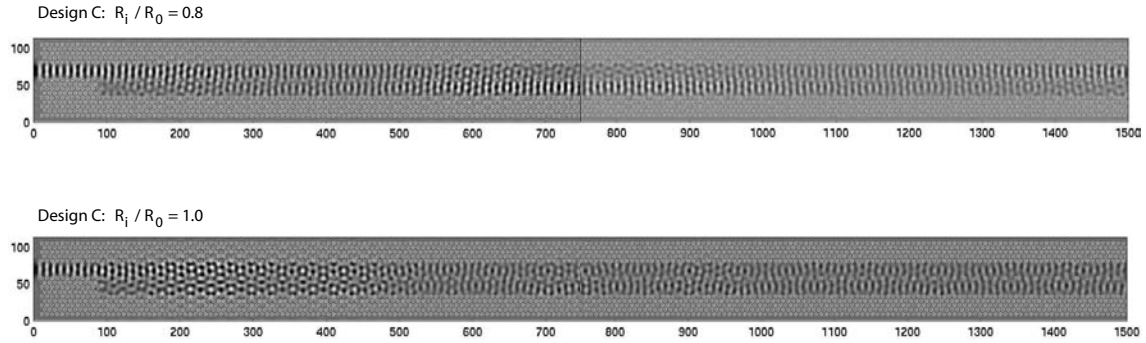
Figure 7.19: FDTD calculation of the magnetic field distribution of the coupler structure design C at $u_0 = 0.223$ for a hole radius ratio R_i/R_0 of 0.8 and 1.0. In the upper case a clear power transfer can be observed whereas in the lower case a lot of scattering to higher order modes occurs (Parameters: $f = 0.28$, $\varepsilon_{sub} = 11.4$, $\varepsilon'' = 0$, $naccx = 14$, $naccy = 12$).
[Calcul FDTD de la distribution du champ magnétique du coupleur de design C à $u_0 = 0.223$ pour un rapport des radius de trous R_i/R_0 de 0.8 et 1.0. Dans le cas du haut un transfert de puissance est clairement visible, tandis que dans le cas du bas le mode est fortement diffusé vers des modes d'ordres supérieurs (Paramètres: $f = 0.28$, $\varepsilon_{sub} = 11.4$, $\varepsilon'' = 0$, $naccx = 14$, $naccy = 12$).]

For barrier holes identical to the surrounding holes ($R_i/R_0 = 1.0$) a strong scattering of the incoming fundamental mode into higher-order modes occurs within the first 50 periods of the coupling section. The actual reason (physical/numerical) has not been tracked down yet. For this reason the relevant data point is missing in Fig. 7.20.

It is interesting to compare the coupling lengths predicted by PWE and FDTD. The FDTD calculation as shown in Fig. 7.18 had to be repeated for 5 different ratios of R_i/R_0. The agreement between the two methods is very good (see Fig. 7.20). The two curves for design B show an exponential decay $y \propto e^{\gamma x}$ with $\gamma = 3.75$ and 3.59 for the PWE and the FDTD calculation, respectively. This exponential decay is due to the evanescent field coupling between the two waveguides, where the evanescent tail decreases exponentially as a function of distance. The fluctuation in the data points of the FDTD calculation may be due to the discretisation error of the holes linked to the small resolution (related to the large size of the simulated structure).
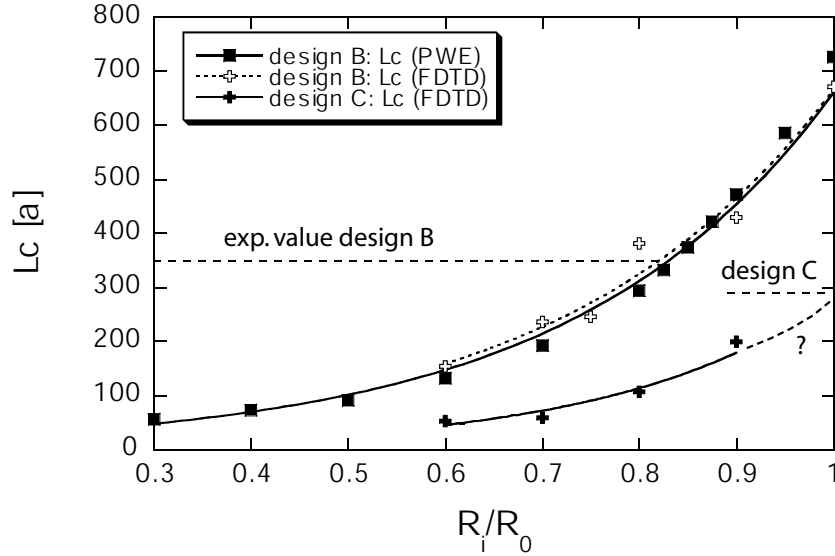
Figure 7.20: Coupling length calculated by FDTD as a function of the ratio R_i/R_0) for design B and C. For the design B there is a good agreement between PWE and FDTD.

[Longueur de couplage calculée par FDTD pour les designs B et C. Pour le cas B il y a un bon accord entre la méthode des ondes planes et le calcul FDTD.]

7.3   Conclusions

In conclusion, it has been shown that the physics of coupled PhC waveguides is very rich and allows for different functionalities (*e.g.* broadband 50/50 intensity coupler, wavelength-dependent devices for filtering and channel dropping). The quality of the experimental measurements has been partly affected by the poor facet quality and the variations of the fill factor. It was, however, still possible to extract quantitative results from a single period. Two designs have been investigated. The first with one single row of holes separation between the two W3 waveguides and the second with a single row as well, but with every second hole omitted. The experimental values of the coupling length for the two designs are of the order of 350 and 290 periods, respectively. These values correspond to absolute lengths of the order of 80 μm. This is significantly below the values of classical integrated optics, but is rather large for PhC circuits, where the smallest elements, *e.g.* bends are around 1 μm.

Two different numerical techniques, *i.e.* PWE and FDTD, have been exploited to calculate the coupling length based on a supermode approach and showed to be in good agreement with the experiment. A third approach, based on coupled modes, considers the coupling phenomenon from a more fundamental point of view. The approach investigates the actual evanescent field coupling and calculates the coupling length from the overlap integrals between the two waveguide modes.

The coupling length proved to be extremely sensible with respect to certain structural parameters (*e.g.* the size of the barrier holes) which allows one to bring the calculation into agreement with the measurements. For example, the value of 350 periods could be explained by the PWE model when assuming that the ratio between the barrier holes and the surrounding holes is $R_i/R_0 = 0.84$. One the one hand, this

high sensitivity of the coupling length introduces severe restrictions for fabrication tolerances. On the other hand, the sensitivity could be exploited for the design of active devices (*e.g.* switches). For example, light can be switched electrically by tuning the electrical conduction and thus the absorption rate ($\Delta\alpha$ switch) [98].

Chapter 8

Coupled Cavity Waveguides (CCWs)

Many efforts in PhC research have been devoted to the conception and fabrication of building blocks for integrated optics, such as add-drop filters, combiners and splitters [104]. In order to connect these functions the need for a PhC-based solution in guiding and bending light beams is widely recognised. One solution, PhC channel waveguides achieved by creating a line defect of missing holes inside a regular lattice, has already been studied in chapter 5. Nevertheless, while performances are satisfactory for straight waveguides, the combination of the small bandwidth and the reported loss levels (*i.e.* -1.1 to -3 dB/bend) [55] for bends is still an obstacle for dense integration. An alternative approach is to align a chain of point defects (*i.e.*, cavities) in a 2D PhC to obtain a structure commonly referred to as coupled cavity waveguide (CCW) [105] (see Fig. 8.1). First proposed by Stefanou *et al.*, [106] this concept was studied by Yariv *et al.* [107] as coupled resonator optical waveguide (CROW) and then applied to different 2D PhC structures (see for example Refs. [108,105]).
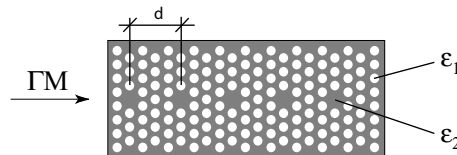
Figure 8.1: Sketch of a coupled cavity waveguide made of hexagonal cavities separated by a spacer d and embedded in a 2D triangular lattice photonic crystal.
[*Schéma d'un guide à cavités couplées formé de cavités hexagonales dans un réseau triangulaire à deux dimensions.*]

These defect cavities are designed such that their resonant frequency falls within the photonic band gap of the surrounding structure, which permits high-Q optical modes. One assumes a sufficiently large separation between the individual cavities that the cavities are weakly coupled [107].

As two cavities are brought in vicinity of each other two separate energy levels are formed for each level of the isolated cavity corresponding to the symmetric and anti-symmetric supermode of the coupled structure. Each additional cavity (supporting M modes) adds M additional energy levels. For example Fig. 8.2 shows the field patterns of the supermodes of two and three coupled H1 cavities, separated by 1 ΓM row.

The energy eigenvalues corresponding to the supermodes in Fig. 8.2 obtained by plane wave expansion (PWE) are plotted in Fig. 8.3. The upper and lower band edge of the inifinite CCW is indicated by dotted lines.

In the limit case, that of an infinite chain of single mode cavities, the coupling between the individual cavities causes the discrete spectral line at ω_0 to turn into a narrow band of guided frequencies slightly shifted from the original frequency ω_0 of the single cavity [109].

The resulting mini-band allows for transmission along the cavity chain. The wave
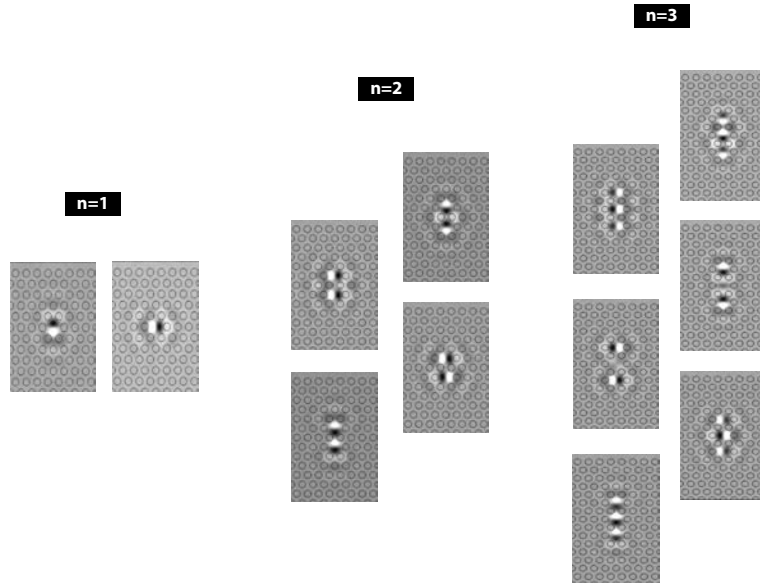
Figure 8.2: Magnetic field maps of coupled H1M cavities separated by one row ΓM for a different number n of cavities (Parameters: $f = 0.37$, $\varepsilon_{\text{sub}} = 11$, ε_{air}, G_{max}, $N = 779$).

[Cartes de champs magnétiques des cavités H1M couplées, séparées par une rangé ΓM pour différents nombres n de cavités (Paramètres: $f = 0.37$, $\varepsilon_{sub} = 11$, ε_{air}, G_{max}, $N = 779$).]
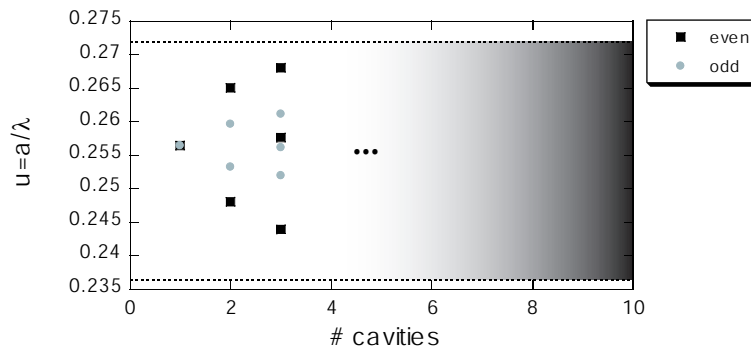
Figure 8.3: Level repulsion of the degenerate cavity modes due to the coupling between H1 cavities separated by 1 row. The graph shows the energy levels of the coupled system for 1, 2 and 3 cavities.

[Anti-croisement des modes de cavité dégénérés dû au couplage entre les cavités H1 séparées d'une rangée. Le graph montre les niveaux d'énergie du système couplé pour 1, 2 et 3 cavités.]

propagation is actually due to the tunneling of radiation between the individual cavities. One hopes that CCWs allow not only to transmit light in straight chains, but also around bends. Provided that the cavity modes are non-degenerate and have hexagonal symmetry, there is no fundamental difference between a straight CCW and a CCW-based bend when considering only the first-neighbor interaction [105].

Correspondingly to the narrow bandwidth of CCW, light inside a CCW propagates with a small group velocity, especially at the band edges. The bandwidth depends greatly on the coupling strength between adjacent cavities and decreases with increasing cavity spacing due to smaller overlap between the neighbouring cavity fields. The existence of low group velocity modes inside CCWs has generated a lot of interest and has been exploited both to reduce interaction lengths in nonlinear processes like second-harmonic generation, [110,111] and to provide delay lines for pulse storage [112].

The group velocity and other crucial CCW parameters can be deduced from the dispersion relation.

8.1 Tight-binding formalism for CCWs

It is widely known that the tight-binding (TB) model [1] can be used to calculate the band structure of bulk PhCs which include small defects [114]. In addition, a TB model also allows one to derive the CCW dispersion [106]. In the literature there are a few specific cases of TB modeling of CCWs, for example, the case of localized cavity states [107,109], and that of circular impurity cells in photonic insulators [106] for which an analytical solution exists. In general, however, these studies deal with oversimplified single mode cavities.

In this section, an *ab initio* TB method is presented where the coupling parameters are calculated from the isolated cavity field distribution. This contrasts with previous work where the coupling parameters are added phenomenologically. As has been alluded to in the experimental work by Karle *et al.* [115], we have explicited here theoretically how the properties of the cavity chain can be related to the field patterns of a single cavity. This is one of the main advantages of the subsequent approach compared to other CCW-oriented TB calculations where, for example, the coupling elements are determined by fitting the dispersion curves obtained experimentally [116] or by a different numerical method (*e.g.* FDTD) [110]. Moreover, it should be emphasized that this latter procedure is problematic for real cavities with *quasi*-degenerate modes since the fitting procedure usually does not lead to an unequivocal set of parameters. Therefore, even if these fitting parameters allow a good agreement to be achieved with the dispersion relations, they cannot be used in further calculations since their individual values may have no physical meaning. Finally, we remark that the subsequent model is not restricted with respect to the geometry (*e.g.* circular) nor with respect to the method used to calculate the field maps (*e.g.* FDTD would also be suitable).

The PWE method is used to obtain the single cavity field profiles which are then inserted into the TB model. Since the PWE method is numerically stable and fast

---

[1]In solid state physics the tight-binding approximation deals with the case in which the overlap of atomic wave functions is enough to require corrections to the picture of isolated atoms, but not so much as to render the atomic description completely irrelevant [113].

for the calculation of the CCW dispersion relations, this method has been chosen as a reference to validate our TB model.

It is worth noting that a better physical insight into the coupling behaviour between adjacent cavities can be obtained from the TB approach than from the PWE approach. This is due to the fact that the TB approach allows one to study the complete inter-action between adjacent cavities, including cross-coupling between different modes of the cavity. Another advantage of our TB model is that it is not limited to the case of straight periodic CCWs.

As will be shown in the next two sections, electrons inside a superlattice potential exhibit strong analogies with photons inside a CCW, *i.e.* the individual cavities in the CCW are the optical counterpart of the isolated atoms, and the high-Q mode in the cavities corresponds to the atomic wave function [107]..

8.1.1 The superlattice potential (electronic case)

An electron subjected to a single quantum well (SQW) potential centered at $\boldsymbol{r} = 0$ is usually described by the time-independent Schrödinger equation: [113]

$$
\begin{aligned}
H_0 &= \frac{\boldsymbol{p}^2}{2m} + V_\infty + \Delta V_0(\boldsymbol{r}) \\
H_0|\psi_0^\alpha\rangle &= E_0^\alpha|\psi_0^\alpha\rangle \qquad \alpha = 1...n_\alpha \\
\langle\psi_0^\alpha|\psi_0^\beta\rangle &= \delta_{\alpha\beta}
\end{aligned}
\tag{8.1}
$$

where ψ_0^α represents the electronic state localised at $\boldsymbol{r} = 0$ with energy E_0^α, and n_α is the total number of QW eigenstates. The potential V_∞ is chosen such that $V_0(\boldsymbol{r}) \to 0$ at infinity. Taking the SQW at $\boldsymbol{r} = \boldsymbol{r_0}$ as the basic building block, more complex potentials can be built up just by stringing together a series of QWs and obtaining the superlattice (SL) structure (see Fig. 8.4).

Like in the Kronig-Penney model, [113] the total SL Hamiltonian reduces to that of a 1D square-well potential (see Fig. 8.5):

$$
H = \frac{\boldsymbol{p}^2}{2m} + V_\infty + \sum_n \Delta V_n(\boldsymbol{r}) \quad \text{with} \quad \Delta V_n = \Delta V_0(\mathbf{r} - \mathbf{r}_n)
$$

$$
H|\chi\rangle = \mathcal{E}|\chi\rangle \tag{8.2}
$$
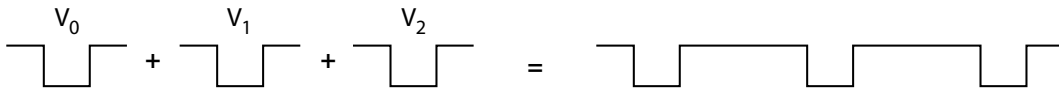
Figure 8.4: The superlattice (SL) potential is obtained by overlaying the single quantum well potentials V_n centred at the position $\mathbf{r} = n\mathbf{d}$.
[Le potentiel du super-réseau peut s'écrire comme superposition des potentiels de puits quantiques centré à $\mathbf{r} = n\mathbf{d}$.]
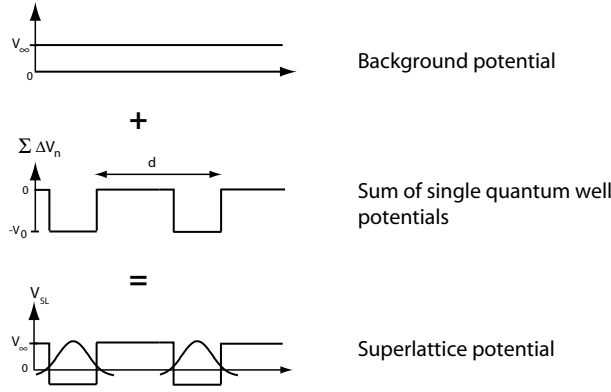
Figure 8.5: The superlattice (SL) potential V_{SL} can be written as the superposition of single quantum well potentials $-\Delta V_n$ plus a constant potential V_∞.
[*Le potentiel du super-réseau V_{SL} peut être écrit comme superposition de potentiels de puits quantiques $-\Delta V_n$ plus un potentiel à valeur constant V_∞.*]

The corresponding eigenstates $|\chi\rangle$ of energy ε is expressed in the non-orthogonal basis of the localized states $|\psi_n^\beta\rangle$, *i.e.*

$$|\chi\rangle = \sum_{n,\beta} c_n^\beta |\psi_n^\beta\rangle \tag{8.3}$$

Then, combining Eqns. (8.3) and (8.2) and projecting on the single cavity mode $|\psi_j^\alpha\rangle$ yields:

$$\left\langle \psi_j^\alpha \middle| H_j + \underbrace{\Delta V_{j-1} + \Delta V_{j+1}}_{\text{first neighbours}} + \underbrace{\sum_{m\neq j, m\neq j\pm 1} \Delta V_m}_{\text{higher order neighbours}} \middle| \sum_{n,\beta} c_n^\beta \psi_n^\beta \right\rangle = \varepsilon \left\langle \psi_j^\alpha \middle| \sum_{n,\beta} c_n^\beta \psi_n^\beta \right\rangle \tag{8.4}$$

If only the first-neighbour interaction is considered and making use of the linearity of the scalar product, the last equation reduces to:

$$\sum_\beta \left[c_j^\beta \left(\frac{\omega_0^\beta a}{c} \right)^2 \delta_{\alpha\beta} + c_{j-1}^\beta \left(\frac{\omega_0^{\alpha*} a}{c} \right)^2 R_{\alpha\beta} + c_{j+1}^\beta \left(\frac{\omega_0^{\alpha*} a}{c} \right)^2 R_{\alpha\beta}^\dagger + c_{j-1}^\beta T_{\alpha\beta}^l \right.$$

$$\left. + c_j^\beta S_{\alpha\beta} + c_{j+1}^\beta T_{\alpha\beta}^r \right] = \varepsilon \sum_\beta \left[c_{j-1}^\beta R_{\alpha\beta} + c_j^\beta \delta_{\alpha\beta} + c_{j+1}^\beta R_{\alpha\beta}^\dagger \right] \tag{8.5}$$

for $\forall \alpha \, \epsilon \, [0, n_\alpha]$ leading to n_α equations. The TB parameters are defined as:

$$R_{\alpha\beta}^l = R_{\alpha\beta} = \left\langle \psi_j^\alpha | \psi_{j-1}^\beta \right\rangle \quad \text{'overlap integral'}$$

$$R_{\alpha\beta}^r = R_{\alpha\beta}^\dagger = \left\langle \psi_j^\alpha | \psi_{j+1}^\beta \right\rangle$$

$$S_{\alpha\beta} = \left\langle \psi_j^\alpha | \Delta V_{j-1} + \Delta V_{j+1} | \psi_j^\beta \right\rangle \quad \text{'shift integral'} \tag{8.6}$$

$$T_{\alpha\beta}^l = \left\langle \psi_j^\alpha | \Delta V_{j-1} | \psi_{j-1}^\beta \right\rangle \quad \text{'transfer integral'}$$

$$T_{\alpha\beta}^r = \left\langle \psi_j^\alpha | \Delta V_{j+1} | \psi_{j+1}^\beta \right\rangle$$

and the superscripts 'l' and 'r' mean 'left' and 'right', respectively. In general, the number n_α of QW localized eigenstates is greater than 1 and the TB parameters R, S, and T are $n_\alpha \times n_\alpha$ matrices and $|c_j\rangle \equiv |c_j^1 \dots c_j^{n_\alpha}\rangle$ is a vector. The TB parameters are E, R, S and T. By analogy to the well-known single-level case: E is the unperturbed energy of the cavity mode, R is the overlap integral, S is the overall shift of the band with respect to E, and T determines the width of the band.
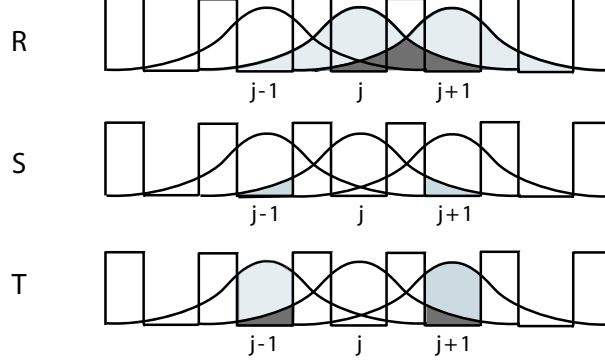
Figure 8.6: Sketch of the three tight-binding parameters describing the interaction between adjacent quantum wells: R (overlap), S (shift) and T (transfer).
[*Aperçu des trois paramètres de liaisons fortes décrivant l'interaction entre puits quantiques adjacents: R (recouvrement), S (décalage), T (transfert).*]

With the matrix formalism Eq. (8.5) writes:

$$(E_j + S_j)|c_j\rangle + E_j R_j |c_{j-1}\rangle + E_j R_j^\dagger |c_{j+1} + T_j^l |c_{j-1}\rangle\rangle$$
$$+ T_j^r |c_{j+1}\rangle = \mathcal{E}[I|c_j\rangle + R_j|c_{j-1}\rangle + R_j^\dagger |c_{j+1}\rangle] \tag{8.7}$$

When the SL is a *periodic* chain of identical QWs, *i.e.*

$$\Delta V_n(\boldsymbol{r}) = \Delta V_0(\boldsymbol{r} - n\boldsymbol{d})$$
$$\psi_n^\alpha(\boldsymbol{r}) = \psi_0^\alpha(\boldsymbol{r} - n\boldsymbol{d}) \tag{8.8}$$

E, R, S, T become independent of j. If several localized eigenstates are allowed in the SQW (*i.e.*, $n_\alpha > 1$), Eq. (8.7) yields the generalized eigenvalue equation:

$$\left(E + S + e^{-iqd}ER + e^{iqd}ER^\dagger + e^{-iqd}T^l + e^{iqd}T^r\right)|c_0\rangle$$
$$= \mathcal{E}\left(I + e^{-iqd}R + e^{iqd}R^\dagger\right)|c_0\rangle \tag{8.9}$$

However, in the case of a single state SQW (*i.e.*, $n_\alpha = 1$) with a symmetric potential with respect to the cavity j (*i.e.*, $T^l = T^r$ and $R = R^*$), Eq. (8.7) leads to the well-known dispersion relation which justifies the chosen nomenclature: [117]

$$\mathcal{E}(q) = E + \frac{S + 2T\cos qd}{1 + 2R\cos qd}$$
$$\text{with} \quad q = \frac{2\pi n}{Nd} \quad \text{and} \quad n \in \left[-\frac{N}{2}, +\frac{N}{2}\right[\tag{8.10}$$

where N is the total number of QWs in the SL.

8.1.2 The coupled cavity waveguide (photon case)

It is well known that there exist strong similarities between electrons subjected to a potential $V(\boldsymbol{r})$ and photons propagating in a medium of dielectric constant $\epsilon(\boldsymbol{r})$ [1]. The first analogy is between electrons inside a bulk crystal and photons inside a perfectly periodic PhC. The electrons are localized in bound states in the vicinity of the individual atoms and interact with the adjacent atoms. In the photon case the holes of the PhC play the role of the atoms. However, the holes act as scattering centers exhibiting resonances, but not real bound states and the analogy with the TB approach for electrons is not perfect. [114] A second correspondence can be established between a SL for electrons and a CCW structure for photons. In this case the SQW corresponds to an isolated PhC cavity with bound states existing for both electrons and photons. Thanks to this complete analogy, the previously discussed TB approach can be extended to the photon case. In particular, if a chain of identical multimode cavities is introduced, the general TB equation can be written adopting the same formalism as Eq. (8.9), the main difference being in the calculation of the matrix elements.

The propagation of photons in an inhomogeneous dielectric medium $\epsilon(\boldsymbol{r})$ can be described by the magnetic field $\boldsymbol{H}$ which is the analog of the electronic wavefunction $\psi(\boldsymbol{r})$. The general eigenvalue problem for the magnetic field is [1]

$$\hat{\theta}\boldsymbol{H} = \left(\frac{\omega a}{c}\right)^2 \boldsymbol{H} \qquad \text{with} \qquad \hat{\theta} = \boldsymbol{\nabla} \times \frac{1}{\varepsilon(\boldsymbol{r})}\boldsymbol{\nabla} \times \qquad (8.11)$$

where $\hat{\theta}$ is an Hermitian operator and $\boldsymbol{r}$ is expressed in reduced units, *i.e.* in units of the lattice constant a. The eigenvalue can be expressed in the reduced energy units $u = a/\lambda = \omega a/(2\pi c)$.

The dielectric map of the CCWs can be separated into a periodic part and a perturbation. The perturbation is a result of the additional dielectric material provided by the cavities (separated by the distance $d = |\boldsymbol{d}|$), *i.e.* :

$$\frac{1}{\varepsilon(\boldsymbol{r})} = \frac{1}{\varepsilon_{per}(\boldsymbol{r})} + \sum_n \zeta_n(\boldsymbol{r}) \quad \text{with } \zeta_n(\boldsymbol{r}) = \zeta_0(\boldsymbol{r} - n\boldsymbol{d}) \qquad (8.12)$$

$$\zeta_0(\boldsymbol{r}) = \begin{cases} \frac{1}{\varepsilon_{sub}} - \frac{1}{\varepsilon_{air}} & \text{inside missing holes} \\ 0 & \text{else} \end{cases} \qquad (8.13)$$

where ε_{air} and ε_{sub} denote the dielectric constant of the air-holes and the substrate, respectively. $\varepsilon_{per}(\boldsymbol{r})$ and $\zeta_n(\boldsymbol{r})$ describe an infinite periodic PhC and the cavity at position n, respectively (see Fig. 8.7).

The CCW states can be expressed in the non-orthogonal basis of the localized cavity states, *i.e.*

$$|\boldsymbol{H}\rangle = \sum_{n,\beta} c_n^\beta |\boldsymbol{H}_n^\beta\rangle \qquad (8.14)$$

where c_n^β is the weighting coefficient of the localized cavity state $|\boldsymbol{H}_n^\beta\rangle$ (*i.e.* cavity mode β in the n-th cavity).

Then, defining the operators

$$\begin{aligned} \hat{\theta}_{per} &= \boldsymbol{\nabla} \times \left[\frac{1}{\varepsilon_{per}(\boldsymbol{r})}\boldsymbol{\nabla} \times \right. \\ \hat{\theta}_n &= \boldsymbol{\nabla} \times [\zeta_n(\boldsymbol{r})\boldsymbol{\nabla} \times \end{aligned} \qquad (8.15)$$
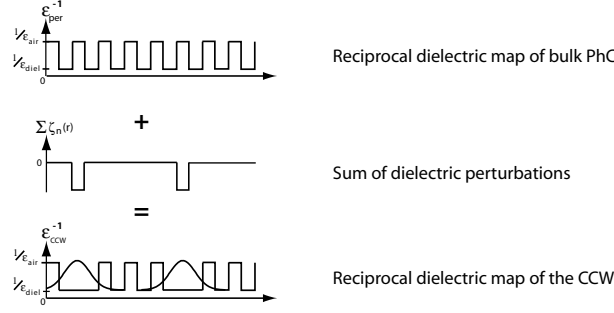
Figure 8.7: The dielectric function ε_{CCW}^{-1} of a coupled cavity waveguide can be expressed as the superposition of the periodic dielectric function ε_{per}^{-1} of the bulk photonic crystal plus a set of perturbations $\zeta_n(\boldsymbol{r})$.
[La fonction diélectrique ε_{CCW}^{-1} d'un guide à cavités couplées peut s'exprimer comme la superposition d'une fonction diélectrique périodique ε_{per}^{-1} du cristal photonique infinie et d'une somme de perturbations $\zeta_n(\boldsymbol{r})$.]

Eq. (8.11) can be rewritten as

$$\hat{\theta}_{per}\boldsymbol{H} + \sum_n \hat{\theta}_n \boldsymbol{H} = \left(\frac{\omega a}{c}\right)^2 \boldsymbol{H} \tag{8.16}$$

Inserting Eq. (8.14) in Eq. (8.16) and projecting it on the cavity mode $|H_j^\alpha\rangle$ in the j-th cavity, one obtains:

$$\left\langle H_j^\alpha \left| \hat{\theta}_{per} + \sum_m \hat{\theta}_m \right| \sum_{n,\beta} c_n^\beta H_n^\beta \right\rangle = \left(\frac{\omega a}{c}\right)^2 \left\langle H_j^\alpha \left| \sum_{n,\beta} c_n^\beta H_n^\beta \right\rangle \right. \tag{8.17}$$

When considering only the first-neighbour interactions, the projection of $|\boldsymbol{H}\rangle$ onto the single mode $|\boldsymbol{H}_j^\alpha\rangle$ of the single cavity j yields the same recursive equation as Eq. (8.7):

$$(E_j + S_j)|c_j\rangle + E_j R_j^l |c_{j-1}\rangle + E_j R_j^r |c_{j+1}\rangle + T_j^l |c_{j-1}\rangle$$
$$+ T_j^r |c_{j+1}\rangle = \varepsilon [I|c_j\rangle + R_j^l |c_{j-1}\rangle + R_j^r |c_{j+1}\rangle] \tag{8.18}$$

with the TB matrix elements:

$$E_{\alpha\beta} = (2\pi u_\alpha)^2 \delta_{\alpha\beta}$$
$$R_{\alpha\beta}^{l/r} = \left\langle \boldsymbol{H}_j^\alpha | \boldsymbol{H}_{j\mp 1}^\beta \right\rangle \quad \text{'overlap integral'}$$
$$S_{\alpha\beta} = \left\langle \boldsymbol{H}_j^\alpha | \hat{\theta}_{j-1} + \hat{\theta}_{j+1} | \boldsymbol{H}_j^\beta \right\rangle \quad \text{'shift integral'} \tag{8.19}$$
$$T_{\alpha\beta}^{l/r} = \left\langle \boldsymbol{H}_j^\alpha | \hat{\theta}_{j\mp 1} | \boldsymbol{H}_{j\mp 1}^\beta \right\rangle \quad \text{'transfer integral'}$$

In general, the number of localized eigenstates per cavity (n_α) is greater than one, the TB parameters E, R, S, and T are $n_\alpha \times n_\alpha$ sized matrices and $|c_j\rangle \equiv |c_j^1 \dots c_j^{n_\alpha}\rangle$ is a vector.

By comparing Eqs. (8.2), (8.3) and (8.16), the following correspondences between the electronic and the photon case can be found:

$$
\begin{aligned}
\psi_j^\alpha &\longleftrightarrow \boldsymbol{H}_j^\alpha \\
\frac{\boldsymbol{p}^2}{2m} + V_\infty &\longleftrightarrow \hat{\theta}_{per} \\
\Delta V_j &\longleftrightarrow \hat{\theta}_j
\end{aligned}
\tag{8.20}
$$

The relations established by Eq. (8.20) allow the calculation of the TB parameters for a CCW in a 2D PhC structure. To evaluate the TB parameters in Eq. (8.19), we numerically solve the integrals of the general form $\langle \boldsymbol{H}_m^\alpha | \hat{\theta}_n | \boldsymbol{H}_j^\beta \rangle$. Using a calculation similar to the one performed in Ref. [109] for a 2D PhC, these integrals yield a line integral over the border of the missing holes that form the adjacent cavity and a surface integral of their cross-section, respectively, *i.e.* :

$$
\begin{aligned}
\langle \boldsymbol{H}_m^\alpha | \hat{\theta}_n | \boldsymbol{H}_j^\beta \rangle = &\int\limits_{\partial A_n} \boldsymbol{ds}\, \zeta_n(\boldsymbol{r}) \left[\nabla \times \boldsymbol{H}_j^\beta(\boldsymbol{r}) \right] \times \boldsymbol{H}_m^{\alpha*}(\boldsymbol{r}) \\
&+ \int\limits_{A_n} dA\, \zeta_n(\boldsymbol{r}) \left[\nabla \times \boldsymbol{H}_j^\beta(\boldsymbol{r}) \right] \left[\nabla \times \boldsymbol{H}_m^{\alpha*}(\boldsymbol{r}) \right]
\end{aligned}
\tag{8.21}
$$

Eq. (8.21) is easily solved in the case of the transverse electric (TE) field. The magnetic field solution which is inserted into Eq. (8.21) is obtained from the PWE method [73] (H_z component, $H_x = H_y = 0$).

8.2   Numerical examples: Dispersion curves

To illustrate the use of this model, chains of cavities defined by missing holes (*i.e.* the circular holes are filled with the dielectric) in a 2D triangular pattern are investigated. Calculations are performed for the TE polarization. The relative dielectric constant of the substrate is $\varepsilon = 11$ and the PhC air-filling factor is $f = 0.37$.

In order to validate the TB approach, the dispersion relations are also calculated with a standard PWE method in combination with a supercell approach. After imposing a wavevector q along the ΓM -direction (see Fig. 8.1), the CCW dispersion curves are obtained by computing the eigenenergies for different q values.

H1-M CCW with 3-row cavity spacing.   In a triangular lattice the simplest cavity configuration consists of a point defect with only one missing hole (H1). Here we consider the case of H1 cavities aligned along the ΓM-direction with 3 rows spacing (see inset of Fig. 8.9).

This basic cavity only supports two degenerate modes. These give rise to two orthogonal CCW bands with no anti-crossing (see Fig. 8.9). The corresponding CCW modes have even (circles) and odd symmetry (squares) with respect to the propagation direction and relative bandwidths of 3.3 % and 0.16 %, respectively. The two solid lines (open symbols) are calculated with the TB approach. The lack of anti-crossing translates into vanishing off-diagonal elements. The explicit numerical values of the TB parameters are specified in Table 8.1. In the case of a straight periodic CCW the
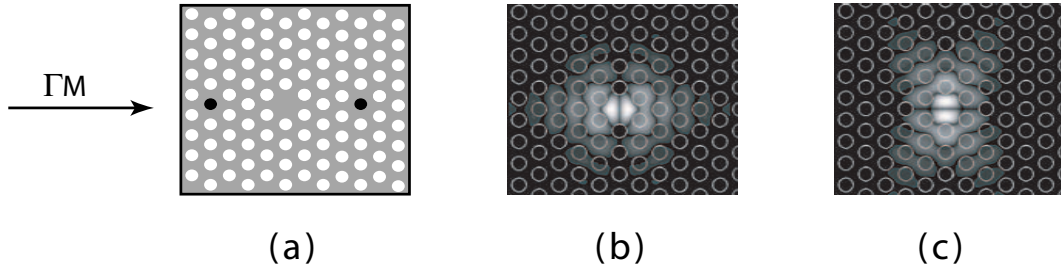
Figure 8.8: a) Sketch of the supercell containing the single cavity j. The black circles evidence the position of the holes that form the adjacent cavities $j \pm 1$, when being omitted. b), c) Modulus of the magnetic field of the even and odd cavity mode, respectively (parity is defined with respect to the ΓM propagation direction).
[a) Schéma de la super-cellule qui contient une seule cavité j. Les cercles noirs représentent la position des trous qui forment les cavités voisines $j \pm 1$ si elles étaient omises. b), c) Module du champ magnétique des mode pairs et impairs, respectivement (la parité est définie selon la future direction de propagation (ΓM).]
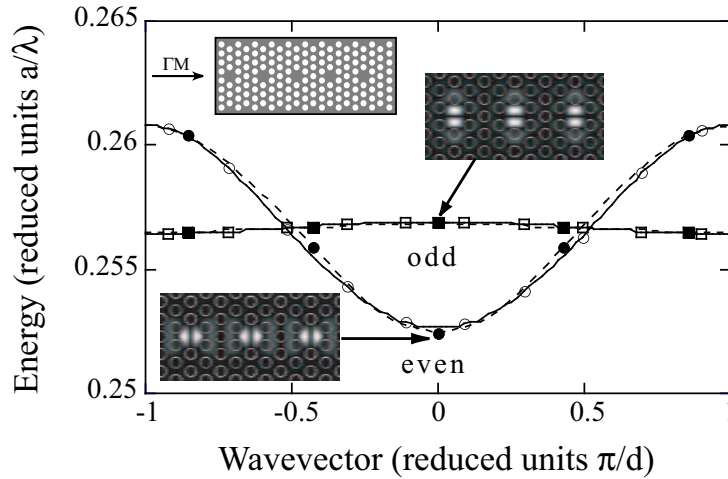
Figure 8.9: Dispersion relation of a coupled cavity waveguide (which is sketched in the inset). Solid and dotted lines correspond to the tight-binding calculation and the standard plane wave expansion method, respectively. The even and odd TE polarized modes are shown by circles and squares respectively. The cavities are separated by 3 PhC rows.
[Relation de dispersion d'un guide à cavités couplées formé par des cavités hexagonales avec un trou manquant, alignées dans la direction ΓM et séparées par 3 rangées de cristaux photoniques (voire inset). La ligne solide correspond au calcul liaisons forte et la ligne pointillée à la méthode 'd'onde plane + super cellule'. Le mode pair est indiqué par des cercles et le mode impair par des carrés.]

dispersion can also be calculated by PWE. The PWE computation yields the dotted lines (solid symbols). The agreement between the two models is good; the mean relative error is 1.4 % and 0.07 % for the even and the odd mode, respectively.

E	R	S	T^l	T^r
$E_{11} = 2.601$	$R_{11} = 0.045$	$S_{11} = -0.005$	$T^l_{11} = -0.041$	$T^r_{11} = -0.041$
$E_{22} = 2.601$			$T^l_{22} = 0.003$	$T^r_{22} = 0.003$

Table 8.1: Tight-binding parameters of an H1-M coupled cavity waveguide with 3-row cavity spacing. Only the non-zero elements are indicated.
[Paramètres de liaisons fortes pour un guide à cavités H1-M couplées avec 3 rangées de séparation. Seul les éléments non-nuls sont indiqués]

H1-M CCW with 1 row cavity spacing. Keeping the same structure as Fig. 8.9 but reducing the inter-cavity spacing to one single row, a stronger coupling between the cavities is obtained (see Fig. 8.10).
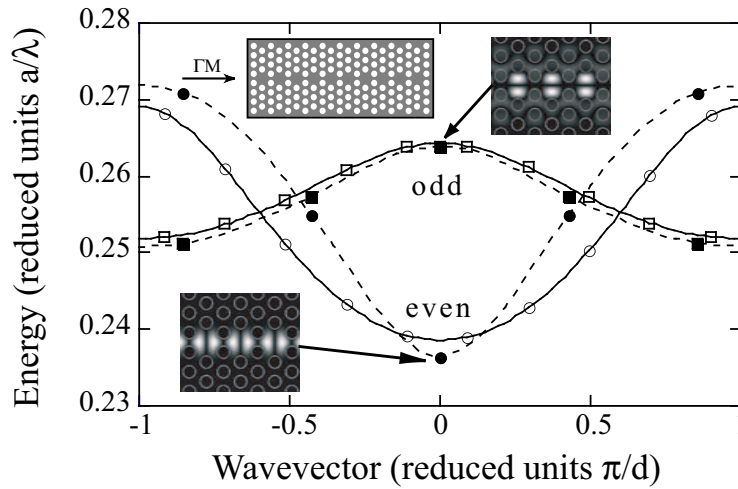
Figure 8.10: Dispersion relation of a coupled cavity waveguide (which is sketched in the inset). Solid and dotted lines correspond to the tight-binding calculation and the standard plane wave expansion method, respectively. The even and odd TE polarized modes are shown by circles and squares respectively. The cavities are separated by 1 PhC row.
[Relation de dispersion d'un guide à cavités couplées formé par des cavités hexagonales avec un trou manquant, alignées dans la direction ΓM et séparées par 1 rangée de cristaux photoniques. La ligne solide correspond au calcul liaisons forte et la ligne pointillée à la méthode 'd'onde plane + super cellule'. Le mode pair est indiqué par des cercles et le mode impair par des carrés.]

This increases the bandwidth of the CCW modes to 13.8 % for the even mode and 5.2 % for the odd mode; unfortunately the mean relative discrepancy between the TB and PWE model also increases to 5 % and 1.9 % respectively. The agreement between the TB and the PWE approaches is still good, even though the relative error is larger than in the previous case. The difference between the dispersion curves calculated with the two models is larger for the even mode than for the odd mode. This may be attributed to different causes. Firstly, we note that the coupling strength for the even mode is much stronger than for the odd mode due to a different symmetry in the field distribution. The explicit numerical values of the TB parameters are specified in Table 8.2. The consequence of this is that the evanescent field extends further into the adjacent cavities. This could lead to a significant coupling contribution from the

second-order interaction which is not accounted for in our TB model. The variation induced should, however, be small because the coupling strength from the second-order interaction was found to be reduced by one order of magnitude compared to the corresponding nearest-neighbour interaction. A second possible cause could arise from the PWE model because of the inaccuracy of the dielectric map in the vicinity of the barrier holes, as the PWE model is limited by the total number of plane waves involved. Small variations in the size of these barrier holes may slightly change the coupling strength. Also, having the higher field intensity in the vicinity of the spacer holes, the even mode is more sensitive to variations in hole shape.

E	R	S	T^l	T^r
$E_{11} = 2.601$	$R_{11} = 0.124$	$S_{11} = -0.121$	$T_{11}^l = -0.157$	$T_{11}^r = -0.157$
$E_{22} = 2.601$	$R_{22} = -0.079$	$S_{22} = 0.01$	$T_{22}^l = 0.06$	$T_{22}^r = 0.06$

Table 8.2: Tight-binding parameters of an H1-M coupled cavity waveguide with 1-row cavity spacing. Only the non-zero elements are indicated.
[*Paramètres de liaisons fortes pour un guide à cavités H1-M couplées avec une rangée de séparation. Seuls les elements non-nuls sont indiqués*]

Elongated cavity-based CCW with 3-row cavity spacing.   Since the present TB approach allows for any number of modes this example is a good candidate to test the formalism on a larger set of interacting bands. In a 2D triangular lattice an elongated cavity may consist of a point defect created by two missing holes. A CCW is obtained by aligning the smallest cavity side along the ΓM-direction and introducing a 3-row cavity spacing (see Fig. 8.11). This structure supports four cavity modes with the reduced energies $u = 0.2379$, 0.2561, 0.2562 and 0.2754. As illustrated in Fig. 8.11, the symmetry of the CCW modes in order of increasing energy is alternately even (circles) and odd (squares).

According to Fig. 8.11, the relative bandwidths of the CCW modes are 0.4 %, 1.7 %, 4.7 % and 0.25 % in order of increasing energy. As in the previous examples, the solid lines (open symbols) are calculated with the TB approach and the explicit numerical values of the TB parameters are specified in Table 8.3: In this case, the TB matrices have non-zero off-diagonal elements due to the interaction between the CCW bands. The agreement between the two models is still good and with increasing energy the relative differences in model calculations for the four modes are 0.3 %, 0.6 %, 1.7 % and 0.3 %. The band crossing between mode 2 and 3 at $q = \pm 0.48$ is due to the different parity of the two modes with respect to the propagation direction (see Fig. 8.11). Dispersion relations of a coupled cavity waveguide formed by elongated cavities with 2 missing holes, are aligned along the ΓM-direction and separated by 3 PhC rows (which is sketched in the inset). Solid and dotted lines correspond to the tight-binding calculation and the standard plane wave expansion method, respectively. The even and odd TE polarized modes are marked with circles and squares respectively.
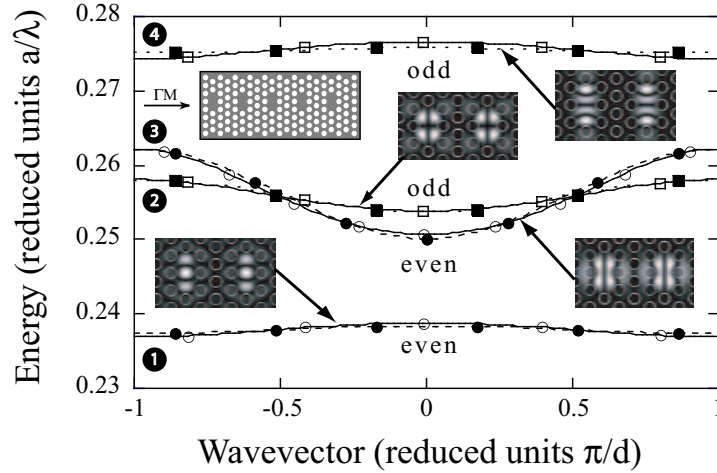
Figure 8.11: Dispersion relation of a coupled cavity waveguide formed by elongated cavities with 2 missing holes, aligned along the ΓM-direction and separated by 3 PhC rows (which is sketched in the inset). Solid and dotted lines correspond to the tight-binding calculation and the standard plane wave expansion method, respectively. The even and odd TE polarized modes are marked with circles and squares respectively.

[Relation de dispersion d'un guide à cavités couplées formé par des cavités allongées avec deux trous manquant, alignées dans la direction ΓM et séparé par 3 rangées de cristaux photoniques. La ligne solide correspond au calcul liaisons forte et la ligne pointillée à la méthode 'd'onde plane + super cellule'. Le mode pair est indiqué par des cercles et le mode impair par des carrés.]

E	R	S	T^l	T^r
$E_{11} = 2.235$	$R_{11} = 0.006$		$T^l_{11} = 0.009$	$T^r_{11} = 0.009$
$E_{22} = 2.589$	$R_{22} = 0.016$	$S_{22} = -0.003$	$T^l_{22} = -0.022$	$T^r_{22} = -0.022$
$E_{33} = 2.591$	$R_{33} = 0.071$	$S_{33} = -0.011$	$T^l_{33} = -0.06$	$T^r_{33} = -0.06$
$E_{44} = 2.995$	$R_{44} = -0.009$		$T^l_{44} = 0.013$	$T^r_{44} = 0.013$
			$T^l_{24} = -0.057i$	$T^r_{24} = 0.057i$
			$T^l_{31} = -0.106i$	$T^r_{31} = 0.106i$
			$T^l_{42} = -0.005i$	$T^r_{42} = 0.005i$

Table 8.3: Tight-binding parameters of an elongated cavity-based coupled cavity waveguide with 3-row cavity spacing. Only the non-zero elements are indicated.

[Paramètres de liaisons fortes pour un guide à cavités allongées couplées avec une rangée de séparation. Seul les éléments non-nuls sont indiqués]

8.3 Conclusions and outlook

In conclusion, we have presented a TB approach for CCWs that allows an accurate calculation of the guided mode dispersion relations. Multimode and degenerate states are supported by the formalism presented. In contrast to previous work, the TB parameters are not introduced as free-fitting parameters but are explicitly calculated from the computed field patterns of a single cavity. The TB calculation shows good agreement with the standard PWE method for three different numerical examples. It should

be noted that the canonical Eq. (8.7) is a recursive equation that may be extended
to the modeling of non-periodic chains of coupled cavities allowing eigenstates and
eigenenergies to be calculated as well as reflection and transmission coefficients. It
should be noted that the formalism presented here is suitable to the calculation of
second-order interactions.

Vaious CCW-based applications have been proposed in literature; Fig. 8.12 gives
an incomplete overview of different CCW-based components: Design (a) addresses the
important issue of coupling from a channel waveguide into a CCW. The proposed
solution is a taper that adiabatically turns on every second hole inside the channel
waveguide until a regular CCW is reached [118]. Design (b) is a power splitter that
induces a 180° phase shift in one of the output channels. It is based on the idea of a
directional coupler with the two parallel waveguides being CCWs. Due to the slow group
velocity, the length of the coupling section can be reduced to about ten periods [119].
On the other hand, one may imagine a Y-powersplitter as sketched in Fig. 8.12(c). In
an optimised version the perfect rotational symmetry might have to be broken in order
to avoid undesired back reflections. Design (d) illustrates how CCWs could help to
build extremely compact Mach-Zehnder interferometers for filtering applications (*e.g.*
notch filters) [120]. The two arm lengths differ by ΔN cavities. Design (b) and (d)
make use of the small group velocity in CCWs to reduce the device in size.
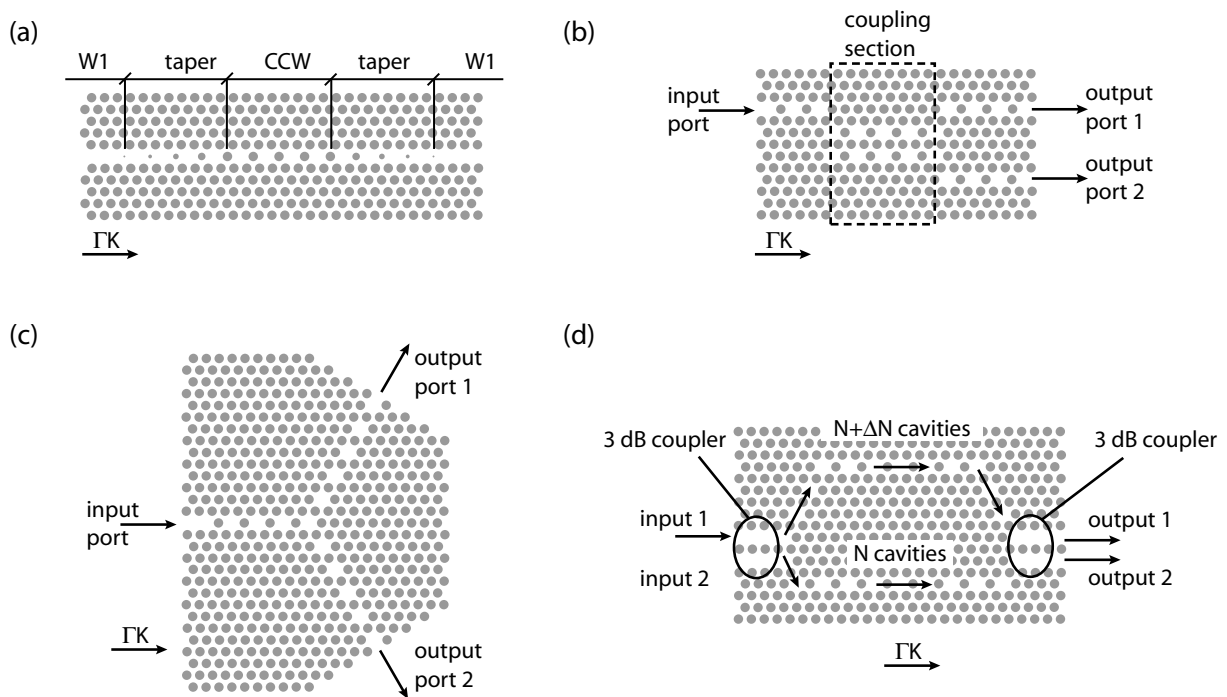
Figure 8.12: Different CCW-based integrated optics components that can be found in the
literature: a) W1 to CCW taper [118], b) PhC 180° CCW-based splitter [119],
c) CCW-based Y-splitter, d) CCW-based Mach-Zehnder interferometer [120].
*[Différentes composantes de l'optique intégrée basées sur les cavités couplées
qu'on peut trouver dans la littérature: a) W1 à CCW taper [118], b) 180°
diviseur [119], c) diviseur de type Y, d) interféromètre de type Mach-Zehnder
[120].]*

Conclusions and outlook

The work on semiconductor-based two-dimensional photonic crystals (PhCs) has been organised into three main parts:

The first part (chapter 1-4) gives a general overview of the physical basis and presents the necessary tools to analyse the experimental results in the second part. This includes a description of the various fabrication steps from the design of the vertical heterostructure to the ultimate dry etching performance reached at the end of the PCIC project. The state-of-the-art etching performance has approached what is recognised from 3D FDTD calculations to be the intrinsic loss limit of $\varepsilon'' = 0.01 - 0.02$ (with respect to the chosen vertical structure).

The technical chapter on fabrication is followed by a detailed description of the internal light source (ILS) setup, our workhorse for optical characterisation. In combination with basic test structures (simple crystals, 1D-cavities) it proved to be a versatile method without stringent limits for assessing the fabrication parameters (air-filling factor and loss) but also proved to be suitable for testing building blocks. The main drawback is that the size of the structures is limited by the reabsorption of the active layer. The ILS technique could, in principle, also be applied to active devices (including optical pumping) that are combined with passive circuits on the same chip. Yet if one has to assess the ultimate low-loss device or if one is interested in the complete power budget (fibre-to-fibre), the end-fire method comes into play. A very useful model for analysis of the out-of-plane losses is the ε''-model. Once validated by three-dimensional FDTD, it allows one to extract the loss-parameters from optical transmission measurements of PhC slab structures. It yields not only the absolute loss level but also the subdivision into the different contributions, *i.e.* the intrinsic losses, losses due to hole depth and to hole form. The loss modeling with the ε''-model in combination with SEM pictures and two-dimensional finite difference time domain (FDTD) simulations can provide accurate information about the depth and the obliqueness of the holes. One notes that the reduction of the angle in the first two decay lengths in the lower cladding section is of great importance and that $1\,°$ is an angle that translates into a ε'' value that can be measured optically. The ε''-model provides valuable indications on which hole parameter should be focused on.

The next chapter gives insight into how the plane wave expansion (PWE) method in combination with a supercell can efficiently be applied to the modelling of cavities, waveguides and coupled cavity waveguides. The method works in the frequency domain and yields the energy eigenvalues as well as the field patterns. One notes that for high accuracy in the energies or for very large supercell sizes the number of plane waves involved grows very rapidly and linked to it the requirements on computer memory. Ho's method provides a means to improve convergence and thus to reduce the number

of plane waves. The PWE method reaches its limits when one tries to model high-index and low-index contrast features inside the same supercell.

The second part is based on measurements of various building blocks implemented in a GaAs sample: The first structure, the hybride waveguides consisting of a ΓM and a ΓK border, allowed us to understand more in detail the formation of the so-called mini-stopband (MSB), *i.e.* the coupling between different modes, in corrugated waveguides. New unexpected effect have been been observed and analysed.

The second type of structures is low symmetry-order (LSO) cavity-based bends and splitters. Bends and Splitters with a high broad-band transmission are very sought-after components in integrated optics. The experimental transmission reaches in the best case a flat plateau situated at $T = 0.25$. Nevertheless substantial insight could be gained by applying the temporal coupled mode theory. It yields valuable information about the trade-off between high-Q cavities (featuring sharp peaks in transmission) and large bandwidth. The optimum of coupling strength between the waveguide and the cavity depends mainly on the desired application (broad bandwidth or selectivity) and on the intrinsic cavity losses (*e.g.* if the losses are high, it is not a good idea to keep the light too long inside the cavity). In order to avoid undesired surprises like the present one, the final design should be tested by 2D FDTD before going into fabrication.

The last structure is a directional coupler, a structure widely used in conventional integrated optics with coupling lengths of the order of $0.1 - 0.5$ mm. The coupling length in these ridge waveguide-based couplers depend exponentially on the separation distance between the waveguides since the power transfer is due to evanescent wave coupling. The same high sensitivity on structural parameters could also be observed in PhC-based couplers. In the case of two W3 waveguides separated by a single row, the coupling length proved to be very dependent on the hole diameter in the single row. For this case the experimentally determined coupling length, which has been confirmed by both PWE and FDTD simulations, was of the order of 350 periods which corresponds to an absolute length of about 80 μm, a value that is small for conventional optics, but rather large for the domain of PhC optics where the propagation losses are usually much higher and the integrated circuit has to be kept small. This value could, however, be reduced by a factor of at least three when reducing the ratio R_i/R_0 to 0.5 .

In the investigated structures it appeared that the multimode nature of the utilised channel waveguides increases the complexity. Care has to be taken that at points of translational symmetry breaking higher-order modes are excited which feature higher propagation losses. On the other hand, the multimode nature adds novel functionalities, *e.g.* exploitation of the MSB.

In the last part of this thesis, a special kind of waveguide, the coupled cavity wave-guide (CCW), is investigated. A tight-binding model has been set-up that describes the interaction between the neighbouring cavities and that allows one to deduce the dispersion properties of the chain from the single cavity field distribution. The model has been successfully applied to three different types of CCWs.

The structures measured in the second part are certainly first iterations and far away from building blocks that could challenge conventional integrated optics. Even though the studied building blocks did not yield the expected performance, the study still allowed us to clarify a lot of open issues. The mask design has been based on some rough ideas, and has not been optimised by drastic modelling efforts. Nevertheless

the discussion and analysis of the experimental results showed a good agreement with today's modelling techniques, leaving room for further optimisation.

One should, however, not forget that once the building blocks for PhC-based integrated optics are established and tested, it will be a challenge to combine them. Especially in the investigated multimode systems the cascading of building blocks is not a straightforward task, because they will interact with each other in a complicated manner (*e.g.* by back-reflections, mode conversion). The knowledge of the transmittance of the individual building blocks is not sufficient, the modal transmission as well as the phase at the interface have to be matched.

One thing is certain, there is still a long way to go before the performance of conventional integrated optics is really challenged, which performs so well, but at high costs and with large space requirements.

Appendix A

Proof of the hermicity of the $\hat{\theta}$-operator

In this section the hermicity of the operator $\hat{\theta} = \nabla \times \left[\frac{1}{\varepsilon(\mathbf{r})} \nabla \times \right.$ is proved by using a procedure very similar to that used in Ref. [121].

$$
(\langle \mathbf{F} | \hat{\theta} |) \mathbf{G} \rangle = \int_{\Omega} dV \left[\nabla \times \underbrace{\left\{ \frac{1}{\varepsilon} \nabla \times \mathbf{F}^* \right\}}_{A} \right] \cdot \underbrace{\mathbf{G}}_{B} \tag{A.1}
$$

By using the vector identity

$$
\nabla \cdot (\mathbf{A} \times \mathbf{B}) = (\nabla \times \mathbf{A}) \cdot \mathbf{B} - \mathbf{A} \cdot (\nabla \times \mathbf{B}) \tag{A.2}
$$

and applying the Gauss divergence theorem, Eq. (A.1) transforms into:

$$
\begin{aligned}
(\langle \mathbf{F} | \hat{\theta} |) \mathbf{G} \rangle &= \underbrace{\int_{\partial \Omega} d\mathbf{S} \left\{ \frac{1}{\varepsilon(\mathbf{r})} \nabla \times \mathbf{F}^* \right\} \times \mathbf{G}}_{=0} + \int_{\Omega} dV \left\{ \frac{1}{\varepsilon(\mathbf{r})} \nabla \times \mathbf{F}^* \right\} \cdot \{ \nabla \times \mathbf{G} \} \\
&= \int_{\Omega} dV \left\{ \nabla \times \underbrace{\mathbf{F}^*}_{A} \right\} \cdot \underbrace{\left\{ \frac{1}{\varepsilon(\mathbf{r})} \nabla \times \mathbf{G} \right\}}_{B}
\end{aligned} \tag{A.3}
$$

The surface integral is equal to zero because: either the fields decay to zero at large distances, or the fields are periodic in the region of interest. By applying the vector identity and Gauss divergence theorem once more, one finally obtains

$$
\begin{aligned}
(\langle \mathbf{F} | \hat{\theta} |) \mathbf{G} \rangle &= \underbrace{\int_{\partial \Omega} d\mathbf{S} \, \mathbf{F}^* \times \left\{ \frac{1}{\varepsilon(\mathbf{r})} \nabla \times \mathbf{G} \right\}}_{=0} + \int_{\Omega} dV \, \mathbf{F}^* \cdot \left\{ \nabla \times \frac{1}{\varepsilon(\mathbf{r})} \nabla \times \mathbf{G} \right\} \\
&= \langle \mathbf{F} | (\hat{\theta} | \mathbf{G} \rangle) \qquad\qquad\qquad \square \quad q.e.d. \quad
\end{aligned} \tag{A.4}
$$

Appendix B

Proof that $\Re_{\frac{\pi}{3}}$ commutes with $\hat{\theta}$

The modes inside the PhC are described by the master equation for the magnetic field:

$$\underbrace{\nabla \times \frac{1}{\varepsilon(\mathbf{r})}\nabla \times}_{\hat{\theta}} \mathbf{H}_\omega(\mathbf{r}) = \left(\frac{\omega}{c}\right)^2 \mathbf{H}_\omega(\mathbf{r}) \tag{B.1}$$

In this appendix it is show that Eq. (B.1) is invariant to rotations by a symmetry angle, and thus $[\hat{\theta}, \Re_{\frac{\pi}{3}}] = 0$. Assuming that a given dielectric map possesses a hexagonal symmetry, *e.g.* a hexagonal cavity surrounded by triangular bulk PhC, then the dielectric map is invariant to a 60°-rotation described by the operator $\Re_{\frac{\pi}{3}}$. Substituting $\mathbf{r}$ by $\mathbf{r}' = R_{\frac{\pi}{3}}^{-1}\mathbf{r}$ inside the master equation is equivalent to rotating the dielectric map and the field profiles by 60°.

$$\nabla \times \frac{1}{\varepsilon(R_{\frac{\pi}{3}}^{-1}\mathbf{r})}\nabla \times \mathbf{H}_\omega(R_{\frac{\pi}{3}}^{-1}\mathbf{r}) = \left(\frac{\omega}{c}\right)^2 \mathbf{H}_\omega(R_{\frac{\pi}{3}}^{-1}\mathbf{r}) \tag{B.2}$$

Instead of rotating the coordinate system, one may also rotate the dielectric map and the field distributions:

$$\left(\nabla \times \Re_{\frac{\pi}{3}}\left(\frac{1}{\varepsilon(\mathbf{r})}\right)\nabla \times R_{\frac{\pi}{3}}\right)\mathbf{H}_\omega(\mathbf{r}) = \left(\frac{\omega}{c}\right)^2 R_{\frac{\pi}{3}}\mathbf{H}_\omega(\mathbf{r}) \tag{B.3}$$

Since $\Re_{\frac{\pi}{3}}(1/\varepsilon) = 1/\varepsilon$ Eq. (B.3) can be written as

$$\Re_{\frac{\pi}{3}}^{-1}\left(\nabla \times \frac{1}{\varepsilon(\mathbf{r})}\nabla \times\right)\Re_{\frac{\pi}{3}}\mathbf{H}_\omega(\mathbf{r}) = \left(\frac{\omega}{c}\right)^2 \mathbf{H}_\omega(\mathbf{r}) \tag{B.4}$$

$$\longrightarrow \quad \Re_{\frac{\pi}{3}}^{-1}\hat{\theta}\Re_{\frac{\pi}{3}}\mathbf{H}_\omega(\mathbf{r}) = \left(\frac{\omega}{c}\right)^2 \mathbf{H}_\omega(\mathbf{r}) \tag{B.5}$$

By comparing again with Eq. B.1, one notes that

$$\hat{\theta} = \Re_{\frac{\pi}{3}}^{-1}\hat{\theta}\Re_{\frac{\pi}{3}} \quad \rightarrow \quad \Re_{\frac{\pi}{3}}\hat{\theta} = \hat{\theta}\Re_{\frac{\pi}{3}} \quad \rightarrow \quad [\hat{\theta}, \Re_{\frac{\pi}{3}}] = 0 \tag{B.6}$$

$$\square \quad q.e.d.$$

Bibliography

[1] J. D. Joannopoulos, R. D. Maede, and J. N. Winn, *Photonic crystals: Molding the flow of light*, Princeton Univ. Press, 1995.

[2] E. Yablonovitch, "Inhibited Spontaneous Emission in Solid-State Physics and Electronics", *Phys. Rev. Lett.*, vol. 58, no. 20, pp. 20592062, 1987.

[3] S John, "Strong localization of photons in certain disordered dielectric superlattices", *Phys. Rev. Lett.*, vol. 58, pp. 2486–2489, 1987.

[4] M Moroditsky, "Spontaneous emission extraction and Purcell enhancement from thin-film 2-D photonic crystals", *J. Lightwave Technol.*, vol. 17, pp. 2096–2112, 1999.

[5] E Yablanovitch, , *J. Phys. Condens. Matter*, vol. 5, no. 16, pp. 2443–2460, 1993.

[6] E.M. Purcell, "Spontaneous Emission Probabilities at Radio Frequencies", *Phys. Rev.*, vol. 69, no. 12, pp. 681, 1946.

[7] J.M. Gérard, "Quantum optics: Boosting photon storage", *Nature Materials*, vol. 2, no. 3, pp. 140–141, 2003.

[8] "Proceeding of a NATO Advanced Study Institute on Quantum Optics in Wavelength Scale Structures, Cargèse Corsica", 1995, Kluwer Academic Publishers.

[9] "Proceedings of the NATO Advanced Study Institute on Photonic Crystals and Light Localization in the 21st Century.", 2000, Kluwer Academic Publishers.

[10] J. D. Joannopoulos, P.R. Villeneuve, and S. Fan, "Photonic crystals: putting a new twist on light", *Nature*, vol. 386, no. 6621, pp. 143–149, 1997.

[11] T.E. Sale, *Vertical cavity surface emitting lasers*, Research Studies Press. Taunton, Somerset, England, 1995.

[12] J. N. Winn, Y. Fink, S. Fan, and J. D. Joannopoulos, "Omnidirectional reflection from a one-dimensional photonic crystal", *Opt. Lett.*, vol. 23, no. 20, pp. 1573–1575, 1998.

[13] Y. Fink, J. N. Winn, S. Fan, Ch. Chen, J. Michel, J.D. Joannopoulos, and E.L. Thomas, "A Dielectric Omnidirectional Reflector", *Science*, vol. 282, no. 5394, pp. 1679–1682, 1998.

[14] A. Birner, R.B. Wehrspohn, U.M. Gösele, and K. Busch, "Silicon-based photonic crystals", *Adv. Mater.*, vol. 6, no. 16, pp. 377–388, 2001.

[15] K Okamoto, *Fundamentals of Optical Waveguides*, Academic Press, New York, 2000.

[16] E. Chow, S. Y. Lin, S. G. Johnson, P.R. Villeneuve, J. D. Joannopoulos, J. R. Wendt, G.A. Vawter, W. Zubrzycki, H. Hou, and A. Alleman, "Three-dimensional control of light in a two-dimensional photonic crystal slab", *Nature*, vol. 407, no. 6807, pp. 983–986, 2000.

[17] N Kawai, K. Inoue, N. Carlsson, N. Ikeda, Y. Sugimoto, and K. Asakawa, "Confined Band Gap in an Air-Bridge Type of Two-Dimensional AlGaAs Photonic Crystal", *Phys. Rev. Lett.*, vol. 86, no. 11, pp. 2289–2292, 2001.

[18] M. Agio, *Optical Properties and Wave Propagation in Semiconductor-Based Two-Dimensional Photonic Crystals*, Ph.D. thesis, Università degli Studi di Pavia, Pavia, Italy and Iowa State University, Ames, Iowa, 2003.

[19] M. Qiu, "Effective index method for heterostructure-slab-waveguide-based two-dimensional photonic crystals", *Appl. Phys. Lett.*, vol. 81, no. 7, pp. 1163–1165, 2002.

[20] W. Bogaerts, P. Bienstman, D. Taillaert, R. Baets, and D. De Zutter, "Out-of-plane scattering in photonic crystal slabs", *IEEE Phot. Technol. Lett.*, vol. 13, no. 6, pp. 565–567, 2001.

[21] K. M. Ho, C. T. Chan, and C. M. Soukoulis, "Existence of a photonic gap in periodic dielectric structures", *Phys. Rev. Letters*, vol. 65, no. 25, pp. 3152, 1990.

[22] E Yablonovitch, T.J. Gmitter, and K.M. Leung, "Photonic band structure: The face-centered-cubic case employing nonspherical atoms", *Phys. Rev. Lett.*, vol. 67, no. 17, pp. 2295–2298, 1991.

[23] A. Chelnokov, K. Wang, S. Rowson, P Garoche, and J.-M. Lourtioz, "Near-infrared Yablonovite-like photonic crystals by focused-ion-beam etching of macroporous silicon", *Appl. Phys. Lett.*, vol. 77, no. 19, pp. 2943–2945, 2000.

[24] S. Y. Lin, J. G. Fleming, D.L. Hetherington, B.K. Smith, R. Biswas, K. M. Ho, M. M. Sigalas, W. Zubrzycki, S.R. Kurtz, and J. Bur, "A three-dimensional photonic crystal operating at infrared wavelengths", *Nature*, vol. 394, no. 6690, pp. 251–253, 1998.

[25] S. Noda, K. Tomoda, N. Yamamoto, and A. Chutinan, "Full Three-Dimensional Photonic Bandgap Crystals at Near-Infrared Wavelengths", *Science*, vol. 289, no. 5479, pp. 604–606, 2000.

[26] B.H. Cumpston, P.S. Ananthavel, S. Barlow, D.L. Dyer, J.E. Ehrlich, L.L. Erskine, A.A. Heikal, S.M. Kuebler, I.-Y. S. Lee, D. Mccord-Maughon, J. Qin, H. Röckel, M. Rumi, X.-L. Wu, S.R. Marder, and J.W. Perry, "Two-photon polymerization initiators for three-dimensional optical data storage and microfabrication", *Nature*, vol. 398, no. 6722, pp. 51–54, 1999.

[27] S. G. Johnson and J. D. Joannopoulos, "Three-dimensionally periodic dielectric layered structure with omnidirectional photonic band gap", *Appl. Phys. Lett.*, vol. 77, no. 22, pp. 3490–3492, 2000.

[28] J. D. Joannopoulos, "Self-assembly lights up", *Nature*, vol. 414, no. 6861, pp. 257–258, 2001.

[29] Y.A. Vlasov, X.-Z. Bo, J.C. Sturm, and D.J. Norris, "On-chip natural assembly of silicon photonic bandgap crystals", *Nature*, vol. 414, no. 6861, pp. 289–293, 2001.

[30] C. Kittel, *Introduction to Solid State Physics*, John Wiley and Sons, New York, fourth corrected printing edition, 1953.

[31] D. Labilloy, *Cristaux photoniques bidimensionnels pour le proche infrarouge: propriétés optiques et confinement*, Ph.D. thesis, Ecole Polytechnique Palaiseau, 1999.

[32] F. Pommerau, L. Le Gouezigou, S. Hubert, S. Sainson, J.-P. Chandouineau, S. Fabre, and G.-H. Duan, "Fabrication of low loss two-dimensional InP photonic crystals by inductively coupled plasma etching", *J. Appl. Phys.*, vol. 95, no. 5, pp. 1–4, 2004.

[33] T. F. Krauss, C. J. M. Smith, S. Vögele, K. Murad, C. D. W. Wilkinson, R. S. Grant, M. G. Burt, and R. M. De La Rue, "Two-dimensional waveguide-based photonic microstructures in GaAs and InP", *J. of Microel. Eng.*, vol. 35, no. 1, pp. 29–32, 1997.

[34] J. Moosburger, M. Kamp, A. Forchel, R. Ferrini, D. Leuenberger, R. Houdré, S. Anand, and J. Berggren, "Nanofabrication of high quality photonic crystals for integrated optics circuits", *Nanotechnology*, vol. 13, no. 3, pp. 341–345, 2002.

[35] T. D. Happ, A. Markard, M. Kamp, A. Forchel, S. Anand, J. L. Gentner, and N. Bouadma, "Nanofabrication of two-dimensional photonic crystal mirrors for 1.5 mu m short cavity lasers", *J. Vac. Sci. Technol. B*, vol. 19, no. 6, pp. 2775–2778, 2001.

[36] M. Mulot, S. Anand, R. Ferrini, B. Wild, R. Houdré, J. Moosburger, and A. Forchel, "Fabrication of 2D InP-based photonic crystals by chlorine based chemically assisted ion beam etching", *to be published*, 2004.

[37] M. Mulot, S. Anand, C. F. Carlstrom, M. Swillo, and A. Talneau, "Dry etching of photonic crystals in InP based materials", *Phys. Scripta*, vol. T101, pp. 106–109, 2002.

[38] *Handbook of Microlithography, Micromachining, and Microfabrication:*, vol. 1, SPIE Optical Engineering Press, Washington, 1997.

[39] L. F. Thompson, C. G. Willson, and M. J. Bowden, *Introduction to microlithography*, ACS professional reference book. American Chemical Society, Washington, DC, 2nd edition, 1994.

[40] R Wüest, P Strasser, M Jungo, F Robin, D Erni, and H. Jäckel, "An efficient proximity-effect correction method for electron-beam patterning of photonic-crystal devices", *Microelectronic Engineering*, vol. 67-68, pp. 182–188, 2003.

[41] R. Ferrini, D. Leuenberger, M. Mulot, M. Qiu, J. Moosburger, M. Kamp, A. Forchel, S. Anand, and R. Houdré, "Optical study of two-dimensional InP-based photonic crystals by internal light source technique", *IEEE J. Quantum Electron.*, vol. 38, no. 7, pp. 786–799, 2002.

[42] D. J. Economou, "Modeling and simulation of plasma etching reactors for microelectronics", *Thin Sol. Films*, vol. 365, no. 2, pp. 148–367, 2000.

[43] C. Cardinaud, M.-C. Peignon, and Tessier P.-Y., "Plasma etching: principles, mechanisms, application to micro- and nano-technologies", *Appl. Surf. Sci.*, vol. 164, no. 1, pp. 72–83, 2000.

[44] J. Moosburger, M. Kamp, A. Forchel, S. Olivier, H. Benisty, C. Weisbuch, and U. Oesterle, "Enhanced transmission through photonic-crystal-based bent waveguides by bend engineering", *Appl. Phys. Lett*, vol. 79, no. 22, pp. 3579–3581, 2001.

[45] R. Ferrini, B. Lombardet, B. Wild, R. Houdré, S. Olivier, H. Benisty, A. Djoudi, L. Legouézigou, S. Hubert, S. Sainson, J.-P. Chandouineau, S. Fabre, F. Pommerau, and G.-H. Duan, "Optical characterisation of 2D InP-based photonic crystals fabricated by inductively coupled plasma etching.", *Electron. Lett.*, vol. 38, no. 17, pp. 962–964, 2002.

[46] M. Mulot, S. Anand, M. Swillo, M. Qiu, B. Jaskorzynska, and A. Talneau, "Low-loss InP-based photonic-crystal waveguides etched with Ar/Cl-2 chemically assisted ion beam etching", *J. Vac. Sci. Technol. B*, vol. 21, no. 2, pp. 900–903, 2003.

[47] M. Mulot, "Private communication", 06.06.2003 2003.

[48] H. Benisty, C. Weisbuch, D. Labilloy, M. Rattier, C. J. M. Smith, T. F. Krauss, R. M. De La Rue, R. Houdré, U. Oesterle, C. Jouanin, and D. Cassagne, "Optical and Confinement Properties of Two-Dimensional Photonic Crystals", *J. Lightwave Technol.*, vol. 17, no. 11, pp. 2063–2077, 1999.

[49] D. Labilloy, H. Benisty, C. Weisbuch, T. F. Krauss, R. Houdré, and U. Oesterle, "Use of guided spontaneous emission of a semiconductor to probe the optical properties of two-dimensional photonic crystals", *Appl. Phys. Lett.*, vol. 71, no. 6, pp. 738–740, 1997.

[50] D. Labilloy, H. Benisty, C. Weisbuch, T. F. Krauss, R. M. DeLaRue, V. Bardinal, R. Houdré, U. Oesterle, D. Cassagne, and C. Jouanin, "Quantitative measurement of transmission, reflection, and diffraction of two-dimensional photonic band gap structures at near-infrared wavelengths", *Phys. Rev. Lett.*, vol. 79, no. 21, pp. 4147–4150, 1997.

[51] D. Labilloy, H. Benisty, C. Weisbuch, T. F. Krauss, D. Cassagne, C. Jouanin, R. Houdré, U. Oesterle, and V. Bardinal, "Diffraction efficiency and guided light control by two-dimensional photonic-bandgap lattices", *IEEE J. Quantum Electron.*, vol. 35, no. 7, pp. 1045–1052, 1999.

[52] D. Labilloy, H. Benisty, C. Weisbuch, C. J. M. Smith, T. F. Krauss, R. Houdré, and U. Oesterle, "Finely resolved transmission spectra and band structure of two-dimensional photonic crystals using emission from InAs quantum dots", *Phys. Rev. B*, vol. 59, no. 3, pp. 1649–1652, 1999.

[53] D. Labilloy, H. Benisty, C. Weisbuch, T. F. Krauss, V. Bardinal, and U. Oesterle, "Demonstration of cavity mode between two-dimensional photonic-crystal mirrors", *Electron. Lett.*, vol. 33, no. 23, pp. 1978–1980, 1997.

[54] C. J. M. Smith, H. Benisty, S. Olivier, M. Rattier, C. Weisbuch, T. F. Krauss, R. M. De La Rue, R. Houdré, and U. Oesterle, "Low-loss channel waveguides with two-dimensional photonic crystal", *Appl. Phys. Lett*, vol. 77, no. 18, pp. 2813–2815, 2000.

[55] H. Benisty, S. Olivier, C. Weisbuch, M. Agio, M. Kafesaki, C. M. Soukoulis, Qiu Min, M. Swillo, A. Karlsson, B. Jaskorzynska, A. Talneau, R. Moosburger, M. Kamp, A. Forchel, R. Ferrini, R. Houdré, and U. Oesterle, "Models and measurements for the transmission of submicron-width waveguide bends defined in two-dimensional photonic crystals", *IEEE J. Quantum Electron.*, vol. 38, no. 7, pp. 770–785, 2002.

[56] S. Olivier, *Nouvelles structures miniatures dans les cristaux photoniques bidimensionels planaires pour les fonctions de l'optique intégrée*, Ph.D. thesis, Université Paris 6, 2002.

[57] R. Ferrini, D. Leuenberger, M. Mulot, M. Qiu, J. Moosburger, M. Kamp, A. Forchel, S. Anand, and R. Houdré, "Optical study of 2D photonic crystals in an InP/GaInAsP slab waveguide structure", *Mat. Res. Soc. Symp. Proc.*, vol. 692, pp. K6.3.1–K6.3.6, 2002.

[58] R. Ferrini, B. Lombardet, B. Wild, R. Houdré, and G.-H. Duan, "Hole depth- and shape-induced radiation losses in two-dimensional photonic crystals", *Appl. Phys. Lett.*, vol. 82, no. 7, pp. 1009–1011, 2003.

[59] R. Ferrini, R. Houdré, H. Benisty, M. Qiu, and J. Moosburger, "Radiation losses in planar photonic crystals: two-dimensional representation of hole depth and shape by an imaginary dielectric constant", *J. Opt. Soc. Am. B*, vol. 20, no. 3, pp. 469–478, 2003.

[60] W. Lukosz, "Light emitted by multipole sources in thin layers. I. Radiation patterns of electric and magnetic dipoles", *J. Opt. Soc. Am.*, vol. 71, pp. 744–754, 1981.

[61] R. P. Stanley, H. Benisty, and M. Mayer, "Method of source terms for dipole emission modification in modes of arbitrary planar structures", *J. Opt. Soc. Am. A*, vol. 15, pp. 1192–1201, 1998.

[62] G. Bastard, *Wave Mechanics Applied to Semiconductor Heterostructures*, Les editions de Physique, Paris, France, 1992.

[63] R. P. Stanley, R. Houdré, U. Oesterle, M. Gailhanou, and M. Ilegems, "Ultra-high Finesse Microcavity with Distributed Bragg Reflectors", *Appl. Phys. Lett.*, vol. 65, no. 15, pp. 1883–1885, 1994.

[64] C. J. M. Smith, R. M. De la Rue, H. Benisty, U. Oesterle, T. F. Krauss, D. Labilloy, C. Weisbuch, and R. Houdré, "In-plane microcavity resonators with two-dimensional photonic bandgap mirrors", *IEE Proc.-Optoelectron.*, vol. 145, no. 6, pp. 373–378, 1998.

[65] M. Rattier, H. Benisty, C. J. M. Smith, A. Beraud, D. Cassagne, C. Jouanin, T. F. Krauss, and C. Weisbuch, "Performance of waveguide-based two-dimensional photonic-crystal mirrors studied with Fabry-Perot resonators", *IEEE J. Quantum. Electron.*, vol. 37, no. 2, pp. 237–243, 2001.

[66] B. E. A. Saleh and M. C. Teich, *Fundamentals of Photonics*, Wiley, New York, 1991.

[67] M. Born and E. Wolf, *Principles of Optics*, Pergamon Press, Oxford, U.K., 1980.

[68] M. Qiu, B. Jaskorzynska, M. Swillo, and H. Benisty, "Time-domain 2D modeling of slab-waveguide-based photonic-crystal devices in the presence of radiation losses", *Microwave and Optical Technology Letters*, vol. 34, no. 5, pp. 387–393, 2002.

[69] H. Benisty, D. Labilloy, C. Weisbuch, C. J. M. Smith, T. F. Krauss, D. Cassagne, A. Béraud, and C. Jouanin, "Radiation losses of waveguide-based two-dimensional photonic crystals: Positive role of the substrate", *Appl. Phys. Lett*, vol. 76, no. 5, pp. 532–534, 2000.

[70] H. Benisty, Ph. Lalanne, S. Olivier, M. Rattier, C. Weisbuch, C. J. M. Smith, T. F. Krauss, C. Jouanin, and D. Cassagne, "Finite-depth and intrinsic losses in vertically etched two-dimensional photonic crystals", *Opt. Quantum Electron.*, vol. 34, pp. 205–215, 2002.

[71] A. Talneau, L. Le Gouezigou, and N. Bouadma, "Spectrally resolved transmission measurements for quantitative evaluation of photonic crystal guiding structures", in *PECS3*, St. Andrews, U.K., 2001.

[72] J.D. Jackson, *Classical Electrodynamics*, J. Wiley and Sons, Inc., New York, second edition edition, 1962.

[73] M. Plihal and A. A. Maradudin, "Photonic band structure of two-dimensional systems: The triangular lattice.", *Phys. Rev. B*, vol. 44, no. 16, pp. 8565–8571, 1991.

[74] H. S. Sözüer, J. W. Haus, and R. Inguva, "Photonic bands: Convergence problems with the plane-wave method", *Phys. Rev. B*, vol. 45, no. 22, pp. 13962–13972, 1992.

[75] H. Benisty, "Private communication", 2000.

[76] E. Hewitt and R. Hewitt, "The Gibbs-Wilbraham Phenomenon: An Episode in Fourier Analysis", *Arch. Hist. Exact Sci.*, vol. 21, pp. 129–160, 1980.

[77] L. Li, "Use of Fourier series in the analysis of discontinuous periodic structures", *J. Opt. Soc. Am. A*, vol. 13, no. 9, pp. 1870–1876, 1996.

[78] P.R. Villeneuve, "Photonic bandgaps: what is the best numerical representation of periodic structures?", *J. Modern Opt.*, vol. 41, no. 2, pp. 241–256, 1994.

[79] M. Doosje, J. Hoenders, and J. Knoester, "Photonic bandgap optimization in inverted fcc photonic crrystals", *J. Opt. Soc. Am. B*, vol. 17, no. 4, pp. 600–606, 2000.

[80] K. Sakoda, "Optical transmittance of two-dimensional triangular photonic lattice", *Phys. Rev. B*, vol. 51, no. 7, pp. 4672–4675, 1995.

[81] K. Sakoda, "Transmittance and Bragg reflectivity of two-dimensional photonic lattices.", *Phys. Rev. B*, vol. 15, no. 12, pp. 89929002, 1995.

[82] C. M. Soukoulis, "Private communication", 2001.

[83] S. Olivier, M. Rattier, H. Benisty, C. Weisbuch, C. J. M. Smith, R. M. De La Rue, T. F. Krauss, U. Oesterle, and R. Houdré, "Mini-stopbands of a one-dimensional system: The channel waveguide in a two-dimensional photonic crystal", *Phys. Rev. B*, vol. 63, pp. 113311, 2001.

[84] M. Notomi, A. Shinya, K. Yamada, J.-I. Takahashi, C. Takahashi, and I. Yokohama, "Structural tuning of guiding modes of line-defect waveguides of silicon-on-insulator photonic crystal slabs", *IEEE J. Quantum Electron.*, vol. 38, no. 7, pp. 736–742, 2002.

[85] P. Yeh, *Optical waves in layered media*, John Wiley and Sons, 1988.

[86] Th. Tamir, *Guided-Wave Optoelectronics*, vol. 26 of *Springer Series in Electronics and Photonics*, Springer-Verlag, New York, 1988.

[87] H. A. Haus, *Waves and fields in Optoelectronics*, Prentice-Hall, 1984.

[88] S. Olivier, H. Benisty, C. Weisbuch, C. J. M. Smith, T. F. Krauss, and R. Houdré, "Coupled-mode theory and propagation losses in photonic crystal waveguides", *Optics Express*, vol. 11, no. 13, pp. 1490–1496, 2003.

[89] S. Olivier, H. Benisty, C. Weisbuch, C. J. M. Smith, T. F. Krauss, R. Houdré, and U. Oesterle, "Improved 60 degrees bend transmission of submicron-width waveguides defined in two-dimensional photonic crystals", *J. Lightwave Technol.*, vol. 20, no. 7, pp. 1198–1203, 2002.

[90] R. L. Espinola, F. P. Ahmad, M. J. Steel, and R. M. Osgood, "A study of high-index-contrast 90 degree waveguide bend structures", *Opt. Lett.*, vol. 8, no. 9, pp. 517–528, 2001.

[91] S. Olivier, H. Benisty, M. Rattier, C. Weisbuch, M. Qiu, A. Karlsson, C. J. M. Smith, R. Houdré, and U. Oesterle, "Resonant and nonresonant transmission through waveguide bends in a planar photonic crystal", *Appl. Phys. Lett*, vol. 79, no. 16, pp. 2514–2516, 2001.

[92] C. J. M. Smith, H. Benisty, D. Labilloy, U. Oesterle, R. Houdré, T. F. Krauss, R. M. De La Rue, and C. Weisbuch, "Near-infrared microcavities confined by two-dimensional photonic bandgap crystals", *Electron. Lett.*, vol. 35, no. 3, pp. 228–230, 1999.

[93] C. J. M. Smith, T. F. Krauss, H. Benisty, M. Rattier, C. Weisbuch, U. Oesterle, and R. Houdré, "Directionally dependent confinement in photonic-crystal microcavities", *J. Opt. Soc. Am. B*, vol. 17, no. 12, pp. 2043–2051, 2000.

[94] O. J. Painter, *Optical Nanocavities in Two-Dimensional Photonic Crystal Planar Waveguides*, Ph.D. thesis, California Institute of Technology, 2001.

[95] S. Fan, S. G. Johnson, J. D. Joannopoulos, C. Manolatou, and H. A. Haus, "Waveguide branches in photonic crystals", *J. Opt. Soc. Am. B*, vol. 18, no. 2, pp. 162–165, 2001.

[96] K Kurokawa, *An introduction to the theory of microwave circuits*, Academic, New York, 1969.

[97] F. Cuesta, A. Griol, A. Martinez, and J. Marti, "Experimental demonstration of photonic crystal directional coupler at microwave frequencies", *Electronics Letters*, vol. 39, no. 5, pp. 455–456, 2003.

[98] A. Sharkawy, S. Y. Shi, D. W. Prather, and R. A. Soef, "Electro-optical switching using coupled photonic crystal waveguides", *Optics Express*, vol. 10, no. 20, pp. 1048–1059, 2002.

[99] A. Martinez, F. Cuesta, and J. Marti, "Ultrashort 2-D photonic crystal directional couplers", *IEEE Photonics Technol. Lett.*, vol. 15, no. 5, pp. 694–696, 2003.

[100] C. Cohen-Tannoudji, B. Diu, and L Lalo, *Mécanique quantique*, vol. 1, Hermann, 1996, Paris, 1996.

[101] S. Olivier, C. Weisbuch, and H. Benisty, "Compact and fault-tolerant photonic crystal add-drop filter", *Opt. Lett.*, vol. 28, no. 22, pp. 2246–2248, 2003.

[102] R.C. Alferness, R.V. Schmidt, and E. H. Turner, "Characteristics of Ti diffused $LiNb0_3$ optical directional couplers", *Appl. Opt.*, vol. 18, pp. 4012, 1979.

[103] S. Boscolo, M. Midrio, and C. G. Someda, "Coupling and decoupling of electromagnetic waves in parallel 2- D photonic crystal waveguides", *Ieee Journal of Quantum Electronics*, vol. 38, no. 1, pp. 47–53, 2002.

[104] T. F. Krauss, T. Baba, and editors, "Feature section on Photonic Crystal Structures and Applications", *IEEE J. Quantum Electron.*, vol. 38, no. 7, 2002.

[105] U. Peschel, A. L. Reynolds, B. Arredondo, F. Lederer, P. J. Roberts, T. F. Krauss, and P. J. I. de Maagt, "Transmission and reflection analysis of functional coupled cavity components", *IEEE J. Quantum Electron.*, vol. 38, no. 7, pp. 830–836, 2002.

[106] N. Stefanou and A. Modinos, "Impurity bands in photonic insulators", *Phys. Rev. B*, vol. 57, no. 19, pp. 12127–12133, 1998.

[107] A. Yariv, Y. Xu, R. K. Lee, and A. Scherer, "Coupled-resonator optical waveguide: a proposal and analysis", *Opt. Lett.*, vol. 24, no. 11, pp. 711–713, 1999.

[108] S. Olivier, C. J. M. Smith, M. Rattier, H. Benisty, C. Weisbuch, T. F. Krauss, R. Houdré, and U. Oesterle, "Miniband transmission in a photonic crystal coupled-resonator optical waveguide", *Opt. Lett.*, vol. 26, no. 13, pp. 1019–1021, 2001.

[109] A. Boag and B. Z. Steinberg, "Narrow-band microcavity waveguides in photonic crystals", *J. Opt. Soc. Am. A*, vol. 18, no. 11, pp. 2799–2805, 2001.

[110] Y. Xu, R. K. Lee, and A. Yariv, "Propagation and second-harmonic generation of electromagnetic waves in a coupled-resonator optical waveguide.", *J. Opt. Soc. Am. B*, vol. 17, no. 3, pp. 387–400, 2000.

[111] S. Mookherjea and A. Yariv, "Second-harmonic generation with pulses in a coupled-resonator optical waveguide", *Phys. Rev. E*, vol. 65, no. 2, pp. 026607–1, 2002.

[112] S. Mookherjea and A. Yariv, "Optical pulse propagation and holographic storage in a coupled-resonator optical waveguide", *Phys. Rev. E*, vol. 64, no. 6, pp. 066602–1, 2001.

[113] N. W. Ashcroft and N. D. Mermin, *Solide State Physics*, Academic Press, 1976.

[114] E. Lidorikis, M. M. Sigalas, E. N. Economou, and C. M. Soukoulis, "Tight-binding parametrization for photonic band gap materials", *Phys. Rev. Letters*, vol. 81, no. 7, pp. 1405–1408, 1998.

[115] T. J. Karle, D. H. Brown, R. Wilson, M. Steer, and T. F. Krauss, "Planar photonic crystal coupled cavity waveguides", *J. Select. Top. Quantum Electron.*, vol. 8, no. 4, pp. 909–918, 2002.

[116] M Bayindir and E. Ozbay, "Heavy photons at coupled-cavity waveguide band edges in a three-dimensional photonic crystal", *Phys. Rev. B*, vol. 62, no. 4, pp. R2247–R2250, 2000.

[117] C. Weisbuch and B. Vinter, *Quantum Semiconductor Structures*, Academic Press, 1995.

[118] P. Sanchis, J. Garcia, A. Martinez, F. Cuesta, A. Griol, and J. Marti, "Analysis of adiabatic coupling between photonic crystal single-line-defect and coupled-resonator optical waveguides", *Opt. Lett.*, vol. 28, no. 20, pp. 1903–1905, 2003.

[119] A. Martinez, F. Cuesta, A. Griol, D. Mira, J. Garcia, P. Sanchis, R. Llorente, and J. Marti, "Photonic-crystal 180° splitter based on coupled-cavity waveguides", *Appl. Phys. Lett.*, vol. 83, no. 15, pp. 3033–3035, 2003.

[120] A. Martinez, A. Griol, P. Sanchis, and J. Marti, "Mach-Zehnder interferometer employing coupled-resonator optical waveguides", *Opt. Lett.*, vol. 28, no. 6, pp. 405, 2003.

[121] K. Sakoda and K. Ohtaka, "Optical response of three-dimensional photonic lattices: Solutions of inhomogeneous Maxwells equations and their applications", *Phys. Rev. B*, vol. 54, no. 8, pp. 5732–5741, 1996.

Publications

. R. Ferrini, D. Leuenberger, M. Mulot, M. Qiu, J. Moosburger, M. Kamp, A. Forchel, S. Anand, and R. Houdré: " Optical study of two-dimensional InP-based photonic crystals by internal light source technique", IEEE J. Quantum Electron. 38 (7), 786-799 (2001).

. R. Ferrini, D. Leuenberger, M. Mulot, M. Qiu, J. Moosburger, M. Kamp, A. Forchel, S. Anand, and R. Houdré: " Optical study of 2D photonic crystals in an InP/GaInAsP slab waveguide structure", MRS Meeting 2001.

. J. Moosburger, M. Kamp, A. Forchel, R. Ferrini, D. Leuenberger, R. Houdré, S. Anand and J. Berggren, "Nanofabrication of high quality photonic crystals for integrated optics circuits", Nanotechnology 13, 341-345 (2002).

. R. Ferrini, B. Wild, B. Lombardet, D. Leuenberger, R. Houdré and H. Benisty, "Out-of-plane losses in bi-dimensional photonic crystals: analytical model and optical measurements", Fourth workshop on photonic and electromagnetic crystal structures (PECS IV), Los Angeles, USA (2002).

. D. Leuenberger, R. Ferrini and R. Houdré: " Tight-binding approach for photonic crystal-based coupled cavity waveguides", J. Appl. Phys. 95 (3), 806-809 (2004).

Conferences and workshops

. Summer school on "Photonic Crystals and light localization", NATO Advanced Study Institute, June 19-30, 2000, Crete, Greece.

. Electromagnetic Crystal Structures - EuroConference on Electromagnetic Confinement From Basic Research to the Marketplace, June 9-14 2001, St. Andrews, Scotland (poster presentation).

. Workshop and EOS Topical meeting on "Two Dimensional Photonic Crystals" August 25-30, 2002 Monte Verità, Ascona, Switzerland (poster presentation).

Acknowledgements

I would like to take this opportunity to thank all the people that have made this thesis possible. First and foremost, I would like to thank Dr. Romuald Houdré as my supervisor for having accepted me in his research group. He is a passionate physician with a strong flair for the beauty and the aesthetic aspects of photonic crystals and of physics in general. He always took the time when I needed his help. Dr. Rolando Ferrini, on the other hand, was of invaluable help for various aspects of my thesis. He provided me with practical advice concerning the optical characterisation of PhC samples and many other things (*e.g.* the correct cooking of Italian pasta). To him I owe the beautiful ILS setup whose performance and reliability are unsurpassed, yes the setup belongs to the 'Rolls Royce' category. Both of them I acknowledge for proofreading the manuscript.

Many thanks go also to the newer members of the PhC group, namely Dr. L. Andrea Dunbar, Benoît Lombardet and Barbara Wild for their kind support and the helpful discussions. Especially the fresh, buddy-like manner of Andrea with a blend of British humour contributed a lot to a relaxed but nevertheless productive atmosphere in the group.

I acknowledge also Prof. M. Ilegems for dealing with all the financial aspects of my thesis as well as his paternal way of motivating and putting me on my feet again when things were at their worst.

Finally, I would like to thank all the people involved in the PCIC project. It was a very fruitful collaboration bringing together the competence from different European universities with differently thinking people; an illustrative example of what Europe actually stands for. Especially I acknowledge Prof. Alfred Forchel for providing me with the necessary samples. My special thanks go to Dr. Mario Agio for his generosity in providing me with his FDTD code which was of inestimable value for the analysis of the characterisation results. Many thanks also go to Dr. Ségolène Olivier and to Prof. Henry Benisty from EPP for helping me to set up the PWE method and for the many helpful discussions.

A thesis is also a psychological challenge and one has to find the proper life-work balance. I often recharged my batteries in the Sat with Alex, Lars, Blandine and Cyril as well as during the famous Friday nights in the Bossette. During summer the social life was dominated by the various nice barbecues on the lake shore. It was also a great enrichment to get to know people outside the 'cake' not doing physics, Barbara, Julie and Christiane, I will never forget you.

I acknowledge Reto, one of the kindest persons I know, for the successful office sharing.

I would also like to mention the 'centre nautique' and its staff (especially Pepe) who

199

provided an oasis in the hectic academic world. A sailing tour (my preferred sport) on Lac Léman with my sailing partners was the best way for me to switch off.

Another enriching and stimulating environment was my music group 'ORjazzM' which I started from scratch when I arrived with my double-bass in Lausanne. Thank you guys and may 'ORjazzM' last forever!

Last but not least, I would like to give a big hug to my family for all the care and support they gave me during the last 29 years. Without them I would definitely not be where I am now.

Curriculum vitae

David Leuenberger

Address (office):	EPFL/SB/IPEQ/LPDS
	Ecole polytechnique fédérale Lausanne
	CH-1015 Lausanne, Switzerland
Phone (office):	+41 21 693 44 22
Fax (office):	+41 21 693 54 90
e-Mail:	david.leuenberger@epfl.ch
Address (home):	Dorfstrasse 53, CH-3032 Hinterkappelen
Birth date:	10$^{\text{th}}$ February 1975
Native place:	Rohrbachgraben (BE)
Nationality:	Swiss

Education

2000-2004	PhD studies at the Swiss Federal Institute of Technology Lausanne (EPFL) on "Photonic crystals for integrated optics" in the framework of the European project PCIC (Information Society Technology). The emphasis is on optical characterisation and modelling.
2000	Diploma in physics from the University of Bern, Switzerland Diploma work on "Investigation of novel pumping schemes for solid state lasers".
1995	Matura from the Scientific Gymnasium Neufeld in Bern, Switzerland.

Internships

1998	Two months of practical work at CSEM in Neuchâtel in the sector "Photonic Microsystems"